Nonlinear Dynamics of Hanging Tubular Cantilevers Subjected to Internal and External Axial Flows

Ahmed Rabie Abdelaziz Abdelbaki

Doctor of Philosophy

Department of Mechanical Engineering

McGill University

Montreal, Québec, Canada

December 2019

A thesis submitted to McGill University in partial fulfillment of the requirements of the degree of Doctor of Philosophy

ABSTRACT

A pipe conveying fluid is a typical example of a fluid-structure-interaction problem, in which the pipe becomes unstable at sufficiently high flow velocities via static divergence or oscillatory motion, namely flutter, depending on the boundary conditions. That particular system has been under study for almost a century and it has become a paradigm in dynamics, especially the cantilevered pipe, not only because of the rich dynamics that this system exhibits, but also for its industrial importance. In addition, the stability of a cantilevered cylindrical structure subjected to axial flow has been investigated over decades; a relatively recent challenge is to consider the inverted problem, in which the upstream end of the cylinder is free and the downstream one is clamped. This inverted system was found to lose stability via flutter at low flow velocities, with potential applications in energy harvesting.

Examining the dynamics of a cantilevered pipe simultaneously subjected to internal and inverted external axial flows is the main objective of this thesis. This system has several industrial applications, such as heat exchangers, drill-strings, and brine-strings that are used in solution mining; moreover, in this latter application, the salt-mined caverns are subsequently used for hydrocarbon storage and retrieval.

Linear and nonlinear theoretical models are developed in this thesis to investigate the stability and to examine the nonlinear dynamics of three systems. Specifically, the systems under study are: (i) a cantilevered cylinder subjected to inverted external axial flow, (ii) a cantilevered pipe discharging fluid with inverted external flow confined over the whole length of the pipe, and (iii) a cantilevered pipe simultaneously subjected to internal flow and inverted external axial flow confined only over its upper portion. The equations of motion are derived using the extended Hamilton's principle and via a Newtonian approach, in some cases with separate derivation of the fluid-related forces. Each equation is discretized

using the Galerkin method to a set of ordinary differential equations which are then solved using the pseudo-arclength continuation method and a direct time integration technique for nonlinear analysis. The results obtained with all three models are compared to experimental observations reported in the literature and to theoretical predictions of earlier linear models. Furthermore, the influence of various system parameters on the dynamical behaviour of these systems is investigated theoretically.

New sets of experiments have been conducted for the third system, and the results are presented in this thesis, supported by a linear theoretical analysis. These experiments are aimed at investigating the effect of the external annular flow on the stability of the system by increasing the ratio of annular to internal flow velocities. It was found that increasing this ratio destabilizes the system drastically. Furthermore, improvements to the initial form of the theory are implemented, which enable achieving good to excellent agreement between theory and experiments, both qualitatively and quantitatively.

RÉSUMÉ

Une conduite parcourue d'un fluide est un exemple typique du problème d'interaction fluide-structure dans lequel la conduite devient instable à des vitesses d'écoulement suffisamment élevées, par divergence statique ou par oscillations, c'est-à-dire par battements, en fonction des conditions aux bords. Ce système est à l'étude depuis près d'un siècle et il est devenu un paradigme en matière de dynamique, en particulier la conduite en porte-à-faux, non seulement en raison de la richesse du comportement dynamique qu'il présente, mais également pour son importance industrielle. De plus, la stabilité d'une structure cylindrique en porte-à-faux soumise à un écoulement axial est étudiée depuis plusieurs décennies ; un défi relativement récent consiste à examiner le problème inversé, pour lequel l'extrémité amont du cylindre est libre et celle en aval est fixe. Il a été constaté que ce système inversé perd sa stabilité par battements à de faibles vitesses d'écoulement, ce qui donne lieu à des applications potentielles en récupération d'énergie.

Examiner la dynamique d'une conduite en porte-à-faux soumise simultanément à des écoulements axiaux interne et externe inversé est l'objectif principal de cette thèse. Ce système a plusieurs applications industrielles, telles que les échangeurs de chaleur, les chaînes de forage et les tuyaux utilisés dans les cavernes de saumure utilisées pour le stockage et la récupération ultérieures d'hydrocarbures.

Des modèles théoriques linéaires et non linéaires sont développés dans cette thèse afin d'étudier la stabilité et d'examiner la dynamique non linéaire à différentes vitesses d'écoulement de trois systèmes. Plus spécifiquement, les systèmes étudiés sont : (i) un cylindre en porte-à-faux soumis à un écoulement axial externe inversé, (ii) une conduite déchargeant un fluide avec écoulement externe inversé et confiné sur toute la longueur du tuyau, et (iii) une conduite en porte-à-faux soumise simultanément à un écoulement interne et à un écoulement

axial externe confiné seulement dans sa partie supérieure. Les équations de mouvement sont dérivées en utilisant le principe de Hamilton étendu et par une approche newtonienne, avec, dans certains cas, une dérivation séparée des forces exercées par le fluide externe. Chaque équation est discrétisée à l'aide de la méthode de Galerkine en un ensemble d'équations différentielles ordinaires, puis résolue à l'aide de la méthode de continuation par pseudo-longueur-d'arc et d'une technique d'intégration temporelle directe pour l'analyse non linéaire. Les résultats obtenus pour les trois modèles sont comparés aux observations expérimentales rapportées dans la littérature et aux prédictions théoriques des modèles linéaires précédents. Par ailleurs, l'influence de divers paramètres des modèles sur le comportement dynamique de ces systèmes est étudiée théoriquement.

De nouvelles séries d'expériences ont été menées pour le troisième système et les résultats sont présentés dans cette thèse, étayés par une analyse théorique linéaire. Ces expériences ont pour but d'examiner l'effet du flux annulaire externe sur la stabilité du système en augmentant le rapport entre les vitesses des flux annulaire et interne. Il a été constaté que l'augmentation de ce rapport déstabilise considérablement le système. Des améliorations de la théorie développée dans cette thèse sont proposées et implémentées, permettant d'obtenir une bonne, voire excellente, conformité entre théorie et expériences, qualitativement et quantitativement.

DEDICATION

This thesis is dedicated to the memory of my father, Rabie Abdelaziz Abdelbaki (1958-2006). Your advice and wise words have made this journey possible.

ACKNOWLEDGMENTS

First and foremost, I would like to express my sincere gratitude and appreciation to Professor Michael P. Païdoussis and Professor Arun K. Misra for supervising this research work. I am very grateful to Prof. Païdoussis for accepting me as a Ph.D. student in the first place. It is a great honour for me to learn Fluid-Structure Interactions from such a distinguished scientist and professional teacher. I thank him for his tremendous kindness, assiduous help, and continuous support. I am also thankful to Prof. Misra for his helpful discussions, insightful comments, and invaluable feedback.

I want to thank Mary Fiorilli for her kind assistance with all administrative matters. Also, I would like to acknowledge the financial support from McGill University, especially the McGill Engineering Doctoral Award (MEDA); the Natural Sciences and Engineering Research Council of Canada (NSERC), the Solution Mining Research Institute (SMRI) and Pipeline Research Council International (PRCI).

I was extremely lucky to be surrounded by wonderful friends and lab-mates during my study; I must thank Mohammad Tavallaeinejad for all the time we spent, conclusions we drew, and future plans we made together. Also, I must thank Stanislas Le Guisquet for all the interesting discussions and brilliant thoughts. I am grateful to Professor Mojtaba Kheiri for his help with AUTO, Professor Farhang Daneshmand for sharing useful results from his computational analysis, and Shufan (Frank) Cao for helping me conducting more experiments toward the end of my study.

In addition, I would like to acknowledge Professor Hamed Farokhi, Professor Ahmad Jamal, and Kyriakos Moditis from whom I benifited a lot at the begining of my Ph.D. study. I am also thankful to all my friends and colleagues in the office and the department, especially

Ahmed Moussa, Osaid Matar, Marius Müller, Raphaël Limbourg, Sophie Minas, Jamil El-Najjar, Ibrahim El-Bojairami, Ahmed Bayoumy, Khalil Alhandawi, and Paola Ulacia Flores.

I would like to extend my deepest gratitute to my family in Egypt, including my in-laws, for their support and encouragement. I am grateful to my beloved mother and dear brother for their faith in me, and for their understanding of my very long round-trips.

Words cannot describe my gratitude to my lovely wife, Basma, and my delightful daughter, Nadine, for their loving support. I would like to express my heartfelt thanks to them for standing beside me, and forgiving me for being always late. Basma, I owe you everything.

PREFACE

This thesis aimed at investigating the stability and examining the nonlinear dynamics, theoretically and experimentally, of a hanging tubular cantilever simultaneously subjected to internal flow and external axial flow confined over the upper portion of the cantilever. However, two other systems, which can be considered as simplified versions of the main one, were also studied. In fact, these simplified systems have important industrial applications and have been under study in the literature for quite a long time. The studies undertaken on all three systems are bonded in the present dissertation, not just because they all help in understanding the influence of various system parameters on the stability of the main system, but also because of the different dynamical behaviour and modes of instability that each system exhibits with increasing flow velocity.

Some of the work presented in this thesis has been published in refereed journals:

1. A. R. Abdelbaki, M. P. Païdoussis, A. K. Misra, A nonlinear model for a free-clamped cylinder subjected to confined axial flow, *Journal of Fluids and Structures*, 80 (2018) 390-404.
2. A. R. Abdelbaki, M. P. Païdoussis, A. K. Misra, A nonlinear model for a hanging tubular cantilever simultaneously subjected to internal and confined external axial flows, *Journal of Sound and Vibration*, 449 (2019) 349-367.
3. A. R. Abdelbaki, M. P. Païdoussis, A. K. Misra, A nonlinear model for a hanging cantilevered pipe discharging fluid with a partially-confined external flow, *International Journal of Non-linear Mechanics*, 118 (2020), Paper 103290.

All the work done in those papers and in all chapters of this thesis including derivations, calculations, analysis, and writing was done by Ahmed R. Abdelbaki, enriched by pertinent comments and input by his supervisors, namely Profs. Païdoussis and Misra.

TABLE OF CONTENTS

LIST OF TABLES

LIST OF FIGURES

NOMENCLATURE

A	cross-sectional area of the cylinder
A_{ch}	cross-sectional area of the annular region
A_i	inner cross-sectional area of the pipe
A_o	outer cross-sectional area of the pipe
C_{Dp}, c_d	dimensional and dimensionless form-drag coefficients
C_f, c_f	dimensional and dimensionless friction coefficients
C_N, c_N	dimensional and dimensionless normal drag coefficients
C_T, c_t	dimensional and dimensionless tangential drag coefficients
D	diameter of the cylinder
D_{ch}	inner diameter of the circular rigid channel
D_h	hydraulic diameter for the external flow over the cantilever
D_i	inner diameter of the pipe
D_o	outer diameter of the pipe
EI	flexural rigidity of the tube
$\bar{\varepsilon}$	strain
f	streamline parameter
F_A	inviscid hydrodynamic force
F_N, F_L	viscous forces in normal and longitudinal directions
F_{px}, F_{py}	hydrostatic forces in x- and y-direction
g	gravitational acceleration
$\bar{\kappa}$	curvature
L	length of the cantilever
L'	length of the annular region surrounding the pipe

$\bar{L}$	lift force per unit length of the cantilever
$\mathcal{M}$	bending moment acting on an element of the pipe
m	mass of the pipe/cylinder per unit length of the cantilever
M	virtual mass of the fluid per unit length of the cylinder
M_i	mass of the internal fluid per unit length of the pipe
M_o	virtual (added) mass related to the external flow per unit length of the pipe
N	number of modes in Galerkin's scheme
ν	kinematic viscosity of the fluid
Ω	circular frequency of oscillations
ω	dimensionless complex eigenfrequency
p	steady-state pressure
p_i	internal fluid pressure
p_o	external fluid pressure
Q	resultant force acting on an element of the pipe
ρ	fluid density
r	ratio between external to internal flow velocities
$\vec{r}$	unit position vector
s	curvilinear coordinate
$\tilde{S}$	Stokes number
s_t	steepness parameter of the logistic function
t	time
T	tension in the pipe or cylinder
T_o	externally applied tension
u	displacement in X direction
$u*$	dimensionless flow velocity
u_{cr}	dimensionless critical flow velocity for instability
u_{if}	dimensionless critical flow velocity for flutter

U	flow velocity
U_i	internal flow velocity
U_o	external flow velocity
$U_{o,1}$	external flow velocity inside the annulus
$U_{o,2}$	external flow velocity below the annulus
v	displacement in Y direction
w	displacement in Z direction
X, Y, Z	Lagrangian coordinate system
x, y, z	Eulerian coordinate system
χ	confinement parameter

CHAPTER 1
Introduction and literature review

1.1 Introduction

A fluid-structure-interaction (FSI) phenomenon entails the deformation of a structure under the action of fluid forces, such that the deformation in turn influences the magnitude of the fluid forces. A typical example of an FSI problem is a pipe conveying fluid; such a system undergoes interesting fluidelastic instabilities of different kinds, depending on the boundary conditions, at sufficiently high flow velocities. For instance, pipes conveying fluid with both ends supported are subject to static instability, i.e. divergence (buckling) at sufficiently high flow velocities; on the other hand, a cantilevered pipe is subject to oscillatory instability, i.e. flutter. The dynamics of cantilevered pipes conveying fluid becomes more complex if a mass is attached to the free end, or if the motion is limited via restraints. Hence, this system received a great deal of researchers' attention and has become a new paradigm in dynamics, as discussed in [1], not just because of the rich dynamics this system displays, but also because of the wide range of applications in which this system is present.

Another common example of an FSI problem is a cylinder subjected to external axial flow. From a practical point of view, this system undergoes fluidelastic instability at flow velocities higher than the normal operating conditions in common engineering applications, and thus some of the research work conducted in this area was initially curiosity-driven [2]. Nevertheless, this system has many important industrial applications, particularly in transportation industries, such as trains [3,4] and slender structures towed by ships or boats, e.g. the "Dracone" and seismic arrays. The "Dracone" is a long towed container, as shown in Fig. 1–1, used for oil and fresh-water transportation by sea. The towed or seismic arrays are extremely long parallel cylinders which are towed by ships on the sea-surface or totally submerged, and are used for oil exploration. They house sonar sensors which pick up acoustic

Figure 1–1: A 500 m^3 Dracone, inflated with air after discharging fresh-water cargo (Dunlop Dracones 1965) from Ref. [2].

signals reflected from the sea-bed strata, as illustrated in Fig. 1–2. The existence of oil or gas in the sea-bottom strata is revealed by analyzing the sonar signals. In addition, cylinders in axial flow also exist in heat exchangers and nuclear reactor fuel channels [5], but as clusters of cylinders, for which the critical flow velocity for instability can be significantly lower, and undesired flow-induced vibrations may arise at normal operating conditions.

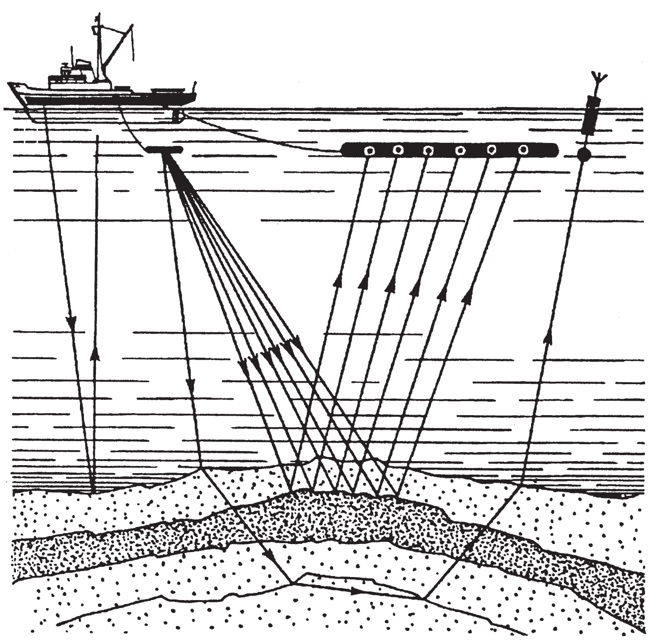

Figure 1–2: Diagrammatic view of a towed acoustic array from Ref. [6].

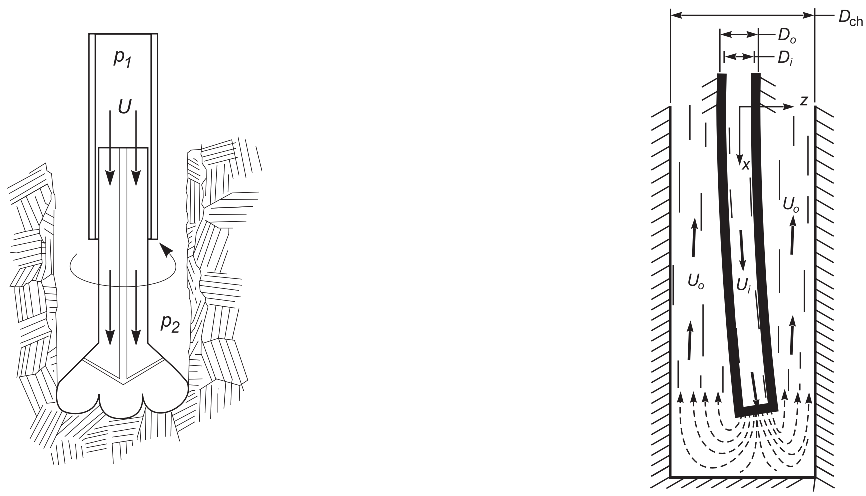

(a) (b)

Figure 1–3: (a) Diagram of a drill string with its drill bit rotating due to the internal flow, from Ref. [9]. (b) Idealization of the drill string by ignoring the drill bit altogether [8].

The dynamics of a pipe simultaneously subjected to internal and external axial flows is the main scope of this thesis. The motivation behind this study comes from the industrial applications that this system has. For example, the tubes in parallel-flow tubular heat exchangers can be modelled as pipes simultaneously subjected to either concurrent or counter-current internal and external axial flows [7]. Also, a drill-string can be idealized, by ignoring the drill bit shown in Fig. 1–3a, and modelled as a hanging pipe discharging fluid downwards, which then flows upwards as a confined axial flow [8], as shown in Fig. 1–3b.

In salt-mined caverns, a hanging pipe is utilized, simultaneously subjected to counter-current internal and external axial flows, where the external flow is confined only over the upper portion of the pipe, as shown in Fig. 1–4. To create the caverns, two flow configurations may be utilized: (i) the hanging pipe discharges fresh-water downwards and brine flows upwards through the casing (outer tubing), as shown in Fig. 1–4a; or (ii) the casing discharges the fresh water downwards and the brine flows upwards through the cantilevered pipe, as illustrated in Fig. 1–4b. This process naturally results in brine-filled caverns that can be used for hydrocarbon storage; choosing which flow configuration to implement is usually based on the desired shape of the cavern, as explained in the caption of Fig. 1–4.

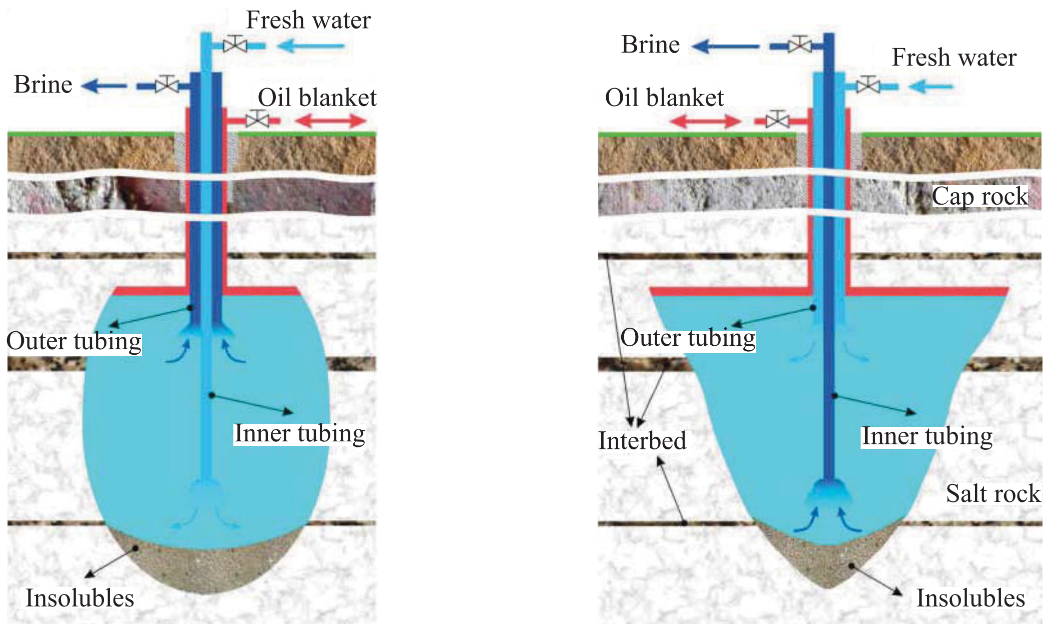

(a) (b)

Figure 1–4: Diagram of a brine-string, from Ref. [10], with (a) fresh-water being pumped-in, flowing downwards through the inner tubing and brine flowing upwards, a flow configuration that favours the lower part of the cavern, (b) fresh-water being discharged through the outer tubing and brine flowing upwards through the inner tubing, favouring the upper part of the cavern.

While filling these salt-mined caverns with the hydrocarbon product, the same flow configurations described in Fig. 1–4 can be utilized. This time the product can be pumped-in, flowing downwards through the outer tubing. The product then pushes the brine upwards via the inner pipe. The reverse process can also be implemented for the subsequent retrieval of the hydrocarbon product; thus the pipe would discharge brine downwards, which would push the product upwards through the casing, as shown in Fig. 1–5a. This system can be simplified and modelled as a hanging pipe discharging fluid downwards while immersed in the same fluid; the fluid then flows upwards through an annular region contained by a rigid tube at the upper portion of the pipe, as shown in Fig. 1–5b. In this system, the internal and external flows are dependent on each other and in opposite directions. Also, the external flow is confined over the upper portion of the pipe.

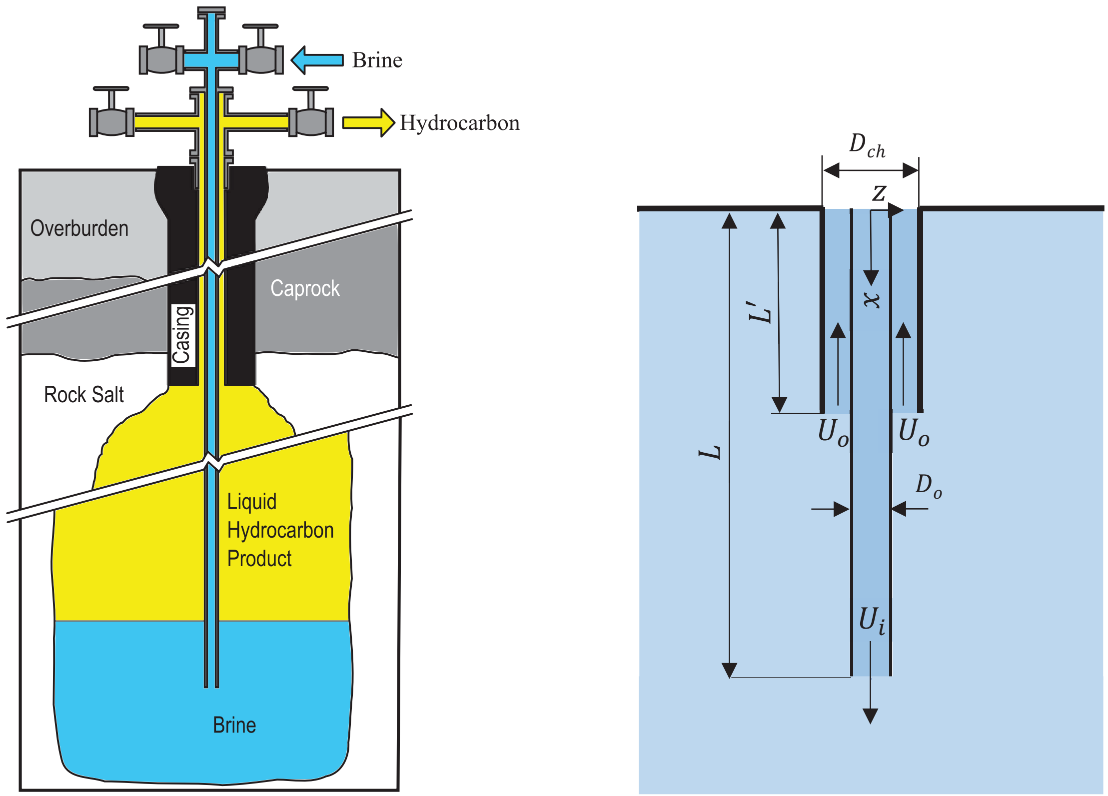

(a) (b)

Figure 1–5: (a) Schematic of the salt-cavern hydrocarbon storage application, from Ref. [11]. (b) Diagram of a pipe simultaneously subjected to internal and partially-confined external axial flows.

1.2 Literature review

In this section, a selective, rather than exhaustive, review is presented for pipes conveying fluid, cylinders in axial flow, and pipes simultaneously subjected to internal and external axial flows. In general, this review focuses on the nonlinear theoretical models and experimental studies, especially for cantilevered pipes and cylinders. It is aimed at outlining the historical background and highlighting some of the most significant studies. For a complete literature review, one can refer to the books of Païdoussis [2, 12].

1.2.1 Pipes conveying fluid

Perhaps the first study on a beam-like structure conveying fluid was undertaken by Bourrières [13] in 1939. In that pioneering study, a linearized equation of motion for a cantilevered pipe was derived and the stability of the system was investigated experimentally. The dynamics of pipes conveying fluid was revisited in the 1950s by Ashley and Haviland [14], followed by the studies in [15–17], in which the effects of the fluid flow on the natural frequencies and stability of flexible pipes with different boundary conditions were investigated. The free motion of a chain of articulated flexibly interconnected pipes conveying fluid was studied by Benjamin [18]. It was found that the system undergoes static buckling or self-excited oscillations at high enough flow velocities; the theoretical model was validated by comparison with experimental observations in [19]. Gregory and Païdoussis [20] extended Benjamin's work; they investigated the stability of continuously flexible tubular cantilevers conveying fluid, and determined theoretically the critical flow velocity for instability. The theoretical analysis was also supported by experiments in [21]. The first nonlinear model for a simply supported pipe conveying fluid was derived by Thurman and Mote [22], building on some earlier work in [13]; this study indicated the limited applicability of linear analysis for such a system, and stressed the relative importance of the nonlinear terms in the equations of motion.

The particular case of a hanging tubular cantilever discharging fluid was considered by Païdoussis [23]. In contrast to its articulated counterpart [18, 19], it was found that the pipe would not buckle with increasing flow velocity; however, it is subjected to oscillatory instability at a specific critical flow velocity. In addition, a "standing" tubular cantilever (free end on top) discharging fluid was also considered in [23], taking into account gravity forces. The discharging fluid was found to stabilize the standing pipe, which may be initially buckled under its own weight, over a certain range of flow velocities, but oscillatory instability does occur at higher velocities. Experiments were conducted using rubber tubes to explore the dynamical behaviour of these systems in the second part of [23].

Pipes of infinite length containing flowing fluid were considered by Stein and Tobriner [24]; they predicted oscillatory instability beyond a certain flow velocity, and provided closed form expressions for the critical flow velocity and frequency of oscillation.

Another aspect of the problem was tackled by Païdoussis and Denise [25,26], who studied very thin pipes conveying fluid with different boundary conditions utilizing thin-shell theory; they predicted instabilities in the shell modes. Shayo and Ellen [27] also studied theoretically flow-induced instabilities of cantilevered pipes in both beam and shell modes.

Païdoussis and Issid [28] investigated theoretically the stability of pipes conveying fluid with clamped-clamped, pinned-pinned, and clamped-free boundary conditions. It was found that pipes with both ends supported lose stability by divergence first and coupled-mode flutter at higher flow velocities, while on the other hand, cantilevered pipes are only subject to single-mode flutter. Furthermore, constant and harmonically time-varying flow velocities were considered in [28]. Shilling and Lou [29] presented an experimental study for a vertical cantilevered pipe discharging fluid while immersed in quiescent fluid, a study that has important offshore applications, such as for marine risers and ocean mining. It was found that the internal flow rate and the depth of immersion in the surrounding fluid significantly affect the natural frequencies of such a system.

The nonlinear theoretical studies of pipes conveying fluid were continued later in the 1970s by Holmes [30, 31], who was the first to use the tools of modern nonlinear dynamics in such problems; he extended the linear equation of motion in [28] by adding a nonlinear term associated with the deflection-induced tension in the pipe. It was proved in [30, 31] that the coupled-mode flutter predicted earlier in [28] for pipes with both ends supported does not materialize, and that a cantilevered pipe loses stability via a Hopf bifurcation with increasing flow velocity. Subsequent research on the nonlinear dynamics of pipes conveying fluid was conducted by Rousselet and Herrmann [32, 33]; nonlinear equations of motion for the pipe were derived by energy and force balance methods. In addition, an equation for the fluid itself was derived in [32, 33], to relate nonlinear pressure loss to the motion of the fluid in the pipe. Lundgren et al. [34] derived a set of integro-differential equations for the same system with an inclined terminal nozzle, which were later used by Bajaj et al. [35] for horizontal pipes with no nozzle, and by Steindl and Troger [36] for pipes with elastic support.

Païdoussis and Moon [37] investigated the planar dynamics of cantilevered pipes conveying fluid with motion-limiting restraints. They showed that the resulting limit cycle is subjected to a cascade of period-doubling bifurcations leading to chaos. Semler [38] derived the nonlinear equations of motion for simply-supported pipes and cantilevered pipes conveying fluid. It was also shown in [38] that chaotic motions may arise if the motions are constrained by motion-limiting restraints. Moreover, the derived equations were compared with other nonlinear models; it was concluded that the equations in [38,39] are the most complete and accurate. The chaotic motions of constrained pipes conveying fluid were further studied by Païdoussis and Semler [40] using the full nonlinear equations of motion. Copeland and Moon [41] found that chaos does not occur for unconstrained cantilevered pipes; however, they proved that chaotic motions are possible when a mass is attached to the free end of the cantilevered pipe. Wadham-Gagnon et al. [42] derived a three-dimensional version of the nonlinear equations of motion in [39]. These equations were used in the third part of the same study to investigate the three-dimensional behaviour of a pipe with an end-mass [43].

The nonlinear dynamics of a pipe conveying fluid has been investigated by other researchers, for example by Jian and Yuying [44] who studied the bifurcations of cantilevered pipes with a terminal nozzle, Sarkar and Païdoussis [45] who constructed a compact model for the planar nonlinear dynamics of cantilevered pipes in the post-flutter region, Modarres-Sadeghi et al. [46] who investigated the three-dimensional flutter in cantilevered pipes conveying fluid, and many others.

Guo et al. [47] investigated the effect of laminar versus turbulent flow profiles on the stability of a fluid-conveying pipe; they modified the equations of motion derived in [28] and predicted critical flow velocities for turbulent profiles lower than that for a laminar profile. Rinaldi and Païdoussis [48] studied, experimentally and theoretically, a hanging pipe discharging fluid, fitted with an end-piece, which makes the fluid to be discharged radially rather than axially. Such an end-piece was found to stabilize the system against flutter over the full range of flow velocities considered. A more elaborate review of these relatively recent studies was undertaken by Ibrahim [49, 50].

The application of the finite element method (FEM) to the problem of pipes conveying fluid was started in the 1980s by Chen and Fan [51]. They considered elastically supported pipes and studied the effects of friction and the presence of a lumped mass. Many other studies followed this work, e.g. in [52, 53].

Most recently, the dynamics of pipes conveying fluid has been studied considering pipes with varying material properties, such as viscoelastic pipes, and nano tubes; see for instance [54–56].

1.2.2 Cylinders in axial flow

The first specific study on cylinders in axial flow is due to Hawthorne [57], who investigated the stability of the "Dracone". Païdoussis [58] extended the work of Hawthorne and derived an equation of motion for flexible cylinders in axial flow with different boundary conditions; the theoretical analysis was supported with the experimental observations reported in [59]. This study was followed by the analysis in [60, 61] for towed totally submerged cylinders. In fact, the dynamics of towed cylinders was extensively investigated, afterwards, not just for oil and water transportation but for oil exploration as well. The studies concerned with towed cylinders were continued in [62–65] and were recently revisited by Kheiri and Païdoussis [66] who investigated the stability of the same system via a modified linear model. The first nonlinear model was derived by Kheiri et al. [67] who also conducted experiments to explore the dynamical behaviour of the system and test the nonlinear model [68]. Generally, it was found that a towed cylinder with a well-streamlined end is subjected to rigid-body instabilities at relatively low towing speeds and flexural instabilities at high speeds (static instability, "yawing", or flutter); on the other hand, a sufficiently blunt tail-end can stabilize the system and suppress both rigid body and flexural instabilities.

Back to the earliest study of Païdoussis [58], an error in the original formulation, specifically in the incorporation of the viscous forces, was noticed and corrected by Païdoussis [5]. The uncorrected equation of motion was used in many other studies, such as [69, 70] leading to incorrect conclusions, especially for long cylinders in axial flow, as discussed in [71]. Moreover, in [5], the theory was further extended to include the case of a cluster of identical cylinders contained in a rigid channel. The dynamics of multiple cylinders in axial flow was examined afterwards in many other studies, e.g. in [72–74], and most recently in [75]. Furthermore, the case of cylinders in highly confined axial flow was considered in [76, 77].

Recently, Rinaldi and Païdoussis [78] studied experimentally a cantilevered cylinder subjected to confined axial air-flow directed from the free end of the cylinder to the clamped one. It was found that at relatively low flow velocities, the cylinder undergoes small-amplitude first-mode flutter, and then static divergence occurs at higher flow velocities. In addition, a simple linear theoretical model was developed in [78] which captures the essentials of the observed dynamical behaviour. This inverted configuration received researchers' attention, especially for cantilevered "flags" (thin elastic plates) in inverted axial flow, which exhibit large amplitude flutter at low flow velocities. Many studies investigated the dynamics of inverted flags and tried to explain the mechanism leading to flutter, e.g. in [79–81]. Such systems can be used in energy harvesting applications; see for instance [82, 83], and in enhancing heat transfer [80, 84].

Païdoussis et al. examined the nonlinear dynamics of cylinders in axial flow for the first time in a three-part study [85–87]. In [85], experiments were conducted on cantilevered cylinders with different downstream-end shapes to study the two-dimensional and three-dimensional motions of the cylinder; cylinders with sufficiently well-streamlined end were found to lose stability by divergence at relatively high flow velocity, and then flutter in different modes at higher flow velocities. A nonlinear partial differential equation of motion for the cylinder was derived in [86], taking into account nonlinear expressions for the inviscid, hydrostatic, as well as frictional forces acting on the cylinder. The equation was discretized using Galerkin's method to a set of ordinary differential equations, which were solved by the Finite Difference Method (FDM) and the pseudo-arclength continuation method in [87]. Moreover, the theoretical results were found to be in good qualitative and quantitative agreement with experimental observations and measurements [87].

Jamal et al. [88] calculated the coefficients of the fluid forces acting on a cantilevered cylinder in axial flow by using experimental data. More recently, Kheiri and Païdoussis [89] derived a linear equation of motion for a pinned-free cylinder in axial flow; they determined the critical flow velocity for divergence as well as the conditions of rigid body oscillations.

The Finite Element Method (FEM) was employed for the first time to investigate the stability of cylinders in axial flow by Vendhan et al. [90]; they conducted linear analysis, and utilized the well-known two-node straight uniform beam element, with two bending degrees of freedom at each node, and the standard beam shape-functions. The model in [90] is sufficient only for cylinders with both ends supported, and thus it was extended and generalized in [91] for different cases with free ends, e.g. cantilevered and towed cylinders. Recently, the application of the FEM has been further extended to solve numerically the coupled computational fluid and structural dynamics; Liu et al. [92] studied the effect of the type of flow, either laminar or turbulent, on the fluid-structure interaction of a flexible cylinder in axial flow. For a clamped-clamped cylinder [92], it was concluded that laminar flow damps the lateral oscillations of the cylinder, and the system remains stable even at high flow velocities. On the other hand, the cylinder is subjected to divergence and flutter at sufficiently high flow velocities when the flow is turbulent.

1.2.3 Pipes simultaneously subjected to internal and external axial flows

Cesari and Curioni [93] were the first to investigate the static instability of pipes with different boundary conditions, simultaneously subjected to internal and external flows. Pipes subjected to concurrent and independent internal and external axial flows were studied theoretically afterwards by Hannoyer and Païdoussis [7]; they assumed small lateral motions, and thus conducted a linear analysis considering the internal dissipation and the effects of gravity as well as the developing boundary layer. They concluded that for a clamped-clamped cylinder, the effect of the internal and external flows is additive. This means that if either the internal or external flow velocity is right at the critical velocity for instability, any increase in the other flow velocity would cause instability. On the other hand, the case of a cantilevered cylinder is different, and the free-end shape plays a key role in the stability of the system. For a blunt end, interestingly, the internal flow becomes dominant and the pipe is subjected to flutter at sufficiently high internal flow velocities; however, increasing the external flow velocity stabilizes the system and can eliminate flutter. The dynamics of the system becomes more complex for a well-streamlined end piece; both divergence and flutter exist, as well as domains of mixed modes. The theoretical predictions were in reasonable agreement with the experimental observations reported in the same study. Moreover, in a two-part study [94,95], the same authors examined the dynamics of a pipe either internally or externally nonuniform, subjected to internal or external flow, or to both flows simultaneously.

The work in [7] was extended by Païdoussis and Besançon [96] who considered arrays of cylinders with internal and external flows, modelling cylindrical structures in heat exchangers, boilers and steam generators. The eigenfrequencies of this system were obtained analytically and their dependence on the internal and external flow velocities was studied theoretically.

Luu [97] examined the dynamics of a long vertical tubular cantilever discharging fluid downwards, which then flows upwards through an annular region contained by a rigid channel. This system was inspired by drilling applications; it idealizes the model of a drill-string by ignoring the drill-bit altogether, as shown in Fig. 1–3b. In fact, the stability of a drill-string system has been investigated extensively in many other studies, e.g. in [9, 98, 99].

Wang and Bloom [100] examined the dynamics of an inclined pipe subjected to internal and partially-confined external flows; they formulated a linearized mathematical model to determine the system eigenfrequencies, and identified the critical parameters pertaining to stability of the system.

Païdoussis et al. [8] revisited the theoretical modelling of a cantilevered pipe discharging fluid downwards, which then flows upwards through an annular region contained by a rigid channel; thus, the internal and external flows are dependent on each other and the external flow is fully confined, i.e. confined over the whole length of the pipe. Two sets of system parameters were considered: one corresponds to a bench-top system, while the other idealizes a drill-string-like system. It was concluded in [8] that if the degree of confinement of the external flow is relatively low, the internal flow dominates and it stabilizes the system at low flow velocities. On the other hand, if the degree of confinement is sufficiently high, the external flow dominates and it destabilizes the system. The effects of reversing the flow direction on the dynamical behaviour of the system in [8] were explored theoretically right after that by Qian et al. [101] who assumed that the hanging pipe is aspirating the fluid in a simple manner. Recently, Fujita and Moriasa [102] considered the same system with the two different directions of flow velocities assumed in [8, 101]; they employed the principle of superposition of linear stability analysis of a pipe subjected to internal and external flows separately to examine the dynamics of the system. Later on, Zhao et al. [103] modelled the drill string as a stepped pipe to take into account the differences between the drill-pipe and the drill-collar diameters; they developed a linear model and explored the influence of various parameters on the stability of the system.

Moditis [104] and Moditis et al. [11] studied the dynamics of a discharging cantilever pipe with reverse, partially-confined, external flow — a system that models one of the *modi operandi* of salt-mined caverns used for storage and subsequent retrieval of hydrocarbons [105], as shown in Fig. 1–5. Moditis et al. extended the theoretical model of [8] and derived a linear equation of motion for the pipe in [11]. The theoretical analysis was validated by comparison with experiments in a bench-top-sized system in the same study. In addition, the linear theory was used to investigate the stability of long brine-string-like systems in [11];

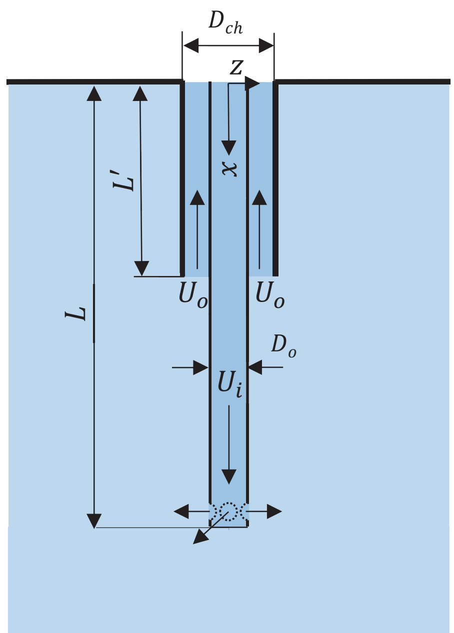

Figure 1–6: Hanging pipe discharging fluid radially, while immersed in the same fluid, with partially-confined external axial flow.

it was found that sufficiently long systems lose stability with increasing flow velocity via divergence rather than flutter, which was the mode of instability observed experimentally in the bench-top-sized system. The same configuration was studied numerically by Kontzialis et al. [106]; the results obtained were in good agreement with the experiments in [11].

Moreover, Minas et al. [107] investigated the effect of adding an end-piece at the free end of the pipe that makes the flow to be discharged radially, as illustrated in Fig. 1–6, instead of axially; this idea was originally explored by Rinaldi and Païdoussis [48] experimentally and theoretically, but for a cantilevered pipe discharging fluid without any external flow. It was concluded in [107] that discharging the flow radially stabilizes the system against flutter, the same conclusion reached earlier in [48].

1.3 Limitations of the studies in the literature

It is evident from the literature review presented in the previous section, that there are not many studies focusing on pipes simultaneously subjected to internal and external axial flows, as compared to pipes conveying fluid and cylinders in axial flow. In particular, few studies are concerned with the case in which the internal and external flows are interdependent and in opposite directions. In fact, the dynamics of such a system has never been examined before by a nonlinear theory.

The linear models available in the literature are only sufficient for determining the critical flow velocity for the first instability; however, to explore the dynamical behaviour at flow velocities beyond this critical value, a nonlinear model becomes essential. Also, a nonlinear model can determine other quantitative facets of the dynamical behaviour, such as the amplitude of static buckling, and the limit cycle amplitude and frequency in case of flutter. Moreover, via nonlinear theory, it is possible to predict sub-critical instabilities or re-stabilization zones, and also show the transition between one mode of instability to another.

In addition, the experimental studies available in the literature for this specific system are very limited, and from a practical point of view, experimental set-ups were designed to keep the diameter of the annular region surrounding the pipe relatively large, so that the pipe can be observed to lose stability before hitting the rigid tube forming the annular region. Since the external flow velocity is dependent on the internal one via continuity, i.e. by the law of conservation of mass, the values of the external flow velocity considered in the literature were generally quite low, relative to the internal one.

1.4 Thesis scope and objectives

This research work is concerned with a hanging cantilevered pipe simultaneously subjected to internal and partially-confined external axial flows, i.e. the system shown in Fig. 1–5b. Investigating the stability and exploring the dynamical behaviour of this system as the flow velocities are varied are the main objectives of this study. However, in order to fully understand the influence of various system parameters on the dynamics of the system, it seemed essential to analyse the effects of the external flow separately. Thus, a free-clamped cylinder subjected to confined axial flow is considered first; linear and nonlinear dynamics of the system are examined at different flow velocities, and the theoretical predictions are compared with experimental data from the literature for the sake of validation. The internal flow is then added to the system, while the external flow is confined over the entire pipe; the stability of this system is investigated, and the influence of several system parameters on the nonlinear dynamics of the system is studied. Eventually, the external flow part is modified to be confined only over the upper portion of the pipe, and the dynamics of this system is examined via a nonlinear theory. The theoretical predictions are compared to experimental observations reported in the literature, where applicable. Moreover, new experimental observations are presented in this study, aimed at exploring the influence of the ratio of the external to internal flow velocities on the stability of the system.

Thus, the objectives of this thesis can be listed as follows:

- developing the first nonlinear analytical model for the dynamics of a free-clamped cylinder subjected to confined external axial flow, and examining the nonlinear dynamics of the system at flow velocities beyond the first critical velocity for instability;
- deriving the first ever nonlinear equation of motion for a cantilevered pipe discharging fluid downwards, which then flows upwards as a fully-confined external axial flow, as well as investigating the influence of various system parameters, e.g. confinement, gravity, mass ratio, drag coefficient, and pipe thickness parameters on the nonlinear dynamics of the system;
- examining the dynamics of a hanging cantilevered pipe simultaneously subjected to internal flow and partially-confined external axial flow over its upper portion via a nonlinear theory, as well as investigating the influence of varying the length of the region over which the external flow is confined and the degree of confinement on the stability and dynamical behaviour of the system;
- exploring experimentally the dynamical behaviour of a pipe simultaneously subjected to internal and partially-confined external axial flows with several ratios of external to internal flow velocities, in order to study the significance of the external flow and its influence on the stability of the system;

- testing the performance of a linearized form of the model by comparing its predictions to the new experimental observations for different ratios of external to internal flow velocities, as well as improving the performance of the model by proposing different models for the discontinuity of the external flow where the flow becomes confined, and exploring the effect of non-zero external flow velocity over the unconfined region.

1.5 Thesis structure

This thesis consists of six chapters including this chapter (Chapter 1: Introduction); the contents of the other five chapters are summarized as follows.

In Chapter 2, a nonlinear analytical model is derived using the extended Hamilton's principle for the dynamics of a free-clamped cylinder subjected to confined axial flow (System I). The effects of confinement of the flow, as well as the boundary conditions associated with the shape of the free end of the cantilever, are taken into account. The nonlinear partial differential equation of motion derived for the cylinder is discretized using Galerkin's method to a set of ordinary differential equations, and then solved using the pseudo-arclength continuation method and a direct time integration technique. The linear and nonlinear dynamics of the system are examined at different flow velocities and model predictions are compared to experimental observations and other theoretical results from the literature.

In Chapter 3, the dynamics of a hanging cantilevered pipe simultaneously subjected to internal and fully-confined external axial flows (System II) are examined via a nonlinear theory. The model is derived and solved using the same methods and techniques detailed in Chapter 2, and the results are compared to the predictions of an earlier linear theoretical model, as well as to some unpublished experimental observations. Moreover, the influence of the degree of confinement of the external flow, drag coefficients, the ratio of the fluid mass to the mass of the system, gravity, and wall-thickness of the pipe on the dynamical behaviour of the system are studied theoretically.

In Chapter 4, a cantilevered pipe discharging fluid downwards, which then flows upwards through an annular region contained by a rigid tube that surrounds the pipe at its upper portion (System III) is considered. A nonlinear analytical model is developed for the dynamics of this system. Calculations are presented for two sets of system parameters corresponding to two pipes of different dimensions and material properties. The predictions of the nonlinear model are compared to experimental observations from the literature. Moreover, the influences of varying the length and tightness of the annular region on the response of the system are investigated theoretically.

In Chapter 5, the significance of the external annular flow in System III is investigated experimentally for higher ratios of external to internal flow velocities than those considered in Chapter 4 and in the literature. Bifurcation diagrams as well as time histories, phase-plane and power-spectral-density plots for the tip of the pipe at different flow velocities are presented for different ratios of external to internal flow velocities. Moreover, these observations are compared to the predictions of a linearized form (Model 1) of the nonlinear model derived in Chapter 4. Also, improvements to Model 1 are effected at the end of the chapter; two other linear models are developed using a force-balance method and are used to investigate the stability of the pipe for different ratios of external to internal flow velocities. The predictions of all the linear theoretical models are compared to experimental observations in the same chapter.

Chapter 6 summarizes the main findings of Chapters 2-5, and discusses directions for future work.

CHAPTER 2
Nonlinear dynamics of a free-clamped cylinder in confined axial flow (System I)

In this chapter, a full nonlinear analytical model is derived for a free-clamped cylinder in axial flow taking into account the effects of the confinement of the flow and also the boundary conditions related to the free end of the cylinder. The notation "free-clamped" indicates that the cylinder is free at the upstream end and clamped at the downstream end. Experiments had been conducted earlier on the same system by Rinaldi and Païdoussis [78] in air flow; first-mode flutter-like oscillations were observed at relatively low flow velocities, and a static divergence occurred at higher flow velocities. In addition, a simple linear theoretical model was developed in [78], which is capable of capturing the essentials of the observed behaviour. In the present study, a nonlinear equation of motion for the cylinder is derived via the extended Hamilton's principle. The fluid-related forces considered are the inviscid hydrodynamic forces, the hydrostatic forces and the viscous forces. A weakly nonlinear equation of motion is derived in Section 2.1, which is exact to third-order of magnitude. The equation is solved using the same system parameters as in [78], and the linear and nonlinear dynamics of the system are examined in Sections 2.2 and 2.3. In Section 2.4, the results of the proposed model are compared to the experimental observations reported in [78] and to the results of other theoretical models from the literature.

2.1 Derivation of the equation of motion

The system under study consists of a flexible cantilevered cylinder of diameter D, length L, flexural rigidity EI and mass per unit length m. The cylinder is centrally located in a rigid channel of diameter D_{ch}, as shown in Fig. 2–1a, and is subjected to an axial flow velocity U, directed from the free end towards the clamped one. The system is vertical, so the undeformed axis of the cylinder coincides with the X-axis and is in the direction of

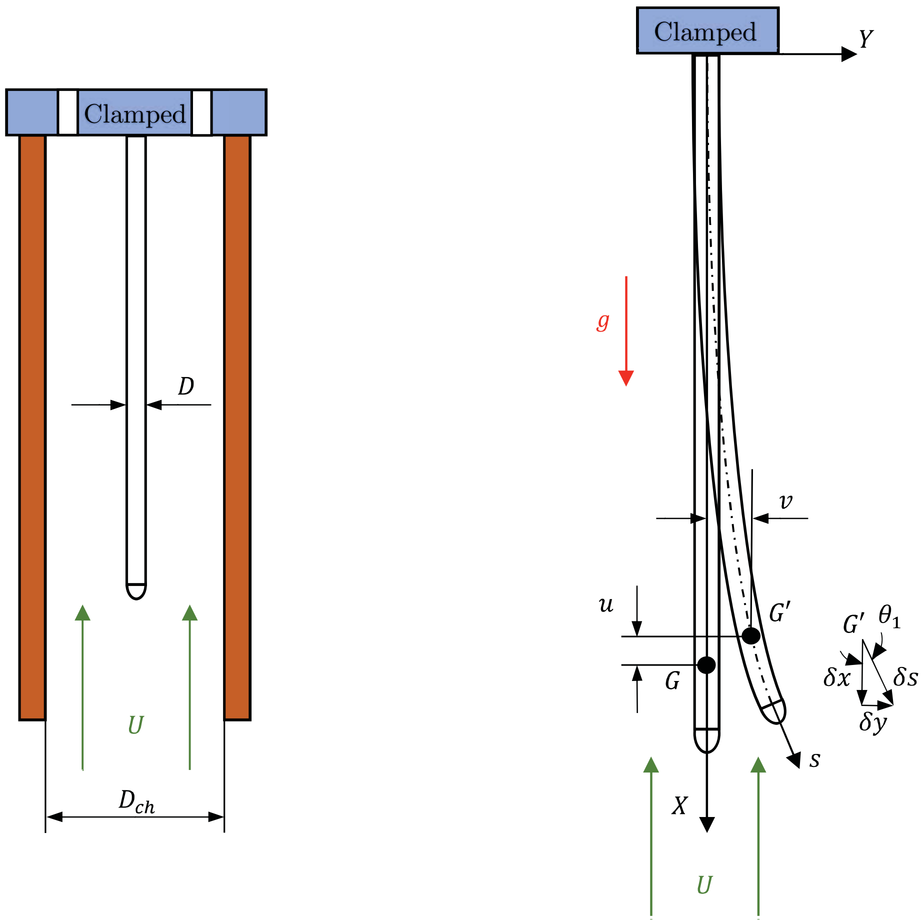

(a) (b)

Figure 2–1: (a) Diagrammatic view of a vertical free-clamped cylinder in axial flow, centrally located in a circular channel. (b) Diagram defining the coordinate systems, where G is a material point on the neutral axis of the cylinder at curvilinear coordinate s, and is located at $G(X,Y)$ before deformation and $G'(x,y)$ afterwards.

gravity, as shown in Fig. 2–1b. In addition, the cylinder is generally fitted with an ogival end-piece at its free end.

The following basic assumptions are made for the cylinder and the fluid: (i) the cylinder length-to-diameter ratio is high enough for Euler-Bernoulli beam theory to apply; (ii) the cylinder centreline is inextensible; (iii) the strains in the cylinder are small, but the deflections can be large; (iv) the motion of the cylinder is assumed to be planar; and (v) the fluid is incompressible with constant mean flow velocity.

Two coordinate systems are used: the Lagrangian (X, Y, Z, t) and the Eulerian (x, y, z, t); the former one is associated with the undeformed state of the cylinder, while the latter is for the deformed state. The displacements of point G on the undeformed cylinder are thus $u = x - X$, $v = y - Y$, and $w = z - Z$. The cylinder centreline motions are assumed to be in the (X-Y) plane, as shown in Fig. 2–1b; hence, $Y = 0$ and $z = Z = w = 0$. The curvilinear coordinate along the cylinder, s, can be related to X by $\partial s/\partial X = 1 + \bar{\varepsilon}$, where $\bar{\varepsilon}$ is the axial strain along the centreline, with $1 + \bar{\varepsilon}(X) = [(\partial x/\partial X)^2 + (\partial y/\partial X)^2]^{1/2}$. However, as the cylinder centreline is assumed to be inextensible, $\bar{\varepsilon} = 0$, $\partial s/\partial X = 1$ and hence $(\partial x/\partial X)^2 + (\partial y/\partial X)^2 = 1$.

The equation of motion is derived via the extended Hamilton's principle,

$$\delta \int_{t_1}^{t_2} \mathcal{L}\,\mathrm{d}t + \int_{t_1}^{t_2} \delta W\,\mathrm{d}t = 0, \tag{2.1}$$

where $\mathcal{L} = \mathcal{T}_c - \mathcal{V}_c$ is the Lagrangian, $\mathcal{T}_c$ being the kinetic energy of the cylinder, $\mathcal{V}_c$ its potential energy, and δW is the virtual work done on the cylinder by the fluid-related forces. The equation to be derived is to be correct to third-order of magnitude, $\mathcal{O}(\epsilon^3)$, for $y = v \sim \mathcal{O}(\epsilon)$ and $u \sim \mathcal{O}(\epsilon^2)$. Hence the expression for the virtual work must be correct to $\mathcal{O}(\epsilon^3)$, while the energy expressions to $\mathcal{O}(\epsilon^4)$.

2.1.1 Kinetic and potential energies of the cylinder

The kinetic and potential energies of the cylinder itself are

$$\mathcal{T}_c = \frac{1}{2}m\int_0^L V_c^2\mathrm{d}X, \quad \mathcal{V}_c = \frac{1}{2}EI\int_0^L \bar{\kappa}^2\mathrm{d}X - mg\int_0^L x\mathrm{d}X, \tag{2.2}$$

where V_c is the velocity of the cylinder element and can be expressed as $\vec{V_c} = \dot{x}\vec{i} + \dot{y}\vec{j}$, in which $\vec{i}$ and $\vec{j}$ represent axial and lateral unit vectors of the undeformed state of the cylinder, respectively, as shown in Fig. 2–2. x and y are related to each other through the inextensibility condition, thus $x = \int_0^s \sqrt{1 - (\partial y/\partial s)^2}\,\mathrm{d}s$. In addition, $\bar{\kappa}$ is the curvature along the deformed cylinder which can be written, according to [39], as follows:

$$\bar{\kappa} = \frac{\partial^2 y/\partial s^2}{\sqrt{1-(\partial y/\partial s)^2}}. \tag{2.3}$$

Based on Eq. (2.2), $\mathcal{T}_c = (m/2)\int_0^L (\dot{x}^2 + \dot{y}^2)\,\mathrm{d}s$, and thus

$$\delta \int_{t_1}^{t_2} \mathcal{T}_c \,\mathrm{d}t = m \int_{t_1}^{t_2} \int_0^L (\dot{x}\delta\dot{x} + \dot{y}\delta\dot{y})\,\mathrm{d}s\,\mathrm{d}t. \tag{2.4}$$

Moreover, from the inextensibility condition, we have $\delta x = -(y' + \frac{1}{2}y'^3)\delta y + \int_0^s (y'' + \frac{3}{2}y'^2 y'')\delta y\,\mathrm{d}s + \mathcal{O}(\epsilon^4)$ and $\dot{x} = -\int_0^s y'\dot{y}'\,\mathrm{d}s$ [39,86]. Therefore, the following expression can be derived by applying integration by parts on Eq. (2.4) while keeping in mind the orders of magnitude of the various quantities:

$$\begin{aligned}\delta \int_{t_1}^{t_2} \mathcal{T}_c \,\mathrm{d}t = -m \int_{t_1}^{t_2} \int_0^L \Big\{ \ddot{y} + y' \int_0^s (\dot{y}'^2 + y'\ddot{y}')\,\mathrm{d}s \\ - y'' \int_s^L \int_0^s (\dot{y}'^2 + y'\ddot{y}')\,\mathrm{d}s\,\mathrm{d}s \Big\} \delta y\,\mathrm{d}s\,\mathrm{d}t + \mathcal{O}(\epsilon^5),\end{aligned} \tag{2.5}$$

For the potential energy, one can write

$$\begin{aligned}\delta \int_{t_1}^{t_2} \mathcal{V}_c dt = EI \int_{t_1}^{t_2} \int_0^L [y'''' + 4y'y''y''' + y''^3 + y''''y'^2]\,\delta y\,\mathrm{d}s\,\mathrm{d}t \\ - mg \int_{t_1}^{t_2} \int_0^L [-(y' + \frac{1}{2}y'^3) + (L-s)(y'' + \frac{3}{2}y''y'^2)]\,\delta y\,\mathrm{d}s\,\mathrm{d}t + \mathcal{O}(\epsilon^5),\end{aligned} \tag{2.6}$$

where $(\ )' = \partial(\ )/\partial s$ and $\dot{(\ )} = \partial(\ )/\partial t$. For more details of the derivation, refer to [39,86].

2.1.2 Fluid-related forces

The forces associated with the fluid are derived separately rather than together, say by the direct application of Navier-Stokes equations, in a similar manner as in [58]. This approach simplifies the analysis considerably and has been shown to give acceptable results, as in [5, 58, 59, 85] for example. An element of the deformed cylinder is subjected to the following set of forces, as shown in Fig. 2–2a: the inviscid fluid dynamic force $F_A\delta s$, the normal and longitudinal viscous forces, $F_N\delta s$ and $F_L\delta s$, respectively, and the hydrostatic forces $F_{px}\delta s$ and $F_{py}\delta s$ in the x- and y-direction, respectively.

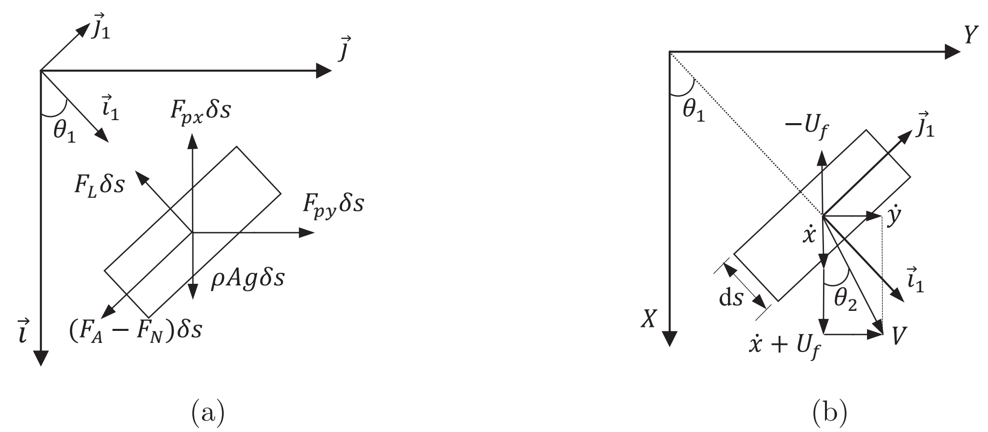

Figure 2–2: (a) Fluid-related forces acting on an element of the cylinder δs, (b) Determination of the relative fluid-cylinder velocity V on an element of the cylinder.

The inviscid fluid dynamic forces

These forces are derived following the procedure described in [86], taking into account the reverse direction of the flow velocity in the problem at hand. The approach adopted is basically an extension of Lighthill's linear slender-body potential flow theory, formulated in [108], to a third-order nonlinear formulation. The velocity potential can be expressed as

$$\phi = -UX + \phi_1, \tag{2.7}$$

where $-UX$ is the potential due to the mean flow, the negative sign appearing because of the inverted flow direction in this study, and ϕ_1 is the potential due to the motion of the body. This potential should satisfy the following assumptions: (i) the fluid velocity at the outer channel is zero; (ii) the fluid does not penetrate the cylinder; (iii) the solution is 2π-periodic around the cylinder; and (iv) the solution is even with respect to Z. Moreover, the velocity potential ϕ is governed by the two-dimensional Laplace equation, $\partial^2\phi/\partial Y^2 + \partial^2\phi/\partial Z^2 = 0$, which is a linear approximation that considers the effects of the fluid as two-dimensional near the cylinder. The pressure, P, is then determined via the Bernoulli equation,

$$P = -\rho\frac{\partial\phi}{\partial t} - \frac{1}{2}\rho(\nabla\phi)^2 + \frac{1}{2}\rho U^2, \tag{2.8}$$

where ρ is the fluid density, as follows:

$$
\begin{aligned}
P = &-\rho\left[\frac{\partial\phi_1}{\partial t} - \frac{\partial u}{\partial t}\left(-U + \frac{\partial\phi_1}{\partial X}\right) - \frac{\partial\phi_1}{\partial Y}\left(\frac{\partial v}{\partial t} - \frac{\partial u}{\partial t}\frac{\partial v}{\partial X}\right)\right] \\
&- \frac{1}{2}\rho\left[\left(1 - \frac{\partial u}{\partial X}\right)\left(-U + \frac{\partial\phi_1}{\partial X}\right) - \frac{\partial\phi_1}{\partial Y}\left(\frac{\partial v}{\partial X} - \frac{\partial u}{\partial X}\frac{\partial v}{\partial X}\right)\right]^2 \\
&- \frac{1}{2}\rho\left(\frac{\partial\phi_1}{\partial Y}\right)^2 - \frac{1}{2}\rho\left(\frac{\partial\phi_1}{\partial Z}\right)^2 + \frac{1}{2}\rho U^2.
\end{aligned}
\tag{2.9}
$$

The pressure can be written as $P = P_0 + P_2 + P_1$, where P_0 is the pressure distribution in the steady flow past the undeformed motionless cylinder, P_2 is the pressure distribution due to steady motion of the cylinder through stagnant fluid, and P_1 the remainder of the pressure distribution, of interest in this derivation, is determined as follows:

$$
\begin{aligned}
P_1 = &-\rho\Bigg\{\left\{\frac{\partial}{\partial t} + \left[-U\left(1 - \frac{\partial u}{\partial X}\right) - \left(\frac{\partial u}{\partial t} - U\frac{\partial u}{\partial X}\right)\right]\frac{\partial}{\partial X}\right\}\phi_1 \\
&+ \frac{1}{2}\left(\frac{\partial\phi_1}{\partial X}\right)^2 - \frac{\partial v}{\partial X}\frac{\partial\phi_1}{\partial Y}\frac{\partial\phi_1}{\partial X}\Bigg\} + \mathcal{O}(\epsilon^5).
\end{aligned}
\tag{2.10}
$$

The lift force per unit length, $\bar{L}(X,t)$, can be obtained by

$$
\bar{L}(X,t) = \oint_{S_X} P_1\,(-\mathrm{d}Z), \tag{2.11}
$$

where S_X is the circumference of the cylinder. A linear expression is determined first for ϕ_1 in the form $\phi_1 = V(X,t)\Phi$, where $V(X,t)$ is the relative fluid-cylinder velocity and Φ is also a solution of the two-dimensional Laplace equation, but with different boundary conditions [86]. This results in a linear expression for the lift, $\bar{L}(X,t) = -(\partial/\partial t - U\,\partial/\partial X)MV$, in which M is the virtual (or added) mass and it is equal to $\chi\rho A$; $\chi = (D_{ch}^2 + D^2)/(D_{ch}^2 - D^2)$ is a confinement parameter, and A is the cylinder cross-sectional area. The nonlinear lift can be determined afterwards, by adding to ϕ_1 above the nonlinear part Ψ, which is correct to fourth-order, thus $\phi_1 = V\Phi + \Psi$; the reader is referred to [86] for a detailed derivation. After many manipulations and truncation to $\mathcal{O}(\epsilon^4)$, the following nonlinear expression for the inviscid hydrodynamic force, which, as used here, has the same magnitude as the lift, but acts in the opposite direction (cf. F_A in Fig. 2–2a), can be obtained:

$$F_A(X,t) = \left\{\frac{\partial}{\partial t} + \left[-U(1-\frac{\partial u}{\partial X}) - (\frac{\partial u}{\partial t} - U)\frac{\partial u}{\partial X}\right]\frac{\partial}{\partial X}\right\}$$
$$\times\left[V - (\frac{\partial u}{\partial t}\frac{\partial v}{\partial X} - 2U\frac{\partial u}{\partial X}\frac{\partial v}{\partial X}) - \frac{1}{2}V(\frac{\partial v}{\partial X})^2\right]M - \frac{1}{2}MV\frac{\partial v}{\partial X}\frac{\partial V}{\partial X} + \mathcal{O}(\epsilon^5). \tag{2.12}$$

In order to derive an expression for the relative fluid-cylinder velocity, an element of the deformed cylinder is considered as in Fig. 2–2b. The unit vector pair $(\vec{i_1}, \vec{j_1})$ is introduced, which is in the tangential and normal to the centreline directions, at angle θ_1 to $(\vec{i}, \vec{j})$. Knowing that $\tan(\theta_1) = \partial y/\partial x = (\partial y/\partial X)(\partial X/\partial x)$, and that $\partial x/\partial X = 1 + \partial u/\partial X$, the following expression can be obtained using series expansion while keeping in mind the orders of magnitude [86]:

$$\theta_1 = y' - u'y' - \frac{1}{3}y'^3 + \mathcal{O}(\epsilon^5). \tag{2.13}$$

The relative velocity of the cylinder with respect to the velocity of the fluid can be expressed as $\vec{V} = \dot{y}\vec{j} + \dot{x}\vec{i} - (-U_f\vec{i})$, and its direction is shown in Fig. 2–2b, where $U_f = U(1 - \partial u/\partial X)$ is the mean axial flow velocity relative to the deforming cylinder. Projecting this on $\vec{j_1}$, the direction normal to the element, leads to $V = \dot{y}\cos(\theta_1) + (\dot{x} + U_f)\cos(\bar{\theta}_1)$, where $\bar{\theta}_1 = \frac{\pi}{2} + \theta_1$. Therefore, the relative fluid-cylinder velocity V can be written as

$$V = \dot{y} - Uy' - \frac{1}{2}\dot{y}y'^2 + 2Uu'y' + \frac{1}{2}Uy'^3 - \dot{x}y' + \mathcal{O}(\epsilon^5). \tag{2.14}$$

The viscous forces

The viscous forces are obtained on the basis of the semi-empirical expressions proposed by Taylor [109], namely

$$F_N = \frac{1}{2}\rho DU^2(C_N \sin i + C_{Dp}\sin^2 i), \quad F_L = \frac{1}{2}\rho DU^2 C_T \cos i, \tag{2.15}$$

where C_N and C_T are friction coefficients and C_{Dp} is a form-drag coefficient; the term that contains C_{Dp} is also known as the normal steady hydrodynamic force per unit length, which comes from a vortex-lift mechanism; refer to [79, 110]. In Eq. (2.15), i is the angle of attack, which can be expressed as $i = \theta_1 - \theta_2$, where $\theta_2 = \tan^{-1}\{(\partial y/\partial t)/[U_f + (\partial x/\partial t)]\}$, as indicated in Fig. 2–2b. Thus, the following expressions can be obtained:

$$
\begin{aligned}
i &= y' - \frac{\dot{y}}{U_f} - u'y' + \frac{\dot{x}\dot{y}}{U_f^2} - \frac{1}{3}\left(y'^3 - \frac{\dot{y}^3}{U_f^3}\right) + \mathcal{O}(\epsilon^5),\\
\cos i &= 1 - \frac{1}{2}\left(y'^2 - 2\frac{y'\dot{y}}{U_f} + \frac{\dot{y}^2}{U_f^2}\right) + \mathcal{O}(\epsilon^4),\\
\sin i &= y' - \frac{\dot{y}}{U_f} - u'y' + \frac{\dot{x}\dot{y}}{U_f^2} - \frac{1}{2}\left(y'^3 - \frac{\dot{y}^3}{U_f^3} - \frac{y'^2\dot{y}}{U_f} + \frac{y'\dot{y}^2}{U_f^2}\right) + \mathcal{O}(\epsilon^5).
\end{aligned}
\tag{2.16}
$$

The normal and longitudinal viscous forces can then be derived as

$$
\begin{aligned}
F_N = \frac{1}{2}\rho D U^2 \Bigg[& C_N\left(y' - \frac{\dot{y}}{U} - \frac{\dot{y}u'}{U} - u'y' + \frac{\dot{x}\dot{y}}{U^2} - \frac{1}{2}\left(y'^3 - \frac{\dot{y}^3}{U^3} - \frac{y'^2\dot{y}}{U} + \frac{y'\dot{y}^2}{U^2}\right)\right)\\
& - C_{Dp}\left(y'|y'| + \frac{y'|\dot{y}| + |y'|\dot{y}}{U} + \frac{\dot{y}|\dot{y}|}{U^2}\right)\Bigg] + \mathcal{O}(\epsilon^5),\\
F_L = \frac{1}{2}\rho D U^2 C_T & \left[1 - \frac{1}{2}\left(y'^2 - 2\frac{y'\dot{y}}{U} + \frac{\dot{y}^2}{U^2}\right)\right] + \mathcal{O}(\epsilon^4).
\end{aligned}
\tag{2.17}
$$

The quadratic terms associated with the form-drag coefficient were modified in order to obtain forces that always oppose motion, as discussed in [86,111], considering also the inverted direction of the flow for the problem at hand.

The hydrostatic forces

The hydrostatic forces, which are the resultants of the steady-state pressure p acting on the cylinder, are derived by the procedure used in [5], assuming a momentarily frozen element, δs, of the cylinder immersed in the fluid. The following set of forces act on the surfaces of this element: F_{px} and F_{py}, on the two normally wet surfaces, and pA and $pA + [\partial(pA)/\partial s]\delta s$ on the normally dry surfaces. The net resultant of all these forces is known; it is the buoyancy force. The pressure gradient can be expressed as follows:

$$
A\left(\frac{\partial p}{\partial x}\right) = \frac{1}{2}\rho D U^2 C_T \frac{D}{D_h} + \rho g A,
\tag{2.18}
$$

where D_h is the hydraulic diameter. The following relation can be obtained by rewriting the derivative in Eq. (2.18) with respect to X and integrating from $X = s$ to L:

$$Ap(s) = Ap(L) - \left(\frac{1}{2}\rho D U^2 C_T \frac{D}{D_h} + \rho g A\right)\left[(L-s) - \int_s^L \frac{1}{2} y'^2 \mathrm{d}s\right] + \mathcal{O}(\epsilon^4). \tag{2.19}$$

Following the analysis in [86], the following expressions are derived for the hydrostatic forces per unit length of the cylinder:

$$\begin{aligned} -F_{px} &= -y'^2 A(\partial p/\partial x) - y'y'' Ap + \mathcal{O}(\epsilon^4), \\ F_{py} &= (y' - u'y' - y'^3)A(\partial p/\partial x) + (y'' - u''y' - u'y'' - \frac{3}{2}y'^2 y'')Ap + \mathcal{O}(\epsilon^5). \end{aligned} \tag{2.20}$$

Substituting Eqs. (2.18) and (2.19) into Eq. (2.20), the nonlinear expressions of the hydrostatic forces can be written as

$$\begin{aligned} -F_{px} &= y'^2\left(-\frac{1}{2}\rho D U^2 C_T \frac{D}{D_h} - \rho g A\right) - y'y'' Ap + \mathcal{O}(\epsilon^4), \\ F_{py} &= (y' - u'y' - y'^3)\left(\frac{1}{2}\rho D U^2 C_T \frac{D}{D_h} + \rho g A\right) \\ &\quad + (y'' - u''y' - u'y'' - \frac{3}{2}y'^2 y'')Ap + \mathcal{O}(\epsilon^5). \end{aligned} \tag{2.21}$$

2.1.3 Equation of motion

The virtual work done on the cylinder by the fluid-related forces can be expressed as follows:

$$\begin{aligned} \int_{t_1}^{t_2} \delta W \,\mathrm{d}t = \int_{t_1}^{t_2}\int_0^L &\{[-F_{px} - F_L\cos\theta_1 + (F_A - F_N)\sin\theta_1]\delta x \\ &+ [F_{py} - F_L \sin\theta_1 - (F_A - F_N)\cos\theta_1]\delta y\}\,\mathrm{d}s\,\mathrm{d}t. \end{aligned} \tag{2.22}$$

By substituting Eqs. (2.12), (2.17) and (2.21) into Eq. (2.22), and with the aid of Eqs. (2.1)-(2.6), (2.13), (2.14), (2.18), and (2.19), after many straightforward manipulations and transformations, the following nonlinear equation of motion can be obtained:

$$
\begin{aligned}
&(m+M)\ddot{y} - 2MU\dot{y}'(1-\frac{1}{4}y'^2) + MU^2y''(1+2y'^2) - \frac{3}{2}M\dot{y}y'(\dot{y}'-Uy'') \\
&- \frac{1}{2}\rho DU^2C_N(y'+\frac{1}{2}y'^3) + \frac{1}{2}\rho DU^2C_T(L-s)(y''+\frac{3}{2}y'^2y'') - Ap(L)(y''+y'^2y'') \\
&- (\frac{1}{2}\rho DU^2C_T\frac{D}{D_h} - mg + \rho gA)[y' + \frac{1}{2}y'^3 - (L-s)(y''+\frac{3}{2}y'^2y'')] \\
&+ EI(y'''' + 4y'y''y''' + y''^3 + y''''y'^2) + \frac{1}{2}\rho DC_N\dot{y}\int_0^s y'\dot{y}'\mathrm{d}s \\
&+ \frac{1}{2}\rho DU^2C_N\left(\frac{\dot{y}}{U} + \frac{1}{2}\frac{y'\dot{y}^2}{U^2} - \frac{1}{2}\frac{y'^2\dot{y}}{U} - \frac{\dot{y}^3}{2U^3}\right) + \frac{1}{2}\rho DU^2C_{Dp}\left(y'|y'| + \frac{y'|\dot{y}|+|y'|\dot{y}}{U} + \frac{\dot{y}|\dot{y}|}{U^2}\right) \\
&- my''\int_s^L\int_0^s(\dot{y}'^2 + y'\ddot{y}')\mathrm{d}s\,\mathrm{d}s + 2M(\dot{y}'-Uy'')\int_0^s y'\dot{y}'\mathrm{d}s \\
&- My''\int_0^s(\ddot{y}y' - 2Uy'\dot{y}' + U^2y'y'')\,\mathrm{d}s + (m+M)y'\int_0^s(y'\ddot{y}' + \dot{y}'^2)\,\mathrm{d}s \\
&- 3MUy'\int_0^s(y'\dot{y}'' + y''\dot{y}')\,\mathrm{d}s + y''\int_s^L\{Ap(L)y'y'' - \frac{1}{4}\rho DC_T\dot{y}^2\}\,\mathrm{d}s \\
&- \frac{1}{2}\rho DU^2y''(C_T-C_N)\int_s^L\left(y'^2 - \frac{y'\dot{y}}{U}\right)\mathrm{d}s = 0,
\end{aligned}
\tag{2.23}
$$

in which it is recalled that $(\ )' = \partial(\ )/\partial s$ and $\dot{(\ )} = \partial(\ )/\partial t$. In this equation, $Ap(L)$ can be expressed as $-\frac{1}{2}\rho D^2U^2C_b$, where C_b is the base drag coefficient.

Defining next the dimensionless quantities

$$
\begin{aligned}
&\xi = \frac{s}{L}, \quad \eta = \frac{y}{L}, \quad \tau = \left(\frac{EI}{m+\rho A}\right)^{1/2}\frac{t}{L^2}, \quad u* = \left(\frac{\rho A}{EI}\right)^{1/2}UL, \\
&\beta = \frac{\rho A}{m+\rho A}, \quad \gamma = \frac{(m-\rho A)gL^3}{EI}, \quad c_N = \frac{4}{\pi}C_N, \quad c_T = \frac{4}{\pi}C_T, \\
&c_d = \frac{4}{\pi}C_{Dp}, \quad \varepsilon = \frac{L}{D}, \quad h = \frac{D}{D_h}, \quad c_b = \frac{4}{\pi}C_b,
\end{aligned}
\tag{2.24}
$$

the equation of motion can be written in the following dimensionless form:

$$
\begin{aligned}
&[1+(\chi-1)\beta]\ddot{\eta} - 2u^*\sqrt{\beta}\chi\dot{\eta}'(1-\frac{1}{4}\eta'^2) + u^{*2}\chi\eta''(1+2\eta'^2) - \frac{3}{2}\chi\dot{\eta}\eta'(\beta\dot{\eta}' - u^*\sqrt{\beta}\eta'') \\
&- \frac{1}{2}u^{*2}\varepsilon c_N[\eta' + \frac{1}{2}\eta'^3] + \frac{1}{2}u^{*2}\varepsilon c_T(1-\xi)(\eta'' + \frac{3}{2}\eta'^2\eta'') + \frac{1}{2}c_b u^{*2}(\eta'' + \eta'^2\eta'') \\
&- (\frac{1}{2}u^{*2}\varepsilon c_T h - \gamma)[\eta' + \frac{1}{2}\eta'^3 - (1-\xi)(\eta'' + \frac{3}{2}\eta'^2\eta'')] \\
&+ \eta'''' + 4\eta'\eta''\eta''' + \eta''^3 + \eta''''\eta'^2 + \frac{1}{2}\varepsilon c_N\beta\dot{\eta}\int_0^\xi \eta'\dot{\eta}'\mathrm{d}\xi \\
&+ \frac{1}{2}u^{*2}\varepsilon c_N\left(\frac{\sqrt{\beta}}{u^*}\dot{\eta} + \frac{1}{2}\frac{\beta}{u^{*2}}\dot{\eta}^2\eta' - \frac{1}{2}\frac{\sqrt{\beta}}{u^*}\dot{\eta}\eta'^2 - \frac{1}{2}\frac{\beta^{3/2}}{u^{*3}}\dot{\eta}^3\right) \\
&+ \frac{1}{2}u^{*2}\varepsilon c_d\left(\eta'|\eta'| + \frac{\sqrt{\beta}}{u^*}(\eta'|\dot{\eta}| + |\eta'|\dot{\eta}) + \frac{\beta}{u^*}\dot{\eta}|\dot{\eta}|\right) \\
&- \eta''(1-\beta)\int_\xi^1\int_0^\xi(\dot{\eta}'^2 + \eta'\ddot{\eta}')\,\mathrm{d}\xi\,\mathrm{d}\xi + 2\chi(\beta\dot{\eta}' - u^*\sqrt{\beta}\eta'')\int_0^\xi \eta'\dot{\eta}'\,\mathrm{d}\xi \\
&- \chi\eta''\int_\xi^1(\beta\ddot{\eta}\eta' - 2u^*\sqrt{\beta}\dot{\eta}'\eta' + u^{*2}\eta''\eta')\,\mathrm{d}\xi + \eta'(1+(\chi-1)\beta)\int_0^\xi(\dot{\eta}'^2 + \eta'\ddot{\eta}')\,\mathrm{d}\xi \\
&+ \eta''\int_\xi^1\{-\frac{1}{2}c_b u^{*2}\eta'\eta'' - \frac{1}{4}\varepsilon c_T\beta\dot{\eta}^2\}\,\mathrm{d}\xi - 3\chi\sqrt{\beta}u^*\eta'\int_0^\xi(\eta'\dot{\eta}'' + \eta''\dot{\eta}')\,\mathrm{d}\xi \\
&- \frac{1}{2}u^{*2}\eta''(\varepsilon c_T - \varepsilon c_N)\int_\xi^1(\eta'^2 - \frac{\sqrt{\beta}}{u^*}\eta'\dot{\eta})\,\mathrm{d}\xi = 0,
\end{aligned}
\tag{2.25}
$$

where $(\ )' = \partial(\ )/\partial\xi$ and $\dot{(\ )} = \partial(\ )/\partial\tau$.

2.1.4 Boundary conditions

The boundary conditions related to the rigid end-piece at the free end of the cylinder are derived to first order, i.e. correct to $\mathcal{O}(\epsilon)$. The virtual work done by all the fluid dynamic forces acting on the end-piece of the cylinder, as shown in Fig. 2–3, can be expressed as

$$
\begin{aligned}
\int_{t_1}^{t_2}\delta W\,\mathrm{d}t = \int_{t_1}^{t_2}\int_{L-l}^{L}\{&[-F_{px}\cos\theta_1 + F_{py}\sin\theta_1 - F_L]\delta u_L \\
&+ [F_{px}\sin\theta_1 + F_{py}\cos\theta_1 - (F_A - F_N)]\delta u_N\}\,\mathrm{d}s\,\mathrm{d}t,
\end{aligned}
\tag{2.26}
$$

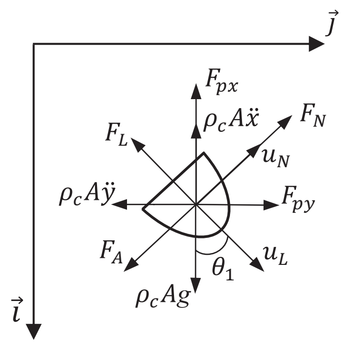

Figure 2–3: Forces acting on the end-piece at the free end of the cylinder; ρ_c is the density of the cylinder and of the end-piece, and $A(s)$ is the cross-sectional area of the end-piece which varies smoothly from A to zero in a distance $l \ll L$.

where l is the length of the end-piece, and δu_L and δu_N are the virtual displacements in the longitudinal and transverse directions; they can be related to δx and δy by

$$\left\{ \begin{array}{c} \delta x \\ \delta y \end{array} \right\} = \begin{bmatrix} \cos\theta_1 & -\sin\theta_1 \\ \sin\theta_1 & \cos\theta_1 \end{bmatrix} \left\{ \begin{array}{c} \delta u_L \\ \delta u_N \end{array} \right\}. \tag{2.27}$$

Eq. (2.26) leads to

$$\begin{aligned} \int_{t_1}^{t_2} \delta W \, \mathrm{d}t = \int_{t_1}^{t_2} \Big\{ & -\cos\theta_1 \int_{L-l}^{L} F_{px} \delta u_L \, \mathrm{d}s \\ & + \sin\theta_1 \int_{L-l}^{L} F_{py} \delta u_L \, \mathrm{d}s - \int_{L-l}^{L} F_L \delta u_L \, \mathrm{d}s \\ & + \sin\theta_1 \int_{L-l}^{L} F_{px} \delta u_N \, \mathrm{d}s + \cos\theta_1 \int_{L-l}^{L} F_{py} \delta u_N \, \mathrm{d}s \\ & - f \int_{L-l}^{L} F_A \delta u_N \, \mathrm{d}s + \int_{L-l}^{L} F_N \delta u_N \, \mathrm{d}s \Big\} \mathrm{d}t, \end{aligned} \tag{2.28}$$

where f is a "streamlining parameter", $0 \leq f < 1$; $f \to 1$ is taken for a well-streamlined end, while $f \to 0$ for a blunt end. The following simplified expressions are used, which lead to the final form of the linear boundary condition:

$$
\begin{aligned}
-F_{px} &= p(\mathrm{d}A(s)/\mathrm{d}s) + \mathcal{O}(\epsilon^2), \\
F_{py} &= y'\left(\frac{1}{2}\rho U^2 C_T \frac{D^2(s)}{D_h} + \rho g A(s) + p(\mathrm{d}A(s)/\mathrm{d}s)\right) + \mathcal{O}(\epsilon^3), \\
F_N &= -\frac{1}{2}\rho D(s) U C_N(\dot{y} - U y') + \mathcal{O}(\epsilon^2), \quad F_L = \frac{1}{2}\rho D(s) U^2 C_T + \mathcal{O}(\epsilon^2), \\
F_A &= \chi\rho(\ddot{y} - U\dot{y}')A(s) - \chi\rho U(\dot{y} - U y')(\mathrm{d}A(s)/\mathrm{d}s) + \mathcal{O}(\epsilon^3), \\
\cos\theta_1 &= 1 + \mathcal{O}(\epsilon^2), \quad \sin\theta_1 = y' + \mathcal{O}(\epsilon^3).
\end{aligned} \tag{2.29}
$$

The variation of the Lagrangian for the ogival end has been derived previously in [86], as follows:

$$
\delta \int_{t_1}^{t_2} \mathcal{L}\mathrm{d}t = -\int_{t_1}^{t_2} \int_{L-l}^{L} [\rho_c A(s)(\ddot{x}\delta x + \ddot{y}\delta y) - \rho_c A(s) g\delta x]\, \mathrm{d}s\, \mathrm{d}t, \tag{2.30}
$$

leading to

$$
\delta \int_{t_1}^{t_2} \mathcal{L}\mathrm{d}t = -\int_{t_1}^{t_2} [m\ddot{y}s_e\delta u_N - mgs_e(\delta u_L - y'\delta u_N)]\mathrm{d}t + \mathcal{O}(\epsilon^3), \tag{2.31}
$$

in which $s_e = (1/A)\int_{L-l}^{L} A(s)\mathrm{d}s$. Using the extended Hamilton's principle, one can obtain the following shear boundary condition at $s = L - l$:

$$
\begin{aligned}
&-EIy''' + [fM(\ddot{y} - U\dot{y}') + m\ddot{y}]s_e + fMU(\dot{y} - Uy') + (m - \rho A)gy's_e \\
&-\frac{1}{2}\rho D U^2 C_T h y' s_e + \frac{1}{2}\rho D U C_N(\dot{y} - Uy')\bar{s}_e - \frac{1}{2}\rho D^2 U^2 C_b y' = 0,
\end{aligned} \tag{2.32}
$$

and $y'' = 0$, where $\bar{s}_e = (1/D)\int_{L-l}^{L} D(s)\mathrm{d}s$. Equations (2.32) can be written in dimensionless form as

$$
\begin{aligned}
&-\eta''' + \chi_e[(1 + (\chi f - 1)\beta)\ddot{\eta} - \chi f u^* \sqrt{\beta}\dot{\eta}'] + (\frac{1}{2}\bar{\chi}_e\varepsilon c_N + \chi f)(u^*\sqrt{\beta}\dot{\eta} - u^{*2}\eta') \\
&+ (-\frac{1}{2}u^{*2}\varepsilon c_T h + \gamma)\chi_e\eta' - \frac{1}{2}c_b u^{*2}\eta' = 0 \quad \text{at } \xi = 1,
\end{aligned} \tag{2.33}
$$

where $\chi_e = s_e/L, \bar{\chi}_e = \bar{s}_e/L$.

2.1.5 Methods of analysis

The final equation of motion including the boundary conditions can be expressed as

$$
F(\eta(\xi,\tau), u^*) + \delta(\xi - 1)\bar{\beta}(\eta(\xi,\tau), u^*) = 0, \tag{2.34}
$$

in which the equation of motion is written as $F(\eta, u^*) = 0$ for simplicity; $\bar{\beta}(\eta, u^*) = 0$ represents the boundary conditions, and $\delta(\xi - 1)$ is the Dirac delta function. Equation (2.34) is discretized by Galerkin's technique, utilizing the cantilevered beam eigenfunctions $\phi_j(\xi)$, available in [112], as comparison functions, since they satisfy the appropriate boundary conditions, after the peculiar shear boundary condition has been included in the equation of motion, as in Eq. (2.34), and $q_j(\tau)$ are the corresponding generalized coordinates; thus,

$$\eta(\xi, \tau) = \sum_{j=1}^{N} \phi_j(\xi) q_j(\tau), \tag{2.35}$$

where N represents the number of modes in the Galerkin scheme. Substituting Eq. (2.35) into the final equation of motion, i.e. Eq. (2.34), multiplying by $\phi_i(\xi)$ and integrating from 0 to 1, leads to the following set of ODEs:

$$\begin{aligned} &M_{ij}\ddot{q}_j + C_{ij}\dot{q}_j + K_{ij}q_j + r_{ijk}q_j|q_k| + \bar{s}_{ijk}|q_j|\dot{q}_k + \tilde{s}_{ijk}q_j|\dot{q}_k| + t_{ijk}\dot{q}_j|\dot{q}_k| \\ &+\alpha_{ijkl}q_jq_kq_l + \beta_{ijkl}q_jq_k\dot{q}_l + \gamma_{ijkl}q_j\dot{q}_k\dot{q}_l + \eta_{ijkl}\dot{q}_j\dot{q}_k\dot{q}_l + \mu_{ijkl}q_jq_k\ddot{q}_l = 0. \end{aligned} \tag{2.36}$$

Only in Eq. (2.36), the repetition of an index implies summation. The linear terms, M_{ij}, C_{ij} and K_{ij}, correspond to elements of the mass, damping and stiffness matrices, respectively, and they are defined by

$$\begin{aligned} M_{ij} &= [1 + (\chi - 1)\beta]\delta_{ij} + [1 + (\chi f - 1)\beta]\chi_e\phi_i(1)\phi_j(1), \\ C_{ij} &= -2\chi u^*\sqrt{\beta}b_{ij} + \frac{1}{2}u^*\varepsilon c_N\sqrt{\beta}\delta_{ij} + (\frac{1}{2}\bar{\chi}_e\varepsilon c_N + \chi f)u^*\sqrt{\beta}\phi_i(1)\phi_j(1) \\ &\quad - \chi f u^*\sqrt{\beta}\chi_e\phi_i(1)\phi_j'(1), \\ K_{ij} &= \chi u^{*2}c_{ij} + (\frac{1}{2}u^{*2}\varepsilon(-c_N - c_T h) + \gamma)b_{ij} + (\frac{1}{2}u^{*2}\varepsilon c_T(1 + h) - \gamma)(-d_{ij} + c_{ij}) + \lambda_j^4\delta_{ij} \\ &\quad + \frac{1}{2}u^{*2}c_b c_{ij} + (\gamma\chi_e - \frac{1}{2}u^{*2}(\bar{\chi}_e\varepsilon c_N + \varepsilon c_T h\chi_e) - \chi f u^{*2} - \frac{1}{2}c_b u^{*2})\phi_i(1)\phi_j'(1), \end{aligned} \tag{2.37}$$

where δ_{ij} is the Kronecker delta function, λ_j is the jth root of the characteristic equation of a cantilevered beam, and the constants b_{ij}, c_{ij} and d_{ij} are defined by

$$b_{ij} = \int_0^1 \phi_i \phi_j' \,\mathrm{d}\xi, \quad c_{ij} = \int_0^1 \phi_i \phi_j'' \,\mathrm{d}\xi, \quad d_{ij} = \int_0^1 \xi \phi_i \phi_j'' \,\mathrm{d}\xi; \tag{2.38}$$

they are available in closed form in [28]. The nonlinear coefficients, r_{ijk}, $\bar{s}_{ijk}$, $\tilde{s}_{ijk}$, t_{ijk}, α_{ijkl}, β_{ijkl}, γ_{ijkl}, η_{ijkl} and μ_{ijkl} in Eq. (2.36), are defined in Appendix A.

2.2 Linear dynamics

In this section, the discretized ODEs obtained in Sub-section 2.1.5 are linearized, which results in a linear model identical to the one derived earlier in [78]. Equation (2.36) can now be written in the following matrix form:

$$\mathbf{M}\ddot{\mathbf{q}} + \mathbf{C}\dot{\mathbf{q}} + \mathbf{K}\mathbf{q} = \mathbf{0}, \tag{2.39}$$

where $\mathbf{M}$, $\mathbf{C}$ and $\mathbf{K}$ are the mass, damping and stiffness matrices, respectively; the elements of these matrices are given in Eq. (2.37). Also, $\mathbf{q} = \{q_1, q_2, \ldots, q_N\}^\mathsf{T}$, $\dot{\mathbf{q}} = \mathrm{d}\mathbf{q}/\mathrm{d}\tau$ and $\ddot{\mathbf{q}} = \mathrm{d}\dot{\mathbf{q}}/\mathrm{d}\tau$. The equations of motion may then be reduced to first-order form, as detailed in [2], by defining

$$\mathbf{z} = \begin{Bmatrix} \dot{\mathbf{q}} \\ \mathbf{q} \end{Bmatrix}, \qquad \mathbf{B} = \begin{bmatrix} \mathbf{0} & \mathbf{M} \\ \mathbf{M} & \mathbf{C} \end{bmatrix}, \qquad \mathbf{E} = \begin{bmatrix} -\mathbf{M} & \mathbf{0} \\ \mathbf{0} & \mathbf{K} \end{bmatrix}, \tag{2.40}$$

which yields

$$\mathbf{B}\dot{\mathbf{z}} + \mathbf{E}\mathbf{z} = \mathbf{0}. \tag{2.41}$$

Seeking oscillatory solutions, $z_j = A_j \mathrm{e}^{\lambda_j \tau} = A_j \mathrm{e}^{\mathrm{i}\omega_j \tau}$, the problem becomes a typical eigenvalue problem in the following form:

$$(\boldsymbol{\lambda}\mathbf{I} - \mathbf{Y})\mathbf{A} = \mathbf{0}, \tag{2.42}$$

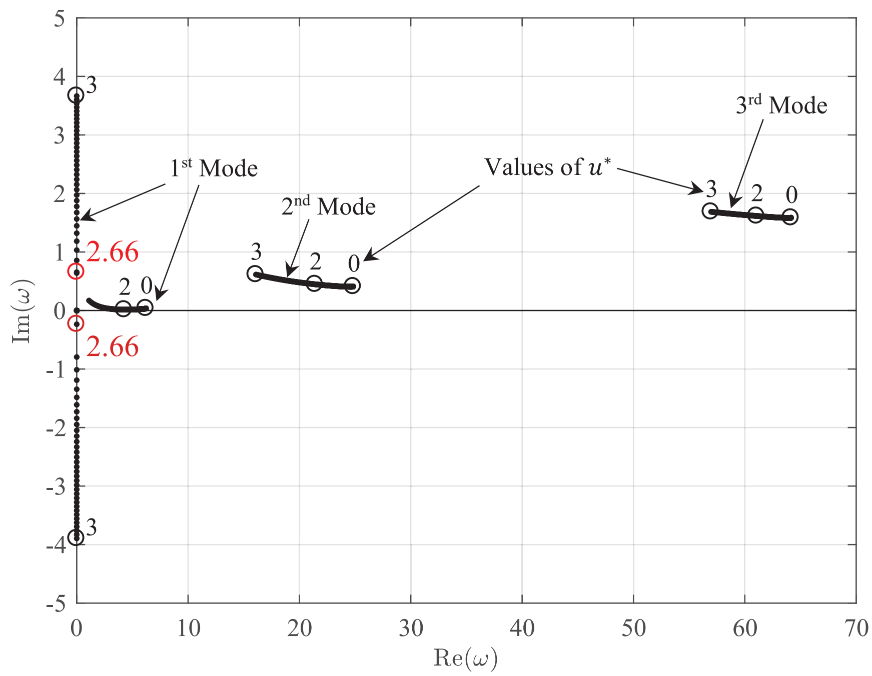

Figure 2–4: Argand diagram showing the imaginary and real parts of the dimensionless complex eigenfrequencies ω_j at different flow velocities u^*.

where $\mathbf{Y} = -\mathbf{B}^{-1}\mathbf{E}$. The eigenvalues λ_j and the corresponding eigenfrequencies ω_j, $j = 1, 2, ..., 2N$, may now be determined.

A system having the following parameters: $\beta = 1.14 \times 10^{-3}$, $\gamma = 17.6$, $\varepsilon = 25.3$, $h = 0.455$, $\chi = 1.22$, $\chi_e = 0.00792$, $c_N = 0.0100$, $c_T = 0.0125$, $f = 0.8$, and $c_b = 1 - f = 0.2$ is considered. This corresponds to a physical system similar to the one considered in the theory and experiments of [78], involving an elastomer cylinder in air-flow, with the following dimensional characteristics: $D_{ch} = 0.0508\,\mathrm{m}$, $D = 0.0159\,\mathrm{m}$, $L = 0.401\,\mathrm{m}$, $EI = 7.63 \times 10^{-3}\,\mathrm{N\,m^2}$, $m = 0.213\,\mathrm{kg\,m^{-1}}$, $\rho A = 2.43 \times 10^{-4}\,\mathrm{kg\,m^{-1}}$, and $s_e = 0.00318$ m. The viscoelastic and hysteretic damping of the cylinder material, $\bar{\alpha}$ and $\bar{\mu}$ are also considered as in [78], by replacing E by $E[1 + (\bar{\alpha} + \bar{\mu}/\Omega)\,\partial/\partial t]$, where Ω is the radian frequency of the motion. The complex eigenfrequencies ω_j are detrmined at each flow velocity u^*, and the results are plotted in a form of an Argand diagram in Fig. 2–4, in which Re(ω) and Im(ω) represent the real and imaginary parts of ω. This Argand diagram is obtained using a ten-mode Galerkin approximation; however, it was found that utilizing only six comparison functions is enough to achieve convergence with a criterion of less than 5%.[1] Only the first three modes are plotted in Fig. 2–4 for convenience, and the corresponding values of u^* are indicated on each mode locus.

As seen in Fig. 2–4, the imaginary part of the first-mode eigenfrequency, $\mathrm{Im}(\omega_1)$, which is associated with the damping of the system becomes negative, at $u^* = 2.66$. This occurs while $\mathrm{Re}(\omega_1)$=0, which is related to the frequency of oscillation. This means that the cylinder loses its stability via a static divergence, i.e. buckling in the first mode at $u^*_{cr} = 2.66$. The second and third modes remain stable, becoming more highly damped with increasing u^*, since the values of the corresponding $\mathrm{Im}(\omega)$ become higher.

2.3 Nonlinear dynamics

In this section, the discretized ODEs obtained in Sub-section 2.1.5 are solved without linearization, considering the same system parameters defined in Section 2.2. A value of $C_{Dp} = 1.1$ is assumed, as in [109], for the normalized drag coefficient of a circular cylinder. In addition, the viscoelastic damping of the cylinder material, $\bar{\alpha}$, is also considered; however, the hysteretic damping considered in [78] is replaced by a viscous damping, k, to be consistent with the nonlinear analysis adopted in the present study. The dimensionless values of the dissipation considered are $\bar{\alpha}^* = [EI/(\rho A + m)]^{1/2}(\bar{\alpha}/L^2) = 0.0009$ and $\kappa = (kL^2)/[EI(m + \rho A)]^{1/2} = 0.3$. The ODEs are solved numerically using AUTO [113], which is based on a collocation method and is adapted to conduct bifurcation analysis for differential equations, and also a MATLAB ODE solver (Mathworks, Inc.) namely ode15i, which utilizes a variable order method [114], for direct time integration purposes.

A bifurcation diagram obtained using a six-mode Galerkin approximation is presented in Fig. 2–5 for the first generalized coordinate q_1, considered to be representative of the behaviour of the system. The black solid line, —, obtained using AUTO shows the stable

[1] The dimensionless critical flow velocity for divergence, u^*_{cr}, obtained using a six-mode Galerkin approximation was found to be $u^*_{cr} = 2.653$, while with ten modes $u^*_{cr} = 2.656$.

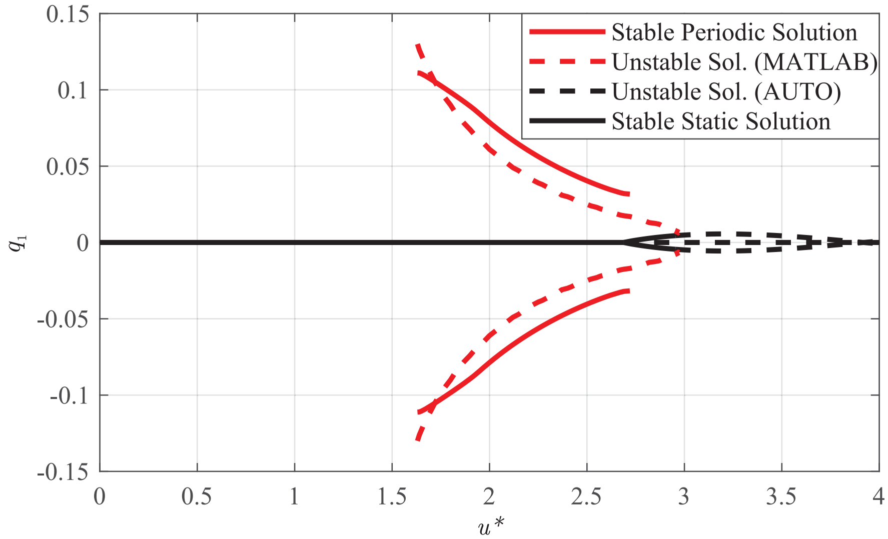

Figure 2–5: Bifurcation diagram showing the first generalized coordinate, q_1, as a function of the dimensionless flow velocity, $u*$.

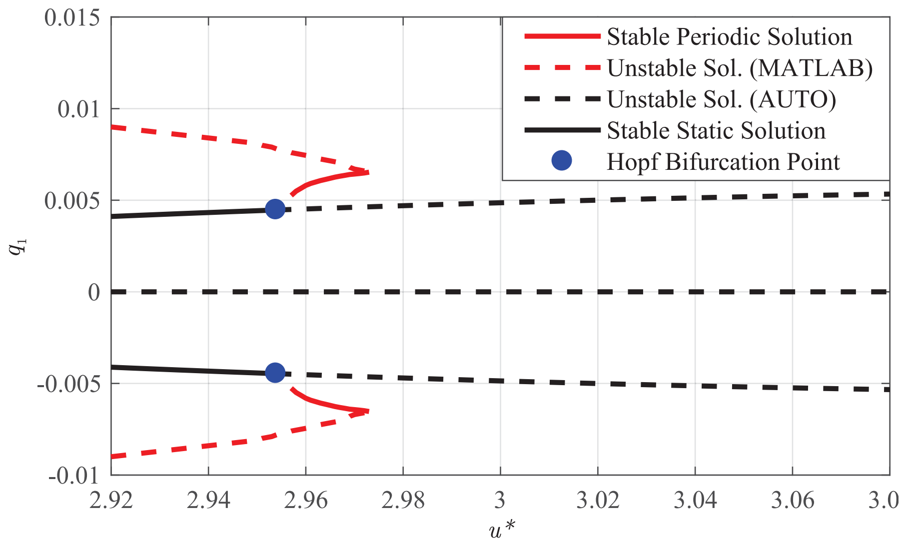

Figure 2–6: Zoomed-in bifurcation diagram showing the dynamical behaviour beyond the pitchfork bifurcation point.

static solution at the original equilibrium state of the cylinder for $u* < 2.69$. At $u* = 2.69$, a branch point is predicted, which leads to divergence in the first mode via a supercritical pitchfork bifurcation; the amplitude of divergence increases slightly with increasing flow velocity. At $u* \approx 2.957$, a supercritical Hopf bifurcation point is predicted on each branch, which leads to flutter in the first mode, corresponding to stable periodic oscillations around

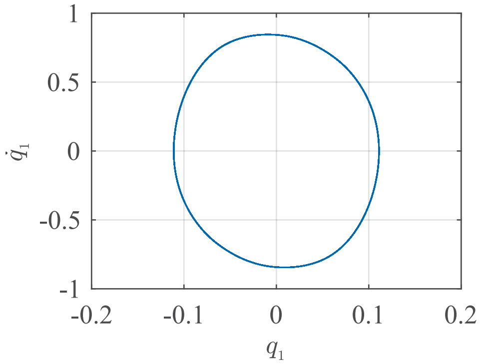

(a) At $u^* = 1.63$ with $q_1(\tau = 0) > 0.13$

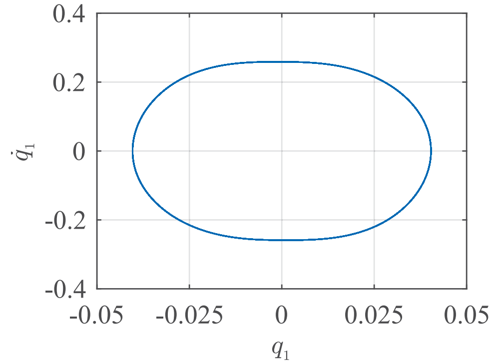

(b) At $u^* = 2.5$ with $q_1(\tau = 0) > 0.025$

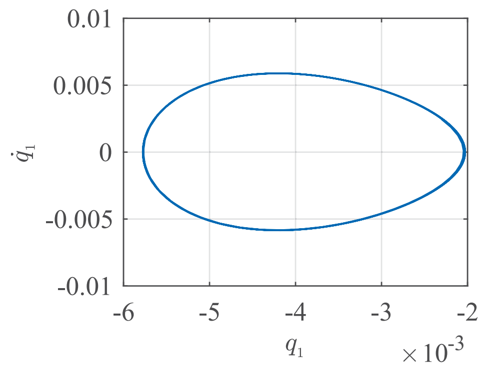

(c) At $u^* = 2.96$ with $q_1(\tau = 0) < 0.00745$

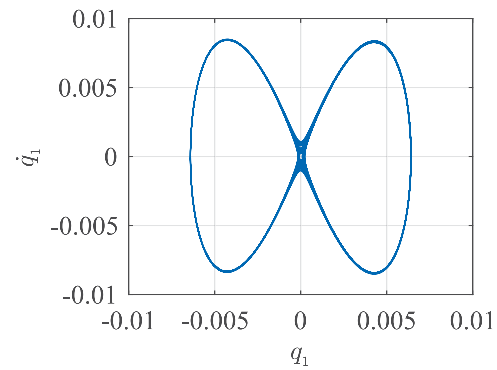

(d) At $u^* = 2.97$ with $q_1(\tau = 0) < 0.0067$

Figure 2–7: Phase-plane plots obtained at various values of the dimensionless flow velocity, u^*.

the deformed, i.e. buckled, position, and right after that, the oscillations occur mainly around the origin; see the zoomed-in bifurcation diagram in Fig. 2–6 and also the phase-plane plots in Fig. 2–7. It should be noted that the stable periodic solution, i.e. —, emanating from the Hopf bifurcation point was numerically followed via MATLAB using the ode15i solver. The solution was obtained at each specific flow velocity, then the maximum and minimum values of q_1 were plotted after reaching the final steady-state. The results obtained by MATLAB are consistent with the results of AUTO up to $u^* \approx 2.97$ (the static solution as well as the dynamic one), where the oscillations are around the origin after being around the buckled position. At that point AUTO fails to converge to any solution, perhaps because of this sudden change of state.

At $u^* = 1.63$, another stable periodic solution is predicted by MATLAB that corresponds to flutter around the origin. An initial guess, i.e. initial perturbation, of at least $q_1(\tau = 0) = 0.131$ and $\dot{q}_1(\tau = 0) = 0$ is required at that flow velocity in order to converge towards this periodic solution, which indicates a saddle-node bifurcation. The periodic solution obtained was added to the bifurcation diagram by plotting the maximum and the minimum values of q_1 at each corresponding flow velocity, after reaching the final steady-state (shown as solid red lines, —, in Fig. 2–5). In addition, the minimum required values of the initial perturbation, i.e. $q_1(\tau = 0)$ with $\dot{q}_1(\tau = 0) = 0$ always, to reach the periodic solution at each flow velocity was plotted as an unstable solution[2] (shown as dashed red lines, - - - - -, in Figs. 2–5 and 2–6). The unstable solution matches with the stable solution that emanates from the Hopf bifurcation point at another saddle-node bifurcation at $u^* \approx 2.973$, while at $2.72 < u^* \leq 2.973$, the unstable solution represents the maximum possible values of the initial perturbation for the model to converge towards a stable solution. At $u^* > 2.973$, the system does not converge to any stable state. The dynamical behaviour of the cylinder predicted by the present model at different flow velocities can be summarized as in Table 2–1.

Table 2–1: Dynamical state of the cylinder predicted by the present model for different ranges of u^*.

Range of u^*	Dynamical state
0 – 1.63	Stable
1.63 – 2.69	Flutter around the origin
2.69 – 2.72	Either divergence or flutter around the origin
2.720 – 2.957	Divergence
2.957 – 2.970	Flutter around the buckled position
2.970 – 2.973	Flutter *mainly* around the origin

Fig. 2–8 shows the time histories at different flow velocities: (a) $u^* = 1.63$, which is the critical flow velocity for flutter instability; (b) $u^* = 2.5$, showing a smaller amplitude

[2] It is not actually a solution that was obtained by solving the ODEs. However, it determines to which stable state the solution will converge.

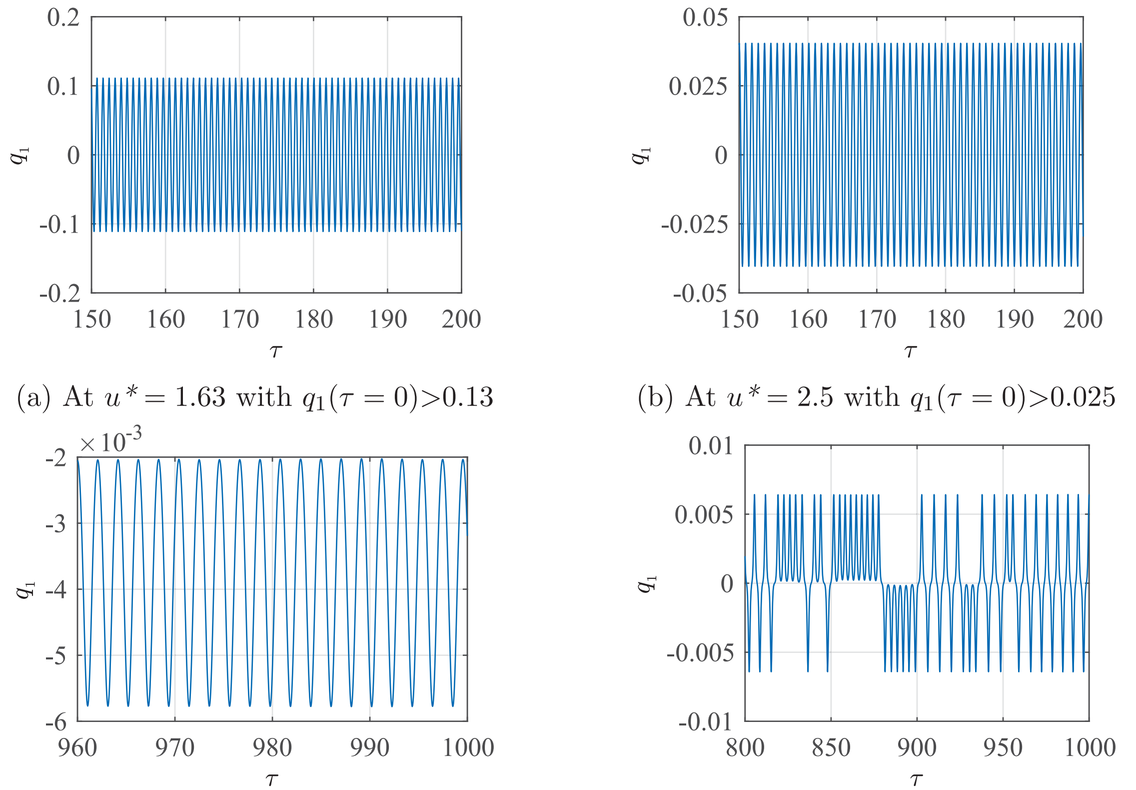

(a) At $u^* = 1.63$ with $q_1(\tau = 0) > 0.13$

(b) At $u^* = 2.5$ with $q_1(\tau = 0) > 0.025$

(c) At $u^* = 2.96$ with $q_1(\tau = 0) < 0.00745$

(d) At $u^* = 2.97$ with $q_1(\tau = 0) < 0.0067$

Figure 2–8: Time history plots at various values of the dimensionless, flow velocity u^*.

of flutter; (c) $u^* = 2.96$, showing that the oscillations are around the buckled position; and (d) $u^* = 2.97$ showing that the oscillations occur *mainly* around the origin again; however, at some ranges of τ, the oscillations are biased towards one of the two buckled positions. The phase-plane plots and the power spectral density plots at the same flow velocities are shown in Figs. 2–7 and 2–9, both of them indicating periodic motions, which tend to become aperiodic for the post-divergence oscillations; see Fig. 2–9d that shows a more dense frequency spectrum.

The flutter predicted by the proposed model is in the first mode; this can be seen clearly in Fig. 2–10, which also shows the maximum dimensionless amplitude of the oscillations. The frequencies of these oscillations at each corresponding flow velocity are presented in Fig. 2–11, which shows a decrease in the frequency with increasing the flow velocity before the onset of buckling.

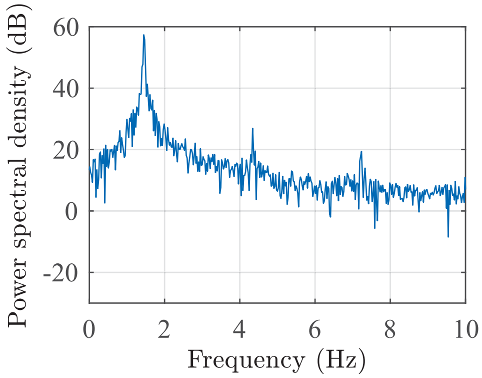

(a) At $u^* = 1.63$ with $q_1(\tau = 0) > 0.13$

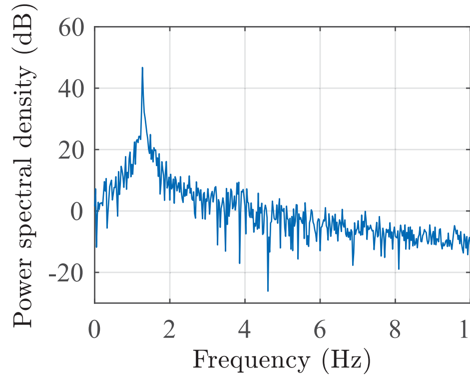

(b) At $u^* = 2.5$ with $q_1(\tau = 0) > 0.025$

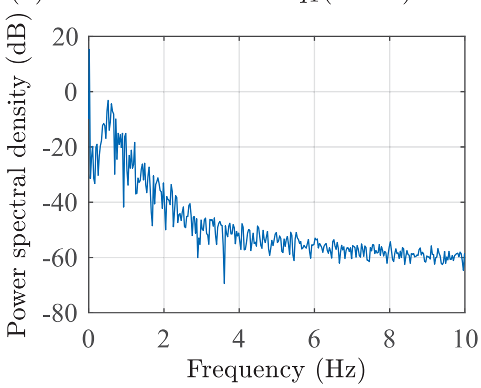

(c) At $u^* = 2.96$ with $q_1(\tau = 0) < 0.00745$

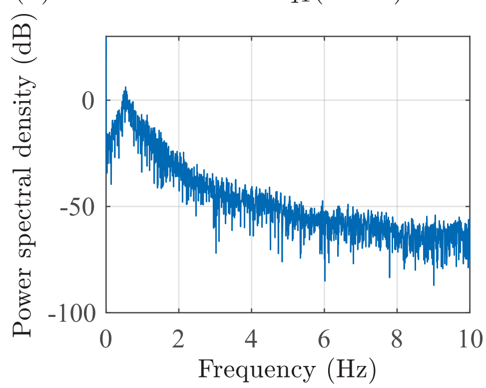

(d) At $u^* = 2.97$ with $q_1(\tau = 0) < 0.0067$

Figure 2–9: Power spectral density plots calculated by direct fast Fourier transform (FFT) for various values of the dimensionless flow velocity, u^*.

2.4 Comparison between the proposed theory and other studies in the literature

The values of the parameters used to solve the ODEs in Sections 2.2 and 2.3 were purposely chosen to allow comparison of the results to the experimental observations and theoretical predictions of Rinaldi and Païdoussis [78]. The results of the proposed model qualitatively agree with the experimental observations, in the sense that in both of them, the cylinder is subject to oscillations first while increasing flow velocity. The amplitude of the oscillation decreases with increasing flow velocity, and a static buckling occurs afterwards. Moreover, post-divergence oscillations were experimentally observed and predicted by this nonlinear model. However, quantitatively, the amplitude of the flutter-like oscillations observed experimentally is of order of only half a cylinder diameter, which is very small

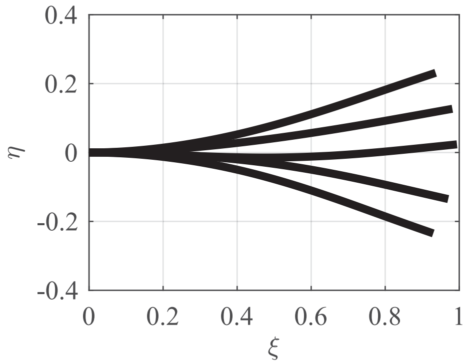

(a) At $u^* = 1.63$ with $q_1(\tau = 0) > 0.13$

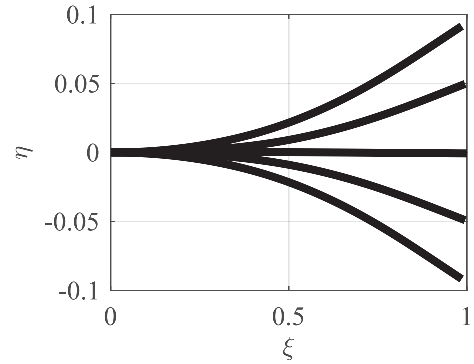

(b) At $u^* = 2.5$ with $q_1(\tau = 0) > 0.025$

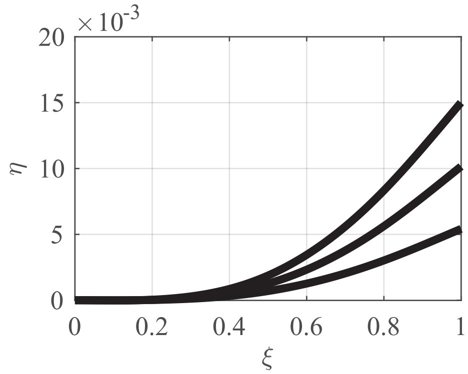

(c) At $u^* = 2.96$ with $q_1(\tau = 0) < 0.00745$

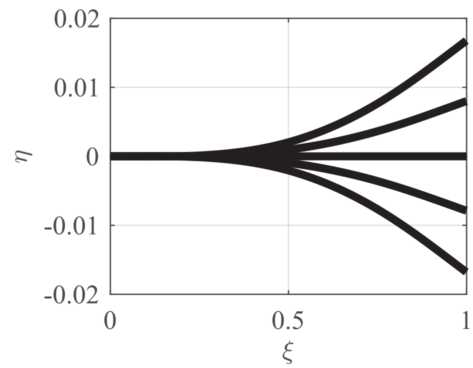

(d) At $u^* = 2.97$ with $q_1(\tau = 0) < 0.0067$

Figure 2–10: Shape of the cylinder at various values of the dimensionless flow velocity, u^*.

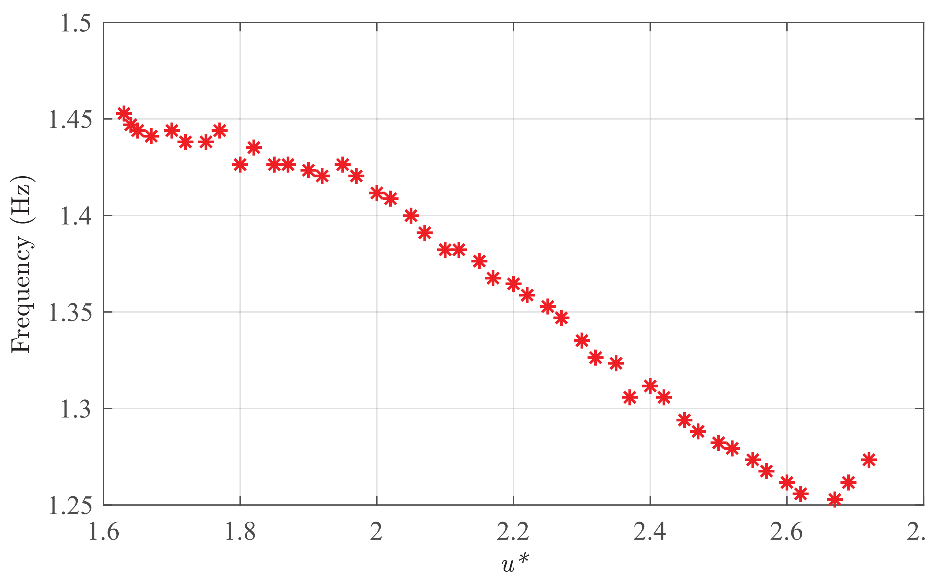

Figure 2–11: Frequency of the oscillations associated with the stable periodic solution obtained for $u^* \geq 1.63$ as a function of the dimensionless flow velocity, u^*.

compared to the amplitude predicted by the proposed model. In addition, the experimentally observed oscillations were at vanishing flow velocities, which is also not the case with the flutter predicted by this theory.

The nonlinear model proposed in this chapter predicts a saddle-node bifurcation at $u^* = 1.63$, which leads to flutter in the first mode, corresponding to stable periodic oscillations around the origin. This value matches with the value of the critical flow velocity of the first instability observed experimentally in [78] at $u^* = 1.64$–1.70, which is a buckling instability as reported. However, Rinaldi and Païdoussis [78] also observed post-divergence oscillations whose nature was difficult to interpret because of the small amplitude, but the oscillations were also in the first mode of the cylinder. Unfortunately, the post-divergence flutter predicted by this theory at $u^* > 2.69$ cannot be compared to the experiments in [78], because it was not possible to reach such high flow velocities in the experiments.

The linear model derived in [78] predicts a static divergence at $u^* \approx 2.66$, which agrees well with the onset of the divergence predicted by the proposed nonlinear model at $u^* = 2.69$. However, the linear model of [78] shows very weak damping at low flow velocities before the onset of instability, as shown in Fig. 2–4, which led the authors of the same study to discuss the possibility of having flow-perturbation excitation in the first mode of the cylinder, instead of flutter, before buckling occurs. The existence of a saddle-node bifurcation was proved by Sader et al. [79] who considered a system with quite similar parameters as in [78]. However, the saddle-node bifurcation obtained in [79] leads to a static divergence, perhaps because only a static analysis was conducted in that study. Moreover, the saddle-node bifurcation was predicted at $u^* = 1.23$ in [79]; this discrepancy can be justified by the fact that the effects of the confined flow and the end-piece were not considered in that study.

2.5 Summary

In this chapter, a weakly nonlinear equation of motion, correct to third-order of magnitude, has been derived for the dynamics of a free-clamped cylinder in confined axial flow; i.e. with the flow directed from the free end towards the clamped one. The lateral deflection is assumed to be of first-order magnitude, while the axial one of second-order. The inviscid, hydrostatic and viscous forces were derived separately, as well as the shear boundary condition related to the free end of the cylinder. The equation of motion was obtained via the extended Hamilton's principle. This is probably not the definitive nonlinear equation of motion for this system, since it was not obtained by a unified nonlinear treatment of the fluid mechanics.

The nonlinear model proposed in this study, for a long elastomer cylinder subjected to confined axial air-flow and fitted with a more or less well-streamlined end-piece, predicts flutter in the first mode at $u^* = 1.63$; its onset requires a large enough perturbation of the cylinder, as a condition of a saddle-node bifurcation. The amplitude and the frequency of the oscillations decrease with increasing flow velocity. At $u^* = 2.69$, a static divergence in the first mode is predicted via a supercritical pitchfork bifurcation; the amplitude of the divergence increases with increasing flow velocity. In addition, post-divergence flutter is also predicted at $u^* \approx 2.957$ via a supercritical Hopf bifurcation, which leads to stable periodic oscillations of relatively smaller amplitudes around the buckled position first, then around the origin at slightly higher flow velocity.

This study presents the first nonlinear analytical study for the inverted flow configuration of a cantilevered cylinder in axial flow. It provides fuller, deeper understanding of the dynamics of the system compared to what can be achieved by the linear theory. For example, the dynamical behaviour beyond the pitchfork bifurcation point, as well as the existence of saddle-node bifurcations, which cannot be predicted by the linear theory, can be explored by the nonlinear theory.

CHAPTER 3
Nonlinear dynamics of a hanging tubular cantilever simultaneously subjected to internal and fully-confined external axial flows (System II)

In this chapter, the dynamics of a hanging tubular cantilever that discharges fluid downwards, which then flows upwards as a confined axial flow, is examined using a nonlinear theory, for the first time. The same system had been studied earlier by Païdoussis et al. [8] using a linear theory and by Rinaldi [115] who conducted experiments with water flow. The nonlinear equation of motion is derived via the extended Hamilton's principle to third-order accuracy in Section 3.1. The equation obtained is expressed in dimensionless form, and then discretized using the Galerkin technique. In Sections 3.2 and 3.3, the discretized equations are solved for system parameters similar to those considered in [8], and the linear and nonlinear dynamics of the system are examined. In Section 3.5, the influence of the dimensionless parameters related to confinement, gravity, mass ratio, drag coefficient, and pipe thickness on the dynamical behaviour of the system are investigated theoretically. Moreover, a comparison between the predictions of the proposed model and the experimental observations reported in [48] is presented in Section 3.5.

3.1 Derivation of the equation of motion

The system under study consists of a slender flexible cantilevered pipe of outer diameter D_o, inner diameter D_i, length L, flexural rigidity EI and mass per unit length m. The pipe discharges fluid of density ρ downwards with velocity U_i, which then flows upwards with velocity U_o through an annular region contained by a cylindrical rigid channel of diameter D_{ch}. Thus, the internal and external flows are interdependent and in opposite directions. The system is vertical, so the undeformed neutral axis of the cantilever coincides with the X-axis and is in the direction of gravity, g, as shown in Fig. 3–1a.

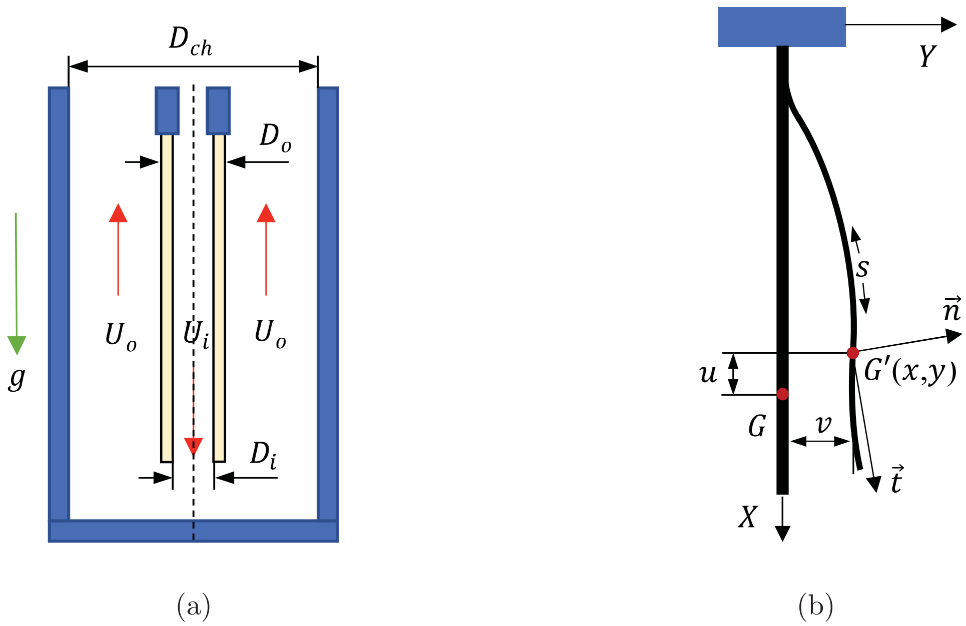

Figure 3–1: (a) Diagrammatic view of a vertical hanging tubular cantilever that discharges fluid downwards, which then flows upwards through an annular region contained by a circular rigid channel. (b) Diagram defining the coordinate systems used, where G is a material point on the neutral axis of the cantilever at curvilinear coordinate s, located at $G(X,0)$ before deformation and $G'(x,y)$ afterwards.

For the structural part of the problem, the assumptions made in Chapter 2 for System I are also made here, namely that (i) the cantilever length-to-diameter ratio is sufficiently high, so that Euler-Bernoulli beam theory is applicable; (ii) the cantilever centreline is inextensible; (iii) the deflections of the cantilever may be large, but with small strains; and (iv) the motion of the cantilevered pipe is planar and in the (X,Y)-plane for simplicity. In addition, the following assumptions are made for the fluid part: (i) the fluid is incompressible; (ii) the mean flow velocity of the internal and external flows are constant; and (iii) the internal and external flows are related to each other via continuity, i.e. via the principle of conservation of mass.

As in Chapter 2, two coordinate systems are utilized in the following analysis: the Lagrangian (X, Y, Z, t), which is associated with the undeformed state of the cantilever, and the Eulerian (x, y, z, t) for the deformed state. The displacements of point G on the centreline of the cantilever, from the undeformed state to the deformed one, are $u = x - X$, $v = y - Y$, and $w = z - Z$. Figure 3–1b shows the curvilinear coordinate, s; since the pipe centreline is assumed to be inextensible, one can write $\partial s/\partial X = 1$ and $(\partial x/\partial X)^2 + (\partial y/\partial X)^2 = 1$.

The equation of motion is derived via the extended Hamilton's principle,

$$\delta \int_{t_1}^{t_2} \mathcal{L}\, \mathrm{d}t + \int_{t_1}^{t_2} \delta W\, \mathrm{d}t = 0, \tag{3.1}$$

where $\mathcal{L} = \mathcal{T}_p - \mathcal{V}_p$ is the Lagrangian, $\mathcal{T}_p$ being the kinetic energy of the pipe including the conveyed fluid, $\mathcal{V}_p$ its potential energy, $\delta W = \delta W_i + \delta W_o$ is the total virtual work done on the pipe, δW_i being the virtual work due to the non-conservative forces associated with the internal flow, which are not included in the Lagrangian, and δW_o the virtual work due to the fluid-related forces associated with the external flow. The equation of motion obtained in this chapter is weakly nonlinear, exact to third-order of magnitude, $\mathcal{O}(\epsilon^3)$, for $y = v \sim \mathcal{O}(\epsilon)$ and $u \sim \mathcal{O}(\epsilon^2)$. Therefore, the expressions for the virtual work have to be exact to $\mathcal{O}(\epsilon^3)$, while the energy expressions to $\mathcal{O}(\epsilon^4)$.

3.1.1 Kinetic and potential energies of the pipe including the conveyed fluid

Expressions for the kinetic and potential energies of a pipe conveying fluid have been derived before in [39]; they are

$$\mathcal{T}_p = \frac{1}{2} m \int_0^L V_p^2 \mathrm{d}X + \frac{1}{2} M_i \int_0^L V_f^2 \mathrm{d}X, \quad \mathcal{V}_p = \frac{1}{2} EI \int_0^L \bar{\kappa}^2 \mathrm{d}X - (m + M_i) g \int_0^L x \mathrm{d}X, \tag{3.2}$$

where V_p is the velocity of a pipe element and can be expressed as $\vec{V}_p = \dot{x}\vec{i} + \dot{y}\vec{j}$, in which $\vec{i}$ and $\vec{j}$ are unit vectors representing the axial and lateral directions of the undeformed state of the pipe, respectively; M_i is the mass of the conveyed fluid per unit length of the pipe; and $\vec{V}_f = \vec{V}_p + U_i \vec{t}$ is the velocity of the fluid element, where $\vec{t}$ is the tangential unit vector along s, as indicated in Fig. 3–1b. By using the inextensibilty condition, one can write $\vec{V}_f = (\partial/\partial t + U_i\, \partial/\partial s)(x\vec{i} + y\vec{j})$. In addition, $\bar{\kappa}$ is the curvature along the deformed pipe which can be written, according to [39], as

$$\bar{\kappa} = \frac{\partial^2 y/\partial s^2}{\sqrt{1 - (\partial y/\partial s)^2}}. \tag{3.3}$$

Based on Eq. (3.2), one can write $\mathcal{T}_p = (m/2)\int_0^L(\dot{x}^2+\dot{y}^2)\mathrm{d}s + (M_i/2)\int_0^L[(\dot{x}+U_i x')^2 + (\dot{y}+U_i y')^2]\mathrm{d}s$ with $(\ )' = \partial(\ )/\partial s$ and $(\dot{\ }) = \partial(\ )/\partial t$, and the following expression for the kinetic energy can be derived while keeping in mind the orders of magnitude; see [39, 86] for details:

$$\begin{aligned}\delta\int_{t_1}^{t_2}\mathcal{T}_p\,\mathrm{d}t = &-\int_{t_1}^{t_2}\int_0^L[(m+M_i)\ddot{x}+2M_iU_i\dot{x}']\delta x\,\mathrm{d}s\,\mathrm{d}t\\ &-\int_{t_1}^{t_2}\int_0^L[(m+M_i)\ddot{y}+2M_iU_i\dot{y}']\delta y\,\mathrm{d}s\,\mathrm{d}t + M_iU_i\int_{t_1}^{t_2}[\dot{x}_{_L}\delta x_{_L}+\dot{y}_{_L}\delta y_{_L}]\,\mathrm{d}t,\end{aligned} \tag{3.4}$$

where $x_{_L} = x(L)$ and $y_{_L} = y(L)$ are the displacements of the pipe at the free end.

For the potential energy, one can write [39]

$$\begin{aligned}\delta\int_{t_1}^{t_2}\mathcal{V}_p\,\mathrm{d}t = EI&\int_{t_1}^{t_2}\int_0^L[y'''' + 4y'y''y''' + y''^3 + y''''y'^2]\,\delta y\,\mathrm{d}s\,\mathrm{d}t\\ &-(m+M_i)g\int_{t_1}^{t_2}\int_0^L[-(y'+\frac{1}{2}y'^3)+(L-s)(y''+\frac{3}{2}y''y'^2)]\,\delta y\,\mathrm{d}s\,\mathrm{d}t + \mathcal{O}(\epsilon^5).\end{aligned} \tag{3.5}$$

It should be noted that δx and δy are interrelated through the inextensibility condition, as follows:

$$\delta x = -(y'+\frac{1}{2}y'^3)\delta y + \int_0^s(y''+\frac{3}{2}y'^2y'')\delta y\,\mathrm{d}s + \mathcal{O}(\epsilon^4). \tag{3.6}$$

3.1.2 Virtual work due to the non-conservative forces associated with the internal flow

In this subsection, the virtual work, δW_i, due to the non-conservative forces associated with the internal flow which are not included in the Lagrangian, is derived. It was shown in [39] that, even if there are no explicit external forces acting on the pipe, δW_i does not vanish if one or both ends of the pipe are not fixed. The virtual work done by the discharging fluid can be written as

$$\delta W_i = -M_iU_i\left(\frac{\partial\vec{r}_{_L}}{\partial t}+U_i\vec{t}_{_L}\right).\,\delta\vec{r}_{_L}, \tag{3.7}$$

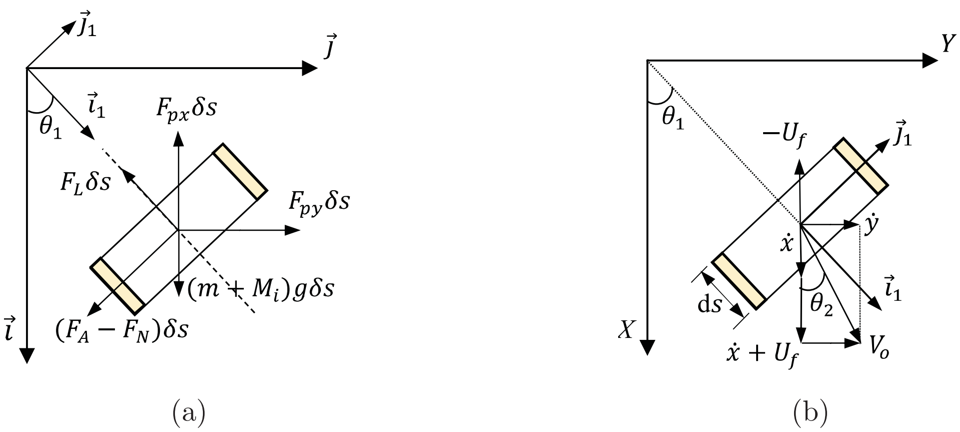

Figure 3–2: (a) Fluid-related forces acting on an element of the cantilevered pipe δs; (b) determination of the relative fluid-body velocity V_o associated with the external flow on an element of the pipe.

where $\vec{r}_{_L}$ and $\vec{t}_{_L}$ represent, respectively, the position vector, $\vec{r}=(x,y)$, and the tangential unit vector at the free end of the pipe. Equation (3.7) leads to

$$\begin{aligned} -\int_{t_1}^{t_2}\delta W_i\,\mathrm{d}t &= M_iU_i\int_{t_1}^{t_2}[(\dot{x}_{_L}+U_ix'_{_L})\delta x_{_L}+(\dot{y}_{_L}+U_iy'_{_L})\delta y_{_L}]\,\mathrm{d}t \\ &= M_iU_i\int_{t_1}^{t_2}(\dot{x}_{_L}\delta x_{_L}+\dot{y}_{_L}\delta y_{_L})\,\mathrm{d}t+M_iU_i^2\int_{t_1}^{t_2}(x'_{_L}\delta x_{_L}+y'_{_L}\delta y_{_L})\,\mathrm{d}t \\ &= A+B. \end{aligned} \tag{3.8}$$

The term A cancels the last term in Eq. (3.4), which is also associated with the discharging fluid flow at the free end of the pipe, and the term B can be re-written as shown below by using the inextensibilty condition and Eq. (3.6):

$$B=M_iU_i^2\int_{t_1}^{t_2}\int_0^s\left[y''+y'^2y''-y''\int_s^L(y'y'')\,\mathrm{d}s\right]\delta y\,\mathrm{d}s\,\mathrm{d}t. \tag{3.9}$$

3.1.3 Fluid-related forces associated with the external flow

The forces associated with the externally flowing fluid are determined separately as explained in Chapter 2. As shown in Fig. 3–2a, an element of the deformed pipe is subjected to the following forces: the inviscid fluid dynamic force $F_A\delta s$, the normal and longitudinal viscous forces, $F_N\delta s$ and $F_L\delta s$, respectively, and the hydrostatic forces in the x- and y-direction, $F_{px}\delta s$ and $F_{py}\delta s$, respectively. The expressions derived for these forces in Chapter 2 are utilized for the problem at hand, since the direction of the external flow is also from the free end towards the clamped one. Hence, the inviscid hydrodynamic forces can be expressed as

$$\begin{aligned} F_A(X,t) = &\left\{\frac{\partial}{\partial t} + \left[-U_o(1-\frac{\partial u}{\partial X}) - (\frac{\partial u}{\partial t} - U_o)\frac{\partial u}{\partial X}\right]\frac{\partial}{\partial X}\right\} \\ &\times \left[V_o - (\frac{\partial u}{\partial t}\frac{\partial v}{\partial X} - 2U_o\frac{\partial u}{\partial X}\frac{\partial v}{\partial X}) - \frac{1}{2}V_o(\frac{\partial v}{\partial X})^2\right]M_o - \frac{1}{2}M_o V_o \frac{\partial v}{\partial X}\frac{\partial V_o}{\partial X} + \mathcal{O}(\epsilon^5), \end{aligned} \tag{3.10}$$

where V_o is the relative fluid-body velocity associated with the external flow, which can be expressed as follows:

$$V_o = \dot{y} - U_o y' - \frac{1}{2}\dot{y}y'^2 + 2U_o u' y' + \frac{1}{2}U_o y'^3 - \dot{x}y' + \mathcal{O}(\epsilon^5) \tag{3.11}$$

and its direction is shown in Fig. 3–2b, $M_o = \chi\rho A_o$ is the virtual added mass, where $\chi = (D_{ch}^2 + D_o^2)/(D_{ch}^2 - D_o^2)$ is the confinement parameter, and $A_o = \pi D_o^2/4$ is the pipe outer cross-sectional area.

The normal and longitudinal viscous forces can be written as

$$\begin{aligned} F_N = &\frac{1}{2}\rho D_o U_o^2\Bigg[C_N\left(y' - \frac{\dot{y}}{U_o} - \frac{\dot{y}u'}{U_o} - u'y' + \frac{\dot{x}\dot{y}}{U_o^2} - \frac{1}{2}\left(y'^3 - \frac{\dot{y}^3}{U_o^3} - \frac{y'^2\dot{y}}{U_o} + \frac{y'\dot{y}^2}{U_o^2}\right)\right) \\ &- C_{Dp}\left(y'|y'| + \frac{y'|\dot{y}| + |y'|\dot{y}}{U_o} + \frac{\dot{y}|\dot{y}|}{U_o^2}\right)\Bigg] - k\dot{y} + \mathcal{O}(\epsilon^5), \\ F_L = &\frac{1}{2}\rho D_o U_o^2 C_T\left[1 - \frac{1}{2}\left(y'^2 - 2\frac{y'\dot{y}}{U_o} + \frac{\dot{y}^2}{U_o^2}\right)\right] + \mathcal{O}(\epsilon^4), \end{aligned} \tag{3.12}$$

where C_N and C_T are friction coefficients and C_{Dp} is a form-drag coefficient. The quadratic terms associated with the form-drag coefficient were modified in the same way as in [86,111], taking into account the opposite direction of the external flow for the problem at hand. Also a viscous damping term, $k\dot{y}$, was added based on the analysis in [2,5]. The value of the viscous damping coefficient, k, is dependent on the frequency of oscillations, as discussed in [8,116].

In addition, the hydrostatic forces, which are the resultants of the steady-state pressure p_o acting on the cantilever are derived following the procedure described in Chapter 2. The outer pressure gradient can be expressed as follows:

$$A_o\left(\frac{\partial p_o}{\partial x}\right)=\frac{1}{2}\rho D_o U_o^2 C_T \frac{D_o}{D_h}+\rho g A_o, \tag{3.13}$$

where D_h is the hydraulic diameter. Equation (3.13) leads to the following relation, after rewriting the derivative with respect to X and integrating from $X = s$ to L:

$$A_o p_o(s) = A p_o(L) - \left(\frac{1}{2}\rho D_o U_o^2 C_T \frac{D_o}{D_h}+\rho g A_o\right)\left[(L-s)-\int_s^L \frac{1}{2}y'^2 \mathrm{d}s\right]+\mathcal{O}(\epsilon^4). \tag{3.14}$$

Following the derivation elaborated in [86], the following nonlinear expressions for the hydrostatic forces per unit length can be obtained:

$$\begin{aligned}
-F_{px} &= y'^2\left(-\frac{1}{2}\rho D_o U_o^2 C_T \frac{D_o}{D_h}-\rho g A_o\right)-y'y''A_o p_o+\mathcal{O}(\epsilon^4),\\
F_{py} &= (y'-u'y'-y'^3)\left(\frac{1}{2}\rho D_o U_o^2 C_T \frac{D_o}{D_h}+\rho g A_o\right)\\
&\quad +(y''-u''y'-u'y''-\frac{3}{2}y'^2 y'')A_o p_o+\mathcal{O}(\epsilon^5).
\end{aligned} \tag{3.15}$$

3.1.4 Virtual work due to the fluid-related forces associated with the external flow

Using the nonlinear expressions derived for the fluid-related forces; i.e. Eqs. (3.10), (3.12) and (3.15), the virtual work done on the cantilever by the fluid-related forces associated with the external flow, δW_o, can be obtained:

$$\begin{aligned}
\int_{t_1}^{t_2}\delta W_o \mathrm{d}t = \int_{t_1}^{t_2}\int_0^L &\{[-F_{px}-F_L\cos\theta_1+(F_A-F_N)\sin\theta_1]\delta x\\
&+[F_{py}-F_L\sin\theta_1-(F_A-F_N)\cos\theta_1]\delta y\}\,\mathrm{d}s\,\mathrm{d}t,
\end{aligned} \tag{3.16}$$

where

$$\theta_1 = y'-u'y'-\frac{1}{3}y'^3+\mathcal{O}(\epsilon^5). \tag{3.17}$$

3.1.5 Pressurization at the free end of the pipe

In order to include the effect of the pressure of the discharging fluid, p_i, as well as the effect of any externally applied tension, T_o, at the free end of the pipe, an element of the

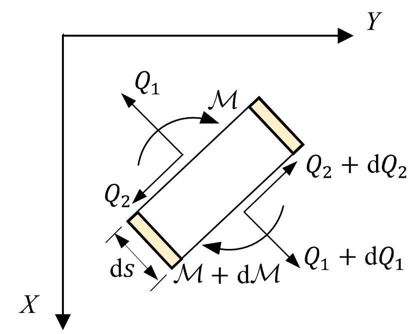

Figure 3–3: Free-body diagram of an element of the cantilevered pipe utilized for the analysis in Sub-section 3.1.5.

pipe of length ds is considered which is subjected to the internal flow only. The axial force, Q_1, shear force, Q_2, and bending moment, $\mathcal{M}$, on the upper and lower cross-sections are shown in Fig. 3–3, as well as $Q + \mathrm{d}Q$ and $\mathcal{M} + \mathrm{d}\mathcal{M}$ on the lower cross-section. Applying a balance of forces leads to

$$\frac{\partial \vec{Q}}{\partial s} + (m + M_i)g\vec{i} = m\frac{\partial^2 \vec{r}}{\partial t^2} + M_i \frac{\mathrm{D}^2 \vec{r}}{\mathrm{D}t^2}, \tag{3.18}$$

where Q is the resultant force and D( )/Dt is the material derivative of the element. Also, a balance of moments leads to

$$\frac{\partial \vec{\mathcal{M}}}{\partial s} + \vec{t} \times \vec{Q} = 0, \tag{3.19}$$

which yields

$$\vec{Q_2} = \vec{t} \times \frac{\partial \vec{\mathcal{M}}}{\partial s}. \tag{3.20}$$

The Euler-Bernoulli beam theory is employed, so the effect of rotary inertia is neglected, and hence the following moment-curvature relation holds [39]:

$$\vec{\mathcal{M}} = EI\vec{t} \times \frac{\partial \vec{t}}{\partial s} = EI\vec{t} \times \bar{\kappa}\vec{n}. \tag{3.21}$$

Decomposing $\vec{Q}$ along $\vec{t}$ and $\vec{n}$ gives $\vec{Q} = \vec{Q_1} + \vec{Q_2}$, with $\vec{Q_1} = (T_o - A_i p_i)\vec{t}$ according to [39]. By using Eq.(3.20), one can write

$$\vec{Q} = (T_o - A_i p_i)\vec{t} + \vec{t} \times \frac{\partial \vec{\mathcal{M}}}{\partial s}, \tag{3.22}$$

where A_i is the inner cross-sectional area of the pipe. By substituting Eqs. (3.21) and (3.22) into Eqs. (3.18) and (3.19), projecting along x and y, and after further manipulations, one can obtain

$$(m+M_i)g - EI\frac{\partial^4 x}{\partial s^4} + \frac{\partial}{\partial s}\left[(T_o - A_i p_i - EI\bar{\kappa}^2)\frac{\partial x}{\partial s}\right] = m\frac{\partial^2 x}{\partial t^2} + M_i\frac{\mathrm{D}^2 x}{\mathrm{D}t^2}, \tag{3.23}$$

$$-EI\frac{\partial^4 y}{\partial s^4} + \frac{\partial}{\partial s}\left[(T_o - A_i p_i - EI\bar{\kappa}^2)\frac{\partial y}{\partial s}\right] = m\frac{\partial^2 y}{\partial t^2} + M_i\frac{\mathrm{D}^2 y}{\mathrm{D}t^2}. \tag{3.24}$$

Integrating Eq. (3.23) from s to L and eliminating the common factor $\partial x/\partial s$ leads to

$$\begin{aligned}(T_o - A_i p_i - EI\bar{\kappa}^2) =& \frac{(m+M_i)g(L-s)}{\partial x/\partial s} + \frac{EI(\partial^3 x/\partial s^3)}{\partial x/\partial s} + \frac{\big[(T_o - A_i p_i)(\partial x/\partial s)\big]_{s=L}}{\partial x/\partial s} \\ & - \frac{\int_s^L \big[m(\partial^2 x/\partial t^2) + M_i(\mathrm{D}^2 x/\mathrm{D}t^2)\big]\,\mathrm{d}s}{\partial x/\partial s}.\end{aligned} \tag{3.25}$$

According to [39], by substituting Eq. (3.25) into Eq. (3.24) and eliminating x through the inextensibility condition, one can obtain an equation of motion for a cantilevered pipe discharging fluid, after many straightforward manipulations. The equation of motion derived in [39] should have the same nonlinear terms as the nonlinear terms associated with the internal flow in the present study, except that in [39] the pipe is assumed to be discharging the fluid to atmosphere, so the third term on the right-hand side of Eq. (3.25) is absent. By keeping that term and proceeding with the derivation, the same equation as in [39] is obtained, but with the following extra term: $-\big[(T_o - A_i p_i)(1-\frac{1}{2}y'^2)\big]_{s=L}(y'' + \frac{3}{2}y''y'^2)$, which appears in the final equation of motion presented in the following subsection.

The relation between $p_o(L)$ and $p_i(L)$ may be determined assuming a smooth transition between the internal and the external annular flows at the free end of the pipe. Thus, one may use the simplified relationship

$$p_i(L) + \frac{1}{2}\rho U_i^2 = p_o(L) + \frac{1}{2}\rho U_o^2 + \rho g h_o, \tag{3.26}$$

where h_o is the head loss due to the sudden enlargement in the flow areas from A_i to $A_{ch} = (\pi/4)(D_{ch}^2 - D_o^2)$, which can be expressed as

$$h_o = \frac{1}{2g} C (U_i - U_o)^2, \tag{3.27}$$

while the value of the coefficient C can be taken as $C = 1$; refer to [8] for details. Based on Eqs. (3.26) and (3.27), one obtains

$$p_i(L) = p_o(L) + \rho U_o (U_o - U_i). \tag{3.28}$$

It should be stressed that U_i and U_o are related to each other through continuity, i.e. $U_i A_i = U_o A_{ch}$.

3.1.6 The equation of motion

By substituting Eqs. (3.4), (3.5), (3.9), and (3.16) into Eq. (3.1), and using Eqs. (3.3) and (3.6), the following nonlinear equation of motion can be obtained after many straightforward manipulations and transformations:

$$
\begin{aligned}
&(m+M_i+M_o)\ddot{y}+2M_iU_i\dot{y}'(1+y'^2)-2M_oU_o\dot{y}'(1-\frac{1}{4}y'^2)+M_iU_i^2y''(1+y'^2)\\
&+M_oU_o^2y''(1+2y'^2)-\frac{3}{2}M_o\dot{y}y'(\dot{y}'-U_oy'')-\frac{1}{2}\rho D_oU_o^2C_N(y'+\frac{1}{2}y'^3)+\frac{1}{2}\rho D_oU_o^2C_T(L-s)\\
&\times(y''+\frac{3}{2}y'^2y'')-Ap_o(L)(y''+y'^2y'')-\left[(T_o-A_ip_i)(1-\frac{1}{2}y'^2)\right]_{s=L}(y''+\frac{3}{2}y'^2y'')\\
&-(\frac{1}{2}\rho D_oU_o^2C_T\frac{D_o}{D_h}-(m+M_i)g+\rho gA_o)[y'+\frac{1}{2}y'^3-(L-s)(y''+\frac{3}{2}y'^2y'')]\\
&+EI(y''''+4y'y''y'''+y''^3+y''''y'^2)+\frac{1}{2}\rho D_oC_N\dot{y}\int_0^s y'\dot{y}'\mathrm{d}s\\
&+\frac{1}{2}\rho D_oU_o^2C_N\left(\frac{\dot{y}}{U_o}+\frac{1}{2}\frac{y'\dot{y}^2}{U_o^2}-\frac{1}{2}\frac{y'^2\dot{y}}{U_o}-\frac{\dot{y}^3}{2U_o^3}\right)+\frac{1}{2}\rho D_oU_o^2C_{Dp}\left(y'|y'|+\frac{y'|\dot{y}|+|y'|\dot{y}}{U_o}+\frac{\dot{y}|\dot{y}|}{U_o^2}\right)\\
&+k\dot{y}-(m+M_i)y''\int_s^L\int_0^s(\dot{y}'^2+y'\ddot{y}')\mathrm{d}s\,\mathrm{d}s+2M_o(\dot{y}'-U_oy'')\int_0^s y'\dot{y}'\mathrm{d}s\\
&-M_oy''\int_0^s(\ddot{y}y'-2U_oy'\dot{y}'+U_o^2y'y'')\,\mathrm{d}s+(m+M_i+M_o)y'\int_0^s(y'\ddot{y}'+\dot{y}'^2)\,\mathrm{d}s\\
&-3M_oU_oy'\int_0^s(y'\dot{y}''+y''\dot{y}')\,\mathrm{d}s+y''\int_s^L\{A_op_o(L)y'y''-\frac{1}{4}\rho D_oC_T\dot{y}^2\}\,\mathrm{d}s\\
&-\frac{1}{2}\rho D_oU_o^2y''(C_T-C_N)\int_s^L\left(y'^2-\frac{y'\dot{y}}{U_o}\right)\mathrm{d}s-y''\int_s^L(2M_iU_iy'\dot{y}'+M_iU_i^2y'y'')\,\mathrm{d}s=0.
\end{aligned}
\tag{3.29}
$$

The internal dissipation in the pipe material is neglected in Eq. (3.29), because its effect has been shown to be much smaller than dissipation associated with the surrounding dense fluid, as discussed in [8,11]. Defining next the dimensionless quantities

$$
\begin{aligned}
&\xi=\frac{s}{L},\quad \eta=\frac{y}{L},\quad \tau=\left(\frac{EI}{m+M_i+\rho A_o}\right)^{1/2}\frac{t}{L^2},\quad u_i=\left(\frac{M_i}{EI}\right)^{1/2}U_iL,\\
&u_o=\left(\frac{\rho A_o}{EI}\right)^{1/2}U_oL,\quad \beta_i=\frac{M_i}{m+M_i+\rho A_o},\quad \beta_o=\frac{\rho A_o}{m+M_i+\rho A_o},\\
&\gamma=\frac{(m+M_i-\rho A_o)gL^3}{EI},\quad \Gamma=\frac{T_o(L)L^2}{EI},\quad c_N=\frac{4}{\pi}C_N,\quad c_T=\frac{4}{\pi}C_T,\\
&c_d=\frac{4}{\pi}C_{Dp},\quad \varepsilon=\frac{L}{D_o},\quad h=\frac{D_o}{D_h},\quad \alpha=\frac{D_i}{D_o},\quad \alpha_{ch}=\frac{D_{ch}}{D_o},\\
&\Pi_{iL}=\frac{A_ip_i(L)L^2}{EI},\quad \Pi_{oL}=\frac{A_op_o(L)L^2}{EI},\quad \kappa=\frac{kL^2}{[EI(m+M_i+\rho A_o)]^{1/2}},
\end{aligned}
\tag{3.30}
$$

the equation of motion is written in the following dimensionless form:

$$
\begin{aligned}
&[1+(\chi-1)\beta_o]\ddot{\eta}+2u_i\sqrt{\beta_i}\dot{\eta}'(1+\eta'^2)-2u_o\sqrt{\beta_o}\chi\dot{\eta}'(1-\frac{1}{4}\eta'^2)+u_o^2\chi\eta''(1+2\eta'^2)\\
&+u_i^2\eta''(1+\eta'^2)-\frac{3}{2}\chi\dot{\eta}\eta'(\beta_o\dot{\eta}'-u_o\sqrt{\beta_o}\eta'')-\frac{1}{2}u_o^2\varepsilon c_N[\eta'+\frac{1}{2}\eta'^3]\\
&+\frac{1}{2}u_o^2\varepsilon c_T(1-\xi)(\eta''+\frac{3}{2}\eta'^2\eta'')-\Pi_{oL}(\eta''+\eta'^2\eta'')-(\Gamma-\Pi_{iL})(\eta''+\frac{3}{2}\eta'^2\eta'')\\
&+\frac{1}{2}(\Gamma-\Pi_{iL})\eta''\left[\eta'^2\right]_{\xi=1}-(\frac{1}{2}u_o^2\varepsilon c_T h-\gamma)[\eta'+\frac{1}{2}\eta'^3-(1-\xi)(\eta''+\frac{3}{2}\eta'^2\eta'')]\\
&+\eta''''+4\eta'\eta''\eta'''+\eta''^3+\eta''''\eta'^2+\frac{1}{2}\varepsilon c_N\beta_o\dot{\eta}\int_0^\xi\eta'\dot{\eta}'\mathrm{d}s\\
&+\frac{1}{2}u_o^2\varepsilon c_N\left(\frac{\sqrt{\beta_o}}{u_o}\dot{\eta}+\frac{1}{2}\frac{\beta_o}{u_o^2}\dot{\eta}^2\eta'-\frac{1}{2}\frac{\sqrt{\beta_o}}{u_o}\dot{\eta}\eta'^2-\frac{1}{2}\frac{\beta_o^{3/2}}{u_o^3}\dot{\eta}^3\right)\\
&+\frac{1}{2}u_o^2\varepsilon c_d\left(\eta'|\eta'|+\frac{\sqrt{\beta_o}}{u_o}(\eta'|\dot{\eta}|+|\eta'|\dot{\eta})+\frac{\beta_o}{u_o}\dot{\eta}|\dot{\eta}|\right)+\kappa\dot{\eta}\\
&-\eta''(1-\beta_o)\int_\xi^1\int_0^\xi(\dot{\eta}'^2+\eta'\ddot{\eta}')\,\mathrm{d}\xi\,\mathrm{d}\xi+2\chi(\beta_o\dot{\eta}'-u_o\sqrt{\beta_o}\eta'')\int_0^\xi\eta'\dot{\eta}'\,\mathrm{d}\xi\\
&-\chi\eta''\int_\xi^1(\beta_o\ddot{\eta}\eta'-2u_o\sqrt{\beta_o}\dot{\eta}'\eta'+u_o^2\eta''\eta')\,\mathrm{d}\xi+\eta'(1+(\chi-1)\beta_o)\int_0^\xi(\dot{\eta}'^2+\eta'\ddot{\eta}')\,\mathrm{d}\xi\\
&+\eta''\int_\xi^1\{\Pi_{oL}\eta'\eta''-\frac{1}{4}\varepsilon c_T\beta_o\dot{\eta}^2\}\,\mathrm{d}\xi-3\chi\sqrt{\beta_o}u_o\eta'\int_0^\xi(\eta'\dot{\eta}''+\eta''\dot{\eta}')\,\mathrm{d}\xi\\
&-\frac{1}{2}u_o^2\eta''(\varepsilon c_T-\varepsilon c_N)\int_\xi^1(\eta'^2-\frac{\sqrt{\beta_o}}{u_o}\eta'\dot{\eta}_o)\,\mathrm{d}\xi-\eta''\int_\xi^1(2u_i\sqrt{\beta_i}\eta'\dot{\eta}'+u_i^2\eta'\eta'')\,\mathrm{d}\xi=0,
\end{aligned}
\tag{3.31}
$$

where $(\ )'=\partial(\ )/\partial\xi$ and $\dot{(\ )}=\partial(\ )/\partial\tau$.

3.1.7 Methods of analysis

The final equation of motion, i.e. Eq. (3.31), is discretized by Galerkin's technique, utilizing the cantilever beam eigenfunctions, $\phi_j(\xi)$, as comparison functions and with $q_j(\tau)$ as the corresponding generalized coordinates; thus,

$$\eta(\xi,\tau)=\sum_{j=1}^{N}\phi_j(\xi)q_j(\tau), \tag{3.32}$$

where N represents the number of modes in the Galerkin scheme. Substituting Eq. (3.32) into Eq. (3.31), multiplying by $\phi_i(\xi)$, and integrating over the domain $[0:1]$ results in the following set of ODEs:

$$\begin{aligned} &M_{ij}\ddot{q}_j + C_{ij}\dot{q}_j + K_{ij}q_j + r_{ijk}q_j|q_k| + \bar{s}_{ijk}|q_j|\dot{q}_k + \tilde{s}_{ijk}q_j|\dot{q}_k| + t_{ijk}\dot{q}_j|\dot{q}_k| \\ &+\alpha_{ijkl}q_jq_kq_l + \beta_{ijkl}q_jq_k\dot{q}_l + \gamma_{ijkl}q_j\dot{q}_k\dot{q}_l + \eta_{ijkl}\dot{q}_j\dot{q}_k\dot{q}_l + \mu_{ijkl}q_jq_k\ddot{q}_l = 0, \end{aligned} \tag{3.33}$$

in which repetition of an index implies summation; M_{ij}, C_{ij} and K_{ij} are elements of the mass, damping and stiffness matrices, respectively, and they are given by

$$\begin{aligned} &M_{ij} = [1 + (\chi - 1)\beta_o]\delta_{ij}, \\ &C_{ij} = -2\chi u_o\sqrt{\beta_o}b_{ij} + \frac{1}{2}u_o\varepsilon c_N\sqrt{\beta_o}\delta_{ij} + \kappa\delta_{ij} + 2u_i\sqrt{\beta_i}b_{ij}, \\ &K_{ij} = \chi u_o^2 c_{ij} + (\frac{1}{2}u_o^2\varepsilon(-c_N - c_T h) + \gamma)b_{ij} + (\frac{1}{2}u_o^2\varepsilon c_T(1 + h) - \gamma)(-d_{ij} + c_{ij}) \\ &\qquad + \lambda_j^4\delta_{ij} - \Pi_{oL}c_{ij} + u_i^2 c_{ij} - (\Gamma - \Pi_{iL})c_{ij}, \end{aligned} \tag{3.34}$$

where λ_j is the jth root of the characteristic equation of a cantilevered beam, and the coefficients b_{ij}, c_{ij} and d_{ij} are integrals defined by Païdoussis and Issid [28], namely

$$b_{ij} = \int_0^1 \phi_i\phi_j' \, \mathrm{d}\xi, \quad c_{ij} = \int_0^1 \phi_i\phi_j'' \, \mathrm{d}\xi, \quad d_{ij} = \int_0^1 \xi\phi_i\phi_j'' \, \mathrm{d}\xi, \tag{3.35}$$

and they are available in closed form. The nonlinear coefficients, r_{ijk}, $\bar{s}_{ijk}$, $\tilde{s}_{ijk}$, t_{ijk}, α_{ijkl}, β_{ijkl}, γ_{ijkl}, η_{ijkl} and μ_{ijkl}, are defined in Appendix B.

3.2 Linear dynamics

In this section, a linearized form of the discretized ODEs obtained in Sub-section 3.1.7 is solved following the procedure detailed in Section 2.2 for a bench-top-sized system. An elastomer pipe with $D_o = 15.7\,\mathrm{mm}$, $D_i = 6.4\,\mathrm{mm}$, $L = 443\,\mathrm{mm}$, and $E = 2.56 \times 10^6\,\mathrm{N/m^2}$ is considered. The corresponding dimensionless parameters are $\alpha = 0.408$, $\varepsilon = 28.2$, $\beta_o = 0.467$, $\beta_i = 0.0776$, $\gamma = 3.14$, and $\alpha_{ch} = 1.2$. The form-drag coefficient due to the external flow is taken as $C_{Dp} = 1$, as for cross-flow over a circular cylinder [109]. Also, the normal and tangential friction coefficients are assumed to have the same value, $C_N = C_T = 0.0125$, as in [8]. The viscous damping coefficient, k, is defined as in [8],

$$k = \frac{2\sqrt{2}}{\sqrt{\tilde{S}}}\frac{1 + \bar{\gamma}^3}{(1 - \bar{\gamma}^2)^2}\rho A_o\Omega, \tag{3.36}$$

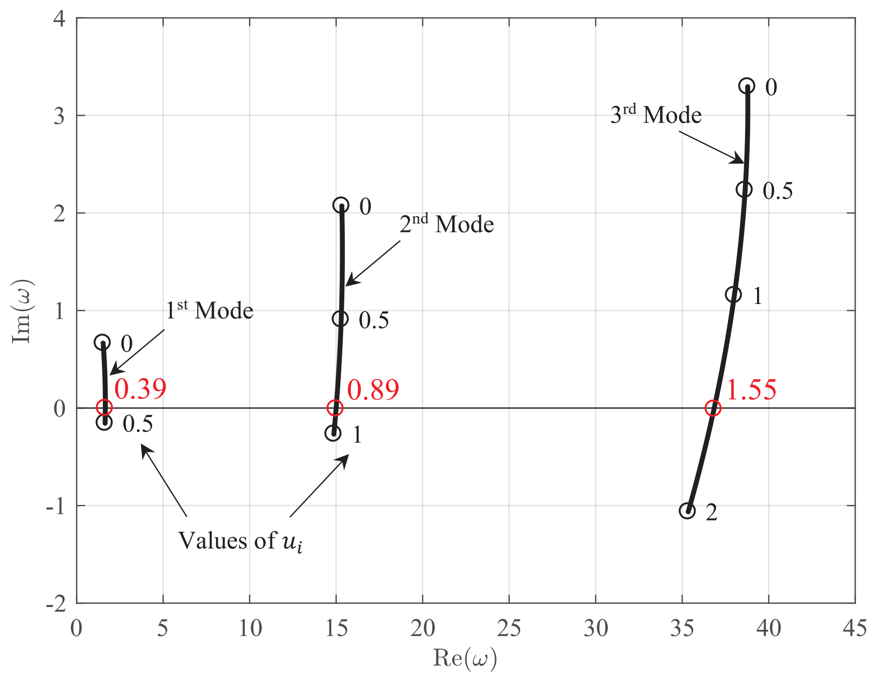

Figure 3–4: Argand diagram showing the imaginary and real parts of the dimensionless complex eigenfrequencies ω_j at different flow velocities u_i.

where $\tilde{S} = \Omega D_o^2/(4\nu)$ is the Stokes number, Ω being the circular frequency of oscillation, and $\bar{\gamma} = D_o/D_{ch}$.

Figure 3–4 shows an Argand diagram obtained using a ten-mode Galrekin approximation for the bench-top-sized system under study.[1] The figure shows that the first three modes become unstable when the dimensionless internal flow velocity u_i is increased beyond a critical value, which is indicated on each mode locus. All the modes become unstable via Hopf bifurcations, as shown in Fig. 3–4, at the following dimensionless critical flow velocities: $u_{cr,1} = 0.39$, $u_{cr,2} = 0.89$ and $u_{cr,3} = 1.55$.

3.3 Nonlinear dynamics

In this section, the nonlinear ODEs obtained in Sub-section 3.1.7 are solved using the system parameters defined in Section 3.2. The viscous damping coefficient, κ, whose value should be dependent on the frequency of oscillations, is given a constant value for each

[1] It was actually found that a six-mode approximation is sufficient to achieve convergence.

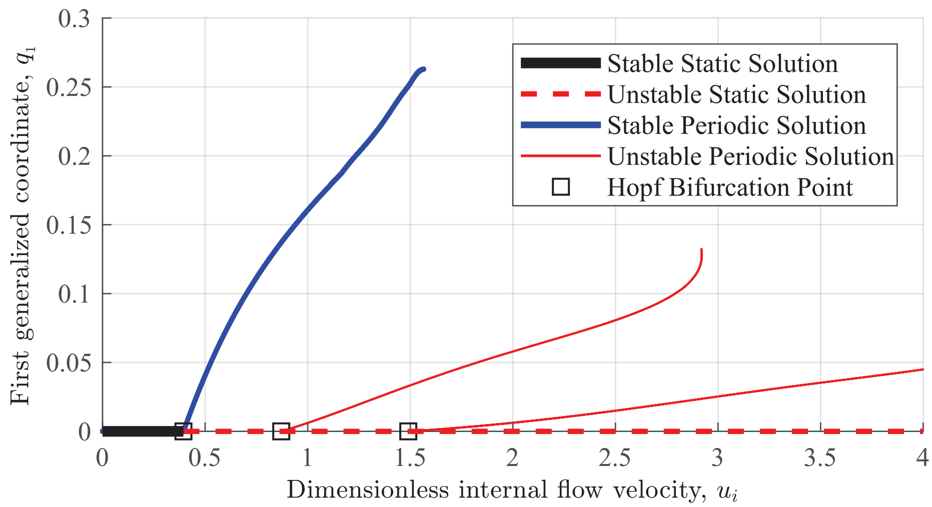

Figure 3–5: Bifurcation diagram showing the first generalized coordinate, q_1, as a function of the dimensionless internal flow velocity, u_i.

mode as discussed in [8]; this constant value is determined based on the average frequency of oscillations for each mode[2] over a specific range of the internal flow velocity, u_i. Thus, the values of κ for six modes computed with $N = 6$, are $\kappa_j = \{4.2, 12.8, 20.3, 27.9, 35.7, 43.4\}$. The ODEs are solved using AUTO [113], which is based on a collocation method and is adapted to conduct bifurcation analysis for differential equations, and also using a MATLAB ODE solver, namely ode15i (Mathworks, Inc.) for direct-time-integration purposes.

A bifurcation diagram obtained via AUTO using a six-mode Galerkin approximation is presented in Fig. 3–5 for the first generalized coordinate, q_1, which is representative of the behaviour of the system, and it is plotted as a function of the dimensionless internal flow velocity, u_i. The figure shows that for u_i <0.394, the cantilever remains stable around the original equilibrium state. At $u_i \approx 0.394$, a Hopf bifurcation is predicted, leading to stable periodic oscillations around the origin corresponding to flutter in the first mode of the cantilever. The maximum value of q_1 as a function of u_i, plotted in Fig. 3–5, shows a

[2] The frequency of oscillations for each mode is obtained by applying linear analysis first, as done in Section 3.2, and determining the real part of the diminsionless eigenfrequency for each mode, $\mathrm{Re}(\omega_i)$, where $i = 1 : N$, which corresponds to the dimensionless frequency of oscillation.

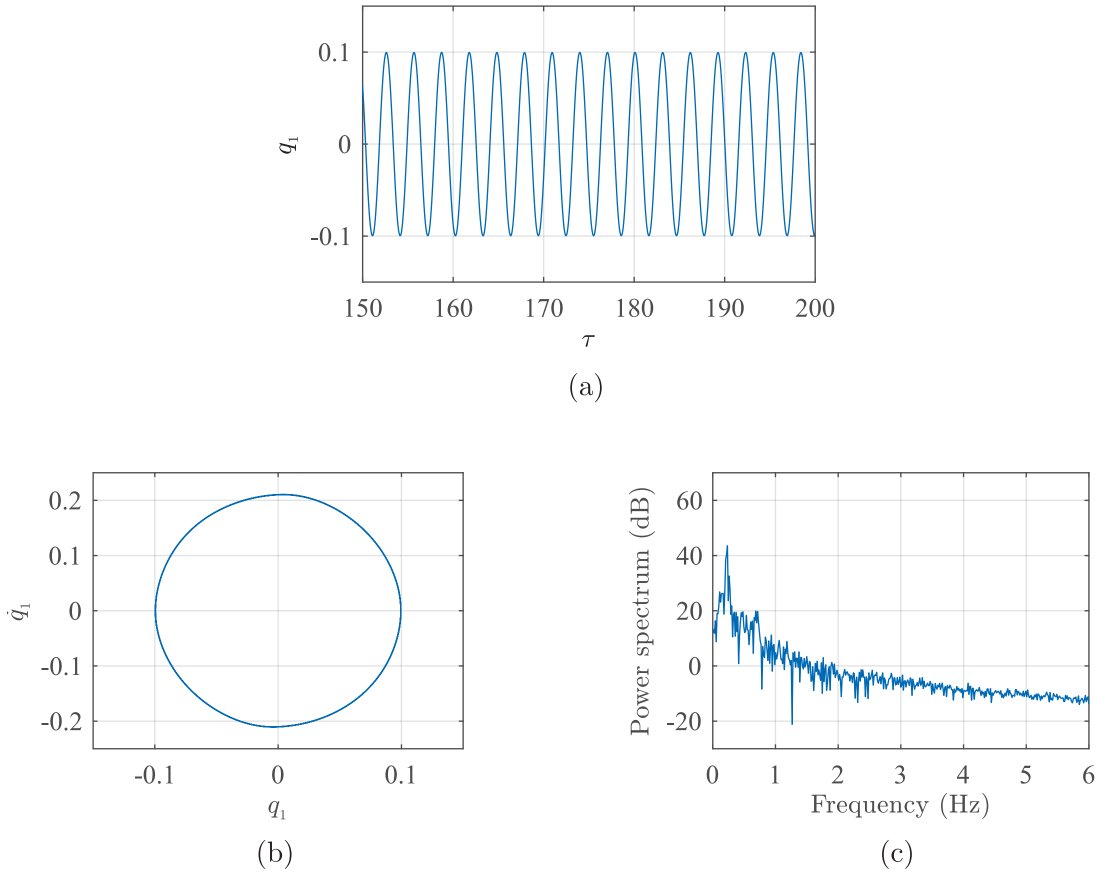

Figure 3–6: At $u_i = 0.7$: (a) time history plot, (b) phase-plane plot, and (c) power spectral density plot.

steady increase in the amplitude of oscillations with increasing flow velocity. At u_i >1.57, the model fails to converge to any stable solution, perhaps because of the large deflection of the cantilever, exceeding the third-order accuracy assumption of the model. Other Hopf bifurcation points are predicted at higher flow velocities, e.g. at $u_i = 0.871$ and 1.49; however the periodic solutions emanating from these points are unstable, i.e. they do not physically exist.

The nonlinear dynamics of the system is examined at two different values of the dimensionless internal flow velocity: $u_i = 0.7$, which is relatively close to the onset of flutter, and $u_i = 1.5$, which is close to the end of the stable periodic solution predicted by this model. The time histories obtained using the MATLAB ODE solver, phase-plane plots, and power-spectral-density plots calculated by direct fast Fourier transform (FFT) are shown in

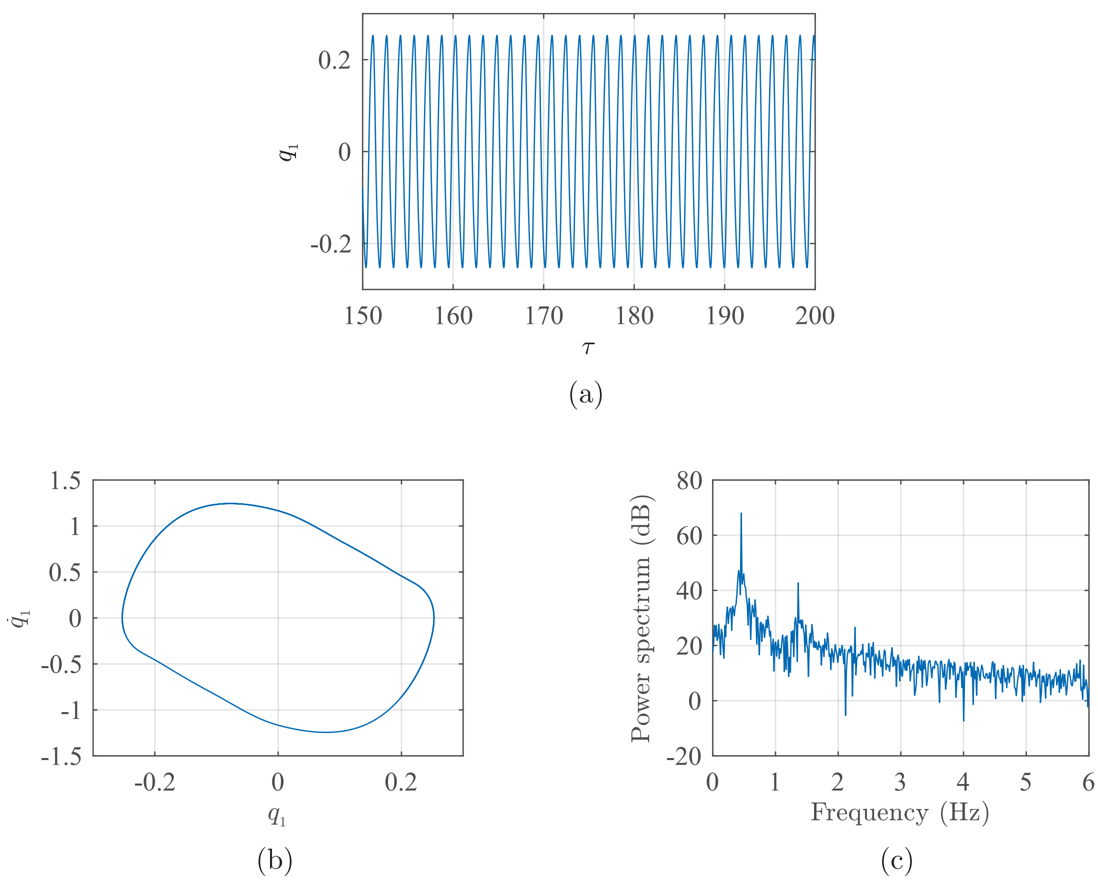

Figure 3–7: At $u_i = 1.5$: (a) time history plot, (b) phase-plane plot, and (c) power spectral density plot.

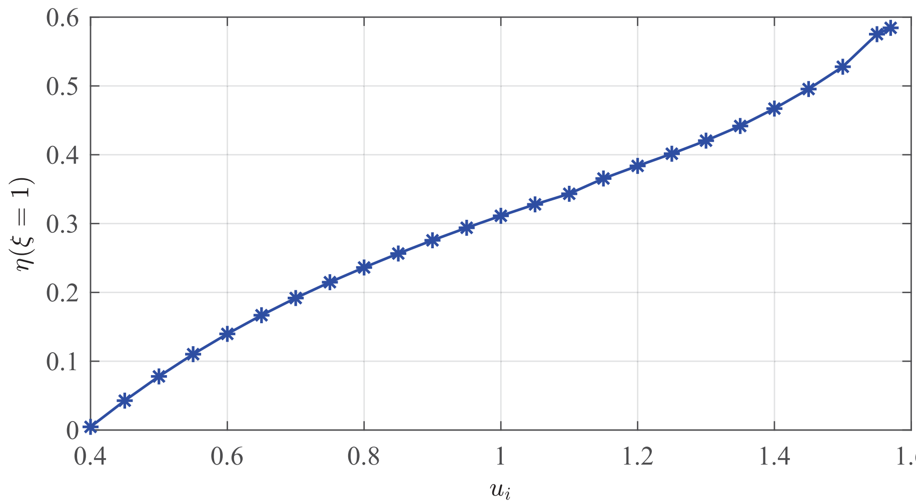

Figure 3–8: Dimensionless amplitude of oscillations at the free end of the cantilever, $\eta(\xi = 1)$, as a function of the dimensionless internal flow velocity, u_i.

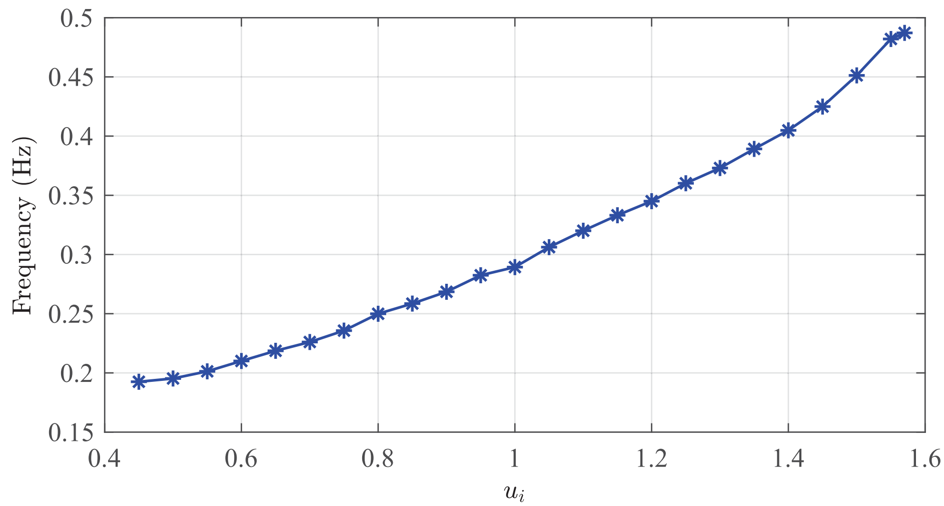

Figure 3–9: Frequency of oscillations a function of the dimensionless internal flow velocity, u_i.

Figs. 3–6 and 3–7 for these two flow velocities. All of them indicate periodic motions with one dominant frequency of oscillations, and a more pronounced nonlinear behaviour at the higher flow velocity.

The dimensionless amplitude of oscillations at the free end of the cantilever, $\eta(\xi = 1)$ and the frequency of oscillations as functions of u_i obtained using the present model are shown in Figs. 3–8 and 3–9, respectively. An increase in the frequency of oscillations with increasing flow velocity is seen in Fig. 3–9. For these results, the number of modes in the Galerkin scheme, N, was increased until the solution obtained would not change any more, both qualitatively and quantitatively. It was found that six comparison functions are sufficient to ensure convergence of the solution, as shown in Appendix C.

3.4 Comparison between the present theory and a linear one from the literature

The values of the parameters used to solve the ODEs in Section 3.3 were purposely chosen to allow comparison between the dynamical behaviour predicted by the present nonlinear model and the linear model in [8] for a bench-top-sized system. The two models, which are identical in the linear limit, except for the approximation made in the damping model in the nonlinear one, predict loss of stability by flutter in the first mode for sufficiently high flow velocity. However, the nonlinear model proves the existence of limit cycle oscillations

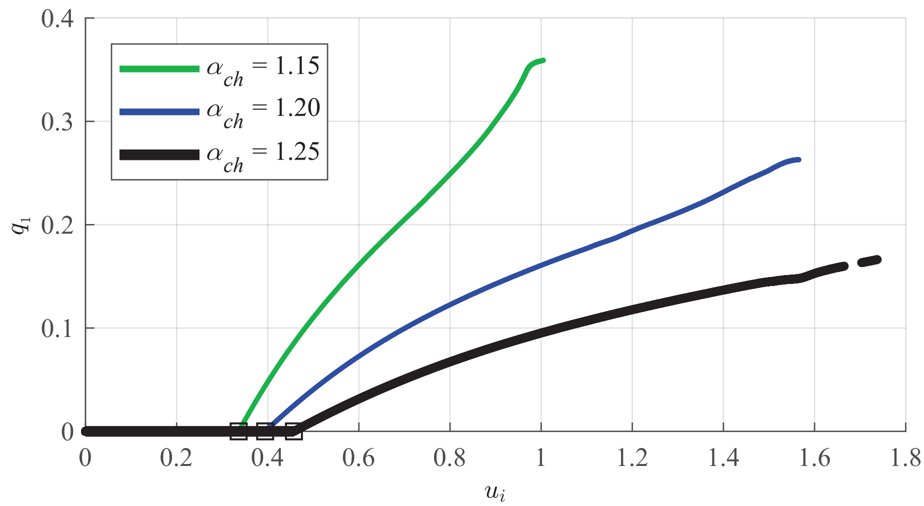

Figure 3–10: Influence of the dimensionless confinement parameter, α_{ch}.

after the first Hopf bifurcation, and shows that the periodic solution emanating from the other Hopf bifurcation points, e.g. for the second and third modes in Fig. 3–5, are unstable. A comparison between the critical flow velocities for instability of the first three modes, as predicted by the two models, is presented in Table 3–1 with maximum difference of 3.9%.

Table 3–1: Comparison between the critical flow velocities for instability of the first three modes as predicted by the proposed theory and the linear theory in [8]. The asterisk denotes that the ensuing solution is unstable.

Theory	First mode	Second mode	Third mode
Present theory	0.39	0.87*	1.49*
Theory in [8]	0.39	0.89	1.55

3.5 Influence of different parameters on the stability of the system and the amplitude of oscillations

In the following subsections, the influence of various system parameters on the onset of instability and the amplitude of the predicted flutter for the bench-top-sized system, considered in Section 3.3, is investigated by means of several bifurcation diagrams. Each parameter is varied separately while keeping the rest constant[3] for appropriate analysis of its effects.

3.5.1 Influence of the degree of confinement of the external flow

Figure 3–10 shows that increasing the value of α_{ch}, which means decreasing the degree of confinement by increasing the diameter of the rigid channel with respect to the outer diameter of the pipe, tends to stabilize the system, moving the first Hopf bifurcation to a higher flow velocity, u_{if}, as shown in Table 3–2. Also, for a given flow velocity, the amplitude of the oscillations is reduced for a higher value of α_{ch}, as shown in Fig. 3–10. This stabilization effect is due to the decrease in the external flow velocity and consequently in the associated destabilizing forces. On the other hand, increasing the degree of confinement by decreasing the value of α_{ch} destabilizes the system and increases the amplitude of flutter.

Table 3–2: Comparison between the critical flow velocities for flutter, u_{if}, for different values of α_{ch}.

	$\alpha_{ch} = 1.15$	$\alpha_{ch} = 1.20$	$\alpha_{ch} = 1.25$
u_{if}	0.336	0.394	0.457

3.5.2 Influence of the gravity parameter

The effects of varying the value of the dimensionless gravity parameter, γ, on the onset of instability are shown in Fig. 3–11 and Table 3–3. Increasing the value of γ stabilizes the system and decreases the amplitude of oscillations, at a specific fixed flow velocity; while decreasing γ to $\gamma = 0$, which means that the system becomes horizontal, destabilizes the system and increases the amplitude of flutter.

3.5.3 Influence of the ratio of the mass of the fluid to the total mass of the system

The influence of varying the ratio of the mass of the internal and external fluids to the total mass of the system, defined in Eq. (3.30), β_i and β_o, is investigated in this subsection.

[3] It should be mentioned that the values given to the dimensionless viscous damping parameter κ_j were updated corresponding to the new value of each parameter under study.

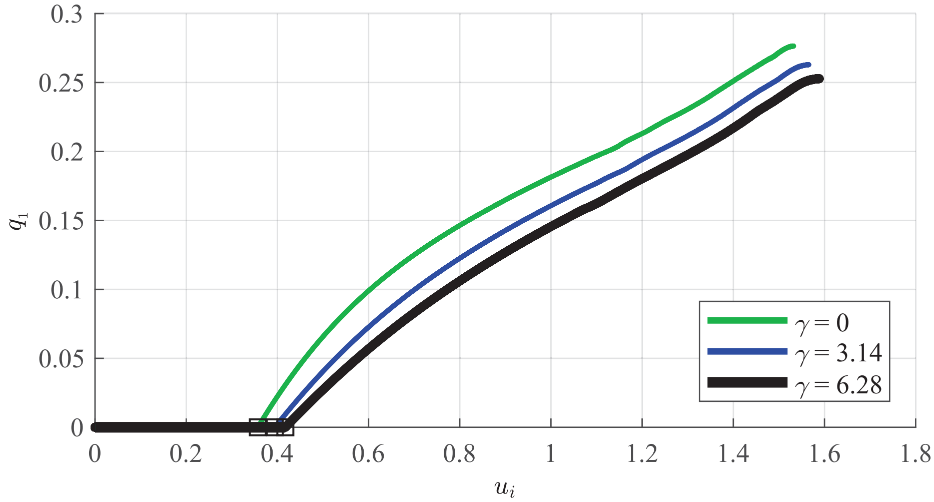

Figure 3–11: Influence of the dimensionless gravity parameter, γ.

Table 3–3: Comparison between the critical flow velocities for flutter, u_{if}, for different values of γ.

	$\gamma = 0$	$\gamma = 3.14$	$\gamma = 6.28$
u_{if}	0.356	0.394	0.417

Since the internal flowing fluid and the external one are assumed to be interdependent and of the same substance, the ratio β_i/β_o is kept constant throughout. For the degree of confinement considered in this study, the external flow is dominant [8], so the effect of varying the mass ratio is basically due to varying the outer one, β_o. Unlike the case of a cantilevered cylinder in axial flow directed from the clamped end to the free one, in which increasing the mass ratio tends to stabilize the system against flutter [87], Fig. 3–12 shows that, for the problem at hand, increasing the mass ratio β_o, has a destabilizing effect. This can be explained by the negative sign of the Coriolis term associated with the external flow in the equation of motion — due to the inverted direction of the external flow in this study. Moreover, for higher values of β_o, the amplitude of flutter increases at a given flow velocity; however, at high values of u_i, the difference in the amplitudes decreases. The values of the critical flow velocity for flutter, u_{if}, for different values of the mass ratio, β_o, are given in Table 3–4.

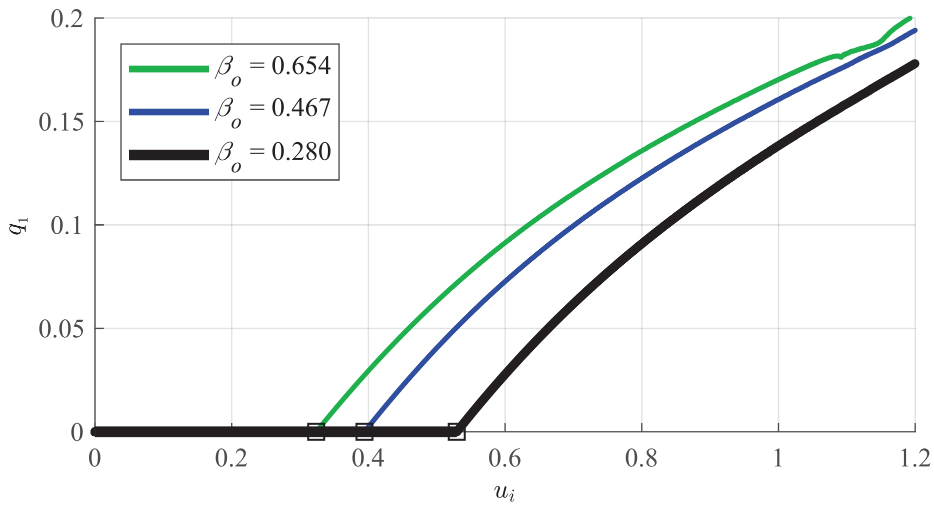

Figure 3–12: Influence of the dimensionless mass ratio parameter associated with the external flow, β_o, keeping the ratio β_i/β_o constant.

Table 3–4: Comparison between the critical flow velocities for flutter, u_{if}, for different values of β_o and $\beta_i/\beta_o = 0.166$.

	$\beta_o = 0.280$	$\beta_o = 0.467$	$\beta_o = 0.654$
u_{if}	0.529	0.394	0.323

3.5.4 Influence of the friction coefficients

In this study, the friction coefficients in the normal and tangential directions are assumed to be the same, as in [8]; i.e. $c_N = c_T = c_f$, and since they appear in the equation of motion multiplied by the dimensionless slenderness parameter, ε, the effect of varying εc_f is investigated in this subsection. Varying the value of εc_f does not have a significant influence on the dynamical response of the system, especially if the value is decreased, as shown in Fig. 3–13; the two lines which represent the response for $\varepsilon c_f = 0.4488$ and $\varepsilon c_f = 0.0449$ are almost identical. However, increasing the value of εc_f tenfold tends to stabilize the system, as seen in Table 3–5, but only slightly, and it slightly decreases the amplitude of oscillations at relatively low flow velocities, as shown in Fig. 3–13.

Table 3–5: Comparison between the critical flow velocities for flutter, u_{if}, for different values of εc_f.

	$\varepsilon c_f = 0.0449$	$\varepsilon c_f = 0.4488$	$\varepsilon c_f = 4.4882$
u_{if}	0.393	0.394	0.415

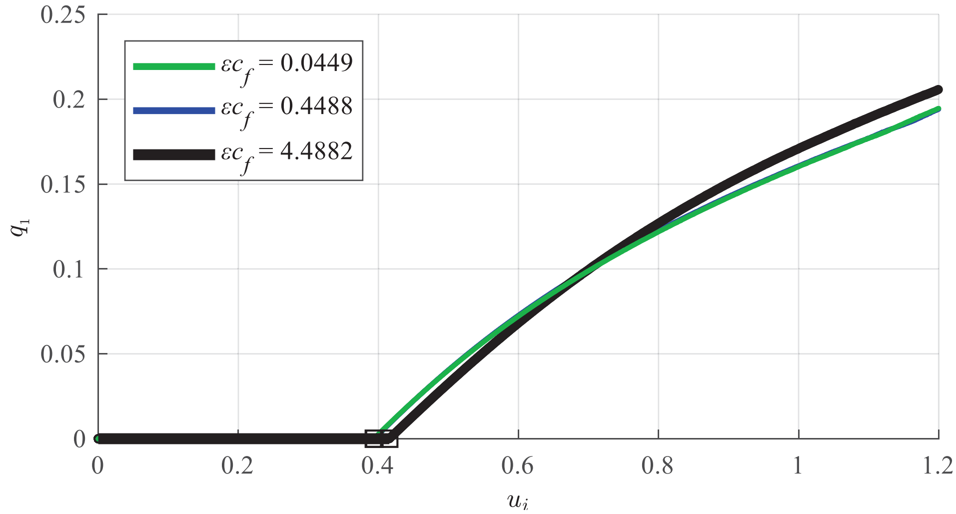

Figure 3–13: Influence of the dimensionless parameter, εc_f.

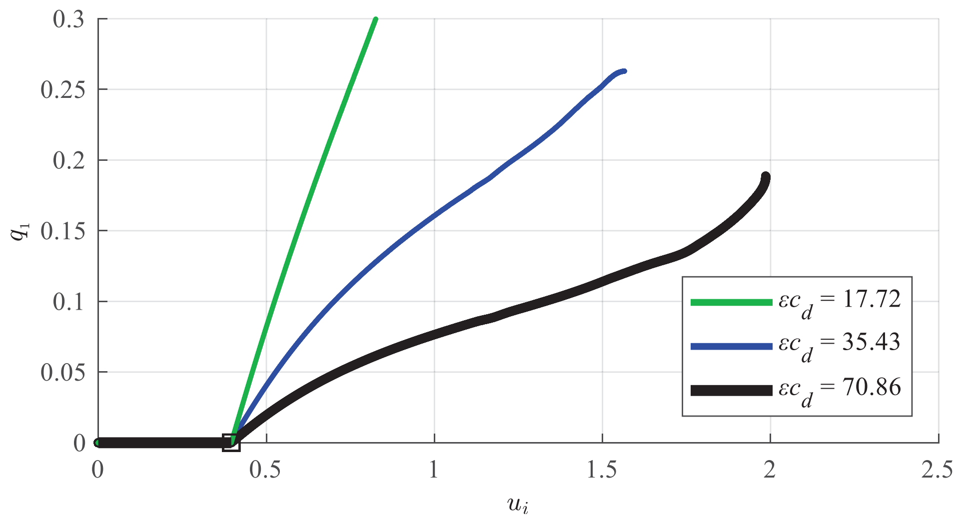

Figure 3–14: Influence of the dimensionless parameter, εc_d.

3.5.5 Influence of the form-drag coefficient

The effect of varying the quantity εc_d on the dynamical behaviour of the system is as follows. As seen in Fig. 3–14, there is no change in the onset of instability for the different values of εc_d considered; this is because the term involving εc_d does not appear in the linearized equation of motion. However, a decrease in the amplitude of the oscillations, at any given flow velocity, is noted when the value of εc_d is increased, and vice versa.

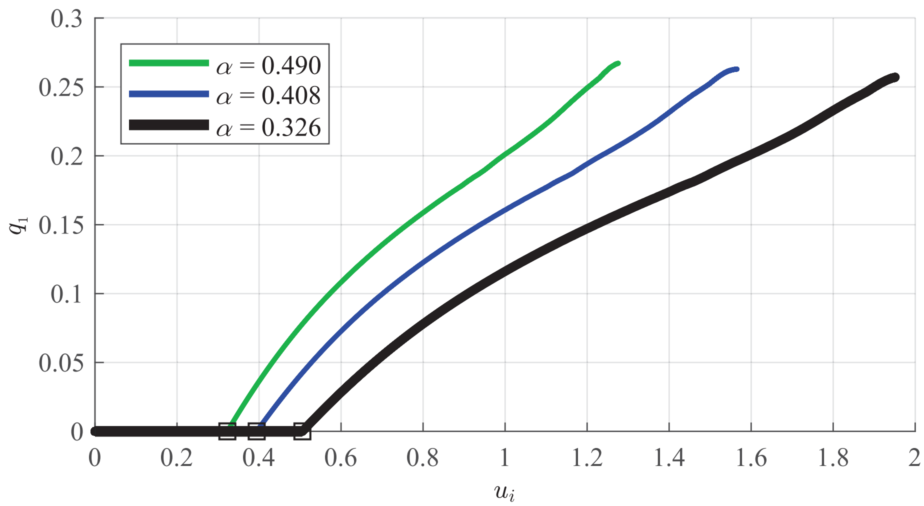

Figure 3–15: Influence of the dimensionless parameter, α.

3.5.6 Influence of the thickness of the pipe

Varying the ratio of the inner diameter of the pipe to the outer one, $\alpha = D_i/D_o$, gives a measure of varying the thickness of the pipe. It is noted that for a thicker pipe wall, i.e. for lower values of α, the pipe is found to be more stable, and hence, flutter occurs at higher flow velocities, as shown in Table 3–6. In addition, decreasing the value of α results in a lower amplitude of oscillations, as shown in Fig. 3–15.

Table 3–6: Comparison between the critical flow velocities for flutter, u_{if}, for different values of α.

	$\alpha = 0.326$	$\alpha = 0.408$	$\alpha = 0.490$
u_{if}	0.506	0.394	0.323

3.6 Comparison between the predictions of the proposed model and experimental observations from the literature

In order to allow comparison between the results of the nonlinear model derived in this chapter and the results of the experimental and theoretical study of Rinaldi [115], Eq. (3.33) is solved using system parameters similar to the ones in [115]. A system with the following parameters is considered: $D_o = 0.0159\,\mathrm{m}$, $D_i = 0.00635\,\mathrm{m}$, $L = 0.343\,\mathrm{m}$, $EI = 1.05 \times 10^{-2}\,\mathrm{N.m^2}$, $m = 0.355\,\mathrm{kg/m}$, $M_i = 0.0317\,\mathrm{kg/m}$, $\rho A_o = 0.198\,\mathrm{kg/m}$, $\beta_o = 0.339$,

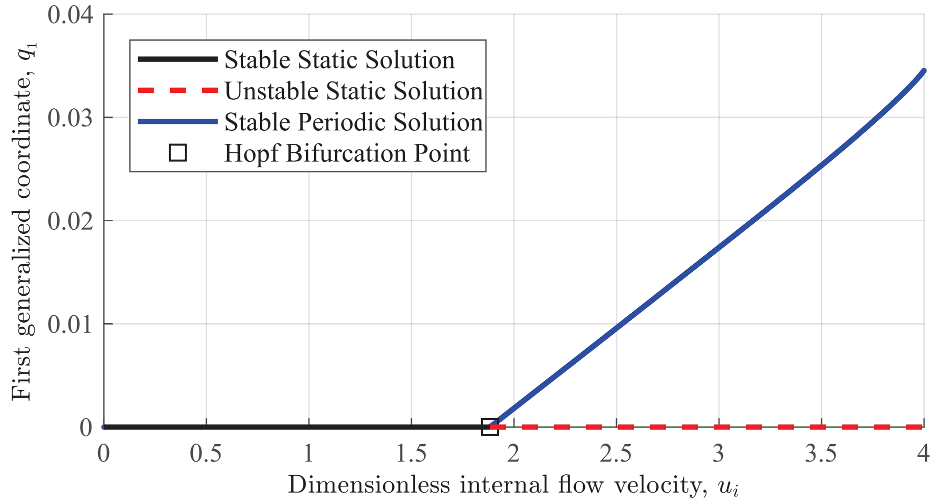

Figure 3–16: Bifurcation diagram for the parameters of [115].

$\beta_i = 0.0542$, $\gamma = 7.14$, and $\alpha_{ch} = 1.6$. In addition, $c_N = c_T = 0.0159$, $c_d = 1.25$, and $\kappa = [4.2,\ 12.8,\ 20.3,\ 27.9]$ for the lowest four modes of the system.

Figure 3–16 shows a bifurcation diagram obtained via a four-mode Galerkin approximation with q_1 being representative of the behaviour of the system. The pipe remains stable around the origin with increasing u_i, but at $u_i = 1.88$, a Hopf bifurcation is predicted leading to flutter in the first mode. Thereafter, the amplitude of oscillations increases almost linearly with increasing u_i. Samples of the time history and phase-plane plot at $u_i = 2.5$ are shown in Figs. 3–17a and 3–17b revealing that the stable periodic oscillations are around the origin. Also, a power spectral density plot at the same flow velocity, calculated by direct fast Fourier transform, is shown in Fig. 3–17c with one dominant frequency of oscillations, $f = 0.76$ Hz (the other sub-harmonics in the PSD conform to $f/2$ and $f/3$). Moreover, the shape of the pipe at the maximum deflected position is plotted in Fig. 3–17d showing that the oscillations are in the first mode.

The results obtained in this study are in good qualitative agreement with the experiments reported in [115], in which first-mode flutter was observed; and the amplitude of the oscillations increases linearly as the internal flow velocity is increased. However, quantitatively, flutter was observed experimentally at vanishing flow velocities as shown in Table 3–7.

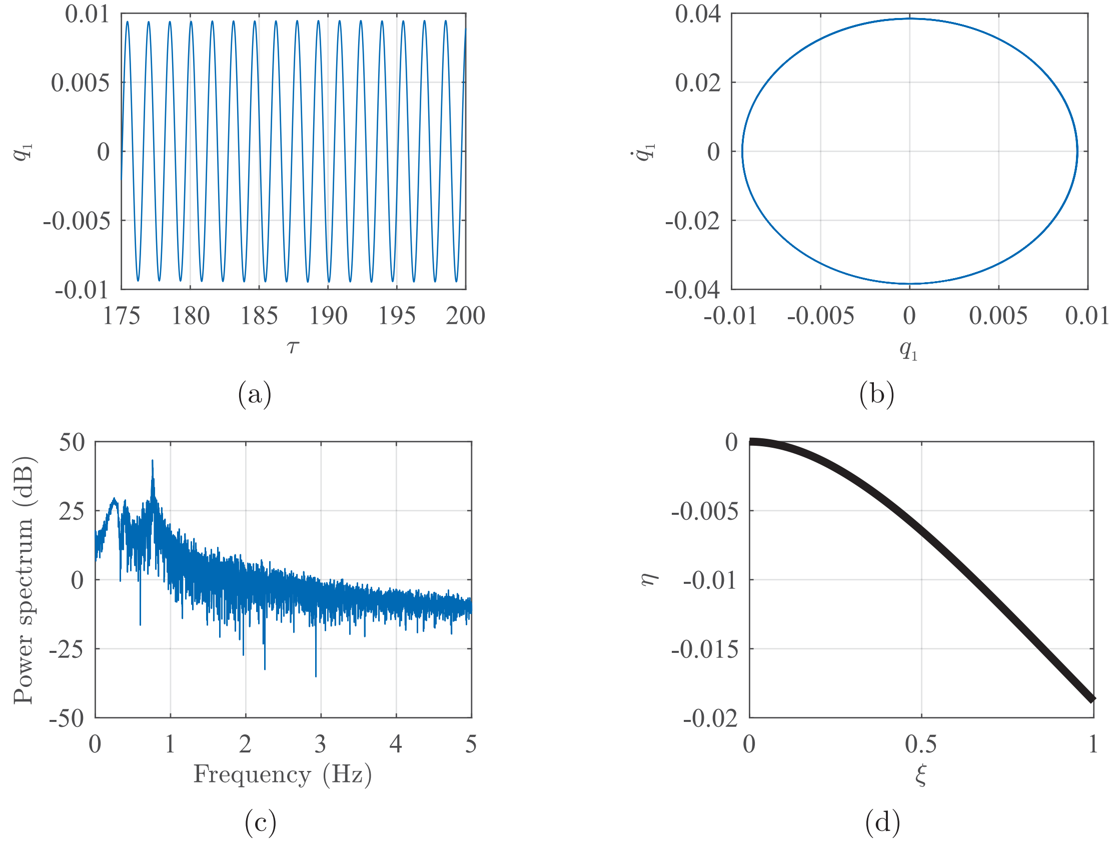

Figure 3–17: At $u_i = 2.5$: (a) time history plot, (b) phase-plane plot, (c) power spectral density plot, and (d) shape of the pipe at the maximum deflected position.

The linear analytical model derived in [115] predicts the same kind of instability, but over-estimates its onset, at u_{if}, compared to the experiments and to this nonlinear theory, as shown in Table 3–7.

Table 3–7: Comparison between the values of u_{if} obtained by different studies.

	Experiments [115]	Theory [115]	Present Theory
u_{if}	0.21	2.25	1.88

The linear model presented in [115] also predicts very weak damping at low flow velocities before flutter occurs, which can lead to flow-perturbation excitation at these low velocities. This could also be the case for the experimentally observed oscillations with small amplitudes at vanishing flow velocities. With increasing flow velocity, a sudden reduction in the recorded amplitude of oscillations was noticed in [115] at $u_i \approx 1.8$, which may indicate a change to fluidelastic instability, namely flutter. This sudden reduction in the amplitude of the oscillations is also noticed in other experiments in [115] for the same system with different parameters.

The amplitude and the frequency of oscillations predicted by the proposed theory are also compared to the experimental data reported in [115] in Tables 3–8 and 3–9, respectively. Table 3–8 shows a reasonable quantitative agreement between the theory and the experiments for the maximum amplitude of oscillations at flow velocities not too close to the onset of flutter, which is expected since the theory overestimates this onset. Also, a good quantitative agreement for the frequency of oscillations can be observed in Table 3–9.

Table 3–8: Comparison between the maximum amplitude of flutter, $y_f(s = L)$, in mm obtained by different studies.

u_i	y_f (Experiments [115])	y_f (Present Theory)
1.90	1.82	0.03
2.25	2.20	1.19
2.50	2.46	1.97

Table 3–9: Comparison between the frequency of oscillations, f, in Hz obtained by different studies.

u_i	f (Experiments [115])	f (Present Theory)
1.90	0.70	0.70
2.25	0.71	0.75
2.50	0.72	0.76

3.7 Summary

In this chapter, a nonlinear analytical model has been derived for the dynamics of a hanging tubular cantilever subjected to interdependent, counter-current internal and confined external axial flows. The equation of motion, which is correct to third-order magnitude, was obtained via the extended Hamilton's principle. The lateral deflection is assumed to be of first-order magnitude, while the axial one is of second-order. The fluid-related forces associated with the external flow, i.e the inviscid, hydrostatic and viscous forces, were derived separately, as well as the non-conservative forces associated with the internal flow. The proposed equation of motion is probably not the definitive nonlinear equation of motion for this system, since it was not obtained by a unified nonlinear treatment of the fluid mechanics.

The nonlinear model proposed in this chapter has proved theoretically the existence of limit-cycle oscillations, corresponding to flutter in the first mode for a slender elastomer tubular cantilever simultaneously subjected to internal and confined external axial flows. The critical value of the dimensionless internal flow velocity for flutter is predicted to be $u_i \approx 0.39$. The amplitude and the frequency of oscillations increase with increasing flow velocity.

In addition, the influences of various dimensionless parameters were investigated in this study. It is shown that increasing the confinement of the external flow or the ratio of the fluid mass to the total mass of the system destabilizes the system. On the other hand, increasing the thickness of the tube or the dimensionless gravity parameter stabilizes the system. Moreover, it was found that the friction and the form-drag coefficients do not have significant effects on the onset of instability of the system.

The equation of motion was also solved using system parameters that correspond to an experimental set-up in the literature. The results predicted by the proposed nonlinear model are in good qualitative and reasonable quantitative agreement with the experimental observations.

This chapter represents the first nonlinear analytical study on such a system. It provides a fuller understanding of the dynamics of the system as compared to linear theories. For example, it provides predictions for the dynamical behaviour beyond the first instability, and the amplitude and frequency of oscillations.

CHAPTER 4
Nonlinear dynamics of a cantilevered pipe discharging fluid with a reverse, partially-confined, external axial flow over its upper portion (System III)

In this chapter, the nonlinear dynamics of a hanging cantilevered pipe simultaneously subjected to internal and *partially-confined* external axial flows is examined by a nonlinear theory. The pipe under consideration discharges fluid downwards in a fluid-filled tank, then the fluid flows upwards through an annular region that surrounds the pipe over its upper portion. A similar system has been studied before, theoretically and experimentally, by Moditis [104] and Moditis et al. [11]. Two different sets of system parameters were considered in the theoretical analysis of [11, 104]: (i) one corresponds to a bench-top system, in which experiments were conducted to validate the theoretical predictions; (ii) another corresponds to a large scale brine-string-like system. For system (i), it was found that the pipe loses stability via flutter in the second mode at sufficiently high flow velocity; for system (ii), a static divergence as well as flutter were predicted, depending on certain parameters.

The nonlinear equation of motion is derived to third-order accuracy in Section 4.1. In Section 4.2, the theoretical model is used to examine the nonlinear dynamics of two pipes of different dimensions and materials, and with different lengths of the annular region. In Section 4.3, the critical flow velocities for instability, as well as the amplitudes and frequencies of oscillations at various flow velocities, obtained using the model developed here, are compared to the experimental data reported in [11] for systems with parameters similar to those considered in Section 4.2. The influence of varying the tightness of the annular region on the stability of the system is investigated theoretically in Section 4.4.

4.1 Derivation of the theoretical model

A long flexible cantilevered pipe such as shown in Fig. 4–1a is considered, with outer diameter D_o, inner diameter D_i, length L, flexural rigidity EI and mass per unit length m.

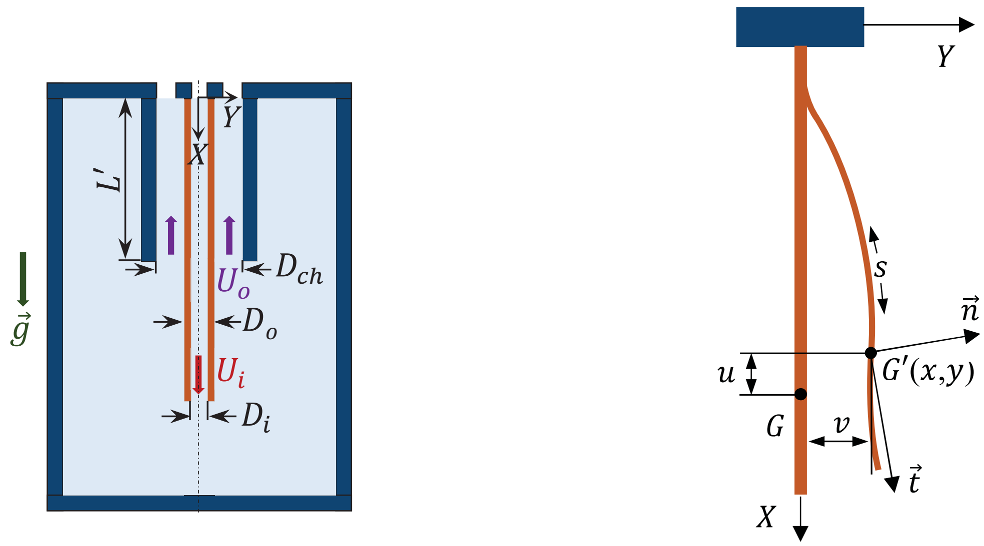

(a) (b)

Figure 4–1: (a) Diagrammatic view of a vertical hanging pipe discharging fluid downwards, which then flows upwards through an annular region surrounding the pipe. (b) Diagram defining the coordinate systems used, and the displacements of point G on the neutral axis of the pipe, located at $G(X,0)$ before deformation and at $G'(x,y)$ after deformation.

The pipe conveys fluid downwards with a uniform flow velocity U_i in a relatively large tank that is filled with the same fluid. The fluid then flows upwards with velocity U_o through an annular region contained by a rigid tube of internal diameter D_{ch} and length L', exiting at $X = 0$. The system is oriented vertically, and the neutral axis of the pipe coincides with the X-axis and the gravity direction, $\vec{g}$, as indicated in Fig. 4–1a.

The main assumptions made earlier for System II are made here also, namely: (i) the pipe is slender and may be modelled via Euler-Bernoulli beam theory; (ii) the centreline of the pipe is inextensible; (iii) the pipe may undergo large deformation, but the strains remain small; (iv) the motion of the pipe is planar, i.e. in the (X,Y)-plane, as shown in Fig. 4–1b, and thus the derived model is two-dimensional; (v) the fluid is incompressible; (vi) the tank size is large enough for the external flow velocity to have a value of U_o in the confined region only, but $U_o = 0$ over the unconfined one; and lastly (vii) the internal flow velocity, U_i, and the external one in the confined region, U_o, are uniform, and they are related to each other according to the law of conservation of mass.

In the following analysis, the Lagrangian coordinate system (X, Y, Z, t) is used to describe the undeformed state of the pipe, while the Eulerian one (x, y, z, t) is used for the deformed state, as in Chapters 2 and 3. Thus, the displacements of a point, say G, on the centreline of the pipe, due to deformation may be determined by $u = x - X$, $v = y - Y$ and $w = z - Z$, with $Y = 0$, $v = y$ and $z = Z = w = 0$, since the pipe is assumed to move only in the (X,Y)-plane — see Fig. 4–1b. In addition, one can write $\partial s/\partial X = 1$, as the pipe centreline is assumed to be inextensible, and hence the curvilinear coordinate along the pipe, s, can be used instead of X. Also, one can derive the following inextensibility condition $(\partial x/\partial X)^2 + (\partial y/\partial X)^2 = 1$, and thus obtain the curvature, $\bar{\kappa}$, along the deformed pipe,

$$\bar{\kappa} = \frac{\partial^2 y/\partial s^2}{\sqrt{1 - (\partial y/\partial s)^2}}. \tag{4.1}$$

The reader is referred to [39] for detailed derivations.

The equation of motion is derived via the extended Hamilton's principle,

$$\delta \int_{t_1}^{t_2} \mathcal{L}\,\mathrm{d}t + \int_{t_1}^{t_2} \delta W\,\mathrm{d}t = 0, \tag{4.2}$$

where $\mathcal{L}$ is the Lagrangian and δW is the total virtual work done on the pipe. The Lagrangian can be determined by $\mathcal{L} = \mathcal{T} - \mathcal{V}$, where $\mathcal{T}$ is the kinetic energy of the pipe including the conveyed fluid, and $\mathcal{V}$ is the associated potential energy. Also, the total virtual work, $\delta W = \delta W_i + \delta W_o$, consists of: δW_i, the virtual work due to the fluid forces related to the internal flow but not included in the Lagrangian, and δW_o, associated with the external flow.

4.1.1 Total kinetic and potential energies of the pipe including the conveyed fluid

The nonlinear expressions for the kinetic and potential energies of a pipe conveying fluid were derived in [39], and detailed in Chapter 2; the same expressions can be used for the configuration under study here, namely

$$\delta \int_{t_1}^{t_2} \mathcal{T}\,\mathrm{d}t = -\int_{t_1}^{t_2}\int_0^L [(m+M_i)\ddot{x} + 2M_iU_i\dot{x}']\delta x\,\mathrm{d}s\,\mathrm{d}t \\ -\int_{t_1}^{t_2}\int_0^L [(m+M_i)\ddot{y} + 2M_iU_i\dot{y}']\delta y\,\mathrm{d}s\,\mathrm{d}t \\ + M_iU_i\int_{t_1}^{t_2} [\dot{x}_{_L}\delta x_{_L} + \dot{y}_{_L}\delta y_{_L}]\,\mathrm{d}t, \tag{4.3}$$

where M_i is the mass of the fluid per unit length of the pipe, $x_{_L} = x(L)$ and $y_{_L} = y(L)$ are the displacements of the free end of the pipe, and $(\ )' = \partial(\ )/\partial s$ and $(\dot{\ }) = \partial(\ )/\partial t$. Additionally,

$$\delta \int_{t_1}^{t_2} \mathcal{V}\,\mathrm{d}t = EI\int_{t_1}^{t_2}\int_0^L [y'''' + 4y'y''y''' + y''^3 + y''''y'^2]\,\delta y\,\mathrm{d}s\,\mathrm{d}t \\ -(m+M_i)g\int_{t_1}^{t_2}\int_0^L [-(y' + \frac{1}{2}y'^3) + (L-s)(y'' + \frac{3}{2}y''y'^2)]\,\delta y\,\mathrm{d}s\,\mathrm{d}t + \mathcal{O}(\epsilon^5). \tag{4.4}$$

It should be noted that the relation between δx and δy can be obtained by applying the variational operator, δ, to the inextensibility condition; this eventually yields

$$\delta x = -(y' + \frac{1}{2}y'^3)\delta y + \int_0^s (y'' + \frac{3}{2}y'^2y'')\delta y\,\mathrm{d}s. \tag{4.5}$$

4.1.2 Virtual work due to the internal-fluid-related forces

It was shown in [39] that the virtual work, δW_i, is non-zero even if there are no explicit external forces applied on the pipe. This is because of the non-conservative nature of the forces associated with the conveyed fluid; these forces are not included in the expression of the Lagrangian. As explained in Chapter 3, the virtual work associated with these forces can be expressed as follows:

$$\begin{aligned}\int_{t_1}^{t_2} \delta W_i \,\mathrm{d}t &= -M_i U_i \int_{t_1}^{t_2} [(\dot{x}_{_L} + U_i x'_{_L})\delta x_{_L} + (\dot{y}_{_L} + U_i y'_{_L})\delta y_{_L}]\,\mathrm{d}t \\ &= -M_i U_i \int_{t_1}^{t_2} (\dot{x}_{_L}\delta x_{_L} + \dot{y}_{_L}\delta y_{_L})\,\mathrm{d}t - M_i U_i^2 \int_{t_1}^{t_2} (x'_{_L}\delta x_{_L} + y'_{_L}\delta y_{_L})\,\mathrm{d}t \\ &= A + B.\end{aligned} \tag{4.6}$$

Term A cancels the last term in Eq. (4.3) and, by employing the inextensibility condition, the following expression for term B can be obtained:

$$B = -M_i U_i^2 \int_{t_1}^{t_2} \int_0^s \left[y'' + y'^2 y'' - y'' \int_s^L (y'y'')\,\mathrm{d}s \right] \delta y \,\mathrm{d}s\,\mathrm{d}t. \tag{4.7}$$

The analysis presented so far follows exactly that provided in [39] for a hanging cantilevered pipe conveying fluid. Therefore, substituting the expressions obtained for the virtual work and the Lagrangian in Hamilton's principle (4.2) leads to the final equation of motion derived in [39]. However, the pipe in [39] is assumed to be unconfined and to discharge the fluid to atmosphere, while in the problem at hand and in System II, the pipe is subjected also to an external flow applied simultaneously with the internal one, and the pipe is discharging the fluid into a tank that is filled with the same fluid. Thus, pressurization at the free end of the pipe is important, and should be taken into account. In the following sub-section, the effects of pressurization and externally applied tension at the free end of the pipe are incorporated.

4.1.3 Pressurization at the free end of the pipe

It was shown in Chapter 3 how the equation of motion for a pipe conveying fluid can be derived via a force-balance method instead of the energy approach: an element of the pipe of length δs is considered, which is subjected only to internal flow, as shown in Fig. 4–2. The axial force, Q_1, shear force, Q_2, and bending moment, $\mathcal{M}$, on the upper and lower cross-sections are indicated in the same figure. By considering the equilibrium of forces, one obtains

$$\frac{\partial \vec{Q}}{\partial s} + (m + M_i) g \vec{i} = m \frac{\partial^2 \vec{r}}{\partial t^2} + M_i \frac{\mathrm{D}^2 \vec{r}}{\mathrm{D}t^2}, \tag{4.8}$$

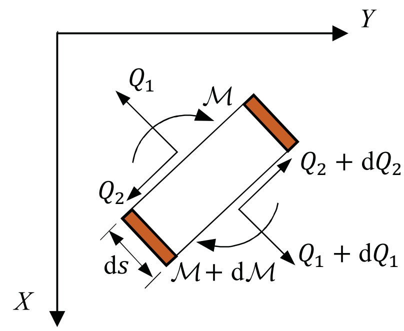

Figure 4–2: Free-body diagram of an element of the cantilevered pipe considering the effects of only the internal flow.

where Q is the resultant force, D( )/Dt is the material derivative. Similarly, applying a balance of moments leads to

$$\frac{\partial \vec{\mathcal{M}}}{\partial s} + \vec{t} \times \vec{Q} = 0. \tag{4.9}$$

By utilizing the approximations of Euler-Bernoulli beam theory and decomposing $\vec{Q}$ along $\vec{t}$ and $\vec{n}$, one can obtain

$$(m + M_i)g - EI\frac{\partial^4 x}{\partial s^4} + \frac{\partial}{\partial s}\left[(T_o - A_i p_i - EI\bar{\kappa}^2)\frac{\partial x}{\partial s}\right] = m\frac{\partial^2 x}{\partial t^2} + M_i\frac{\mathrm{D}^2 x}{\mathrm{D}t^2}, \tag{4.10}$$

$$-EI\frac{\partial^4 y}{\partial s^4} + \frac{\partial}{\partial s}\left[(T_o - A_i p_i - EI\bar{\kappa}^2)\frac{\partial y}{\partial s}\right] = m\frac{\partial^2 y}{\partial t^2} + M_i\frac{\mathrm{D}^2 y}{\mathrm{D}t^2}, \tag{4.11}$$

where T_o is an externally applied tension, p_i is the pressure of the internal fluid, and $A_i = (\pi/4)D_i^2$ is the inner cross-sectional area of the pipe. Integrating Eq. (4.10) from s to L and dividing it by $\partial x/\partial s$ yields

$$\begin{aligned}(T_o - A_i p_i - EI\bar{\kappa}^2) =& \frac{1}{\partial x/\partial s}\Bigg\{(m + M_i)g(L - s) + EI(\partial^3 x/\partial s^3) + [(T_o - A_i p_i)(\partial x/\partial s)]_{s=L} \\ &- \int_s^L [m(\partial^2 x/\partial t^2) + M_i(\mathrm{D}^2 x/\mathrm{D}t^2)]\,\mathrm{d}s\Bigg\}.\end{aligned} \tag{4.12}$$

Substituting Eq. (4.12) into Eq. (4.11) and utilizing the inextensibility condition to eliminate x leads to the same equation of motion obtained via Hamilton's principle, as concluded in [39]. However, the third term on the right-hand side of Eq. (4.12) was not present in [39], because the pipe was assumed to discharge the fluid to atmosphere and hence there was no tension applied at the free end. By keeping that term and following the same procedure, one obtains the same equation as in [39], but with the following extra term: $-\left[(T_o - A_i p_i)(1 - \frac{1}{2}y'^2)\right]_{s=L}(y'' + \frac{3}{2}y''y'^2)$. This term appears in the final equation of motion obtained in this chapter.

Moreover, the relation between the external pressure at the free end of the pipe, $p_o(L)$, and the internal one, $p_i(L)$, can be determined by an energy balance of the fluid at $s = L$. Thus,

$$p_i(L) = p_o(L) - \frac{1}{2}\rho U_i^2 + \rho g h_e, \tag{4.13}$$

where $h_e = K_e U_i^2/(2g)$ is the head-loss due to the sudden enlargement of the internal flow into the surrounding fluid, with $K_e = 1$ according to [117].

4.1.4 Fluid-related forces associated with the external flow

In this subsection, the external-fluid part of the problem is analysed. Since the tank, into which the hanging pipe is discharging fluid, is assumed to be large, the external flow velocity over the unconfined region, i.e. before the flow enters the annular region, is assumed to be $U_o = 0$. However, once the fluid enters the annular region, $U_o \neq 0$; the value of U_o can be determined via continuity as follows: $U_o = U_i(A_i/A_{ch})$, where $A_{ch} = (\pi/4)(D_{ch}^2 - D_o^2)$. In the linear study of [11], the Heaviside step function was utilized to model this discontinuity in the external flow velocity over the length of the pipe; reasonable to good quantitative agreement between the theory and the experiment was achieved in that study. In addition, the logistic function, which provides a smoother transition as compared to the Heaviside step function, was considered by Abdelbaki et al. [118] to model the discontinuity in the external flow velocity for the same system; this approximation will be discussed in greater detail in Chapter 5. An improvement in the capability of the model to predict the threshold of instability and the corresponding frequency of oscillations was reached in [118] as compared to [11]; however, the improvement was only slight, as discussed in [118]. Besides, the Heaviside step function results in relatively simpler expressions compared to the logistic one and,

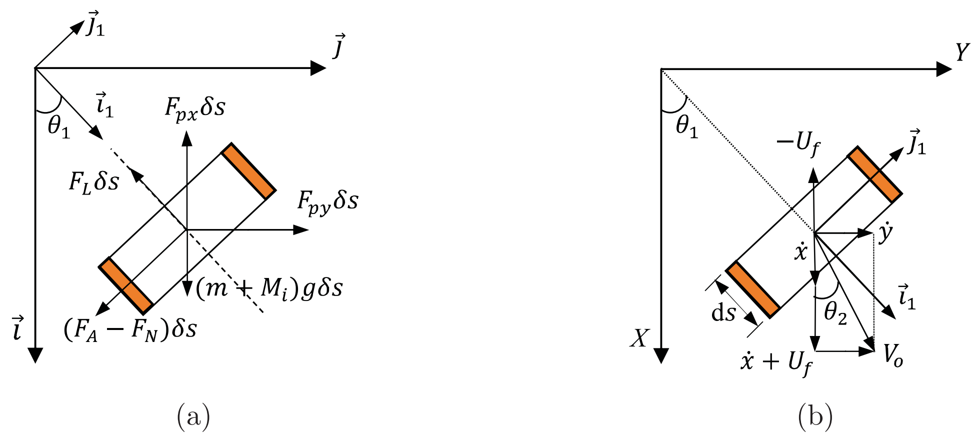

Figure 4–3: (a) Fluid-related forces acting on an element of the cantilevered pipe δs; (b) determination of the relative fluid-body velocity V_o associated with the external flow on an element of the pipe.

therefore, it was decided to model the discontinuity in the external flow velocity by means of the Heaviside step function in this chapter. Hence, one can write $U_o(s) = U_o[1 - \mathrm{H}(s - L')]$.

The fluid-related forces due to the external flowing fluid are derived in a separate manner, as in the previous chapters, rather than by the direct application of the Navier-Stokes equations. This approach has been shown in the literature to be quite reasonable and it has been used to simplify the analysis considerably, as discussed in Chapters 2 and 3.

An element of the deformed pipe, at $s \leq L'$, is considered to be subjected only to the external flow; the following set of forces acting on the element, as shown in Fig. 4–3a, are: the inviscid fluid dynamic force $F_A\delta s$, the normal and longitudinal viscous forces, $F_N\delta s$ and $F_L\delta s$, respectively, and the hydrostatic forces in the x- and y-direction, $F_{px}\delta s$ and $F_{py}\delta s$, respectively. In the following, nonlinear expressions for these forces are obtained, following closely the derivations presented in Chapters 2 and 3, since the external flow in the system under study is in the same direction as in Systems I and II.

The inviscid fluid dynamic force, $\boldsymbol{F_A}$

The nonlinear expression derived for this force in Chapter 3 can be utilized here, after some modifications to account for the discontinuity in the external flow velocity along s;

hence, one can write

$$
\begin{aligned}
F_A(X,t) = & \left\{ \frac{\partial}{\partial t} + \left[-U_o[1-\mathrm{H}(s-L')](1-\frac{\partial u}{\partial X}) - (\frac{\partial u}{\partial t} - U_o[1-\mathrm{H}(s-L')])\frac{\partial u}{\partial X} \right] \frac{\partial}{\partial X} \right\} \\
& \times \left[V_o - (\frac{\partial u}{\partial t}\frac{\partial v}{\partial X} - 2U_o[1-\mathrm{H}(s-L')]\frac{\partial u}{\partial X}\frac{\partial v}{\partial X}) - \frac{1}{2}V_o(\frac{\partial v}{\partial X})^2 \right] M_o \\
& - \frac{1}{2}M_o V_o \frac{\partial v}{\partial X}\frac{\partial V_o}{\partial X} + \mathcal{O}(\epsilon^5),
\end{aligned}
\tag{4.14}
$$

where V_o is the relative fluid-pipe velocity and its direction is indicated in Fig. 4–3b, M_o is the virtual added mass, and $A_o = \pi D_o^2/4$ is the pipe outer cross-sectional area. Moreover, the expression of the virtual added mass has to be modified to $M_o = [\chi + (1-\chi)\mathrm{H}(s-L')]\rho A_o$, where $\chi = (D_{ch}^2 + D_o^2)/(D_{ch}^2 - D_o^2)$ is the confinement parameter; the linear form of the relative fluid-pipe velocity is expressed as $V_o = \dot{y} - U_o[1-\mathrm{H}(s-L')]y'$.

The viscous forces $\boldsymbol{F_N}$ and $\boldsymbol{F_L}$

By following the framework presented in [86,119] and taking into account the difference in the value of $U_o(s)$ outside and inside the annular region, the normal and longitudinal viscous forces can be expressed as

$$
\begin{aligned}
F_N = & \frac{1}{2}\rho D_o U_o^2[1-\mathrm{H}(s-L')]\Bigg[C_N \Bigg(y' - \frac{\dot{y}}{U_o} - \frac{\dot{y}u'}{U_o} - u'y' + \frac{\dot{x}\dot{y}}{U_o^2} \\
& - \frac{1}{2}\left(y'^3 - \frac{\dot{y}^3}{U_o^3} - \frac{y'^2\dot{y}}{U_o} + \frac{y'\dot{y}^2}{U_o^2} \right)\Bigg) - C_{Dp}\left(y'|y'| + \frac{y'|\dot{y}| + |y'|\dot{y}}{U_o} + \frac{\dot{y}|\dot{y}|}{U_o^2} \right) \Bigg] - k\dot{y} + \mathcal{O}(\epsilon^5), \\
F_L = & \frac{1}{2}\rho D_o U_o^2[1-\mathrm{H}(s-L')]C_T\left[1 - \frac{1}{2}\left(y'^2 - 2\frac{y'\dot{y}}{U_o} + \frac{\dot{y}^2}{U_o^2} \right) \right] + \mathcal{O}(\epsilon^4),
\end{aligned}
\tag{4.15}
$$

where C_N and C_T are friction coefficients in the normal and tangential directions of the pipe centreline, respectively, and C_{Dp} is a form-drag coefficient. It should be noted that the quadratic terms associated with the form-drag coefficient were modified in a similar way as in [86,111] to obtain forces that are always opposing motion. Also a viscous damping term, $k\dot{y}$, has been added, based on the analysis in [5,11]. The value of the viscous damping coefficient, k, should be dependent on the frequency of oscillations and the degree of confinement of the surrounding flow [11,116,120]. One can make use of the following expression provided in [11]: $k = k_u(1+\bar{\gamma}^3)/(1-\bar{\gamma}^2)^2$, in which $\bar{\gamma} = D_o/D_{ch}$ and $k_u = 2\sqrt{2}\rho A_o \mathcal{R}(\Omega)/\sqrt{\tilde{S}}$, with $\mathcal{R}(\Omega)$ being the circular frequency of oscillations, $\tilde{S} = \mathcal{R}(\Omega)D_o^2/4\nu$ the Stokes number, also known as the oscillatory Reynolds number, and ν the kinematic viscosity of the fluid. Here, k is modified to account for the difference between the confined and unconfined regions of the flow around the pipe, and thus one can write

$$k = k_u\left[\frac{1+\bar{\gamma}^3}{(1-\bar{\gamma}^2)^2} + \mathrm{H}(s-L')\left(1-\frac{1+\bar{\gamma}^3}{(1-\bar{\gamma}^2)^2}\right)\right]. \tag{4.16}$$

The hydrostatic forces $\boldsymbol{F_{px}}$ and $\boldsymbol{F_{py}}$

These forces are the resultants of the external steady-state pressure p_o acting on the pipe. The procedure described in [5, 86] for a cantilevered cylinder in axial flow is used to derive nonlinear expressions for these forces, taking into account the inverse direction of the annular flow in the problem under study. The outer pressure gradient for the problem in hand can be expressed as follows:

$$A_o\left(\frac{\partial p_o}{\partial x}\right) = \frac{1}{2}\rho D_o U_o^2[1-\mathrm{H}(X-L')]C_T\frac{D_o}{D_h} + \rho g A_o + A_o\left(\frac{1}{2}\rho U_o^2 + \rho g h_a\right)\delta_D(X-L'), \tag{4.17}$$

where $D_h = D_{ch} - D_o$ is the hydraulic diameter, δ_D is the Dirac delta function, and $h_a = K_1 U_o^2/(2g)$ is the head-loss associated with the stagnant fluid entering the annular region, with $0.8 \leq K_1 \leq 0.9$ [117]. By rewriting the derivative in Eq. (4.17) with respect to X and integrating from $X = s$ to L, one can obtain:

$$\begin{aligned} A_o p_o(s) = {} & A_o p_o(L) - \left(\frac{1}{2}\rho D_o U_o^2[1-\mathrm{H}(s-L')]C_T\frac{D_o}{D_h}\right)\left[(L'-s) - \int_s^L \frac{1}{2}y'^2 \mathrm{d}s\right] \\ & - \rho g A_o\left[(L-s) - \int_s^L \frac{1}{2}y'^2\mathrm{d}s\right] - A_o\left(\frac{1}{2}\rho U_o^2 + \rho g h_a\right)[1-\mathrm{H}(s-L')] \\ & + A_o\left(\frac{1}{2}\rho U_o^2 + \rho g h_a\right)\int_s^L \frac{1}{2}y'^2\delta_D(s-L')\mathrm{d}s + \mathcal{O}(\epsilon^4). \end{aligned} \tag{4.18}$$

Proceeding with the derivation – thus following the derivation as in [86] – and by using Eqs. (4.17) and (4.18), the following expressions for the hydrostatic forces are obtained:

$$\begin{aligned}
-F_{px} &= y'^2\bigg(-\frac{1}{2}\rho D_o U_o^2[1-\mathrm{H}(s-L')]C_T\frac{D_o}{D_h}-\rho g A_o \\
&\quad - A_o\bigg(\frac{1}{2}\rho U_o^2+\rho g h_a\bigg)\delta_D(s-L')\bigg) - y'y''A_o p_o + \mathcal{O}(\epsilon^4), \\
F_{py} &= (y'-u'y'-y'^3)\bigg(\frac{1}{2}\rho D_o U_o^2[1-\mathrm{H}(s-L')]C_T\frac{D_o}{D_h} \\
&\quad + \rho g A_o + A_o\bigg(\frac{1}{2}\rho U_o^2+\rho g h_a\bigg)\delta_D(s-L')\bigg) \\
&\quad + (y''-u''y'-u'y''-\frac{3}{2}y'^2y'')A_o p_o + \mathcal{O}(\epsilon^5).
\end{aligned} \tag{4.19}$$

4.1.5 Virtual work due to the fluid-related forces associated with the external flow

Referring to Fig. 4–3a, an expression for the virtual work done on the pipe by the external-fluid-related forces can be written as

$$\begin{aligned}
\int_{t_1}^{t_2}\delta W_o \mathrm{d}t = \int_{t_1}^{t_2}\int_0^L &\{[-F_{px}-F_L\cos\theta_1+(F_A-F_N)\sin\theta_1]\delta x \\
&+ [F_{py}-F_L\sin\theta_1-(F_A-F_N)\cos\theta_1]\delta y\}\,\mathrm{d}s\,\mathrm{d}t,
\end{aligned} \tag{4.20}$$

where

$$\theta_1 = y' - u'y' - \frac{1}{3}y'^3 + \mathcal{O}(\epsilon^5). \tag{4.21}$$

By substituting Eqs. (4.14), (4.15) and (4.19) into Eq. (4.20), and with the aid of Eqs. (4.5) and (4.21), the virtual work can finally be determined.

4.1.6 Equation of motion and boundary conditions

The following nonlinear equation of motion for the pipe can be obtained by substituting Eqs. (4.3), (4.4), (4.7), and the final form of Eq. (4.20) into Eq. (4.2), after many straightforward but tedious manipulations and transformations, and by truncating to third order of magnitude:

$$
\begin{aligned}
&\{m + M_i + [\chi + (1-\chi)\mathrm{H}(s-L')]\rho A_o\}\ddot{y} + 2M_iU_i\dot{y}'(1+y'^2) - 2\chi\rho U_o[1-\mathrm{H}(s-L')]\dot{y}' \\
&\times\left(1-\frac{1}{4}y'^2\right) + M_iU_i^2y''(1+y'^2) + \chi\rho U_o^2[1-\mathrm{H}(s-L')]y''(1+2y'^2) \\
&-\frac{3}{2}[\chi+(1-\chi)\mathrm{H}(s-L')]\rho A_o\dot{y}y'\dot{y}' + \frac{3}{2}[\chi+(1-\chi)\mathrm{H}(s-L')]\rho A_oU_o[1-\mathrm{H}(s-L')]\dot{y}y'y'' \\
&-\frac{1}{2}\rho D_oU_o^2[1-\mathrm{H}(s-L')]C_N\left(y'+\frac{1}{2}y'^3\right) + \frac{1}{2}\rho D_oU_o^2[1-\mathrm{H}(s-L')]C_T(L'-s)\left(y''+\frac{3}{2}y'^2y''\right) \\
&-Ap_o(L)(y''+y'^2y'') - \left[(T_o - A_ip_i)(1-\frac{1}{2}y'^2)\right]_{s=L}(y''+\frac{3}{2}y'^2y'') \\
&-\left\{\frac{1}{2}\rho D_oU_o^2[1-\mathrm{H}(s-L')]C_T\frac{D_o}{D_h} - (m+M_i)g + \rho gA_o + A_o\left(\frac{1}{2}\rho U_o^2+\rho gh_a\right)\delta_D(s-L')\right\} \\
&\times\left(y'+\frac{1}{2}y'^3\right) + \frac{1}{2}\rho D_oU_o^2[1-\mathrm{H}(s-L')]C_T\frac{D_o}{D_h}(L'-s)\left(y''+\frac{3}{2}y'^2y''\right) \\
&+[\rho gA_o - (m+M_i)g](L-s)\left(y''+\frac{3}{2}y'^2y''\right) + A_o\left(\frac{1}{2}\rho U_o^2+\rho gh_a\right)[1-\mathrm{H}(s-L')] \\
&\times\left(y''+\frac{1}{2}y'^2y''\right) + EI(y'''' + 4y'y''y''' + y''^3 + y''''y'^2) + \frac{1}{2}\rho D_oC_N\dot{y}\int_0^s y'\dot{y}'\mathrm{d}s \\
&+\frac{1}{2}\rho D_oU_o^2[1-\mathrm{H}(s-L')]C_N\left(\frac{\dot{y}}{U_o} + \frac{1}{2}\frac{y'\dot{y}^2}{U_o^2} - \frac{1}{2}\frac{y'^2\dot{y}}{U_o} - \frac{\dot{y}^3}{2U_o^3}\right) \\
&+\frac{1}{2}\rho D_oU_o^2[1-\mathrm{H}(s-L')]C_{Dp}\left(y'|y'| + \frac{y'|\dot{y}| + |y'|\dot{y}}{U_o} + \frac{\dot{y}|\dot{y}|}{U_o^2}\right) \\
&+k\dot{y} - (m+M_i)y''\int_s^L\int_0^s(\dot{y}'^2 + y'\ddot{y}')\mathrm{d}s\,\mathrm{d}s + 2[\chi+(1-\chi)\mathrm{H}(s-L')]\rho A_o\dot{y}'\int_0^s y'\dot{y}'\mathrm{d}s \\
&-2\chi\rho A_oU_o[1-\mathrm{H}(s-L')]y''\dot{y}'\int_0^s y'\dot{y}'\mathrm{d}s - [\chi+(1-\chi)\mathrm{H}(s-L')]\rho A_oy''\int_s^L\{\ddot{y}y' \\
&-2U_o[1-\mathrm{H}(s-L')]y'\dot{y}' + U_o^2y'y''[1-\mathrm{H}(s-L')]\}\,\mathrm{d}s + \{m+M_i+[\chi \\
&+(1-\chi)\mathrm{H}(s-L')]\rho A_o\}y'\int_0^s(y'\ddot{y}'+\dot{y}'^2)\,\mathrm{d}s - 3\chi\rho A_oU_o[1-\mathrm{H}(s-L')]y'\int_0^s(y'\dot{y}'' \\
&+y''\dot{y}')\,\mathrm{d}s + y''\int_s^L\{Ap_o(L)y'y'' - \frac{1}{4}\rho D_oC_T\dot{y}^2\}\,\mathrm{d}s - \frac{1}{2}\rho D_oU_o^2y''(C_T-C_N) \\
&\times\int_s^L\left(y'^2 - \frac{y'\dot{y}}{U_o}\right)[1-\mathrm{H}(s-L')]\,\mathrm{d}s - y''\int_s^L(2M_iU_iy'\dot{y}' + M_iU_i^2y'y'')\,\mathrm{d}s - \frac{1}{4}y''\rho D_oU_o^2C_T\frac{D}{D_h} \\
&\times\int_s^L y'^2[(L'-s)\delta_D(s-L') - \mathrm{H}(s-L')]\,\mathrm{d}s - y''A_o\left(\frac{1}{2}\rho U_o^2+\rho gh_a\right)\int_s^L y'y''\,\mathrm{d}s = 0.
\end{aligned}
\tag{4.22}
$$

The boundary conditions are the classical ones for a cantilevered beam, namely

$$y(0) = 0, y'(0) = 0, y''(L) = 0, \text{and } y'''(L) = 0. \tag{4.23}$$

Defining next the dimensionless quantities

$$\begin{aligned}
&\xi = \frac{s}{L}, \quad \eta = \frac{y}{L}, \quad \tau = \left(\frac{EI}{m + M_i + \rho A_o}\right)^{1/2} \frac{t}{L^2}, \quad u_i = \left(\frac{M_i}{EI}\right)^{1/2} U_i L, \\
&u_o = \left(\frac{\rho A_o}{EI}\right)^{1/2} U_o L, \quad \beta_i = \frac{M_i}{m + M_i + \rho A_o}, \quad \beta_o = \frac{\rho A_o}{m + M_i + \rho A_o}, \\
&\gamma = \frac{(m + M_i - \rho A_o) g L^3}{EI}, \quad \Gamma = \frac{T_o(L) L^2}{EI}, \quad c_N = \frac{4}{\pi} C_N, \quad c_T = \frac{4}{\pi} C_T, \\
&c_d = \frac{4}{\pi} C_{Dp}, \quad \varepsilon = \frac{L}{D_o}, \quad h = \frac{D_o}{D_h}, \quad \alpha = \frac{D_i}{D_o}, \quad \alpha_{ch} = \frac{D_{ch}}{D_o}, \quad r_{ann} = \frac{L'}{L}, \\
&\Pi_{iL} = \frac{A_i p_i(L) L^2}{EI}, \quad \Pi_{oL} = \frac{A_o p_o(L) L^2}{EI}, \quad \kappa = \frac{k L^2}{[EI(m + M_i + \rho A_o)]^{1/2}},
\end{aligned} \tag{4.24}$$

the equation of motion can be written in the following dimensionless form:

$$
\begin{aligned}
&\{1+\beta_o(\chi-1)[1-\mathrm{H}(\xi-r_{ann})]\}\ddot{\eta}+2u_i\sqrt{\beta_i}\dot{\eta}'(1+\eta'^2)-2\chi u_o\sqrt{\beta_o}[1-\mathrm{H}(\xi-r_{ann})]\dot{\eta}'\\
&\times(1-\frac{1}{4}\eta'^2)+u_i^2\eta''(1+\eta'^2)+\chi u_o^2[1-\mathrm{H}(\xi-r_{ann})]\eta''(1+2\eta'^2)\\
&-\frac{3}{2}[\chi+(1-\chi)\mathrm{H}(\xi-r_{ann})]\beta_o\dot{\eta}\eta'\dot{\eta}'+\frac{3}{2}\chi u_o[1-\mathrm{H}(\xi-r_{ann})]\sqrt{\beta_o}\dot{\eta}\eta'\eta''\\
&-\frac{1}{2}u_o^2[1-\mathrm{H}(\xi-r_{ann})]\varepsilon c_N[\eta'+\frac{1}{2}\eta'^3]+\frac{1}{2}u_o^2[1-\mathrm{H}(\xi-r_{ann})]\varepsilon c_T(r_{ann}-\xi)(\eta''+\frac{3}{2}\eta'^2\eta'')\\
&-\Pi_{oL}(\eta''+\eta'^2\eta'')-(\Gamma-\Pi_{iL})(\eta''+\frac{3}{2}\eta'^2\eta'')+\frac{1}{2}(\Gamma-\Pi_{iL})\eta''\left[\eta'^2\right]_{\xi=1}\\
&-\left\{\frac{1}{2}u_o^2[1-\mathrm{H}(\xi-r_{ann})]\varepsilon c_T h-\gamma+\frac{1}{2}u_o^2(1+K_1)\delta_D(\xi-r_{ann})\right\}(\eta'+\frac{1}{2}\eta'^3)\\
&+\frac{1}{2}u_o^2[1-\mathrm{H}(\xi-r_{ann})]\varepsilon c_T h(r_{ann}-\xi)(\eta''+\frac{3}{2}\eta'^2\eta'')-\gamma(1-\xi)(\eta''+\frac{3}{2}\eta'^2\eta'')\\
&+\frac{1}{2}u_o^2(1+K_1)[1-\mathrm{H}(\xi-r_{ann})](\eta''+\frac{1}{2}\eta'^2\eta'')+\eta''''+4\eta'\eta''\eta'''+\eta''^3+\eta''''\eta'^2\\
&+\frac{1}{2}\varepsilon c_N\beta_o\dot{\eta}\int_0^\xi\eta'\dot{\eta}'\mathrm{d}s+\frac{1}{2}u_o^2[1-\mathrm{H}(\xi-r_{ann})]\varepsilon c_N\left(\frac{\sqrt{\beta_o}}{u_o}\dot{\eta}+\frac{1}{2}\frac{\beta_o}{u_o^2}\dot{\eta}^2\eta'-\frac{1}{2}\frac{\sqrt{\beta_o}}{u_o}\dot{\eta}\eta'^2-\frac{1}{2}\frac{\beta_o^{3/2}}{u_o^3}\dot{\eta}^3\right)\\
&+\frac{1}{2}u_o^2[1-\mathrm{H}(\xi-r_{ann})]\varepsilon c_d\left(\eta'|\eta'|+\frac{\sqrt{\beta_o}}{u_o}(\eta'|\dot{\eta}|+|\eta'|\dot{\eta})+\frac{\beta_o}{u_o}\dot{\eta}|\dot{\eta}|\right)+\kappa\dot{\eta}\\
&-\eta''(1-\beta_o)\int_\xi^1\int_0^\xi(\dot{\eta}'^2+\eta'\ddot{\eta}')\,\mathrm{d}\xi\,\mathrm{d}\xi+2[\chi+(1-\chi)\mathrm{H}(\xi-r_{ann})]\beta_o\dot{\eta}'\int_0^\xi\eta'\dot{\eta}'\,\mathrm{d}\xi\\
&-2\chi\sqrt{\beta_o}u_o[1-\mathrm{H}(\xi-r_{ann})]\eta''\int_0^\xi\eta'\dot{\eta}'\,\mathrm{d}\xi-[\chi+(1-\chi)\mathrm{H}(\xi-r_{ann})]\eta''\int_\xi^1\Big\{\beta_o\ddot{\eta}\eta'\\
&-2u_o\sqrt{\beta_o}[1-\mathrm{H}(\xi-r_{ann})]\dot{\eta}'\eta'+u_o^2[1-\mathrm{H}(\xi-r_{ann})]\eta''\eta'\Big\}\,\mathrm{d}\xi\\
&+\{1+(\chi-1)\beta_o[1-\mathrm{H}(\xi-r_{ann})]\}\eta'\int_0^\xi(\dot{\eta}'^2+\eta'\ddot{\eta}')\,\mathrm{d}\xi-3\chi\sqrt{\beta_o}u_o[1-\mathrm{H}(\xi-r_{ann})]\eta'\\
&\times\int_0^\xi(\eta'\dot{\eta}''+\eta''\dot{\eta}')\,\mathrm{d}\xi+\eta''\int_\xi^1\{\Pi_{oL}\eta'\eta''-\frac{1}{4}\varepsilon c_T\beta_o\dot{\eta}^2\}\,\mathrm{d}\xi-\frac{1}{2}u_o^2(\varepsilon c_T-\varepsilon c_N)\eta''\\
&\times\int_\xi^1(\eta'^2-\frac{\sqrt{\beta_o}}{u_o}\eta'\dot{\eta})[1-\mathrm{H}(\xi-r_{ann})]\,\mathrm{d}\xi-\eta''\int_\xi^1(2u_i\sqrt{\beta_i}\eta'\dot{\eta}'+u_i^2\eta'\eta'')\,\mathrm{d}\xi-\frac{1}{4}u_o^2\varepsilon c_T h\eta''\\
&\times\int_\xi^1\eta'^2[(r_{ann}-\xi)\delta_D(\xi-r_{ann})-\mathrm{H}(\xi-r_{ann})]\,\mathrm{d}\xi-\frac{1}{2}u_o^2(1+K_1)\eta''\int_\xi^1\eta'\eta''\mathrm{d}\xi=0,
\end{aligned}
\tag{4.25}
$$

where $(\ )'=\partial(\ )/\partial\xi$ and $\dot{(\ )}=\partial(\ )/\partial\tau$. The viscous damping coefficient may be expressed in dimensionless form as follows: $\kappa=\kappa_u\big\{1+[1-\mathrm{H}(\xi-r_{ann})][(1+\alpha_{ch}^{-3})/(1-\alpha_{ch}^{-2})^2-1]\big\}$.

4.1.7 Methods of analysis

As detailed before in Chapters 2 and 3, Galerkin's technique is employed to discretize the partial differential equation of motion (4.25) into a set of ordinary differential equations (ODEs). Thus, $\eta(\xi,\tau)=\sum_{j=1}^{N}\phi_j(\xi)q_j(\tau)$. In the Galerkin scheme, N represents the number of comparison functions used in the analysis; $\phi_j(\xi)$, with $j=1:N$, are the comparison functions, which are chosen to be the cantilever-beam eigenfunctions, as they satisfy the boundary conditions; $q_j(\tau)$ are the corresponding generalized coordinates. The resultant equations are then multiplied by $\phi_i(\xi)$, with $i=1:N$, and integrated over the domain $[0:1]$, which leads to the following ODEs:

$$\begin{aligned}&M_{ij}\ddot{q}_j+C_{ij}\dot{q}_j+K_{ij}q_j+r_{ijk}q_j|q_k|+\bar{s}_{ijk}|q_j|\dot{q}_k+\tilde{s}_{ijk}q_j|\dot{q}_k|+t_{ijk}\dot{q}_j|\dot{q}_k|\\&+\alpha_{ijkl}q_jq_kq_l+\beta_{ijkl}q_jq_k\dot{q}_l+\gamma_{ijkl}q_j\dot{q}_k\dot{q}_l+\eta_{ijkl}\dot{q}_j\dot{q}_k\dot{q}_l+\mu_{ijkl}q_jq_k\ddot{q}_l=0,\end{aligned}\tag{4.26}$$

in which the repetition of an index implies summation. Also, the coefficients of the linear terms: M_{ij}, C_{ij} and K_{ij} correspond to the mass, damping and stiffness matrices, respectively,

$$\begin{aligned}M_{ij}&=a_{ij\,(0,1)}-\beta_o(1-\chi)a_{ij\,(0,r_{ann})},\\C_{ij}&=2u_i\sqrt{\beta_i}b_{ij\,(0,1)}-2\chi u_o\sqrt{\beta_o}b_{ij\,(0,r_{ann})}+\frac{1}{2}u_o\varepsilon c_N\sqrt{\beta_o}a_{ij\,(0,r_{ann})}+\kappa_u a_{ij\,(0,1)}\\&\quad+\kappa_u\left[\frac{1+\alpha_{ch}^{-3}}{(1-\alpha_{ch}^{-2})^2}-1\right]a_{ij\,(0,r_{ann})},\\K_{ij}&=\lambda_j^4a_{ij\,(0,1)}+\gamma b_{ij\,(0,1)}-\frac{1}{2}u_o^2\varepsilon c_Thb_{ij\,(0,r_{ann})}-\frac{1}{2}u_o^2\varepsilon c_Nb_{ij\,(0,r_{ann})}\\&\quad-\frac{1}{2}u_o^2(1+K_1)(\phi_i|_{\xi=r_{ann}}\phi_j'|_{\xi=r_{ann}})-(\Gamma-\Pi_{iL}+\Pi_{oL})c_{ij\,(0,1)}-\gamma(c_{ij\,(0,1)}-d_{ij\,(0,1)})\\&\quad+\frac{1}{2}u_o^2\varepsilon c_T(1+h)(r_{ann}c_{ij\,(0,1)}-d_{ij\,(0,1)})+\frac{1}{2}u_o^2(1+K_1^2)c_{ij\,(0,r_{ann})}+u_i^2c_{ij\,(0,1)}\\&\quad+\chi u_o^2c_{ij\,(0,r_{ann})},\end{aligned}\tag{4.27}$$

Table 4–1: Properties of the flexible pipes.

Pipe	Material	D_i (mm)	D_o (mm)	L (mm)	EI (N m^2)	m (kg m^{-1})
1	Silicone-rubber	6.35	16	431	7.37×10^{-3}	0.194
2	Thermoplastic-rubber	6.35	9.53	443	9.33×10^{-3}	4.07×10^{-2}

Table 4–2: Dimensionless parameters of the two systems under study.

System	α	α_{ch}	β_i	β_o	γ	ε	h
Pipe 1	0.397	1.97	7.41×10^{-2}	0.470	2.69	26.9	1.03
Pipe 2	0.666	3.31	0.22	0.496	0.104	46.5	0.434

where λ_j is the jth eigenvalue of the dimensionless cantilevered beam characteristic equation, and the constants a_{ij}, b_{ij}, c_{ij} and d_{ij} are defined as follows [28]:

$$a_{ij\,(a,b)} = \int_a^b \phi_i \phi_j \,\mathrm{d}\xi, \quad b_{ij\,(a,b)} = \int_a^b \phi_i \phi_j' \,\mathrm{d}\xi, \quad c_{ij\,(a,b)} = \int_a^b \phi_i \phi_j'' \,\mathrm{d}\xi, \quad d_{ij\,(a,b)} = \int_a^b \xi \phi_i \phi_j'' \,\mathrm{d}\xi. \tag{4.28}$$

For convenience, the rather long expressions of the nonlinear coefficients, r_{ijk}, $\bar{s}_{ijk}$, $\tilde{s}_{ijk}$, t_{ijk}, α_{ijkl}, β_{ijkl}, γ_{ijkl}, η_{ijkl} and μ_{ijkl} are given in Appendix D.

4.2 Results of the theoretical model

In this section, the discretized ODEs obtained in Sub-section 4.1.7 are solved for two different flexible pipes, the dimensions and material characteristics of which are listed in Table 4–1. Also, the internal diameter of the rigid tube forming the annulus surrounding the pipes is taken to be $D_{ch} = 31.5$ mm; its length can have one of the following three values: 109 mm, 206.5 mm, 304.5 mm. The corresponding dimensionless parameters of the two systems under study are listed in Table 4–2. In addition, the confinement length parameter, $r_{ann} = L'/L$, corresponding to the different lengths of the annular region, are $r_{ann} = 0.253$, 0.478, 0.705 for Pipe 1, and $r_{ann} = 0.246$, 0.467, 0.688 for Pipe 2. The value of the form-drag coefficient due to the external flow inside the annular region is taken as $C_{Dp} = 1.1$, as in [109]. Also, the normal and tangential friction coefficients are assumed to be $C_N = C_T = 0.0125$, as in [8, 11]. In addition, the viscous damping coefficient, κ_u, is given a constant value for each mode j. This value is determined based on the average frequency of oscillations for

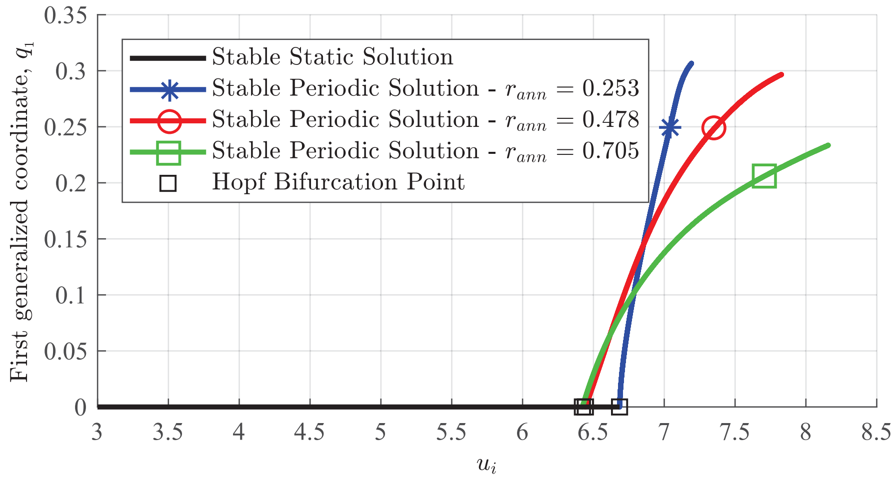

Figure 4–4: Bifurcation diagrams for Pipe 1 with different lengths of the annular region showing the first generalized coordinate, q_1, as a function of the dimensionless internal flow velocity, u_i.

each mode[1] over a specific range of interest of the internal flow velocity, u_i. Thus, the values of κ_u for six modes, i.e. $N = 6$, are $\kappa_{uj} = \{0.36, 0.81, 1.43, 2.02, 2.60, 3.18\}$ for Pipe 1 and $\kappa_{uj} = \{0.43, 0.99, 1.83, 2.61, 3.39, 4.16\}$ for Pipe 2.[2] The ODEs are solved by employing the pseudo-arclength continuation method using AUTO [113], which is adapted to conduct bifurcation analysis for differential equations, and also via the MATLAB ode15i solver (Mathworks, Inc.) for direct time-integration purposes.

4.2.1 Results for Pipe 1

Figure 4–4 shows bifurcation diagrams obtained via AUTO using a six-mode Galerkin approximation;[3] the first generalized coordinate, q_1, which is considered to be representative of the behaviour of the system, is plotted versus the dimensionless internal flow velocity, u_i.

[1] The frequency of oscillation for each mode is obtained by applying linear analysis for the problem at hand, solving the eigenvalue problem, and taking an average value, over a specific range of flow velocity, of the real part of the dimensionless eigenfrequency for each mode, $\mathcal{R}(\omega_i)$, where $i = 1 : N$.

[2] These values for κ_u were calculated for an annular region of 109 mm length; they were recalculated for the other lengths of the annulus.

[3] The number of modes was increased till convergence was achieved; the convergence criterion for the onset of instability and the amplitude of oscillations was set at 5%.

The figure shows the dynamical behaviour of Pipe 1 with different lengths of the annular region. For $r_{ann} = 0.253$, the pipe remains stable around the original equilibrium state for all $u_i < 6.69$. At $u_i \approx 6.69$, a Hopf bifurcation is predicted that leads to stable periodic oscillations around the origin, corresponding to flutter in the second mode of the pipe. The maximum value of q_1 is plotted in Fig. 4–4, and it increases with increasing flow velocity u_i. At $u_i > 7.19$, the model fails to converge to any stable solution, perhaps because the large amplitude of oscillation involved requires a finer model than one correct only one to third-order accuracy; however, at a value of u_i less than that, $u_i \approx 6.77$, the pipe is predicted to start hitting the annulus-forming tube, as shown in Fig. 4–5a, and this eventuality is not accounted for in the model. Increasing the length of the annular region destabilizes the system; i.e., it causes the flutter to occur at lower flow velocities, as shown in Fig. 4–4, and decreases the amplitude of oscillation at higher flow velocities, beyond the onset of flutter.

It is clear from Fig. 4–5 that the flutter predicted for this system is in the second mode of the pipe. The nonlinear dynamics of the pipe with different lengths of the annular region are examined right before the pipe starts hitting the outer rigid tube. Samples of time histories obtained using the MATLAB ODE solver are shown in Figs. 4–6, 4–7 and 4–8 for $r_{ann} = 0.253$, $r_{ann} = 0.478$ and $r_{ann} = 0.705$, respectively; these time histories are calculated at a point very close to the free end of the pipe; i.e. at $\xi = 0.97$. In addition, phase-plane, and power-spectral-density (PSD) plots calculated by direct fast Fourier transform (FFT) are shown in the same figures. All of these plots indicate regular periodic motions with one dominant frequency of oscillation; the other strong peaks that appear in the PSD plots, in Figs. 4–6c and 4–7c, correspond to the third and fifth harmonics of the main frequency.

The frequency of oscillation, f, is plotted against the dimensional internal flow velocity U_i in Fig. 4–9; it is seen that increasing the length of the annular region decreases the frequency of oscillation, as a result of the increase in the added mass; on the other hand, increasing the flow velocity increases the frequency of oscillation slightly.

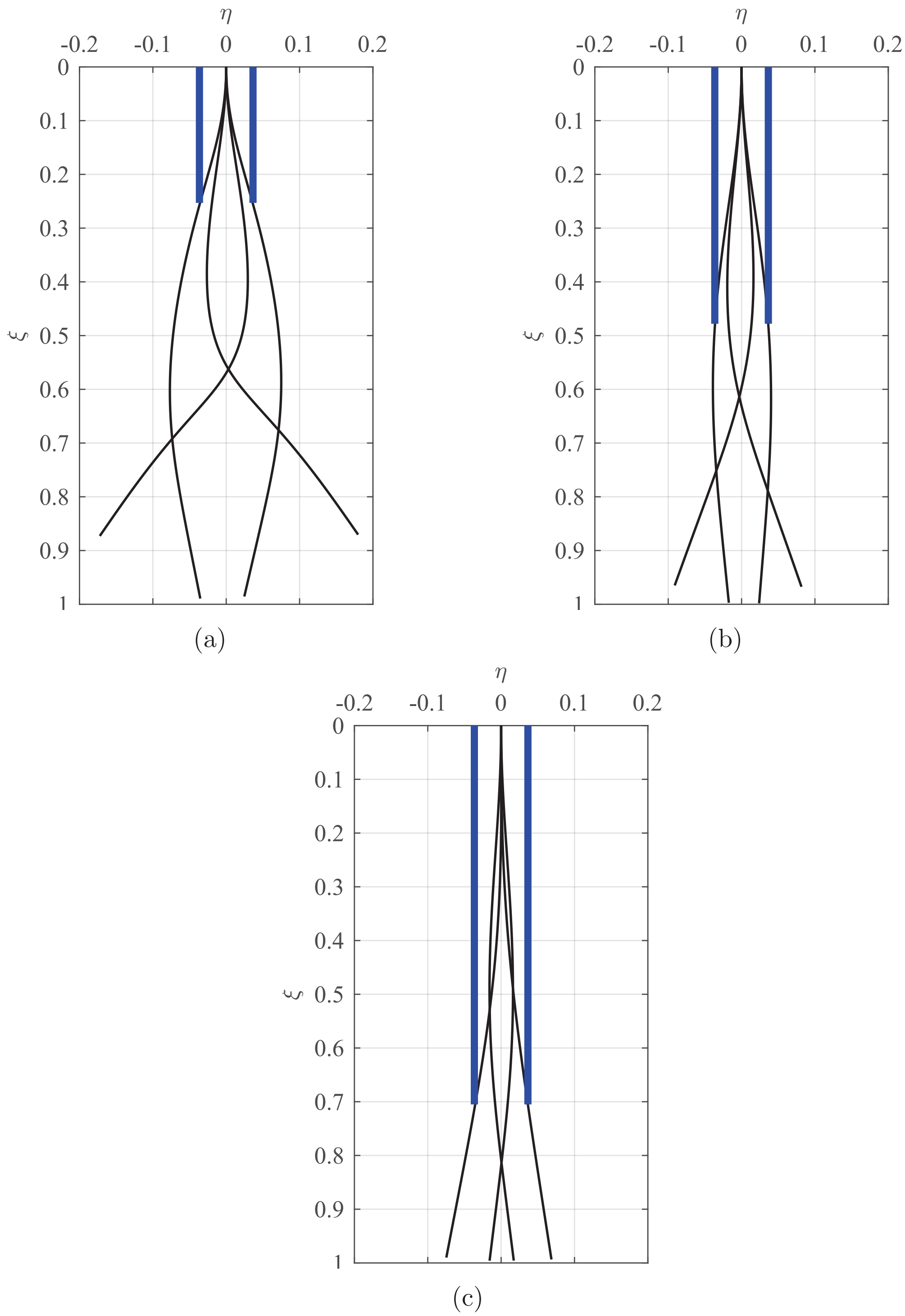

Figure 4–5: Shapes of the oscillating Pipe 1 just before impacting the annulus-forming tube for: (a) $r_{ann} = 0.253$ at $u_i = 6.77$, (b) $r_{ann} = 0.478$ at $u_i = 6.57$, and (c) $r_{ann} = 0.705$ at $u_i = 6.51$.

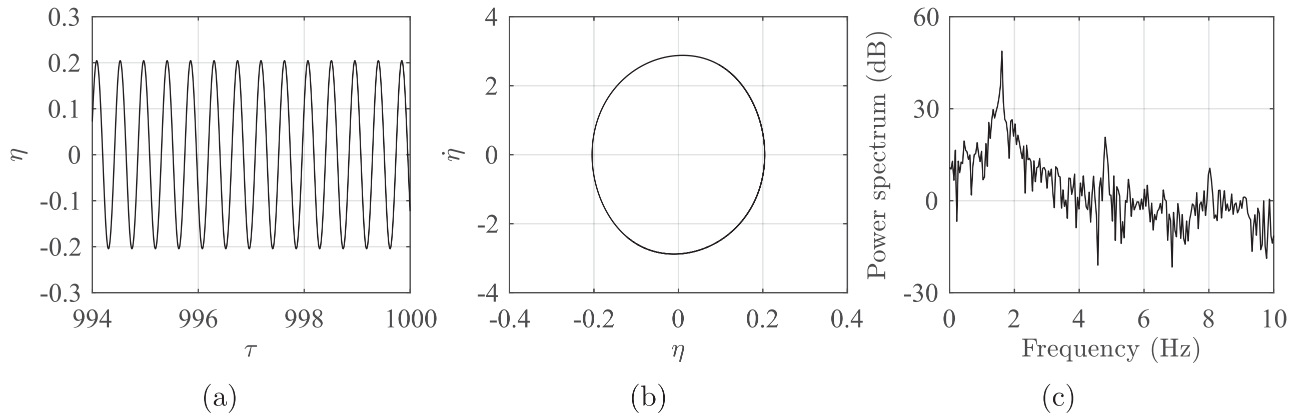

Figure 4–6: (a) Time history plot, (b) phase-plane plot, and (c) power spectral density plot of Pipe 1 at $u_i = 6.77$ for $r_{ann} = 0.253$.

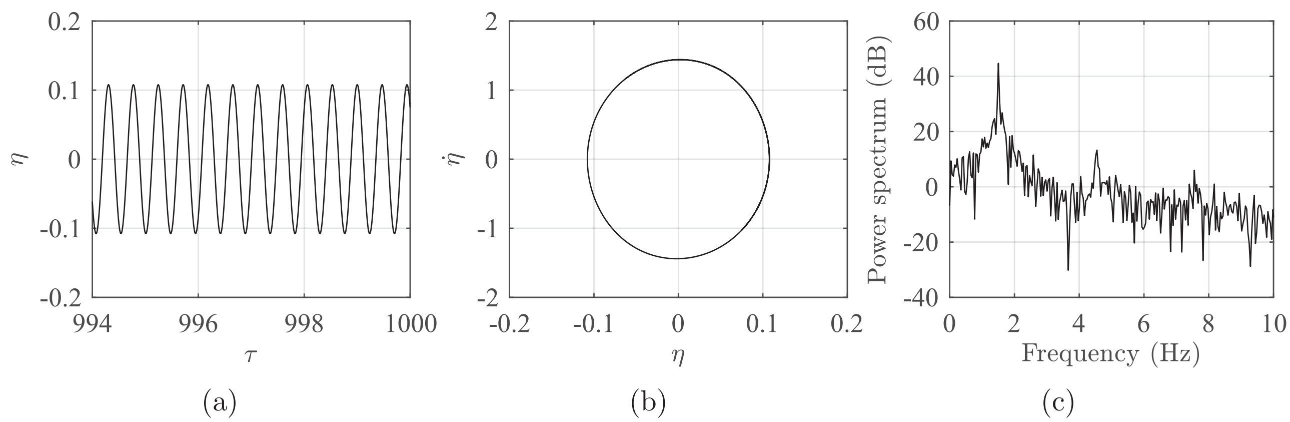

Figure 4–7: (a) Time history plot, (b) phase-plane plot, and (c) power spectral density plot of Pipe 1 at $u_i = 6.57$ for $r_{ann} = 0.478$.

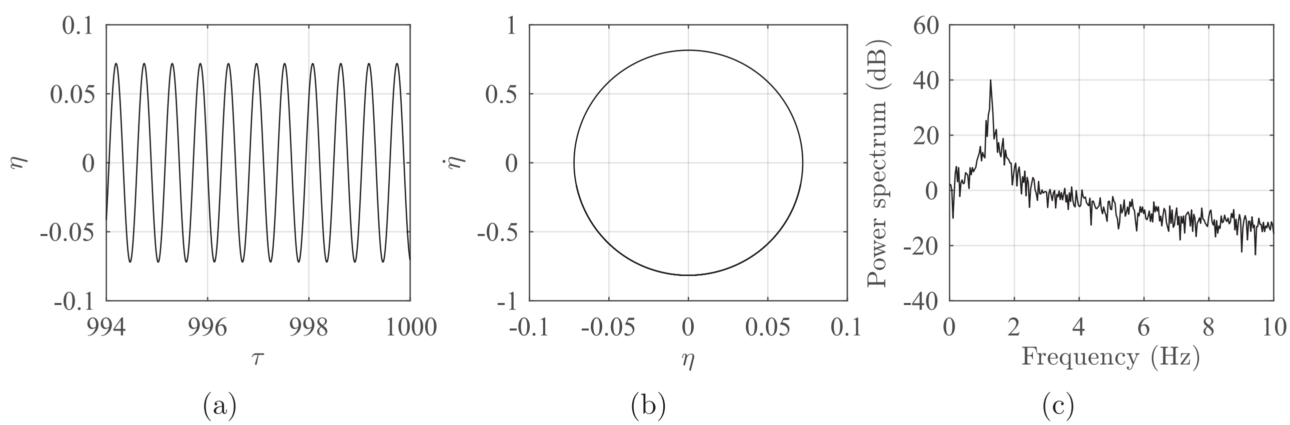

Figure 4–8: (a) Time history plot, (b) phase-plane plot, and (c) power spectral density plot of Pipe 1 at $u_i = 6.51$ for $r_{ann} = 0.705$.

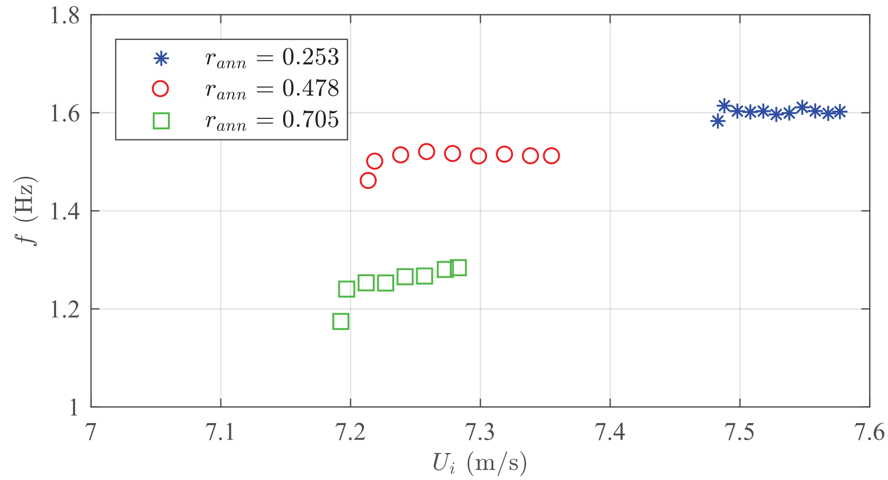

Figure 4–9: Frequency of oscillations, f, in Hz, for Pipe 1 as a function of the dimensional internal flow velocity, U_i in m/s.

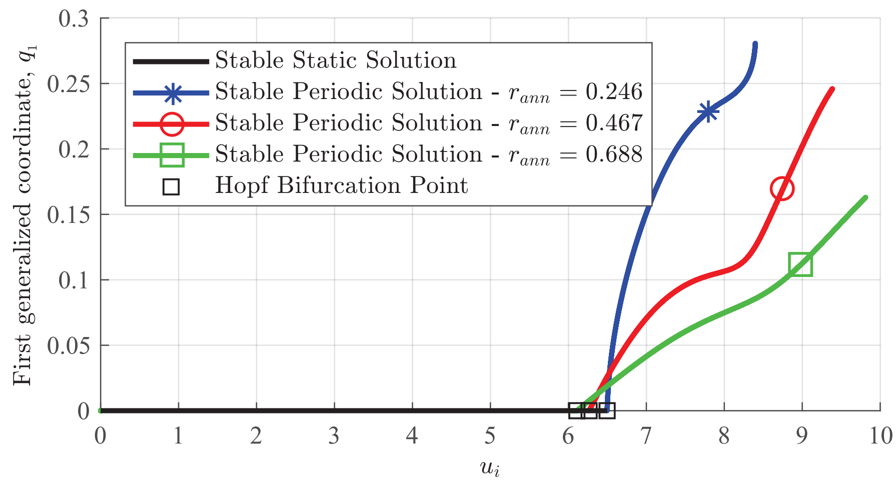

Figure 4–10: Bifurcation diagrams for Pipe 2 with different lengths of the annular region showing the first generalized coordinate, q_1, as a function of the dimensionless internal flow velocity, u_i.

4.2.2 Results for Pipe 2

The dynamical behaviour for Pipe 2 with increasing flow velocity is similar to that obtained for Pipe 1. In general, the pipe loses stability via flutter in the second mode with increasing internal flow velocity u_i. Bifurcation diagrams for the pipe with different values of r_{ann} are shown in Fig. 4–10. As concluded for Pipe 1, increasing the level of confinement by increasing the length of the annular region destabilizes the system and significantly decreases the amplitude of oscillation at high flow velocities. Furthermore, from Fig. 4–10, one can see that the amplitude of oscillation increases with increasing flow velocity, and the pipe starts to hit the outer tube at high enough flow velocities, as shown in Fig. 4–11. The nonlinear dynamic characteristics of the system at these flow velocities are illustrated in Figs. 4–12, 4–13 and 4–14 for a point located at $\xi = 0.98$; again, simple periodic motions are predicted with one dominant frequency of oscillation. This frequency is plotted versus u_i in Fig. 4–15. Interestingly, this time, the length of the annular region does not have significant influence on the frequency of oscillation at relatively high flow velocities; this may be due to the small outer diameter of Pipe 2 as compared to Pipe 1; hence the degree of confinement of the external flow is weak even for the longer annular regions. Nevertheless, increasing r_{ann} slightly decreases the frequency of oscillation. Moreover, increasing the flow velocity increases the frequency slightly, for flow velocities higher than the onset of instability.

4.3 Comparison between the results of the present model and other studies from the literature

4.3.1 Critical flow velocities, frequencies and amplitudes of flutter

The two sets of parameters used to solve the equation of motion were purposely chosen to allow comparison between the results obtained by this nonlinear model and experimental observations, as well as the theoretical predictions by Moditis et al. [11] for the bench-top-size system. It was observed experimentally and proved by a linear theoretical model [11] that both pipes lose stability at sufficiently high flow velocity via flutter in the second mode. The amplitude of oscillation recorded experimentally increases with increasing flow velocity, and eventually the pipes start hitting the rigid tube. These observations are in excellent qualitative agreement with the results of the present model.

The critical flow velocities for instability predicted by this model are summarized in Table 4–3, and they are compared to those reported in [11]. For Pipe 1, linear and nonlinear

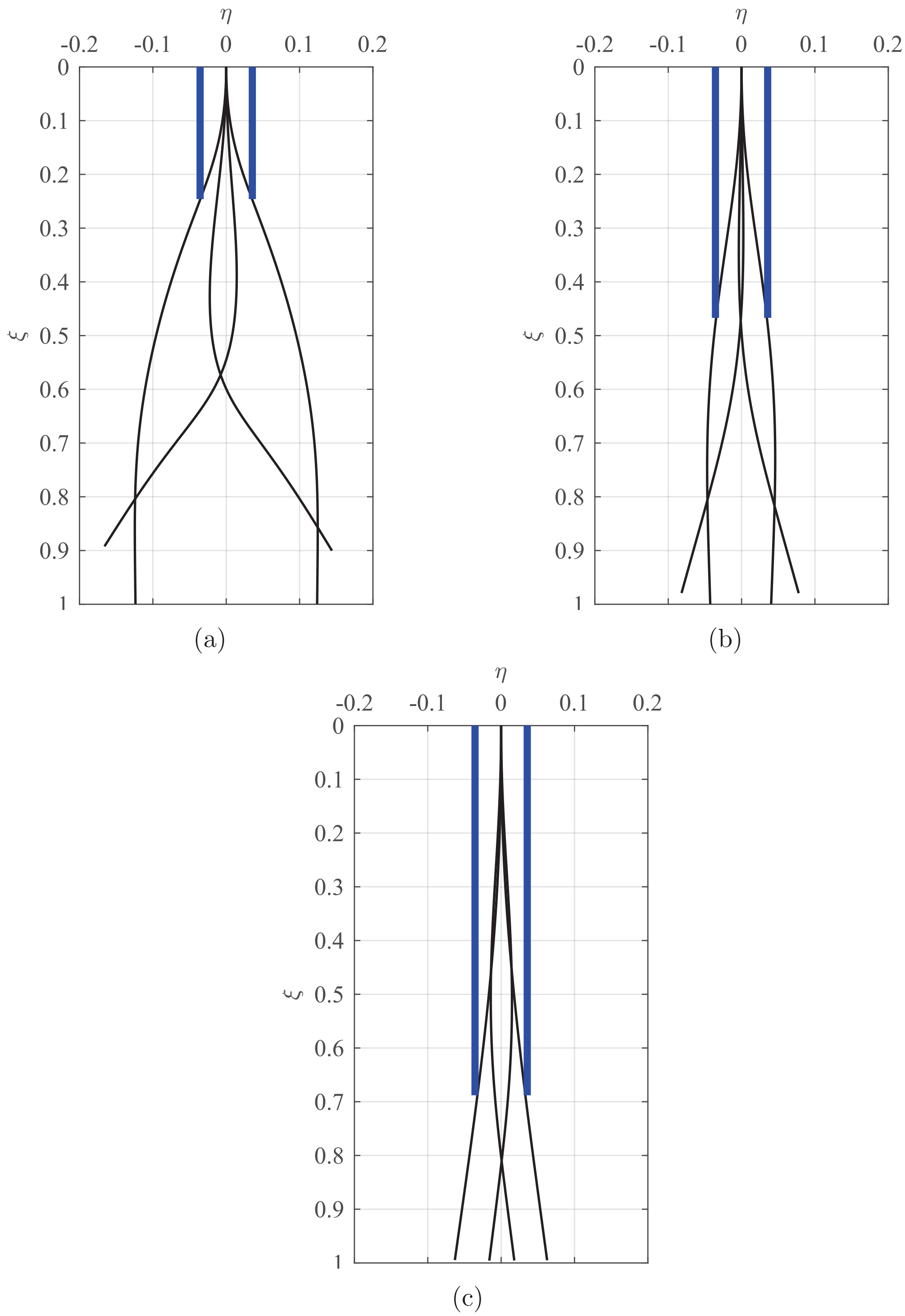

Figure 4–11: Shapes of oscillating Pipe 2 just before impacting the annulus-forming tube for: (a) $r_{ann} = 0.246$ at $u_i = 6.80$, (b) $r_{ann} = 0.467$ at $u_i = 6.71$, and (c) $r_{ann} = 0.688$ at $u_i = 6.74$.

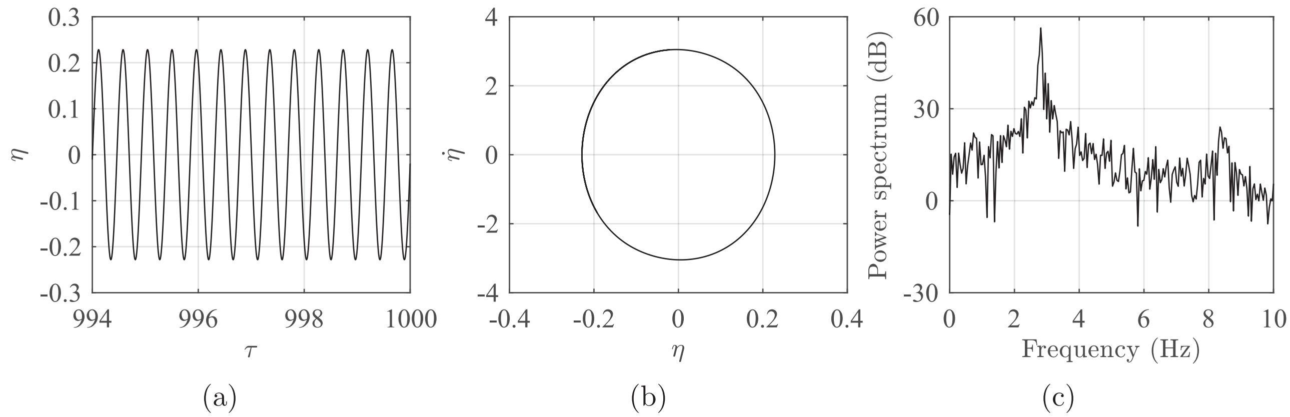

Figure 4–12: (a) Time history plot, (b) phase-plane plot, and (c) power spectral density plot of Pipe 2 at $u_i = 6.80$ for $r_{ann} = 0.246$.

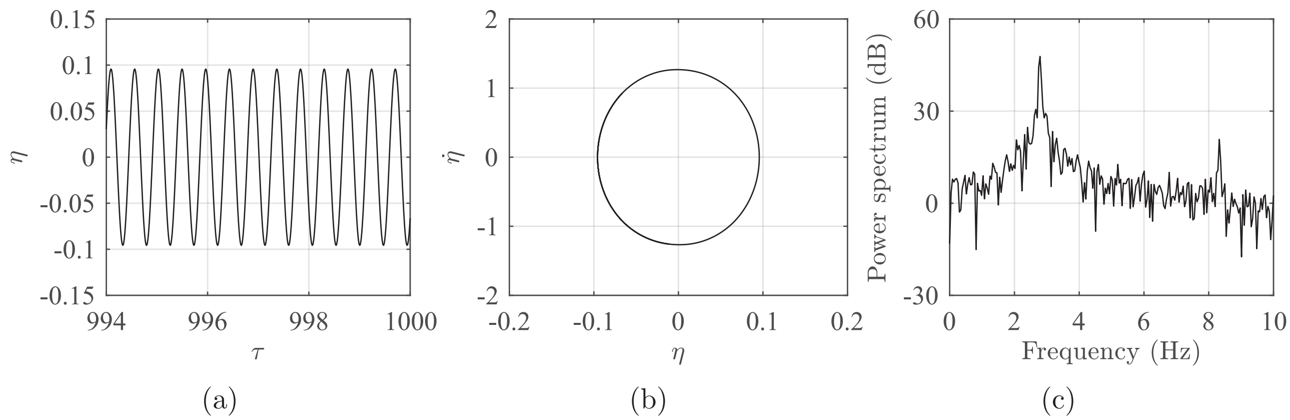

Figure 4–13: (a) Time history plot, (b) phase-plane plot, and (c) power spectral density plot of Pipe 2 at $u_i = 6.71$ for $r_{ann} = 0.467$.

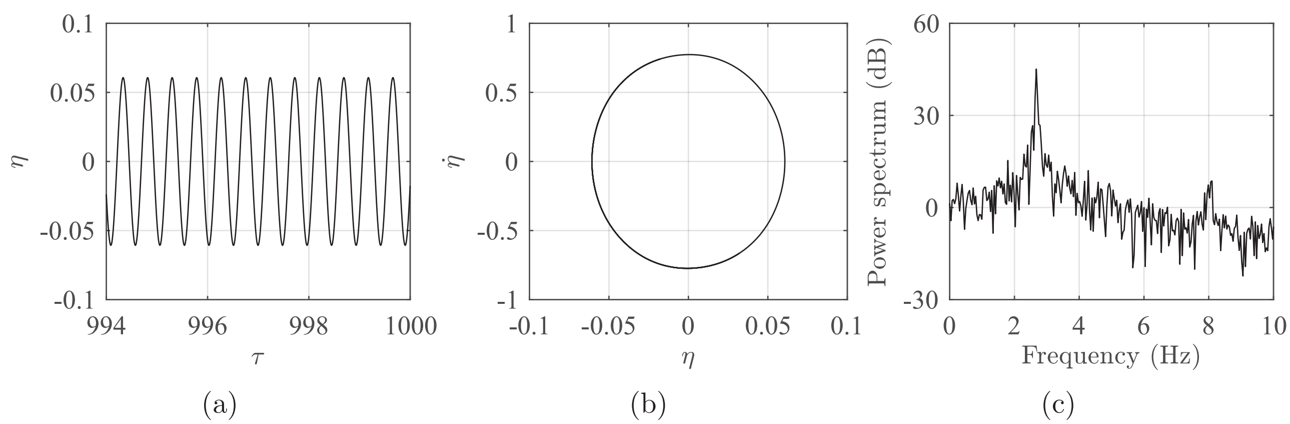

Figure 4–14: (a) Time history plot, (b) phase-plane plot, and (c) power spectral density plot of Pipe 2 at $u_i = 6.74$ for $r_{ann} = 0.688$.

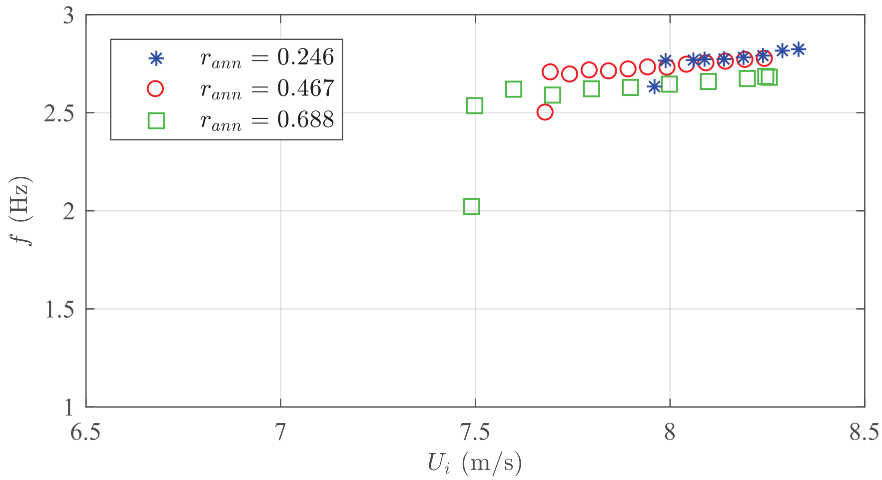

Figure 4–15: Frequency of oscillations, f, in Hz for Pipe 2 as a function of the dimensional internal flow velocity, U_i in m/s.

model predictions are quite similar;[4] both models overestimate the values of u_{if} with respect to the experimental values. In contrast, for Pipe 2, both linear theory and nonlinear theories predict the onset of instability with 3% maximum difference with respect to the experimental data.

Table 4–3: Comparison between the critical flow velocities for instability, u_{if}, for Pipes 1 and 2 with various lengths of the annular region obtained by different studies.

Pipe	r_{ann}	Linear theory [11]	Nonlinear theory	Experiments [11]
	0.253	6.69	6.69	5.12
1	0.478	6.47	6.44	5.29
	0.705	6.44	6.42	5.05
	0.246	6.44	6.49	6.29
2	0.467	6.27	6.27	6.16
	0.688	6.15	6.11	6.03

The nonlinear theory can also predict additional quantitative facets of the dynamical behaviour of the system as compared to the linear one, such as limit-cycle amplitudes and frequencies. Figures 4–16 and 4–17 show a comparison between the root-mean-square of

[4] It should be noted that the proposed model is identical to the one in [11] in the linear limit, except that in the present study the viscous damping coefficient is given a constant value for each mode. This most likely is the reason for the small discrepancies.

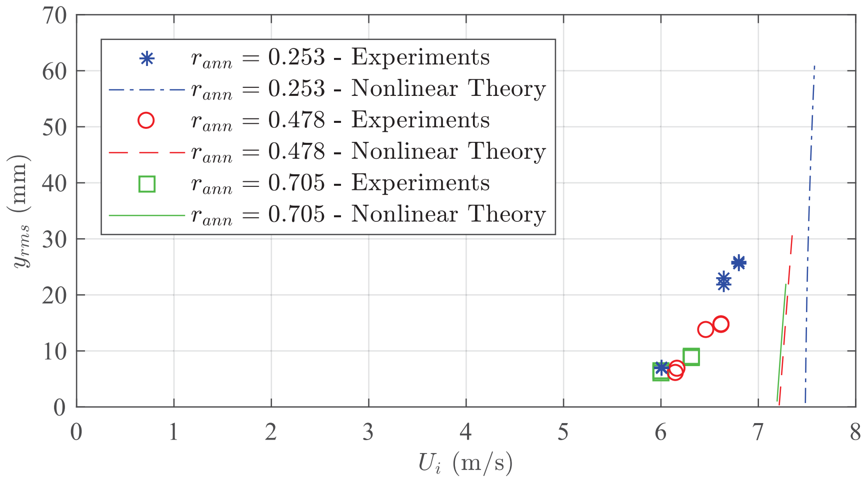

Figure 4–16: Rms amplitude of oscillation, y_{rms}, for Pipe 1, 11 mm above the free end, as a function of the dimensional internal flow velocity, U_i.

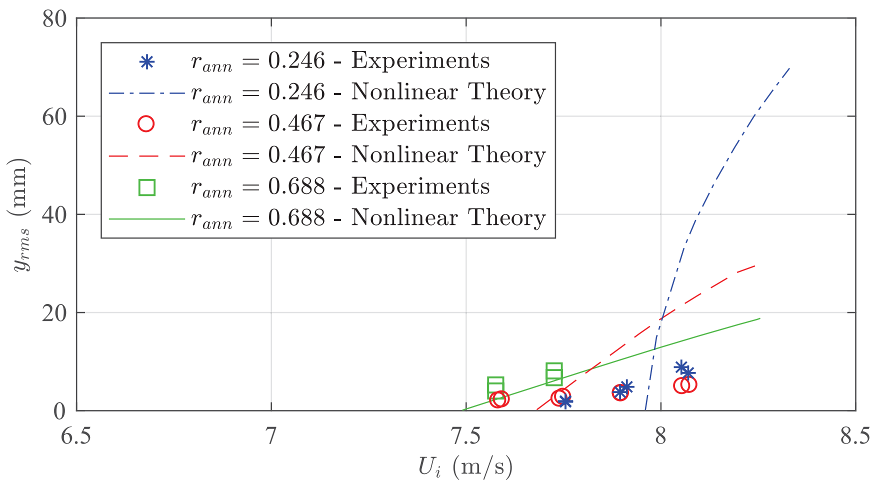

Figure 4–17: Rms amplitude of oscillation, y_{rms}, for Pipe 2, 11 mm above the free end, as a function of the dimensional internal flow velocity, U_i.

the amplitudes of oscillation with increasing flow velocity for Pipes 1 and 2, respectively, obtained by the present model and those recorded experimentally by Moditis [104], for the experiments reported in [11]. All the results presented hereafter are calculated for a point very close to the free end of the pipe (11 mm above the free end), at the same location as the experimental data. It can be seen in Fig. 4–16 that the model can predict the amplitude of oscillation for Pipe 1 within a small range of flow velocities beyond the onset of instability — see Fig. 4–18 as well — considering the fact that the model overestimates that onset. However, the model also overestimates the amplitude of oscillations right before the pipe

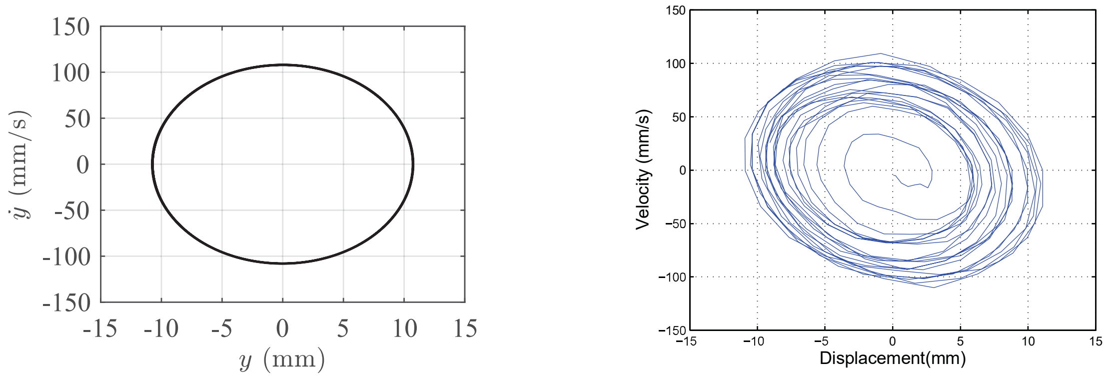

(a) (b)

Figure 4–18: Phase-plane plots for Pipe 1 with $r_{ann} = 0.253$, 11 mm above the free end, obtained by (a) the present nonlinear model at $U_i = 7.49$ m/s, and (b) experiments in [104] at $U_i = 6.00$ m/s.

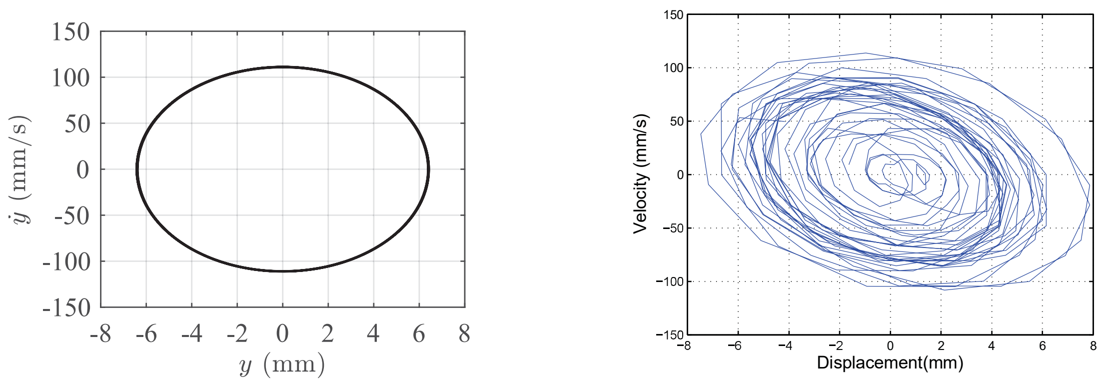

(a) (b)

Figure 4–19: Phase-plane plots for Pipe 2 with $r_{ann} = 0.246$, 11 mm above the free end, obtained by (a) the present nonlinear model at $U_i = 7.97$ m/s, and (b) experiments in [104] at $U_i = 7.89$ m/s.

starts hitting the outer rigid tube, which is the maximum limit set in the figure. This may be partly due to the third-order approximation of the model. The uncertainty in the values given to the friction and form-drag coefficients, as well as the approximation made for the damping model, could also have contributed to the discrepancy. Almost the same comments apply to Fig. 4–17 (Pipe 2); however, interestingly, the discrepancy between the amplitude of oscillation predicted theoretically and that recorded experimentally for the larger lengths of the annulus, in the case of Pipe 2, is significantly smaller.

Phase-plane plots obtained at flow velocities very close to the critical ones are compared to those acquired experimentally and reported in [104] for the two pipes in Figs. 4–18 and 4–19; the figures show almost identical displacement amplitudes and velocities. However, it is worth mentioning that the experimental time history [104] for Pipe 2 with $r_{ann} = 0.246$ displays an intermittent motion, which results in a more densely populated phase-plane plot in Fig. 4–19b than in Fig. 4–18b, making it more difficult to determine the limit cycle. The experiments in [104] were conducted using two cameras at 90° to each other. Almost identical phase-plane plots were reported for the front- and side-camera time histories, which suggests a planar motion with slowly rotating plane, as discussed in [11, 104]. This justifies the basic assumption made in the present model that motions are two-dimensional; nevertheless, it is recognized that to fully capture the motion a three-dimensional model is required.

The frequencies of oscillation obtained right after the initiation of limit-cycle oscillation are presented in Table 4–4 for the two pipes. The frequencies obtained by the present model are in excellent agreement with those observed experimentally, better than predictions by the linear theory, for both pipes and for the different lengths of the annular region.

Table 4–4: Comparison between the frequency of oscillations in Hz at the onset of flutter for Pipe 1 with various lengths of the annular region obtained by different studies.

Pipe	r_{ann}	Linear theory [11]	Nonlinear theory	Experiments [11]
	0.253	1.60	1.58	1.57
1	0.478	1.51	1.46	1.45
	0.705	1.22	1.17	1.13
	0.246	2.78	2.63	2.63
2	0.467	2.70	2.49	2.47
	0.688	2.58	2.02	2.03

4.3.2 Discussion on the effect of annulus length

We first consider the results obtained by both linear and nonlinear theory for Pipe 1 in Table 4–3, together with the modal shapes in Fig. 4–5. It is noticed that the three values of r_{ann} are roughly 0.25, 0.50 and 0.70, thus they are almost linearly related. The values of u_{if} in Table 4–3, on the other hand, decrease nonlinearly, with the increase from $r_{ann} \simeq 0.25$ to

$r_{ann} \simeq 0.50$ being much larger percentage-wise than that for $r_{ann} \simeq 0.50$ to $r_{ann} \simeq 0.70$.[5] Referring now to Fig. 4–5 it is noticed that the modal antinode for $r_{ann} \simeq 0.25$ is outside the annulus, while for $r_{ann} \simeq 0.50$ it is just inside the annulus, and more definitely inside for $r_{ann} \simeq 0.70$.[6] Since the antinode is associated with the maximum disturbance to the flow if it is in the confined space of the annulus, rather than outside, this may well result in the nonlinear effect for u_{if} discussed above.

The same applies to Pipe 2 (refer to Table 4–3 and Fig. 4–11), although the nonlinearity in this case is weaker. In this connection, however, it must be remembered that D_o for this pipe is smaller that for Pipe 1, and hence the annulus is relatively wider.

In any case, the effect of increasing the length of the annulus involves the balance of two opposing trends: (i) there is annular flow over a larger portion of the pipe, which is destabilizing, and (ii) there is increased added mass, which is stabilizing.

4.4 Influence of varying the tightness of the outer rigid tube

In this section the influence of varying the tightness of the annular region surrounding the pipe is investigated theoretically; there are no experimental data to compare with. The inner diameter of the outer rigid tube, D_{ch}, is varied resulting in different values of α_{ch}, and also χ and h. The other parameters of the system are kept constant to isolate the effect of the parameter of interest. The critical flow velocities, u_{if}, for each pipe with different r_{ann} and α_{ch} are listed in Table 4–5.[7] It may be concluded that increasing α_{ch} has a stabilizing effect on the system, leading to higher values of u_{if}; this is due to the decrease in the external

[5] Calculations for $r_{ann} = 0$ to $r_{ann} = 1$ confirm this nonlinear effect.

[6] It should be recalled that the modal shapes involve a travelling wave component, which makes these statements less than absolutely definite; the antinode travels along the pipe, as seen in Figs 4–5 and 4–11 (cf. Figs. 3.48 and 3.51 in [12] and Fig. 2.22 in [2]).

[7] The results shown in Table 4–5 are obtained using a linearized form of the model derived in the present study, utilizing a ten-mode Galerkin approximation. Hence, slight differences with respect to the predictions of the nonlinear model are seen in the table for the original systems, i.e. $\alpha_{ch} = 1.97$ for Pipe 1 and 3.31 for Pipe 2; however, the maximum difference is less than 3%.

flow velocity with increasing D_{ch}. Interestingly, decreasing α_{ch} not only decreases u_{if}, but it causes both pipes to undergo flutter in the first mode instead of the second, for $r_{ann} \approx 0.70$. The same mode of instability was predicted in [8, 121] for a pipe discharging fluid with an external flow that is confined over the whole length of the pipe (System II).

Table 4–5: The onset of instability, u_{if}, for Pipes 1 and 2 for different $\alpha_{ch} = D_{ch}/D_o$ and different lengths of the annular region, $r_{ann} = L'/L$. The asterisk denotes that the predicted flutter is in the first mode of the pipe.

Pipe	α_{ch}	$r_{ann} \approx 0.25$	$r_{ann} \approx 0.47$	$r_{ann} \approx 0.70$
	1.50	6.37	5.68	5.06*
1	1.97	6.65	6.47	6.46
	2.50	6.71	6.61	6.64
	1.50	5.30	3.78	3.27*
2	3.31	6.53	6.35	6.24
	5.00	6.58	6.49	6.45

Figures 4–20 and 4–21 show samples of the bifurcation diagrams obtained by the nonlinear model[8] for Pipes 1 and 2, respectively, with $r_{ann} \approx 0.47$ and using different values of α_{ch}. Increasing α_{ch} to higher values than the original ones (i.e. $\alpha_{ch} = 1.97$ for Pipe 1 and 3.31 for Pipe 2) does not affect the stability of the system as dramatically as compared to decreasing α_{ch}, especially for Pipe 2, for which the original value of α_{ch} is relatively higher. This effect is not unexpected, as the flow velocity in the annulus scales inversely as the square of the annular flow area.

4.5 Summary

In this chapter, a nonlinear equation of motion has been derived for a cantilevered pipe simultaneously subjected to internal and partially-confined external annular flows. The equation of motion is exact to third-order of magnitude, assuming the lateral and axial displacements to be of first- and second-order of magnitude, respectively. The extended

[8] In terms of the critical flow velocities for the two pipes with different r_{ann} and α_{ch}, the maximum difference between the predictions of the nonlinear model and the linearized one shown in Table 4–5 was again less than 3%.

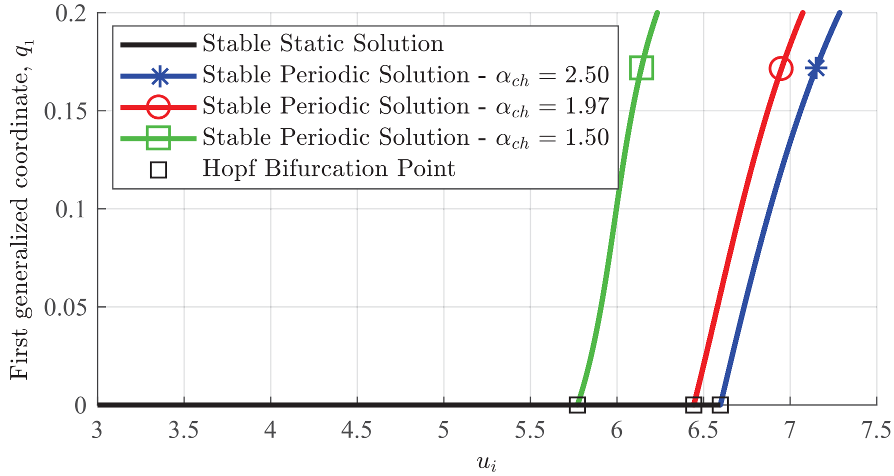

Figure 4–20: Bifurcation diagrams for Pipe 1 with $r_{ann} = 0.478$ obtained for different values of α_{ch}.

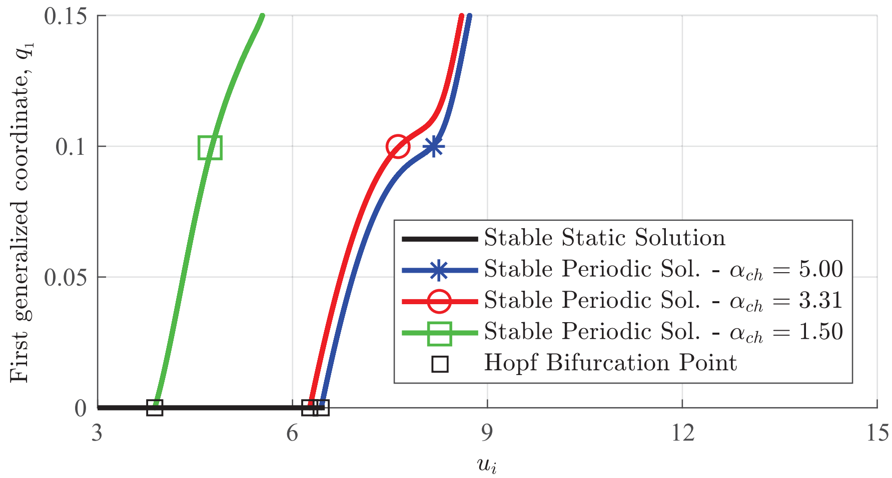

Figure 4–21: Bifurcation diagrams for Pipe 2 with $r_{ann} = 0.467$ obtained for different values of α_{ch}.

Hamilton's principle was used to obtain the equation of motion with a separate derivation of the fluid-related forces associated with the external flow, as well as the non-conservative forces due to the discharging fluid at the free end of the pipe. This equation is probably not the definitive nonlinear equation of motion for this system, since it was not obtained by a unified treatment of the fluid mechanics.

Two long flexible pipes of different dimensions and materials were considered in this study. The stability of these systems has been investigated with increasing internal flow velocity, which also results in increasing the external flow velocity in the annulus, as they are related to each other by continuity. The proposed nonlinear model predicts that the pipes lose stability via flutter in the second mode at sufficiently high flow velocity. The amplitude of the oscillations increases with increasing flow velocity and the pipes eventually hit the rigid tube forming the annulus. Quantitatively, the model overestimates the onset of instability for Pipe 1 with respect to experimental data available in the literature. However, excellent agreement with the experiments was found for Pipe 2, which is more slender and with a smaller wall-thickness as compared to Pipe 1. In addition, other aspects of the predicted dynamical behaviour were compared to the experimental observations; generally, the model can predict the frequency of oscillations right after the onset of instability accurately, but it overestimates the amplitude of the oscillations at higher flow velocities.

The influence of varying the length and tightness of the annular region was also investigated theoretically in this chapter. It was shown that increasing the length of the annulus decreases the critical flow velocity of instability for both pipes, and it decreases the predicted amplitude and frequency of oscillation at high flow velocities. Increasing the tightness of the annular region by decreasing the inner diameter of the outer rigid tube has a destabilizing effect and it can result in first-mode rather than second-mode flutter for sufficiently long annular regions.

Furthermore, it can be concluded that the performance of the present model is significantly better for higher lengths of confinement. Excellent agreement between the amplitude of oscillations obtained by this model and recorded experimentally was found for Pipe 2, when the external flow is confined over $\approx 70\%$ of the length of the pipe.

CHAPTER 5
Experimental and theoretical investigation into the influence of varying the ratio of the annular flow velocity to the inner one on the stability of System III

In this chapter, the influence of varying the ratio of the external flow velocity inside the annulus of System III to the internal one inside the pipe; i.e. $r = U_o/U_i$, is investigated experimentally and theoretically. Experiments on this flow configuration were conducted before by Jamin [122], followed by the experiments of Moditis [104] and Moditis et al. [11] that were discussed in Chapter 4. In those experiments the ratio of U_o/U_i was determined via continuity; i.e. the law of conservation of mass. Thus, based on the dimensions given in Table 4–1 for the inner and outer diameters of the pipes, D_i and D_o, as well as the inner diameter of the outer rigid tube, D_{ch}, the ratio $U_o/U_i \approx 0.05$ in [11,104]. Minas [123] was the first to conduct experiments for the same system, i.e. System III, in which the ratio of U_o/U_i was varied; this was done by using two pumps in her experimental set-up instead of one. One pump was used to control the volumetric flow rate in the pipe, Q_i, thus determining U_i, while the other was used to introduce additional flow into the test-section, Q_a. Hence, the outlet flow rate, Q_o, is determined by $Q_o = Q_i + Q_a$. Thus, the value of $r = U_o/U_i$ can be controlled by varying Q_a via the second pump. It was found in [123] that increasing the ratio of U_o/U_i destabilizes the system, resulting in lower values for the critical flow velocity of instability. However, no theoretical analysis was undertaken in parallel to these experimental observations.

New sets of experiments are presented in this thesis for ratios of $U_o/U_i = 0.055$, 0.2, 0.4, 0.6 and 0.8. A detailed description of the utilized apparatus and experimental procedure is provided in Section 5.1, followed by the experimental results and a discussion of these results in the same section. In Section 5.2, different linear theoretical models are developed

(a)

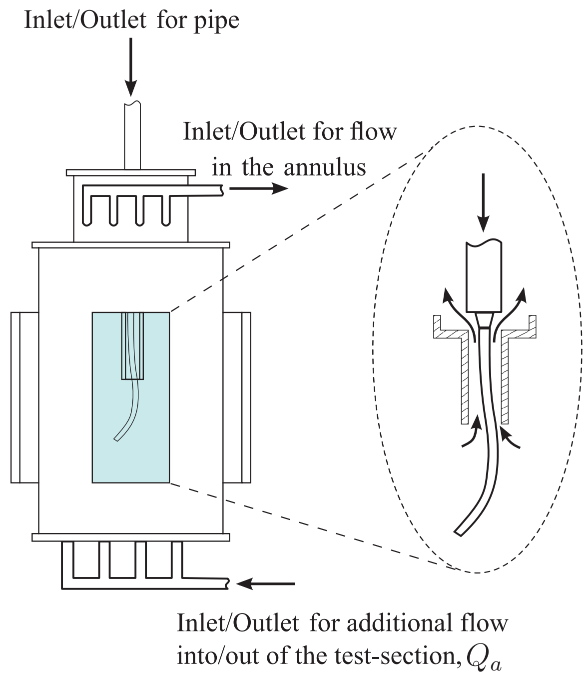

(b)

Figure 5–1: (a) The SMRI/PRCI apparatus. (b) Simplified schematic of the apparatus.

to investigate the stability of System III for varying U_o/U_i. A comparison between the experimental results and the predictions of the theoretical models is presented in Section 5.3.

5.1 Experimental investigation

Experiments were conducted in the Fluid-Structure Interactions Laboratory in the Department of Mechanical Engineering at McGill University using the SMRI/PRCI apparatus, built under contract with the Solution Mining Research Institute and Pipeline Research Council International. This apparatus, shown in Fig. 5–1a, was designed to simulate a brine-string and casing existing in salt-mined caverns that are used for hydrocarbon storage [122].

5.1.1 Experimental apparatus

The test-section consists of a stainless steel pressure vessel of approximately 0.11 m^3 volume and 0.48 m inner diameter. Four rectangular plexiglas windows are symmetrically located on the sides of the vessel, which allow viewing and access to the test chamber. The maximum attainable flow rate is limited by the pressure that the vessel can sustain without significant leakage, namely to 205 kPa (40 psi). Also, two manual bleed ports are installed to enable de-aeration of the system.

The fluid used in the experiments is water and it is stored in a tank beside the apparatus. Two 2.2 kW (3 HP) electric centrifugal pumps are used to draw water from the bottom of the water-holding tank. One of the pumps is responsible for providing flow in the flexible pipe, and the other is used to convey additional flow to the test-section from the bottom, when higher ratios of U_o/U_i are sought, as shown in Fig. 5–1b. The pumps can be set manually and they are controlled by dedicated digital controllers.

The test specimen is a flexible pipe made of Silastic RTV, which is a castable two-part silicone-rubber mixture that has been widely used for years by Païdoussis et al. in their research. The dimensions and material properties of this pipe are listed in Table 5–1. A rigid plexiglas tube of larger diameter than the pipe, $D_{ch} = 31.5$ mm, and 206.5 mm length is used to form the annular region surrounding the pipe at its upper portion. The reason for making D_{ch} almost double of D_o is entirely due to practical considerations, so that the pipe can undergo oscillatory motions without hitting the surrounding tube, at the threshold of flutter and for a range of U_i beyond.

Table 5–1: Properties of the flexible pipe used in the experiments.

Material	D_i (mm)	D_o (mm)	L (mm)	EI (N m^2)	m (kg m^{-1})
Silicone-rubber	6.35	16	441	7.37 $\times 10^{-3}$	0.191

5.1.2 Data acquisition

Two magnetic flow-meters with integrated display were used to determine the flow rates associated with the two pumps, thus determining the inlet flow rate, Q_i, and the additional one, Q_a. Based on continuity, the outlet flow rate can be written as $Q_o = Q_i + Q_a$, and hence the ratio of U_o/U_i can be calculated as

$$\frac{U_o}{U_i} = \frac{A_i}{A_{ch}}\left(1 + \frac{Q_a}{Q_i}\right), \tag{5.1}$$

where A_i is the inner cross-sectional area of the pipe and $A_{ch} = (\pi/4)(D_{ch}^2 - D_o^2)$. The magnetic flow-meters used in these experiments have a resolution of 0.001 Lt/s.

To ensure the integrity of the pressure vessel, i.e. to avoid leaks, the mean pressure in the test-section was monitored all the time; it was measured via a conventional Bourdon tube gauge. The gauge was installed on the bleed line to obtain reliable pressure readings.

The motion of a point near the free end of the flexible pipe; i.e. approximately at 18 mm above the free end, was captured using a dual-camera system. Two FLIR Grasshopper3 2.3 MP cameras (Sony Pregius IMX174) were used, set at 90^o to each other and placed at equal height and distance from two windows of the pressure vessel. This allowed to capture the three-dimensional motion of the pipe. The settings of the cameras were adjusted to capture 64 frames per second (fps) with a 5 ms shutter to minimize motion blur. The cameras were triggered simultaneously via a function generator to guarantee synchronization of the recorded motions from the two sides. The cameras were focused on the lowest 36 mm of the flexible pipe, which were marked in red to facilitate post-processing of the recorded videos.

5.1.3 Experimental protocol

The experiments were conducted as follows:

1. The flexible pipe and the outer rigid tube were installed vertically in the test-section.
2. Each of the two magnetic flow-meters was installed between the corresponding pump and the test-section.
3. The water-holding tank was filled with water, and then the pumps were turned on to fill the pressure vessel. The system was left running for a length of time, while bleeding all air from the test-section.
4. For each ratio of U_o/U_i, the internal flow velocity was increased step-wise by controlling the first pump; i.e. the one responsible for Q_i. After setting the flow velocity, the ratio of U_o/U_i was adjusted via the second pump that controls Q_a. It is worth mentioning that adjusting one pump influences the flow rate of the other one, and thus both pumps need to be repeatedly adjusted until the required values of Q_i and Q_a were reached.

5. At each flow velocity step, the system was kept running long enough to achieve steady state, then 300 seconds of the motion of the marked portion of the pipe were recorded using the dual-camera system.
6. Experiments were repeated three times for each ratio of U_o/U_i, to ensure consistency and validity of results.

5.1.4 Data analysis

The recorded videos were loaded into Matlab (Mathworks, Inc.) for processing. A script was written to determine the location of the centroid of the red band on the pipe detected in each processed frame. The pixel locations were used to calculate the displacements making use of the known width of the red band; i.e. the outer diameter of the pipe, as a reference. The displacement time series were smoothed using a polynomial spline, and used afterwards for further processing, such as to plot the phase portraits and power spectral densities, in order to identify the nature of the observed motions.

5.1.5 Experimental results

Results for a ratio of $U_o/U_i = 0.055$

For this particular ratio, only the first pump was turned on, and the internal flow velocity was increased by increasing the gain of this pump.

At low internal flow velocity, the pipe remained stable around its original undeformed position with almost no motion. Very weak oscillations started to be visually observable at $U_i \approx 2$ m/s. The amplitude of these oscillations increased with increasing U_i, reaching a maximum value of around 3 mm at $U_i = 4$ m/s, yet no dominant frequency could be determined, and thus these oscillations may be associated with accentuation of pipe imperfections and excitation by flow turbulence. The oscillations looked significantly stronger at $U_i \approx 5.68$ m/s with a frequency $f \approx 1.37$ Hz, and the pipe exhibited flutter in the second mode. Increasing the flow velocity further resulted in much higher amplitudes of oscillation and the pipe eventually hit the rigid tube which forms the annular region.

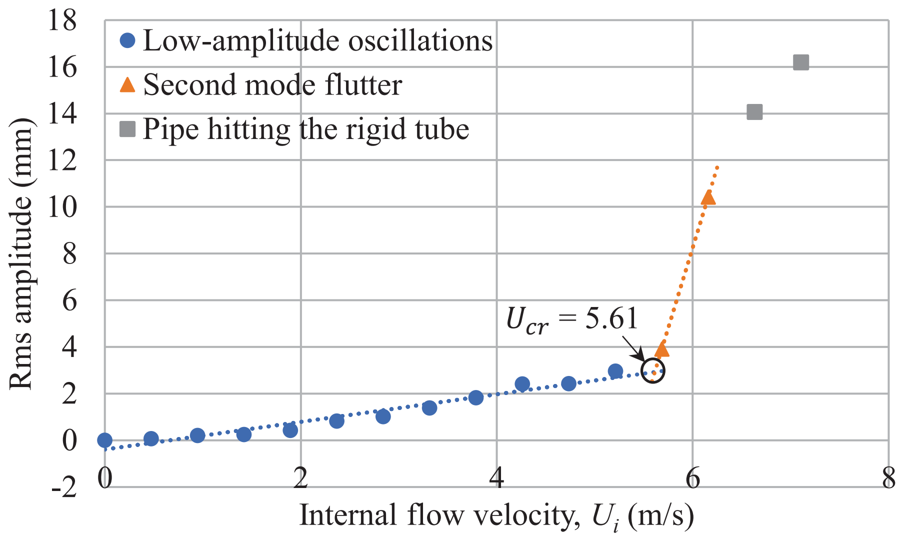

Figure 5–2: Bifurcation diagram showing the experimental rms amplitude of oscillation as a function of the internal flow velocity for $U_o/U_i = 0.055$.

For the sake of validation, one can compare these results to those reported in [11, 104] for Pipe 1 with $r_{ann} = 0.478$, which has system parameters close to the ones under study. The critical flow velocity and frequency of oscillation observed here, i.e. $U_{cr} = 5.61$ m/s and $f_{cr} = 1.36$ Hz, are not too far from those in [11, 104] nor from those in [123] for a similar system, as shown in Table 5–2.

Table 5–2: Critical flow velocity for flutter, U_{cr}, in m/s and the corresponding frequency of oscillation, f_{cr}, in Hz obtained by different studies for $U_o/U_i \approx 0.05$.

	Present experiments	Experiments in [11, 104]	Experiments in [123]
U_{cr} (m/s)	5.61	5.92	5.00
f_{cr} (Hz)	1.36	1.45	1.60

The root mean square (rms) of the amplitude of oscillation is plotted versus the internal flow velocity and the critical flow velocity for instability is determined once a significant increase in the slope is detected, as shown in Fig. 5–2.

At $U_i \approx 6.16$ m/s, samples of the time history captured by the front and side cameras for a point near the free end of the pipe are shown in Fig. 5–3. In addition, a sample of the trajectory of the same point is plotted in Fig. 5–4 showing the three-dimensional nature and unsteadiness of the observed motion. An average power spectral density (PSD) was

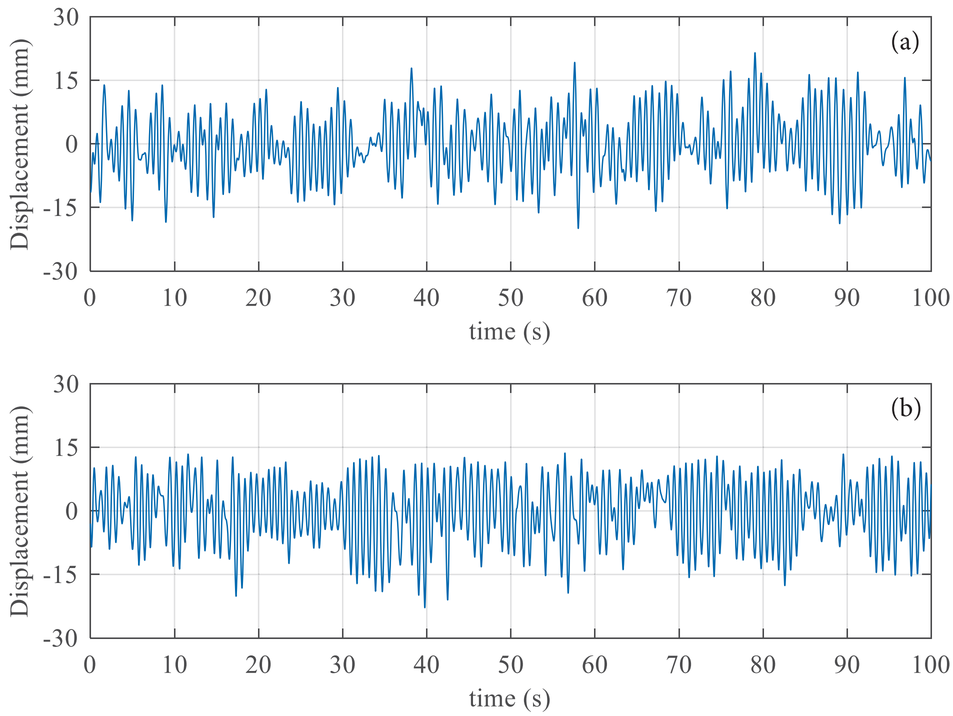

Figure 5–3: Samples of the time series recorded by (a) front camera, (b) side camera, at $U_i = 6.16$ m/s for $U_o/U_i = 0.055$.

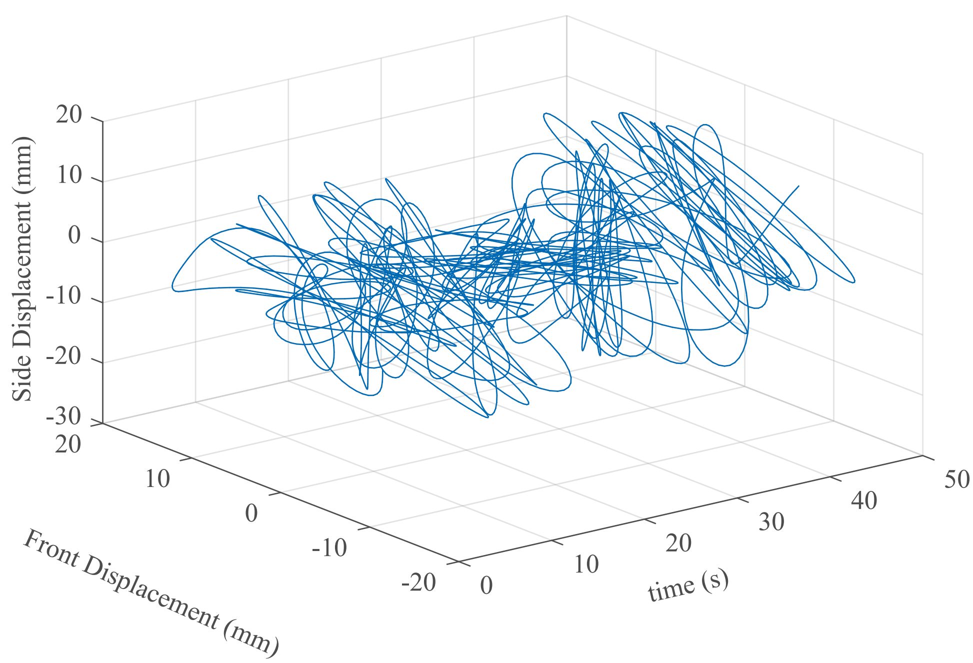

Figure 5–4: Sample of the trajectory of a point near the free end of the pipe, at $U_i = 6.16$ m/s for $U_o/U_i = 0.055$.

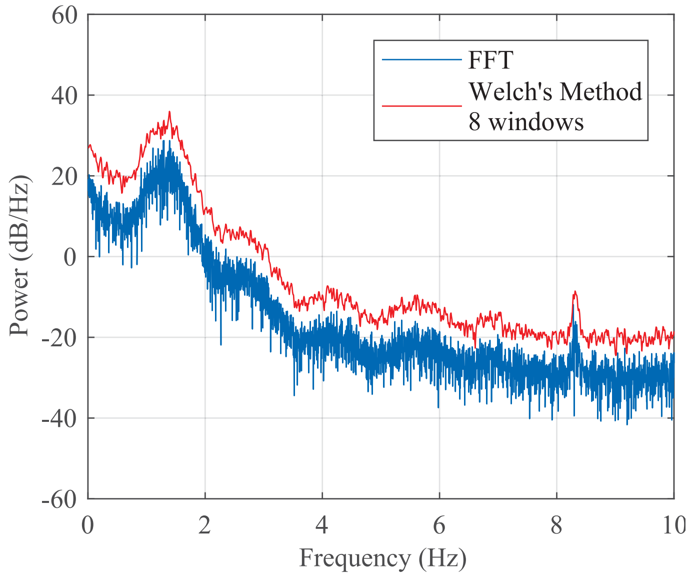

Figure 5–5: Power spectral density plot for the observed motion at $U_i = 6.16$ m/s for $U_o/U_i = 0.055$.

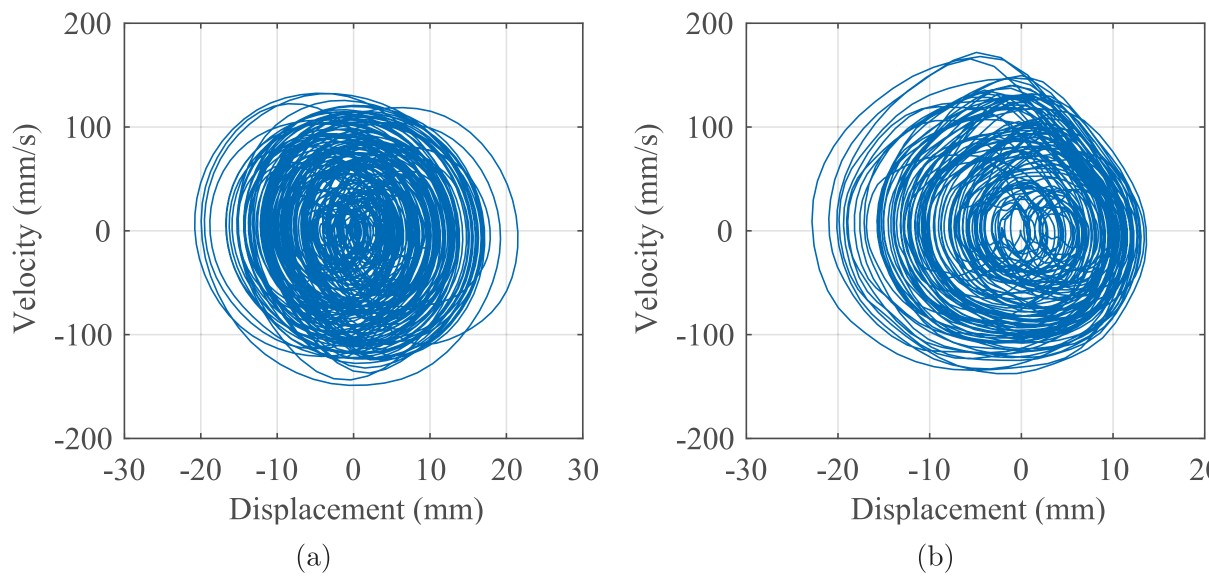

Figure 5–6: (a) Front phase-plane plot, and (b) side phase-plane plot for $U_i = 6.16$ m/s and $U_o/U_i = 0.055$.

calculated based on the front and side time series via direct fast Fourier transform (FFT) and Welch's method with eight windows; the PSD plot is presented in Fig. 5–5 indicating one dominant frequency of oscillation around 1.39 Hz. The other smaller peaks existing in Fig. 5–5 correspond to harmonics, and they became stronger with increasing flow velocity

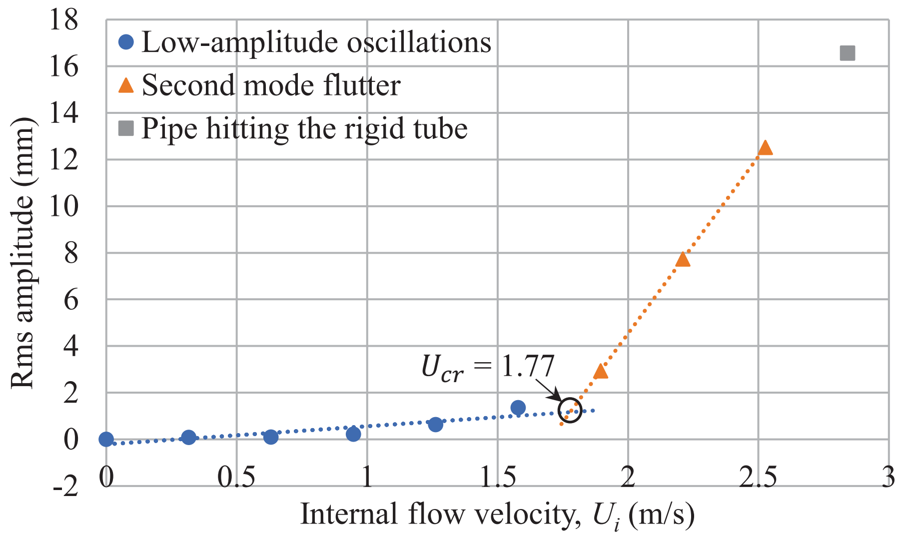

Figure 5–7: Bifurcation diagram showing the experimental rms amplitude of oscillation as a function of the internal flow velocity for $U_o/U_i = 0.2$.

due to impacting with the outer rigid tube. Moreover, phase-plane plots for time-series obtained via the front and side cameras are shown in Figs. 5–6a and 5–6b, respectively; they reveal a periodic three-dimensional motion; however, since the motion seems intermittent in Fig. 5–3, the phase-plane plots fill the space, all the way to the origin, making it difficult to determine a limit cycle.

Almost the same remarks on the dynamical behaviour were reported in [104]; the front and side phase-plane plots for Pipe 1 with $r_{ann} = 0.478$ shown in [104] look quite similar to those presented here.

Results for a ratio of $U_o/U_i = 0.2$

Starting with a ratio of $U_o/U_i = 0.2$, and for higher ones, the second pump, supplying Q_a, was turned on. For each flow velocity step in U_i, the second pump was adjusted to maintain a ratio of $U_o/U_i = 0.2$ all the time.

With increasing U_i, weak oscillations started to develop at $U_i \approx 1.6$ m/s. However, increasing the flow velocity slightly, to $U_i \approx 1.9$ m/s, led to stronger oscillations of the pipe, which also tended to move towards one side of the rigid tube. This could be attributed to the velocity of the annular flow being higher as compared to the case when $U_o/U_i = 0.055$,

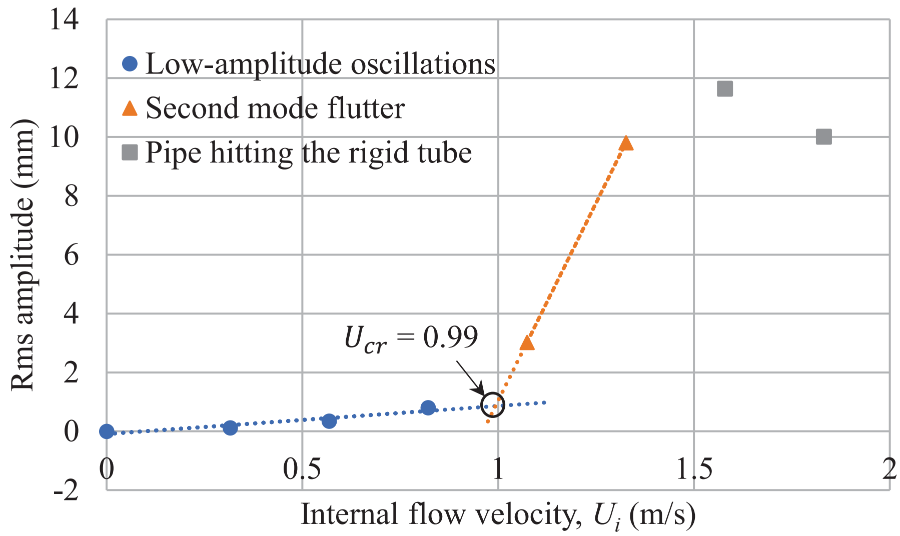

Figure 5–8: Bifurcation diagram showing the experimental rms amplitude of oscillation as a function of the internal flow velocity for $U_o/U_i = 0.4$.

and the pipe not being perfectly concentric with the outer rigid tube. The pipe developed flutter in the second mode at $U_i \approx 2.2$ m/s; while oscillating, it stuck to one side of the rigid tube from time to time. Increasing the flow velocity further, for $U_i > 2.5$ m/s, resulted in the pipe hitting the rigid tube often.

Figure 5–7 shows a bifurcation diagram for the rms amplitude of oscillation versus the internal flow velocity U_i. As seen in the figure, the velocity at which a sudden increase in the slope is observed, i.e. the onset of instability, is $U_{cr} = 1.77$ m/s. The frequency of the recorded motion right after U_{cr} was $f_{cr} = 2.09$ Hz.

The value of U_{cr} determined in the present study is again comparable to the one reported in [123]: $U_{cr} = 1.54$ m/s, for the same ratio of U_o/U_i.

Results for a ratio of $U_o/U_i = 0.4$

For this ratio, the dynamical behaviour observed for the system with increasing flow velocity is qualitatively similar to that for $U_o/U_i = 0.2$; the pipe remained stable with very small motions for $U_i < 0.8$ m/s. At $U_i \approx 1.0$ m/s, oscillations started to develop, and the pipe suffered from the same inclination towards one side of the rigid tube, while oscillating. At $U_i \approx 1.3$ m/s, the pipe clearly showed flutter in the second mode with higher frequency

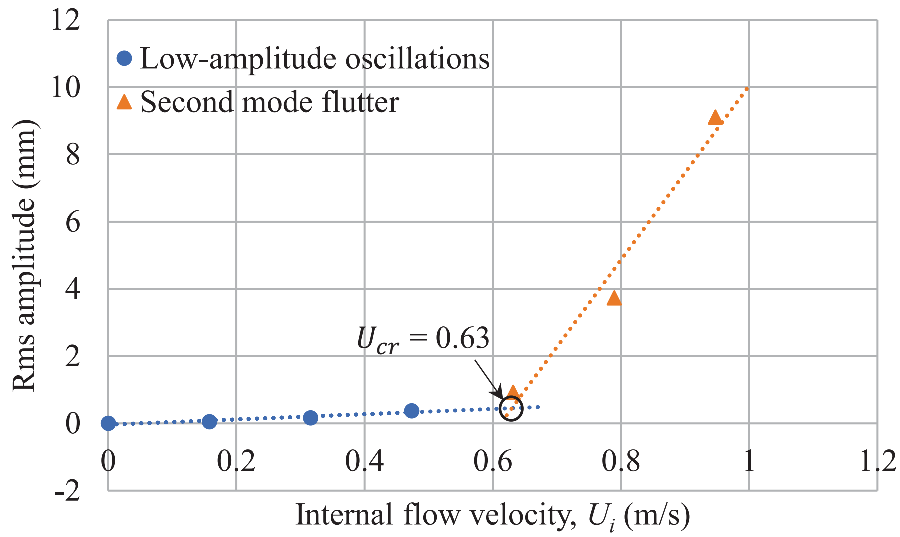

Figure 5–9: Bifurcation diagram showing the experimental rms amplitude of oscillation as a function of the internal flow velocity for $U_o/U_i = 0.6$.

as compared to the previous flow-velocity ratios, $f = 2.78$ Hz. Increasing the flow velocity further resulted in high-amplitude oscillations, with the pipe hitting the outer rigid tube.

The critical flow velocity for instability for this flow-velocity ratio, i.e. $U_o/U_i = 0.4$, was found to be $U_{cr} = 0.99$ m/s, as shown in Fig. 5–8, and the critical frequency of oscillation was $f_{cr} = 2.69$ Hz. This value of U_{cr} is in an excellent agreement with the value observed earlier by Minas [123]: $U_{cr} = 1.01$ m/s for $U_o/U_i = 0.4$.

Results for a ratio of $U_o/U_i = 0.6$

For a ratio of $U_o/U_i = 0.6$, the dynamics of the pipe was quite similar to that described earlier for smaller U_o/U_i. However, the critical flow velocity for instability continued to decrease with increasing U_o/U_i. This time the oscillations started to be observable by the naked eye at $U_i \approx 0.63$. The pipe exhibited flutter in the second mode with critical frequency of oscillation, $f_{cr} = 2.55$ Hz.

Fig. 5–9 shows the rms amplitude of the observed oscillations as a function of U_i; the onset of instability occurred at $U_{cr} = 0.63$. Increasing the flow velocity further resulted in oscillations of higher amplitude, but the motion became strongly irregular, with the pipe hitting the rigid tube.

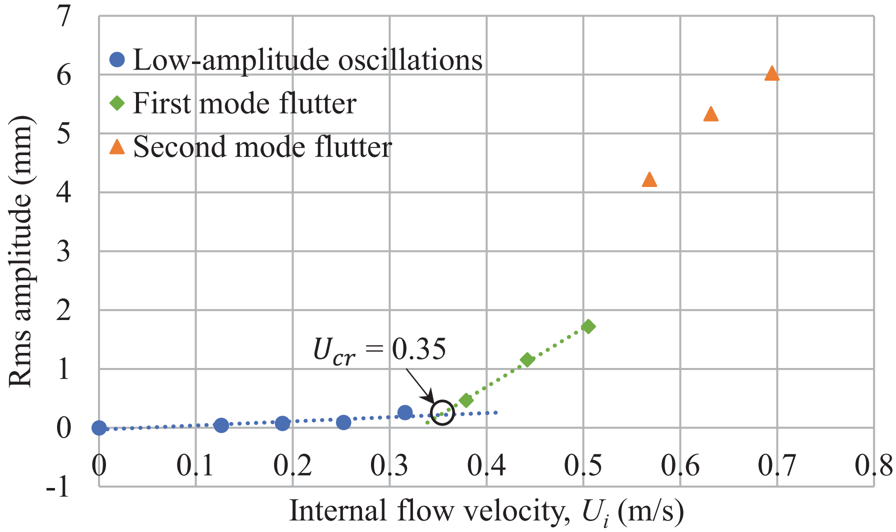

Figure 5–10: Bifurcation diagram showing the experimental rms amplitude of oscillation as a function of the internal flow velocity for $U_o/U_i = 0.8$.

Results for a ratio of $U_o/U_i = 0.8$

This is the highest value of U_o/U_i considered in the present study. The system exhibited weak oscillations at very low flow velocity, $U_i < 0.3$ m/s. The motion observed was quite irregular with increasing flow velocity; however, first-mode flutter-like oscillations were recorded at $U_i = 0.38$ m/s. The amplitude of these oscillations increased almost linearly with increasing U_i. At $U_i = 0.57$ m/s, a sudden jump in the amplitude of oscillation was observed; the oscillations became much stronger, with higher frequency, and with the pipe performing second mode flutter. The amplitude of oscillation kept increasing with further increase in U_i; however, the motion became more and more irregular and the pipe started hitting the outer rigid tube.

Figure 5–10 shows the onset of instability for the first mode flutter observed at $U_{cr,1} = 0.35$ m/s. The critical frequency of oscillation at $U_i = 0.37$ can be determined from the PSD plot in Fig. 5–11: $f_{cr,1} = 0.35$ Hz. The sudden jump in the rms amplitude of oscillation occurred at $U_i = 0.57$ m/s, which can be considered as the onset of second mode flutter, $U_{cr,2}$. The frequency at $U_i = 0.57$ m/s, increased to $f_{cr,2} = 2.26$ Hz, as shown in Fig. 5–12.

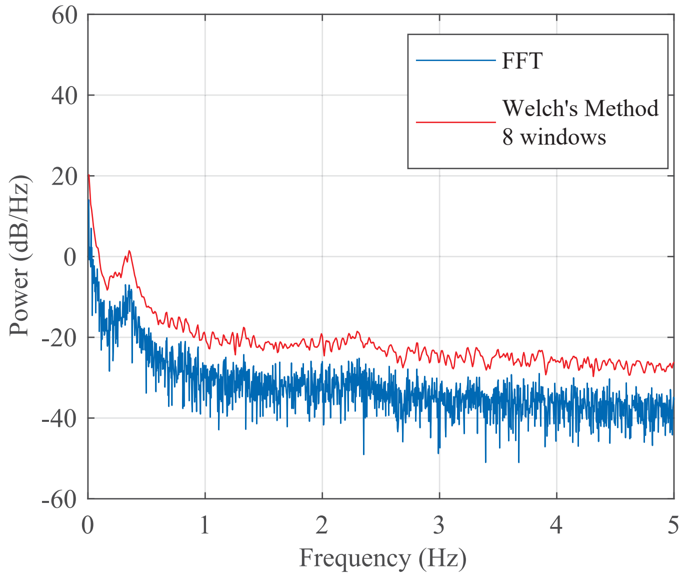

Figure 5–11: Power spectral density plot for the observed motion at $U_i = 0.38$ m/s for $U_o/U_i = 0.8$.

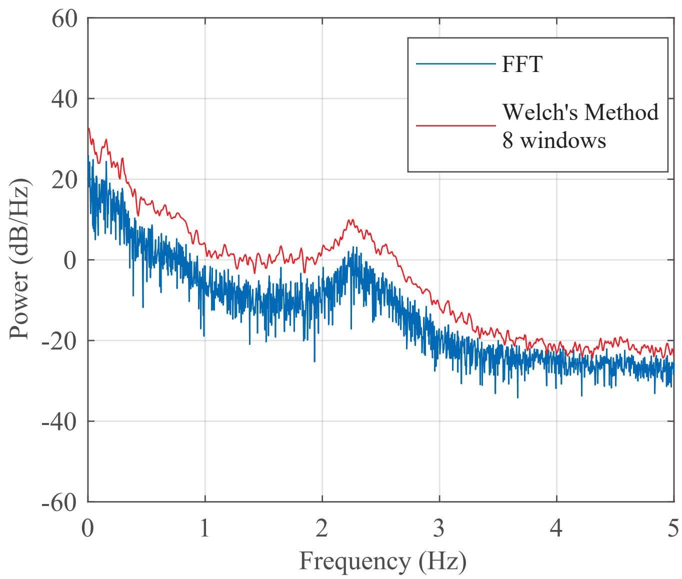

Figure 5–12: Power spectral density plot for the observed motion at $U_i = 0.57$ m/s for $U_o/U_i = 0.8$.

The ratio between the frequency of the observed first-mode flutter to the second-mode one is $f_{cr,2}/f_{cr,1} \approx 6.4$, as typically expected for a cantilevered beam.

The onset of the first instability observed in this experiment is almost 60% higher than what was observed in Minas' experiments [123], in which $U_{cr} = 0.22$ m/s for $U_o/U_i = 0.8$.

5.2 Theoretical investigation

In this section, linear models are derived for the dynamics of System III. Earlier, Moditis et al. [11] derived a theoretical model for this system, in which the Heaviside step function was utilized to model the discontinuity in the external flow velocity that occurs as the flow becomes confined; i.e. where the fluid enters the annular region. In that earlier analysis a low value for the ratio of $U_o/U_i \approx 0.05$ was considered exclusively. Furthermore, it was assumed in [11] that $U_o = 0$ outside the annular region. Abdelbaki et al. [118] made the same assumption, but the logistic function was utilized instead of the Heaviside step one, providing a smoother and more realistic modelling of the external flow.

In the following subsections, the linear models of Moditis et al. [11] and Abdelbaki et al. [118] are used to investigate the dynamics of the system for different values of U_o/U_i. In addition, an improvement is proposed by considering a non-zero value for the external flow velocity below the annular region.

5.2.1 Linear theoretical model for System III, based on the Heaviside step function (Model 1)

The derivation of the linear model proposed by Moditis et al. [11] is outlined in this subsection to allow the reader to follow the improvements proposed in the present study, detailed in the following subsections.

This time the equation of motion is derived by a Newtonian method, instead of Hamilton's principle, i.e. energy approach, that was used in the previous chapters of this thesis. Nevertheless, the same equation can be derived via Hamilton's principle by simply linearizing the derivation and obtaining the final equation of motion for System III in Chapter 4.

Figure 5–13 shows the structural and hydrodynamic forces acting on an element of the deformed pipe; summation of these forces in the x- and z-direction, respectively, yields the following relations:

$$\frac{\partial T}{\partial x} - \frac{\partial}{\partial x}\left(Q\frac{\partial w}{\partial x}\right) + M_t g - (F_{in} + F_{en})\frac{\partial w}{\partial x} + F_{it} - F_{et} = 0, \tag{5.2}$$

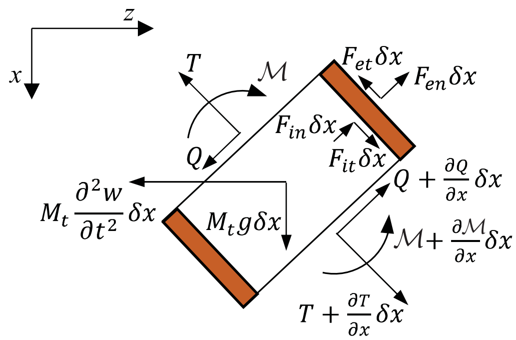

Figure 5–13: Forces acting on an element of length δx of the deformed pipe.

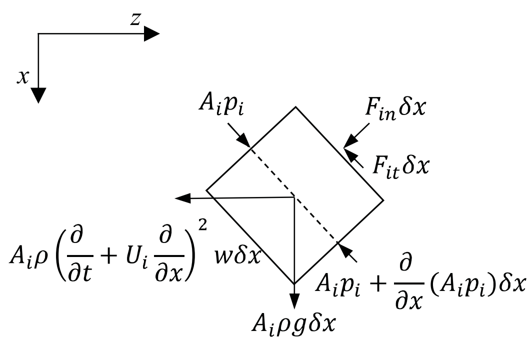

Figure 5–14: Forces acting on an element of length δx of the internal fluid.

$$\frac{\partial}{\partial x}\left(T\frac{\partial w}{\partial x}\right)+\frac{\partial Q}{\partial x} - M_t\frac{\partial^2 w}{\partial t^2} + F_{in} + F_{en} + (F_{it} - F_{et})\frac{\partial w}{\partial x} = 0, \tag{5.3}$$

where w is the lateral deflection in the z-direction, M_t is the mass of the pipe per unit length, T is the tension in the tube, Q is the shear force, $\mathcal{M}$ is the bending moment, F_{in} and F_{it} are the normal and tangential hydrodynamic forces, respectively, associated with the internal flow, and F_{en} and F_{et} are those associated with the external flow.

Using Euler-Bernoulli beam theory, the shear force can be approximated as

$$Q = -\,\partial(EI\,\partial^2 w/\partial x^2)/\partial x\,. \tag{5.4}$$

In addition, F_{in} and F_{it} can be determined by a force balance on an element δx of the internal fluid, as shown in Fig. 5–14. The resulting expressions in the x- and z-direction, respectively, can be written as

$$F_{it} - F_{in}\frac{\partial w}{\partial x} = M_i g - \frac{\partial}{\partial x}(A_i p_i), \tag{5.5}$$

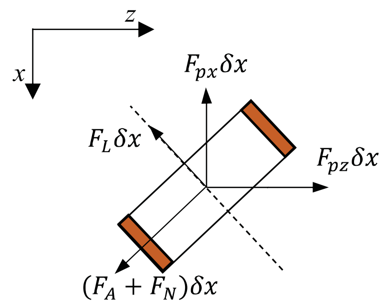

Figure 5–15: External fluid-related forces acting on an element of length δx of the cantilever.

$$-\left(F_{in} + F_{it}\frac{\partial w}{\partial x}\right) = M_i\left(\frac{\partial}{\partial t} + U_i\frac{\partial}{\partial x}\right)^2 w + \frac{\partial}{\partial x}\left(A_i p_i \frac{\partial w}{\partial x}\right), \tag{5.6}$$

in which $M_i = \rho A_i$ and $\left(\partial/\partial t + U_i\,\partial/\partial x\right)^2$ denotes repeated application of the operator in parentheses.

By substituting Eqs. (5.5) and (5.6) into Eqs. (5.2) and (5.3), and by using the approximations of Euler-Bernoulli theory, one can write

$$\frac{\partial T}{\partial x} + M_t g + \left[M_i g - \frac{\partial}{\partial x}(A_i p_i)\right] - F_{en}\frac{\partial w}{\partial x} - F_{et} = 0, \tag{5.7}$$

$$\begin{aligned} EI\frac{\partial^4 w}{\partial x^4} - \frac{\partial}{\partial x}\left(T\frac{\partial w}{\partial x}\right) + M_t\frac{\partial^2 w}{\partial t^2} - \Bigg[M_i\left(\frac{\partial}{\partial t} + U_i\frac{\partial}{\partial x}\right)^2 w \\ + \frac{\partial}{\partial x}\left(A_i p_i\frac{\partial w}{\partial x}\right)\Bigg] - F_{en} + F_{et}\frac{\partial w}{\partial x} = 0. \end{aligned} \tag{5.8}$$

The hydrodynamic forces due to the external flow are derived separately as discussed before in Chapter 2, by modelling the external flow as the superposition of a perturbation potential due to the pipe vibrations in the mean axial flow, and then adding the viscosity-related forces, which are treated as distinct from this potential flow. This approach has been used before in many fluid-structure interaction problems and has been proved to give acceptable results; see [2] for more details. An element of the pipe is subjected to the following set of external fluid-related forces: the inviscid fluid dynamic force F_A, the normal and longitudinal viscous forces, F_N and F_L, respectively, and the hydrostatic forces in the x-

and z-direction, F_{px} and F_{pz}, respectively, as shown in Fig. 5–15. By projecting these forces in the x- and z-direction, one can obtain the following force-balance relations:

$$-F_{en}\frac{\partial w}{\partial x} - F_{et} = -F_L - F_{px}, \tag{5.9}$$

$$-F_{en} + F_{et}\frac{\partial w}{\partial x} = (F_A + F_N) - F_{pz} + F_L\frac{\partial w}{\partial x}. \tag{5.10}$$

The external flow velocity is assumed to have zero value in the unconfined region, as if the pipe were submerged in stagnant fluid, and a value of U_o in the confined region. Thus, with the aid of the Heaviside step function, one can write

$$U_o(x) = U_o[1 - \mathrm{H}(x - L')]. \tag{5.11}$$

The virtual added mass is defined as $M_o = \rho A_o$ over the unconfined region and $M_o = \chi\rho A_o$ over the confined one [5,116], where $\chi = (D_{ch}^2 + D_o^2)/(D_{ch}^2 - D_o^2)$ is a confinement parameter. Hence, to account for the variation of confinement along the pipe, one can write

$$M_o = [\chi + (1-\chi)\mathrm{H}(x - L')]\rho A_o. \tag{5.12}$$

In addition, the original formulation for the inviscid force, F_A, derived by Lighthill [108] and elaborated by Païdoussis [5] can be modified and expressed as follows:

$$\begin{aligned} F_A =& \left(\frac{\partial}{\partial t} - U_o\frac{\partial}{\partial t} + U_o\mathrm{H}(x-L')\frac{\partial}{\partial x}\right)\Bigg\{[\chi + (1-\chi)\mathrm{H}(x-L')]\rho A_o\Bigg(\frac{\partial w}{\partial t} \\ & - U_o\frac{\partial w}{\partial x} + U_o\mathrm{H}(x-L')\frac{\partial w}{\partial x}\Bigg)\Bigg\}. \end{aligned} \tag{5.13}$$

Thus, after further manipulation, one obtains

$$\begin{aligned} F_A =& \chi\rho A_o\frac{\partial^2 w}{\partial t^2} + (1-\chi)\rho A_o\mathrm{H}(x-L')\frac{\partial^2 w}{\partial t^2} - 2\chi\rho A_o U_o\frac{\partial^2 w}{\partial x\partial t} \\ & + 2\chi\rho A_o U_o\mathrm{H}(x-L')\frac{\partial^2 w}{\partial x\partial t} - \chi\rho A_o U_o^2\mathrm{H}(x-L')\frac{\partial^2 w}{\partial x^2} + \chi\rho A_o U_o^2\frac{\partial^2 w}{\partial x^2}. \end{aligned} \tag{5.14}$$

The hydrostatic forces are derived by the procedure utilized in [5], which leads to $F_{px} = 0$ and $F_{pz} = A_o(\partial w/\partial x)(\partial p_o/\partial x) + A_o p_o(\partial^2 w/\partial x^2)$, after linearization. Following the analysis detailed in [11], the outer pressure gradient can be expressed as

$$
\begin{aligned}
A_o\left(\frac{\partial p_o}{\partial x}\right) = & \ \frac{1}{2}\rho D_o C_f\left(\frac{D_o}{D_h}\right)U_o^2[1-\mathrm{H}(x-L')] + \rho g A_o \\
& + A_o\left(\frac{1}{2}\rho U_o^2 + \rho g h_a\right)\delta_D(x-L'),
\end{aligned}
\tag{5.15}
$$

where $h_a = K_1 U_o^2/(2g)$ is the head-loss associated with the stagnant fluid entering the annular region, with $0.8 \le K_1 \le 0.9$ [117]. Integration of Eq. (5.15) over the domain $[x : L]$, leads to the following expression for the outer pressure distribution:

$$
\begin{aligned}
A_o p_o(x) = A_o p_o(L) - & \left(\frac{1}{2}\rho D_o U_o^2[1-\mathrm{H}(x-L')]C_f\frac{D_o}{D_h}\right)(L'-x) \\
& - \rho g A_o(L-x) - A_o\left(\frac{1}{2}\rho U_o^2 + \rho g h_a\right)[1-\mathrm{H}(x-L')].
\end{aligned}
\tag{5.16}
$$

The hydrostatic forces in x- and z-direction can now be written as

$$
\begin{aligned}
F_{px} = & \ 0, \\
F_{pz} = & \ \Bigg(\frac{1}{2}\rho D_o U_o^2[1-\mathrm{H}(x-L')]C_f\frac{D_o}{D_h} \\
& + \rho g A_o + A_o\left(\frac{1}{2}\rho U_o^2 + \rho g h_a\right)\delta_D(x-L')\Bigg)\frac{\partial w}{\partial x} + A_o p_o\frac{\partial^2 w}{\partial x^2}.
\end{aligned}
\tag{5.17}
$$

The viscous forces in the longitudinal and normal directions, F_L and F_N, respectively, are derived on the basis of the semi-empirical formulas proposed by Taylor [109] and detailed in [5]; they can be adapted for the system under study, as follows:

$$
\begin{aligned}
F_L = & \ \frac{1}{2}\rho D_o C_f U_o^2[1-\mathrm{H}(x-L')], \\
F_N = & \ \frac{1}{2}\rho D_o C_f U_o[1-\mathrm{H}(x-L')]\left(\frac{\partial w}{\partial t} - U_o[1-\mathrm{H}(x-L')]\frac{\partial w}{\partial x}\right) + k\frac{\partial w}{\partial t},
\end{aligned}
\tag{5.18}
$$

where k is a viscous-drag coefficient, expressed as

$$
k = k_u\left[\frac{1+\bar{\gamma}^3}{\left(1-\bar{\gamma}^2\right)^2} + \mathrm{H}(x-L')\left(1-\frac{1+\bar{\gamma}^3}{\left(1-\bar{\gamma}^2\right)^2}\right)\right],
\tag{5.19}
$$

in which $k_u = 2\sqrt{2}\rho A_o \Omega/\sqrt{\tilde{S}}$ [116], $\tilde{S} = \Omega D_o^2/(4\nu)$ is the Stokes number, and $\bar{\gamma} = D_o/D_{ch}$.

Substitution of Eqs. (5.14), (5.17) and (5.18) into Eq. (5.10) and subsequent substitution of the result into Eq. (5.8), and using Eqs. (5.7), (5.9), (5.15), (5.16) and (5.19), the final equation of motion can be derived in the z-direction, as follows:

$$\begin{aligned}
&EIw'''' + \left\{(M_t + M_i - \rho A_o)g - \frac{1}{2}\rho D_o C_f U_o^2\left(\frac{D_o}{D_h} + 1\right)[1 - \mathrm{H}(x - L')]\right.\\
&\left. - A_o\left(\frac{1}{2}\rho U_o^2 + \rho g h_a\right)\delta_D(x - L')\right\}w' + \left\{(-M_t - M_i + \rho A_o)g(L - x)\right.\\
&+ \frac{1}{2}\rho D_o U_o^2 C_f\left(\frac{D_o}{D_h} + 1\right)(L' - x)[1 - \mathrm{H}(x - L')] + A_o\left(\frac{1}{2}\rho U_o^2 + \rho g h_a\right)\\
&\left.\times [1 - \mathrm{H}(x - L')] - (T - A_i p_i + A_o p_o)|_L\right\}w'' + M_t\ddot{w} + M_i\ddot{w} + 2M_iU_i\dot{w}'\\
&+ M_iU_i^2w'' + A_o\rho\chi\ddot{w} + (1 - \chi)\rho_f A_o \mathrm{H}(x - L')\ddot{w} - 2A_o\rho\chi U_o[1 - \mathrm{H}(x - L')]\dot{w}'\\
&+ A_o\rho\chi U_o^2[1 - \mathrm{H}(x - L')]w'' + \frac{1}{2}\rho D_o C_f U_o[1 - \mathrm{H}(x - L')]\dot{w}\\
&+ k_u\left\{1 + [1 - \mathrm{H}(x - L')]\left(\frac{1 + \bar{\gamma}^3}{\left(1 - \bar{\gamma}^2\right)^2} - 1\right)\right\}\dot{w} = 0,
\end{aligned} \tag{5.20}$$

where $(\;)' = \partial(\;)/\partial x$, $(\dot{\;}) = \partial(\;)/\partial t$, and $(\;)|_L$ denotes the value of the quantity in parentheses at the free end of the pipe, i.e. at $x = L$.

Defining next the following dimensionless quantities:

$$\begin{aligned}
&\xi = \frac{x}{L}, \quad \eta = \frac{w}{L}, \quad \tau = \left(\frac{EI}{M_t + M_i + \rho A_o}\right)^{1/2}\frac{t}{L^2}, \quad u_i = \left(\frac{M_i}{EI}\right)^{1/2}U_iL,\\
&u_o = \left(\frac{\rho A_o}{EI}\right)^{1/2}U_oL, \quad \beta_i = \frac{M_i}{M_t + M_i + \rho A_o}, \quad \beta_o = \frac{\rho A_o}{M_t + M_i + \rho A_o},\\
&\gamma = \frac{(M_t + M_i - \rho A_o)gL^3}{EI}, \quad \Gamma = \frac{T(L)L^2}{EI}, \quad c_f = \frac{4}{\pi}C_f, \quad \alpha = \frac{D_i}{D_o},\\
&\alpha_{ch} = \frac{D_{ch}}{D_o}, \quad \Pi_{iL} = \frac{A_ip_i(L)L^2}{EI}, \quad h = \frac{D_o}{D_h}, \quad \Pi_{oL} = \frac{A_op_o(L)L^2}{EI}, \quad r_{ann} = \frac{L'}{L}\\
&\kappa_u = \frac{k_uL^2}{[EI(M_t + M_i + \rho A_o)]^{1/2}}, \quad \varepsilon = \frac{L}{D_o}, \quad \omega = \left(\frac{M_t + M_i + \rho A_o}{EI}\right)^{1/2}L^2\Omega,
\end{aligned} \tag{5.21}$$

the equation of motion can be expressed in dimensionless form as follows:

$$
\begin{aligned}
&\eta'''' + \left\{\gamma - \frac{1}{2}\varepsilon c_f u_o^2(1+h)[1-\mathrm{H}(\xi - r_{ann})] - \frac{1}{2}u_o^2(1+K_1)\delta_D(\xi - r_{ann})\right\}\eta' \\
&- \left\{(\Gamma - \Pi_{iL} + \Pi_{oL}) + \gamma(1-\xi) - \frac{1}{2}\varepsilon c_f u_o^2(1+h)(r_{ann} - \xi)[1-\mathrm{H}(\xi - r_{ann})] \right. \\
&\left. - \frac{1}{2}u_o^2(1+K_1)[1-\mathrm{H}(\xi - r_{ann})]\right\}\eta'' + \{1 + \beta_o(\chi - 1)[1-\mathrm{H}(\xi - r_{ann})]\}\ddot{\eta} \\
&+ \{2u_i\sqrt{\beta_i} - 2\chi u_o\sqrt{\beta_o}[1-\mathrm{H}(\xi - r_{ann})]\}\dot{\eta}' + \left\{u_i^2 + \chi u_o^2[1-\mathrm{H}(\xi - r_{ann})]\right\}\eta'' \\
&+ \frac{1}{2}\varepsilon c_f u_o\sqrt{\beta_o}[1-\mathrm{H}(\xi - r_{ann})]\dot{\eta} + \kappa_u\left\{1 + [1-\mathrm{H}(\xi - r_{ann})]\left(\frac{1+\alpha_{ch}^{-3}}{\left(1-\alpha_{ch}^{-2}\right)^2} \right.\right. \\
&\left.\left. - 1\right)\right\}\dot{\eta} = 0,
\end{aligned}
\tag{5.22}
$$

where $(\ )' = \partial(\ )/\partial\xi$, $(\dot{\ }) = \partial(\ )/\partial\tau$. Also, according to [11], $\Pi_{iL} = \alpha^2\Pi_{oL} - (1/2)u_i^2 + A_i\rho g h_e L^2/(EI)$, where $h_e = U_i^2/(2g)$ is the head-loss due to sudden enlargement of the internal flow into the surrounding fluid [117], and $\Pi_{oL} = (1/2)\varepsilon c_f h r_{ann} u_o^2 + (1/2)u_o^2(1 + K_1) + A_o\rho g L^3/(EI)$.

5.2.2 Linear theoretical model for System III, based on the logistic function (Model 2)

In Abdelbaki et al. [118], a modification has been made to the model described in Sub-section 5.2.1. The logistic function was utilized instead of the Heaviside step function to model the discontinuity in the external axial flow velocity over the pipe, and also in the virtual added mass, M_o. Hence,

$$U_o(x) = \frac{U_o}{1 + \mathrm{e}^{s_t(x-L')/L}} = U_o S, \tag{5.23}$$

$$M_o = \rho A_o(\chi - 1)S + \rho A_o, \tag{5.24}$$

where s_t represents the steepness of the logistic function and $S = 1/(1 + \mathrm{e}^{s_t(x-L')/L})$.

This modification affects all the expressions derived in Sub-section 5.2.1, for the fluid forces associated with the external flow. Thus, the inviscid hydrodynamic force is now written as

$$F_A = M_o\frac{\partial^2 w}{\partial t^2} - 2M_oU_oS\frac{\partial^2 w}{\partial x\partial t} + M_oU_o^2S^2\frac{\partial^2 w}{\partial x^2}. \tag{5.25}$$

The viscous forces are also modified accordingly and expressed as

$$\begin{aligned} F_L =& \frac{1}{2}\rho D_oC_fU_o^2S^2, \\ F_N =& \frac{1}{2}\rho D_oC_fU_oS\left(\frac{\partial w}{\partial t} - U_oS\frac{\partial w}{\partial x}\right)+k\frac{\partial w}{\partial t}, \end{aligned} \tag{5.26}$$

where k is the viscous-drag coefficient,

$$k = k_u\left(\frac{1+\bar{\gamma}^3}{\left(1-\bar{\gamma}^2\right)^2} - 1\right)S + k_u. \tag{5.27}$$

In addition, the pressure gradient outside the pipe becomes

$$A_o(\frac{\partial p_o}{\partial x}) = \frac{1}{2}\rho D_oC_f\left(\frac{D_o}{D_h}\right)U_o^2S^2 + \rho gA_o + A_o\left(\frac{1}{2}\rho U_o^2 + \rho gh_a\right)\frac{\mathrm{d}S^{*2}}{\mathrm{d}x}, \tag{5.28}$$

where $S^* = 1/(1+\mathrm{e}^{-s_t(x-L')/L})$. Integration of Eq. (5.28) over the domain $[x : L]$, leads to the following outer pressure distribution:

$$\begin{aligned} A_op_o(x) =& A_op_o(L) - \frac{1}{2}\rho D_oU_o^2C_f\left(\frac{D_o}{D_h}\right)\int_x^L\left\{\left[1-\frac{1}{2}\left(\frac{\partial w}{\partial x}\right)^2\right]S^2\right\}\mathrm{d}x \\ &- \rho gA_o\left[(L-x) - \frac{1}{2}\int_x^L\left(\frac{\partial w}{\partial x}\right)^2\mathrm{d}x\right] - A_o\left(\frac{1}{2}\rho U_o^2 + \rho gh_a\right) \\ &\times\int_x^L\left\{\left[1-\frac{1}{2}\left(\frac{\partial w}{\partial x}\right)^2\right]\frac{\mathrm{d}S^{*2}}{\mathrm{d}x}\right\}\mathrm{d}x. \end{aligned} \tag{5.29}$$

Finally, the hydrostatic forces in x- and z-direction can now be written as

$$\begin{aligned} F_{px} =& 0, \\ F_{pz} =& \left\{\frac{1}{2}\rho D_oC_f\left(\frac{D_o}{D_h}\right)U_o^2S^2 + \rho gA_o\right. \\ &\left. + A_o\left(\frac{1}{2}\rho U_o^2 + \rho gh_a\right)\frac{\mathrm{d}S^{*2}}{\mathrm{d}x}\right\}\frac{\partial w}{\partial x} + A_op_o\frac{\partial^2 w}{\partial x^2}. \end{aligned} \tag{5.30}$$

Substitution of Eqs. (5.25), (5.26) and (5.30) into Eq. (5.10) and subsequent substitution of the result in Eq. (5.8), and using Eqs. (5.7), (5.9), (5.28), (5.29) and (5.27), the final equation of motion in the z-direction can be derived, namely

$$
\begin{aligned}
&EIw'''' + \left\{(M_t + M_i - \rho A_o)g - \frac{1}{2}\rho D_o C_f U_o^2 S^2\left(\frac{D_o}{D_h} + 1\right)\right. \\
&\left. - A_o\left(\frac{1}{2}\rho U_o^2 + \rho g h_a\right)\frac{\mathrm{d}S^{*2}}{\mathrm{d}x}\right\}w' + \left\{(-M_t - M_i + \rho A_o)g(L - x)\right. \\
&+ \frac{1}{2}\rho D_o U_o^2 C_f\left(\frac{D_o}{D_h} + 1\right)\int_x^L S^2\mathrm{d}x + A_o(\frac{1}{2}\rho U_o^2 + \rho g h_a)\int_x^L \frac{\mathrm{d}S^{*2}}{\mathrm{d}x}\mathrm{d}x \\
&\left. - (T - A_i p_i + A_o p_o)|_L\right\}w'' + M_t\ddot{w} + M_i\ddot{w} + 2M_iU_i\dot{w}' + M_iU_i^2 w'' \\
&+ M_o\ddot{w} - 2M_oU_oS\dot{w}' + M_oU_o^2S^2w'' + \frac{1}{2}\rho D_o C_f U_o S\dot{w} \\
&+ \left[k_u\left(\frac{1 + \bar{\gamma}^3}{\left(1 - \bar{\gamma}^2\right)^2} - 1\right)S + k_u\right]\dot{w} = 0.
\end{aligned}
\tag{5.31}
$$

Using the dimensionless parameters defined in Eq. (5.21), as well as the following quantities:

$$
\begin{aligned}
&S = \frac{1}{1 + \mathrm{e}^{s_t(x - L')/L}} = \frac{1}{1 + \mathrm{e}^{s_t(\xi - r_{ann})}}, \quad \bar{S} = \frac{1}{1 + \mathrm{e}^{s_t(r_{ann} - 1)}}, \\
&S^* = \frac{1}{1 + \mathrm{e}^{s_t(r_{ann} - \xi)}}, \quad G = \frac{1}{L}\int_x^L \frac{1}{\left(1 + \mathrm{e}^{s_t(x - L')/L}\right)^2}\mathrm{d}x,
\end{aligned}
\tag{5.32}
$$

the equation of motion can be written in the following dimensionless form:

$$
\begin{aligned}
&\eta'''' + \left\{\gamma - \frac{1}{2}\varepsilon c_f u_o^2(1 + h)S^2 - u_o^2(1 + K_1)s_t\mathrm{e}^{(r_{ann} - \xi)}S^{*3}\right\}\eta' \\
&- \left\{\gamma(1 - \xi) - \frac{1}{2}\varepsilon c_f u_o^2(1 + h)G - \frac{1}{2}u_o^2(1 + K_1)(\bar{S}^2 - S^{*2})\right. \\
&\left. + (\Gamma - \Pi_{iL} + \Pi_{oL})\right\}\eta'' + [1 + \beta_o(\chi - 1)S]\ddot{\eta} + \{2u_i\sqrt{\beta_i} \\
&- 2u_o\sqrt{\beta_o}[(\chi - 1)S + 1]S\}\dot{\eta}' + \left\{u_i^2 + u_o^2[(\chi - 1)S + 1]S^2\right\}\eta'' \\
&+ \frac{1}{2}\varepsilon c_f u_o\sqrt{\beta_o}S\dot{\eta} + \kappa_u\left[\left(\frac{1 + \alpha_{ch}^3}{\left(1 - \alpha_{ch}^2\right)^2} - 1\right)S + 1\right]\dot{\eta} = 0.
\end{aligned}
\tag{5.33}
$$

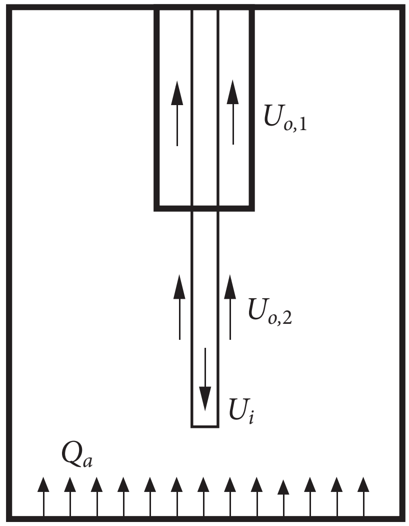

Figure 5–16: Sketch shows the modification proposed in Model 3 by considering a non-zero value for the external flow velocity below the annulus, $U_{o,2}$.

5.2.3 Linear theoretical model for System III, based on the Heaviside step function, considering a value for the flow velocity below the annular region (Model 3)

In this model, two values for the external axial flow velocity around the pipe are defined: $U_{o,1}$ that represents the flow velocity within the annular region, and $U_{o,2} \neq 0$[1] for the flow velocity below the annular region; i.e. before the fluid enters the outer rigid tube, as shown in Fig. 5–16. This discontinuity in the value of the external flow velocity, $U_o(x)$, is modelled using the Heaviside step function,[2] as for Model 1. Thus, one can generally write

$$U_o(x) = U_{o,1}[1 - \mathrm{H}(x - L')] + U_{o,2}\mathrm{H}(x - L'). \tag{5.34}$$

[1] In yet unpublished computational fluid dynamics simulations by Prof. Daneshmand and by the author, it was found that there are flow structures in the tank which result in a non-zero axial flow velocity below the annular region.

[2] The simpler formulations via the Heaviside step function is adopted here, because, as will be seen in the results (Sub-sections 5.2.5 and 5.2.6), the results of Model 1 and Model 2 are quite similar.

The expressions of the external-fluid-related forces derived for Model 1 are modified accordingly to account for the new velocity $U_{o,2}$. The inviscid forces are now written as

$$\begin{aligned}F_A =&\chi\rho A_o\frac{\partial^2 w}{\partial t^2} + (1-\chi)\rho A_o\mathrm{H}(x-L')\frac{\partial^2 w}{\partial t^2} - 2\chi\rho A_o U_{o,1}\frac{\partial^2 w}{\partial x\partial t}\\ &+ 2\chi\rho A_o U_{o,1}\mathrm{H}(x-L')\frac{\partial^2 w}{\partial x\partial t} - \chi\rho A_o U_{o,1}^2\mathrm{H}(x-L')\frac{\partial^2 w}{\partial x^2}\\ &+ \chi\rho A_o U_{o,1}^2\frac{\partial^2 w}{\partial x^2} - 2\rho A_o U_{o,2}\mathrm{H}(x-L')\frac{\partial^2 w}{\partial x\partial t} + \rho A_o U_{o,2}^2\mathrm{H}(x-L')\frac{\partial^2 w}{\partial x^2}.\end{aligned} \tag{5.35}$$

Also, the viscous forces are modified as follows:

$$\begin{aligned}F_L =&\ \frac{1}{2}\rho D_o C_f U_{o,1}^2[1-\mathrm{H}(x-L')] + \frac{1}{2}\rho D_o C_f U_{o,2}^2\mathrm{H}(x-L'),\\ F_N =&\ \frac{1}{2}\rho D_o C_f U_{o,1}[1-\mathrm{H}(x-L')]\left(\frac{\partial w}{\partial t} - U_{o,1}[1-\mathrm{H}(x-L')]\frac{\partial w}{\partial x}\right) + k\frac{\partial w}{\partial t}\\ &+ \frac{1}{2}\rho D_o C_f U_{o,2}\mathrm{H}(x-L')\frac{\partial w}{\partial t} - \frac{1}{2}\rho D_o C_f U_{o,2}^2\mathrm{H}(x-L')\frac{\partial w}{\partial x}.\end{aligned} \tag{5.36}$$

Moreover, the outer pressure gradient are expressed as

$$\begin{aligned}A_o\left(\frac{\partial p_o}{\partial x}\right) =&\ \frac{1}{2}\rho D_o C_f\left(\frac{D_o}{D_h}\right)U_{o,1}^2[1-\mathrm{H}(x-L')] + \frac{1}{2}\rho D_o C_f\left(\frac{D_o}{D_h^*}\right)U_{o,2}^2\mathrm{H}(x-L')\\ &+ \rho g A_o + A_o\left(\frac{1}{2}\rho U_{o,1}^2 + \rho g h_a\right)\delta_D(x-L'),\end{aligned} \tag{5.37}$$

where D_h^* is the hydraulic diameter for the flow beneath the annular region, which can be calculated as: $D_h^* = D_t - D_o$, with D_t being the inner diameter of the pressure vessel that forms the test-section. Integration of Eq. (5.37) over the domain $[x : L]$, leads to

$$\begin{aligned}A_o p_o(x) =&\ A_o p_o(L) - \left(\frac{1}{2}\rho D_o U_{o,1}^2[1-\mathrm{H}(x-L')]C_T\frac{D_o}{D_h}\right)(L'-x)\\ &+ \frac{1}{2}\rho D_o C_f\left(\frac{D_o}{D_h^*}\right)U_{o,2}^2[(L-L') - (x-L')\mathrm{H}(x-L')]\\ &- \rho g A_o(L-x) - A_o\left(\frac{1}{2}\rho U_{o,1}^2 + \rho g h_a\right)[1-\mathrm{H}(x-L')].\end{aligned} \tag{5.38}$$

The hydrostatic forces in x- and z-direction are now written as

$$
\begin{aligned}
F_{px} =\;& 0, \\
F_{pz} =\;& \left(\frac{1}{2}\rho D_o U_{o,1}^2[1-\mathrm{H}(x-L')]C_T\frac{D_o}{D_h} + \frac{1}{2}\rho D_o C_f\left(\frac{D_o}{D_h^*}\right)U_{o,2}^2\mathrm{H}(x-L')\right. \\
&\left. + \rho g A_o + A_o\left(\frac{1}{2}\rho U_{o,1}^2 + \rho g h_a\right)\delta_D(x-L')\right)\frac{\partial w}{\partial x} + A_o p_o\frac{\partial^2 w}{\partial x^2}.
\end{aligned} \tag{5.39}
$$

The new expressions derived in Eqs. (5.35)-(5.39) can be utilized, as done before for Models 1 and 2, to obtain the following equation of motion:

$$
\begin{aligned}
& EIw'''' + \left\{(M_t + M_i - \rho A_o)g - \frac{1}{2}\rho D_o C_f U_{o,1}^2\left(\frac{D_o}{D_h}+1\right)[1-\mathrm{H}(x-L')]\right. \\
& \left. - \frac{1}{2}\rho D_o C_f U_{o,2}^2\left(\frac{D_o}{D_h^*}+1\right)\mathrm{H}(x-L') - A_o\left(\frac{1}{2}\rho U_{o,1}^2+\rho g h_a\right)\delta_D(x-L')\right\}w' \\
& + \left\{(-M_t - M_i + \rho A_o)g(L-x) - \frac{1}{2}\rho D_o C_f U_{o,2}^2\left(\frac{D_o}{D_h^*}\right)[(L-L')\right. \\
& - (x-L')\mathrm{H}(x-L')] + \frac{1}{2}\rho D_o U_{o,1}^2 C_f\left(\frac{D_o}{D_h}+1\right)(L'-x)[1-\mathrm{H}(x-L')] \\
& \left. + A_o\left(\frac{1}{2}\rho U_{o,1}^2+\rho g h_a\right)[1-\mathrm{H}(x-L')] - (T - A_i p_i + A_o p_o)|_L\right\}w'' \\
& + M_t\ddot{w} + M_i\ddot{w} + 2M_iU_i\dot{w}' + M_iU_i^2w'' + A_o\rho\chi\ddot{w} + (1-\chi)\rho_f A_o\mathrm{H}(x-L')\ddot{w} \\
& - 2A_o\rho\chi U_{o,1}[1-\mathrm{H}(x-L')]\dot{w}' - 2A_o\rho U_{o,2}\mathrm{H}(x-L')\dot{w}' + A_o\rho\chi U_{o,1}^2[1-\mathrm{H}(x-L')]w'' \\
& + A_o\rho U_{o,2}^2\mathrm{H}(x-L')w'' + \frac{1}{2}\rho D_o C_f U_{o,1}[1-\mathrm{H}(x-L')]\dot{w} \\
& + \frac{1}{2}\rho D_o C_f U_{o,2}\mathrm{H}(x-L')\dot{w} + k_u\left\{1 + [1-\mathrm{H}(x-L')]\left(\frac{1+\bar{\gamma}^3}{\left(1-\bar{\gamma}^2\right)^2}-1\right)\right\}\dot{w} = 0.
\end{aligned} \tag{5.40}
$$

Also,

$$
\begin{aligned}
p_o(L) =& \frac{1}{2A_o}C_f\rho_f D_o U_{o,1}^2 L'\left(\frac{D_o}{D_h}\right) + \frac{1}{2A_o}C_f\rho_f D_o U_{o,2}^2(L-L')\left(\frac{D_o}{D_h^*}\right) \\
& + \rho g L + \frac{1}{2}\rho U_{o,1}^2 + \frac{1}{2}\rho U_{o,2}^2 + \rho g h_a, \\
p_i(L) =& p_o(L) - \frac{1}{2}\rho U_i^2 + \frac{1}{2}\rho U_{o,2}^2 + \rho g h_e.
\end{aligned} \tag{5.41}
$$

It should be mentioned that h_a and h_e in Eq. (5.41) are now defined as: $h_a = K_1(U_{o,1}^2 - U_{o,2}^2)/(2g)$ and $h_e = K_2(U_i^2 - U_{o,2}^2)/(2g)$.

By using the dimensionless quantities given in (5.21), the equation of motion can be written as

$$\begin{aligned}
&\eta'''' + \Big\{\gamma - \frac{1}{2}\varepsilon c_f u_{o,1}^2(1+h)[1-\mathrm{H}(\xi - r_{ann})] - \frac{1}{2}\varepsilon c_f u_{o,2}^2(1+h^*)\mathrm{H}(\xi - r_{ann}) \\
&- \frac{1}{2}u_{o,1}^2(1+K_1)\delta_D(\xi - r_{ann})\Big\}\eta' - \Big\{(\Gamma - \Pi_{iL} + \Pi_{oL}) + \gamma(1-\xi) \\
&- \frac{1}{2}\varepsilon c_f u_{o,1}^2(1+h)(r_{ann} - \xi)[1-\mathrm{H}(\xi - r_{ann})] - \frac{1}{2}u_{o,1}^2(1+K_1)[1-\mathrm{H}(\xi - r_{ann})] \\
&- \frac{1}{2}\varepsilon c_f u_{o,2}^2(1+h^*)(1-r_{ann}) + \frac{1}{2}\varepsilon c_f u_{o,2}^2(1+h^*)(\xi - r_{ann})\mathrm{H}(\xi - r_{ann})\Big\}\eta'' \\
&+ \{1+\beta_o(\chi-1)[1-\mathrm{H}(\xi - r_{ann})]\}\ddot{\eta} + \{2u_i\sqrt{\beta_i} - 2\chi u_{o,1}\sqrt{\beta_o}[1-\mathrm{H}(\xi - r_{ann})] \\
&- 2u_{o,2}\sqrt{\beta_o}\mathrm{H}(\xi - r_{ann})\}\dot{\eta}' + \big\{u_i^2 + \chi u_{o,1}^2[1-\mathrm{H}(\xi - r_{ann})] + u_{o,2}^2\mathrm{H}(\xi - r_{ann})\big\}\eta'' \\
&+ \frac{1}{2}\varepsilon c_f u_{o,1}\sqrt{\beta_o}[1-\mathrm{H}(\xi - r_{ann})]\dot{\eta} + \frac{1}{2}\varepsilon c_f u_{o,2}\sqrt{\beta_o}\mathrm{H}(\xi - r_{ann}) \\
&+ \kappa_u\Big\{1 + [1-\mathrm{H}(\xi - r_{ann})]\Big(\frac{1+\alpha_{ch}^{-3}}{\big(1-\alpha_{ch}^{-2}\big)^2} - 1\Big)\Big\}\dot{\eta} = 0,
\end{aligned} \tag{5.42}$$

where $h^* = D_o/D_h^*$. In addition, we have

$$\begin{aligned}
\Pi_{oL} =& \frac{1}{2}c_f h r_{ann}\varepsilon u_{o,1}^2 + \frac{1}{2}c_f h^* \varepsilon u_{o,2}^2(1-r_{ann}) \\
&+ \frac{A_o \rho g L^3}{EI} + \frac{1}{2}u_{o,1}^2(1+K_1) + \frac{1}{2}u_{o,2}^2(1-K_1), \\
\Pi_{iL} =& \alpha^2\Pi_{oL} - \frac{1}{2}u_i^2 + \frac{1}{2}u_{o,2}^2 + \rho A_i g h_e\Big(\frac{L^2}{EI}\Big),
\end{aligned} \tag{5.43}$$

with D_h^* as defined below Eq. (5.37).

5.2.4 Methods of analysis for the linear models

In general, the equations of motion obtained in the previous sub-sections, i.e. (5.22), (5.33) and (5.42), are discretized using Galerkin's technique, with the cantilever beam eigenfunctions, $\phi_j(\xi)$, as comparison functions and with $q_j(\tau)$ as the corresponding generalized coordinates; thus,

$$\eta(\xi,\tau) = \sum_{j=1}^{N}\phi_j(\xi)q_j(\tau), \tag{5.44}$$

where N represents the number of modes in the Galerkin scheme. Substituting Eq. (5.44) into the equation of motion, multiplying by $\phi_i(\xi)$, and integrating over the domain [0 : 1] results in a set of ordinary differential equations that can be written in the following matrix form:

$$\mathbf{M}\ddot{\mathbf{q}} + \mathbf{C}\dot{\mathbf{q}} + \mathbf{K}\mathbf{q} = \mathbf{0}, \tag{5.45}$$

where $\mathbf{M}$, $\mathbf{C}$ and $\mathbf{K}$ denote the mass, damping and stiffness matrices, respectively. Also, $\mathbf{q} = \{q_1, q_2, \ldots, q_N\}^\intercal$, $\dot{\mathbf{q}} = \mathrm{d}\mathbf{q}/\mathrm{d}\tau$ and $\ddot{\mathbf{q}} = \mathrm{d}\dot{\mathbf{q}}/\mathrm{d}\tau$. The equations of motion may then be reduced into first-order form, and by seeking an oscillatory solution, $q_j = A_j \mathrm{e}^{\mathrm{i}\omega_j \tau}$, the problem becomes a typical eigenvalue problem, as detailed in [2]. The stability of the system is investigated by solving the eigenvalue problem and determining the complex eigenfrequencies, ω_j, for a given internal flow velocity u_i. The real part of the eigenfrequency, $\mathrm{Re}(\omega_j)$, is associated with the frequency of oscillations, while the imaginary part, $\mathrm{Im}(\omega_j)$, is related to the damping of the system. $\mathrm{Im}(\omega_j) < 0$ is indicative of instability; if it occurs while $\mathrm{Re}(\omega) = 0$, this denotes a static divergence, meaning that the pipe would buckle. However, if $\mathrm{Im}(\omega_j) < 0$ and $\mathrm{Re}(\omega_j) > 0$, this is associated with a Hopf bifurcation, which would cause the pipe to undergo flutter.

In the following, the mass, damping, and stiffness matrices for each model are defined, as obtained after employing the Galerkin technique.

Model 1:

$$\begin{aligned}
M_{ij} &= a_{ij\,(0,1)} - \beta_o(1-\chi)a_{ij\,(0,r_{ann})}, \\
C_{ij} &= 2u_i\sqrt{\beta_i}b_{ij\,(0,1)} - 2\chi u_o\sqrt{\beta_o}b_{ij\,(0,r_{ann})} + \frac{1}{2}u_o\varepsilon c_f\sqrt{\beta_o}a_{ij\,(0,r_{ann})} \\
&\quad + \kappa_u a_{ij\,(0,1)} + \kappa_u\left[\frac{1+\alpha_{ch}^{-3}}{(1-\alpha_{ch}^{-2})^2} - 1\right]a_{ij\,(0,r_{ann})}, \\
K_{ij} &= \lambda_j^4 a_{ij\,(0,1)} + \gamma b_{ij\,(0,1)} - \frac{1}{2}u_o^2\varepsilon c_f h b_{ij\,(0,r_{ann})} - \frac{1}{2}u_o^2\varepsilon c_f b_{ij\,(0,r_{ann})} \\
&\quad - \frac{1}{2}u_o^2(1+K_1)(\phi_i|_{\xi=r_{ann}}\phi_j'|_{\xi=r_{ann}}) - (\Gamma - \Pi_{iL} + \Pi_{oL})c_{ij\,(0,1)} \\
&\quad - \gamma(c_{ij\,(0,1)} - d_{ij\,(0,1)}) + \frac{1}{2}u_o^2\varepsilon c_f(1+h)(r_{ann}c_{ij\,(0,1)} - d_{ij\,(0,1)}) \\
&\quad + \frac{1}{2}u_o^2(1+K_1^2)c_{ij\,(0,r_{ann})} + u_i^2 c_{ij\,(0,1)} + \chi u_o^2 c_{ij\,(0,r_{ann})},
\end{aligned} \tag{5.46}$$

where λ_j is the jth eigenvalue of the dimensionless cantilevered beam characteristic equation, and the constants a_{ij}, b_{ij}, c_{ij} and d_{ij} are:

$$\begin{aligned}
a_{ij\,(a,b)} &= \int_a^b \phi_i \phi_j \,\mathrm{d}\xi, \quad b_{ij\,(a,b)} = \int_a^b \phi_i \phi_j' \,\mathrm{d}\xi, \\
c_{ij\,(a,b)} &= \int_a^b \phi_i \phi_j'' \,\mathrm{d}\xi, \quad d_{ij\,(a,b)} = \int_a^b \xi \phi_i \phi_j'' \,\mathrm{d}\xi,
\end{aligned} \tag{5.47}$$

available in closed-form in [2].

Model 2:

$$\begin{aligned}
M_{ij} =& \bar{A}_{ij} + \beta_o(\chi - 1)\bar{I}_{ij}, \\
C_{ij} =& 2u_i\beta_i^{\frac{1}{2}}\bar{B}_{ij} - 2u_o\beta_o^{\frac{1}{2}}\bar{K}_{ij} - 2u_o\beta_o^{\frac{1}{2}}(\chi - 1)\bar{C}_{ij} \\
&+ \frac{1}{2}\varepsilon c_f u_o \beta_o^{\frac{1}{2}}\bar{I}_{ij} + \kappa_u\bar{A}_{ij} + \kappa_u\left(\frac{1+\alpha_{ch}^{-3}}{\left(1-\alpha_{ch}^{-2}\right)^2} - 1\right)\bar{I}_{ij}, \\
K_{ij} =& \lambda_j^4\bar{A}_{ij} + \gamma\bar{B}_{ij} - \frac{1}{2}\varepsilon c_f u_o^2(1+h)\bar{C}_{ij} - u_o^2(1+K_1)s_t\bar{D}_{ij} \\
&+ \frac{1}{2}u_o^2(1+K_1)\bar{S}^2\bar{F}_{ij} - \frac{1}{2}u_o^2(1+K_1)\bar{H}_{ij} + u_i^2\bar{F}_{ij} \\
&+ u_o^2\bar{H}_{ij} + (\chi - 1)u_o^2\bar{L}_{ij} - (\Gamma - \Pi_{iL} + \Pi_{oL})\bar{F}_{ij} \\
&- \gamma(\bar{F}_{ij} - \bar{J}_{ij}) + \frac{1}{2}\varepsilon c_f u_o^2(1+h)\bar{E}_{ij},
\end{aligned} \tag{5.48}$$

where the constants $\bar{A}_{ij}$, $\bar{B}_{ij}$, $\bar{C}_{ij}$, $\bar{D}_{ij}$, $\bar{E}_{ij}$, $\bar{F}_{ij}$, $\bar{H}_{ij}$, $\bar{I}_{ij}$, $\bar{J}_{ij}$, $\bar{K}_{ij}$ and $\bar{L}_{ij}$ are defined by

$$\begin{aligned}
\bar{A}_{ij} &= \int_0^1 \phi_i\phi_j \,\mathrm{d}\xi, \quad \bar{B}_{ij} = \int_0^1 \phi_i\phi_j' \,\mathrm{d}\xi, \quad \bar{C}_{ij} = \int_0^1 \phi_i\phi_j' S^2 \,\mathrm{d}\xi, \\
\bar{D}_{ij} &= \int_0^1 \phi_i\phi_j'\left(\mathrm{e}^{s_t(r_{ann}-\xi)}\right)S^{*3} \,\mathrm{d}\xi, \quad \bar{E}_{ij} = \int_0^1 G\phi_i\phi_j'' \,\mathrm{d}\xi, \\
\bar{F}_{ij} &= \int_0^1 \phi_i\phi_j'' \,\mathrm{d}\xi, \quad \bar{H}_{ij} = \int_0^1 \phi_i\phi_j'' S^2 \,\mathrm{d}\xi, \\
\bar{I}_{ij} &= \int_0^1 \phi_i\phi_j S \,\mathrm{d}\xi, \quad \bar{J}_{ij} = \int_0^1 \xi\phi_i\phi_j'' \,\mathrm{d}\xi, \quad \bar{K}_{ij} = \int_0^1 \phi_i\phi_j' S \,\mathrm{d}\xi, \\
\bar{L}_{ij} &= \int_0^1 \phi_i\phi_j'' S^3 \,\mathrm{d}\xi.
\end{aligned} \tag{5.49}$$

Model 3:

$$
\begin{aligned}
M_{ij} &= a_{ij\,(0,1)} - \beta_o(1-\chi)a_{ij\,(0,r_{ann})},\\
C_{ij} &= 2u_i\sqrt{\beta_i}b_{ij\,(0,1)} - 2\chi u_{o,1}\sqrt{\beta_o}b_{ij\,(0,r_{ann})} - 2u_{o,2}\sqrt{\beta_o}b_{ij\,(r_{ann},1)}\\
&\quad + \frac{1}{2}u_{o,1}\varepsilon c_f\sqrt{\beta_o}a_{ij\,(0,r_{ann})} + \frac{1}{2}u_{o,2}\varepsilon c_f\sqrt{\beta_o}a_{ij\,(r_{ann},1)}\\
&\quad + \kappa_u a_{ij\,(0,1)} + \kappa_u\left[\frac{1+\alpha_{ch}^{-3}}{(1-\alpha_{ch}^{-2})^2} - 1\right]a_{ij\,(0,r_{ann})},\\
K_{ij} &= \lambda_j^4 a_{ij\,(0,1)} + \gamma b_{ij\,(0,1)} - \frac{1}{2}u_{o,1}^2\varepsilon c_f h b_{ij\,(0,r_{ann})}\\
&\quad - \frac{1}{2}u_{o,1}^2\varepsilon c_f b_{ij\,(0,r_{ann})} - \frac{1}{2}u_{o,2}^2\varepsilon c_f b_{ij\,(r_{ann},1)}(1+h^*)\\
&\quad - \frac{1}{2}u_{o,1}^2(1+K_1)(\phi_i|_{\xi=r_{ann}}\phi_j'|_{\xi=r_{ann}}) - (\Gamma - \Pi_{iL} + \Pi_{oL})c_{ij\,(0,1)}\\
&\quad - \gamma(c_{ij\,(0,1)} - d_{ij\,(0,1)}) + \frac{1}{2}u_{o,1}^2\varepsilon c_f(1+h)(r_{ann}c_{ij\,(0,1)} - d_{ij\,(0,1)})\\
&\quad - \frac{1}{2}u_{o,2}^2\varepsilon c_f(1+h^*)(1-r_{ann})c_{ij\,(0,1)} + \frac{1}{2}u_{o,2}^2\varepsilon c_f(1+h^*)(d_{ij\,(r_{ann},1)}\\
&\quad - r_{ann}c_{ij\,(r_{ann},1)}) + \frac{1}{2}u_{o,1}^2(1+K_1^2)c_{ij\,(0,r_{ann})} + u_i^2 c_{ij\,(0,1)}\\
&\quad + \chi u_{o,1}^2 c_{ij\,(0,r_{ann})} + u_{o,2}^2 c_{ij\,(r_{ann},1)},
\end{aligned}
\tag{5.50}
$$

where a_{ij}, b_{ij}, c_{ij} and d_{ij} are the same as defined in Eq. (5.47).

5.2.5 Theoretical results obtained by Model 1

A flexible pipe with dimensions and material properties identical to those in Table 5–1 is considered for the theoretical analysis to allow comparison between the results to be obtained and the experimental data. A rigid tube of 206.5 mm length and 31.5 mm diameter is considered to surround the pipe at its upper portion, as in the experiments. The corresponding dimensionless system parameters are listed in Table 5–3. In addition, the friction coefficients in the normal and tangential directions are assumed to have the same value, $c_f = 0.0125$.

In general, the results obtained using the linear theoretical models developed in this study are presented in the form of Argand diagrams, in which the imaginary part of the eigenfrequencies, $\mathrm{Im}(\omega_j)$, is plotted versus the real part, $\mathrm{Re}(\omega_j)$, with increasing u_i to u_{cr}

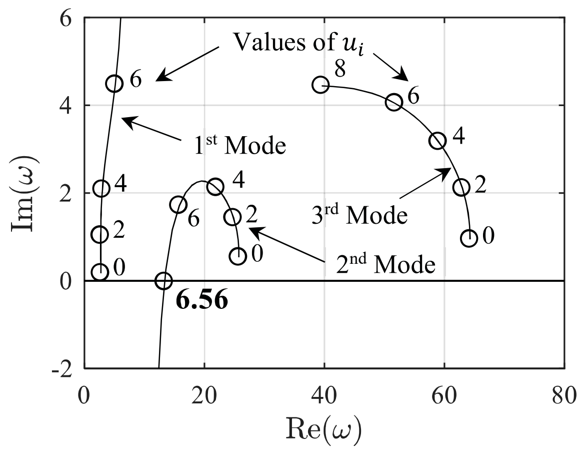

Figure 5–17: Argand diagram obtained via Model 1 for $U_o/U_i = 0.055$.

Table 5–3: Dimensionless parameters of the system under study.

α	β_i	β_o	γ	ε	α_{ch}	h	r_{ann}
0.397	7.47×10^{-2}	0.475	2.69	27.56	1.97	1.03	0.468

and beyond, where u_{cr} is the dimensionless critical flow velocity for instability. In these Argand diagrams, the number of comparison functions utilized in the Galerkin scheme has been increased until convergence was achieved; in this case, eight modes were sufficient.

Figure 5–17 shows an Argand diagram obtained via Model 1 for U_o/U_i=0.055. The first three modes are plotted in this figure. With increasing internal flow velocity, u_i, the first and the third mode remain stable and the associated damping of the system, represented by Im(ω), is increasing. However, the second mode becomes unstable via a Hopf bifurcation at $u_i = 6.56$. Thus, it is predicted that the pipe loses stability by flutter in the second mode at $u_{cr} = 6.56$.

The Argand diagrams calculated for higher ratios of $U_o/U_i = 0.2$, 0.4, 0.6, and 0.8 are shown in Fig. 5–18. Clearly, increasing the ratio of U_o/U_i has a severe destabilizing effect on the system, causing the critical flow velocity for instability, u_{cr}, to decrease dramatically. Interestingly, increasing the ratio to $U_o/U_i = 0.4$ and higher results in increasing the critical frequency of oscillation, i.e. the value of Re(ω) at the onset of flutter, $u_i = u_{cr}$.

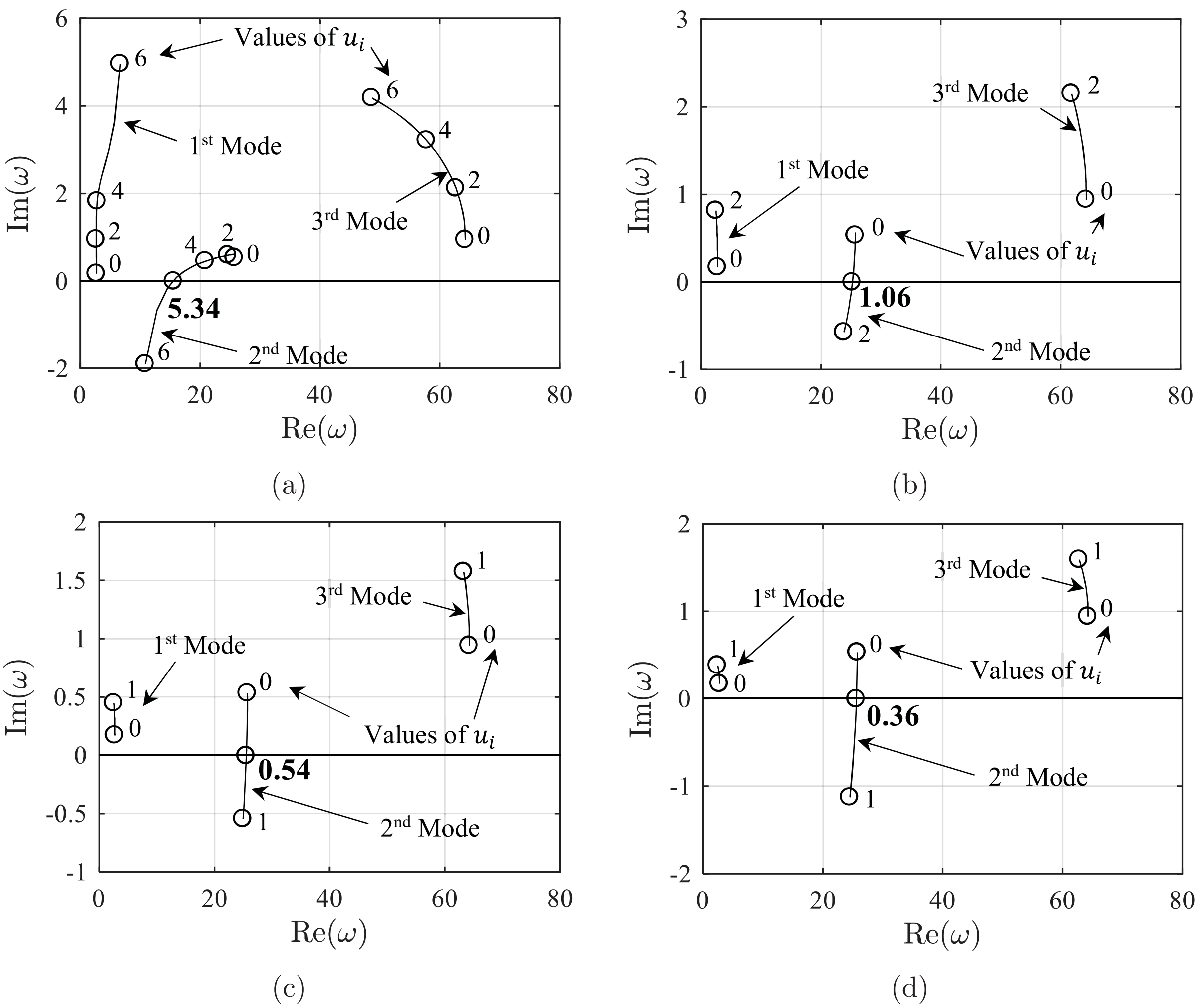

Figure 5–18: Argand diagrams obtained via Model 1 for: (a) $U_o/U_i = 0.2$, (b) $U_o/U_i = 0.4$, (c) $U_o/U_i = 0.6$, and (d) $U_o/U_i = 0.8$.

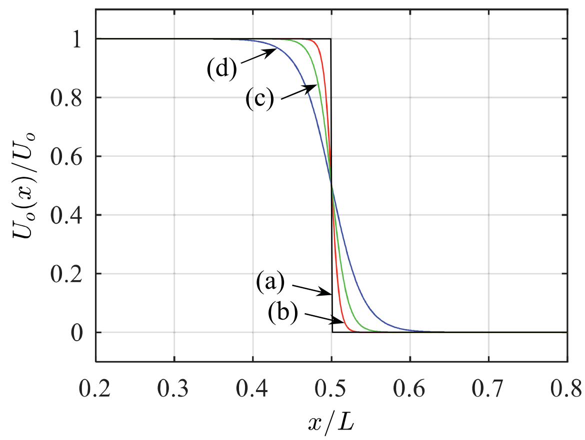

Figure 5–19: Comparison between (a) the Heaviside step function and (b,c,d) logistic functions with steepness $s_t = 200$ in (b), $s_t = 100$ in (c) and $s_t = 50$ in (d).

5.2.6 Theoretical results obtained by Model 2

The main difference between Model 2 and Model 1, is that the logistic function is utilized instead of the Heaviside step function to model the discontinuity in the external flow velocity that occurs once the flow becomes confined. The steepness parameter, s_t, defined in Eq. (5.23) controls how smooth the transition in the external flow velocity, $U_o(x)$, is; the higher the value of s_t is, the closer it becomes to the Heaviside step function, as shown in Fig. 5–19.

Since the exact value of s_t is very hard to determine either experimentally or theoretically, different estimated values are tested to understand its effect on the dynamical behaviour of the system. A relatively high value of the steepness, $s_t = 200$, which is very close to the Heaviside step function, as seen in Fig. 5–19, is chosen to start with. An Argand diagram calculated for $U_o/U_i = 0.055$ is shown in Fig. 5–20. The first and third mode remain stable with increasing u_i, but the second mode becomes unstable via a Hopf bifurcation at $u_{cr} = 6.58$, which is very close to the value obtained by Model 1; i.e. $u_{cr} = 6.56$, as shown in Fig. 5–17.

For higher ratios of U_o/U_i, Argand diagrams obtained by assuming $s_t = 200$ are presented in Fig. 5–21. Similar to what was concluded previously for Fig. 5–18, increasing the ratio of U_o/U_i results in lower values of u_{cr}. Also, utilizing the logistic function generally

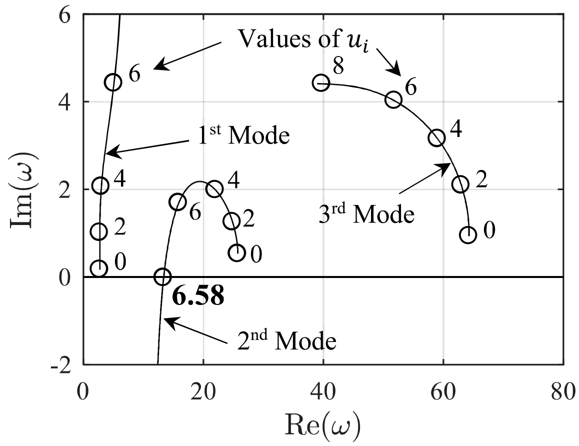

Figure 5–20: Argand diagram obtained via Model 2 for $U_o/U_i = 0.055$, assuming $s_t = 200$.

results in higher u_{cr} for $U_o/U_i \leq 0.4$ and lower u_{cr} for $U_o/U_i \geq 0.6$ with respect to the results obtained by the Heaviside step function.

Lower values of the steepness parameter, i.e. $s_t = 100$ and $s_t = 50$, are also tested in this study. The results obtained for the different ratios of U_o/U_i and s_t are all summarized in Table 5–4.

Table 5–4: Summary of the theoretical results obtained via Model 2.

	$s_t = 200$		$s_t = 100$		$s_t = 50$	
U_o/U_i	u_{cr}	f_{cr} (Hz)	u_{cr}	f_{cr} (Hz)	u_{cr}	f_{cr} (Hz)
0.055	6.58	1.44	6.58	1.44	6.59	1.44
0.2	6.25	1.26	6.27	1.27	6.32	1.28
0.4	1.20	2.71	1.24	2.71	1.39	2.69
0.6	0.46	2.75	0.46	2.76	0.49	2.75
0.8	0.29	2.76	0.29	2.76	0.31	2.76

For the system with $U_o/U_i = 0.055$, varying the value of s_t has almost no influence on u_{cr} nor f_{cr}. However, an increase in u_{cr} with decreasing s_t is noticed for higher ratios of U_o/U_i in Table 5–4.

5.2.7 Theoretical results obtained by Model 3

The only difference between this model and Model 1 is that a non-zero value is given for the external flow velocity outside the annular region, $U_{o,2} \neq 0$. Unfortunately, there is no simple way to determine the exact value of $U_{o,2}$ for the different ratios of $U_{o,1}/U_i$.

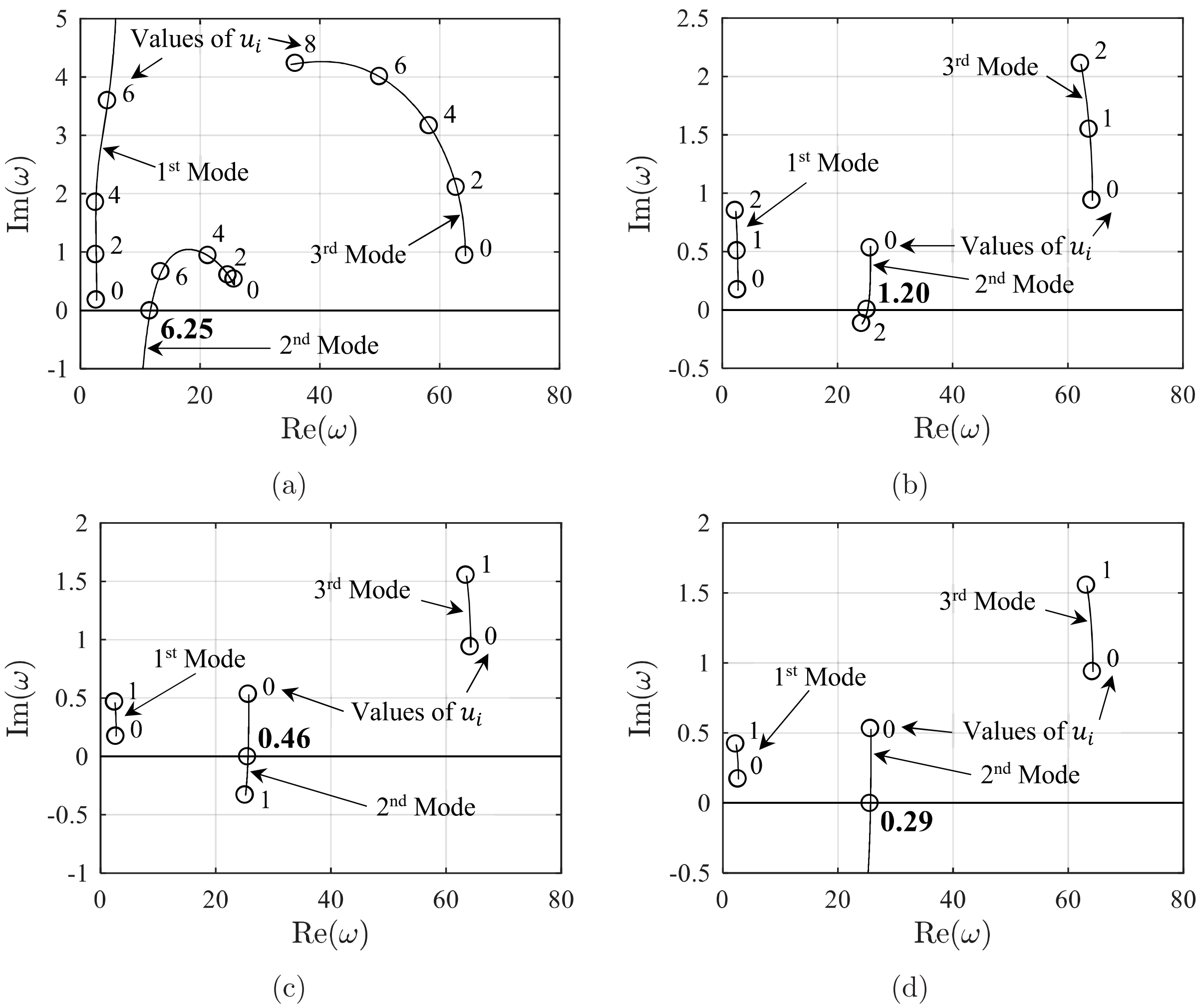

Figure 5–21: Argand diagrams obtained via Model 2 for: (a) $U_o/U_i = 0.2$, (b) $U_o/U_i = 0.4$, (c) $U_o/U_i = 0.6$, and (d) $U_o/U_i = 0.8$, assuming $s_t = 200$.

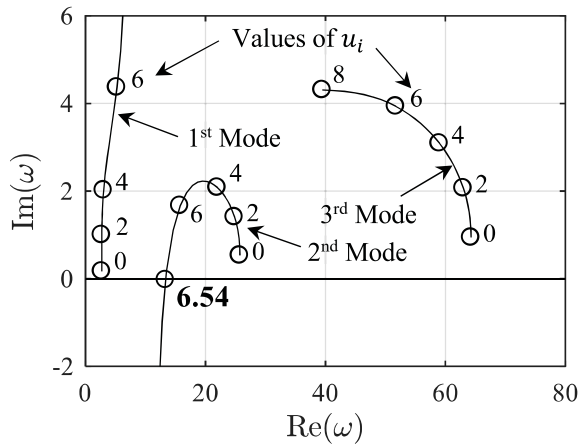

Figure 5–22: Argand diagram obtained via Model 3 for $U_{o,1}/U_i = 0.055$, assuming $U_{o,2}/U_{o,1} = 0.1$.

Thus, an estimated value will be used, just to provide an idea about the behaviour of the model, when $U_{o,2} \neq 0$. Additionally, some preliminary computational fluid dynamics (CFD) simulation trials conducted by the author, which are not presented in this thesis, suggest that $U_{o,2}/U_{o,1} = 0.1$ may be a reasonable approximation. Thus, $U_{o,2}$ and $U_{o,1}$ are assumed to be in the same direction; i.e. from the free end towards the clamped one, which could also be justified by the fact that the additional flow is added to the pressure vessel from the bottom and exits from the top with appreciable flow rates, especially for high ratios of $U_{o,1}/U_i$.

For the original system, in which the ratio of $U_{o,1}/U_i = 0.055$, an Argand diagram is shown in Fig. 5–22. Almost no difference between Fig. 5–22 and Fig. 5–17 can be noted, except that the value of u_{cr} becomes slightly smaller, $u_{cr} = 6.54$ versus 6.58.

Figure 5–23 shows the Argand diagrams calculated for higher ratios of $U_{o,1}/U_i$ via Model 3, assuming $U_{o,2}/U_{o,1} = 0.1$. One can notice a decrease in the values of u_{cr} as compared to the Argand diagrams shown in Fig. 5–18. Therefore, it can be generally concluded that considering a non-zero value for the external flow velocity outside the annulus, in the same direction as the flow velocity inside the annulus, has a destabilizing effect on the system.

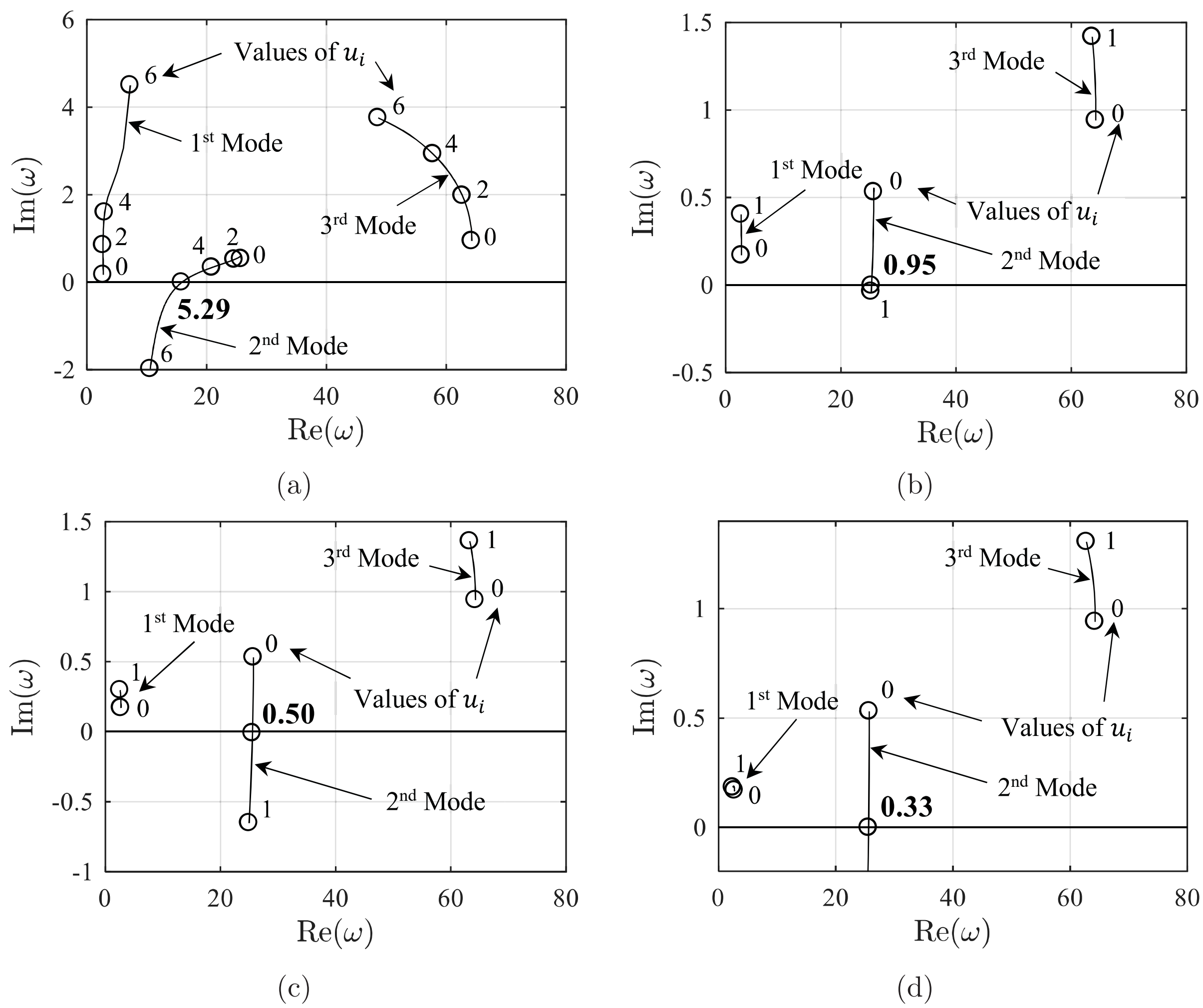

Figure 5–23: Argand diagrams obtained via Model 3 for: (a) $U_{o,1}/U_i = 0.2$, (b) $U_{o,1}/U_i = 0.4$, (c) $U_{o,1}/U_i = 0.6$, and (d) $U_{o,1}/U_i = 0.8$, assuming $U_{o,2}/U_{o,1} = 0.1$.

5.3 Comparison between experimental observations and theoretical results

In general, the predictions of the theoretical models are in good qualitative agreement with the experimental observations for most of the ratios tested for U_o/U_i. The pipe is found to lose stability via flutter in the second mode at a sufficiently high internal flow velocity for $U_o/U_i = 0.055$, and the critical flow velocity of instability decreases with increasing U_o/U_i.

Table 5–5 summarizes the experimental and theoretical results obtained in this study for different ratios of U_o/U_i; it is seen that a reasonable quantitative agreement generally exists between the experimental and theoretical results.

Table 5–5: Summary of the experimental and theoretical results obtained for different ratios of U_o/U_i.

	Experiments		Model 1		Model 2 $s_t = 200$		Model 3 $U_{o,2}/U_{o,1} = 0.1$	
U_o/U_i	u_{cr}	f_{cr} (Hz)	u_{cr}	f_{cr} (Hz)	u_{cr}	f_{cr} (Hz)	u_{cr}	f_{cr} (Hz)
0.055	5.13	1.37	6.56	1.44	6.58	1.44	6.54	1.44
0.2	1.61	2.09	5.34	1.68	6.25	1.26	5.29	1.71
0.4	0.91	2.69	1.06	2.72	1.20	2.71	0.95	2.73
0.6	0.56	2.55	0.54	2.75	0.46	2.75	0.50	2.76
0.8	0.32*, 0.52	0.35*, 2.25	0.36	2.76	0.29	2.76	0.33	2.76

The asterisk (*) denotes flutter-like oscillations in the first mode of the pipe.

For a ratio of $U_o/U_i = 0.055$, all the theoretical models predict almost the same value for the critical flow velocity and frequency of oscillation. However, they overestimate the onset of instability with respect to the experiments by approximately 28%; they also overestimate the frequency, but by only 5%.

The most significant discrepancy between the results of the theoretical models and experiments is for the ratio of $U_o/U_i = 0.2$. The onset of instability predicted theoretically is three to four times higher than what was observed experimentally. However, the results of Model 3 are the closest ones to the experimental observations, which encouraged the author to undertake calculations with $U_{o,2}/U_{o,1}$ higher than 0.1 and examine the effect on the stability of the system. As seen in Table 5–6, increasing the $U_{o,2}/U_{o,1}$ ratio decreases the onset of instability; yet, increasing it to a relatively high value, to the unrealistic value of $U_{o,2}/U_{o,1} = 0.5$, is still insufficient to come close to the u_{cr} observed experimentally.

Table 5–6: Critical flow velocity for instability, u_{cr}, obtained by Model 3 for $U_{o,1}/U_i = 0.2$ considering different values for the improvement ratio, $U_{o,2}/U_{o,1}$.

$U_{o,2}/U_{o,1}$	0	0.1	0.2	0.3	0.4	0.5
u_{cr}	5.34	5.29	5.16	4.73	3.92	3.24

For a ratio of $U_o/U_i = 0.4$, excellent agreement between the results of Model 3 and the experiments is predicted, with a difference less than 5% for both u_{cr} and f_{cr}. Model 1, without any improvements, is also successful in predicting the values of f_{cr} almost exactly, and u_{cr} with a difference of approximately 16%. However, Model 2 overestimates that onset with a difference $> 30\%$.

Moreover, very good agreement between Model 1 and the experiments can be observed in Table 5–6 for $U_o/U_i = 0.6$; the difference between theory and experiments is 4% for u_{cr} and 8% for f_{cr}. Model 3 also predicts the same value of f_{cr} as Model 1, but underestimates u_{cr} by 10% with respect to the experiments.

For a ratio of $U_o/U_i = 0.8$, the models predict loss of stability via flutter in the second mode of the pipe at $u_i \approx 0.3$. However, near that value, weak flutter-like oscillations in the first mode of the pipe were observed experimentally. All the models underestimate the onset of second-mode flutter with respect to the experiments; however, one can say that Model 1 is the most successful with 30% difference for u_{cr} and 23% difference for f_{cr}.

One can also examine the performance of Model 3 for the same ratio of $U_{o,1}/U_i = 0.8$, but with higher $U_{o,2}/U_{o,1}$ ratio. For such a high ratio of $U_{o,1}/U_i$, Q_a is quite large and thus $U_{o,2}$ could probably be higher than just $0.1U_{o,1}$. Table 5–7 shows the results obtained for higher ratios of $U_{o,2}/U_{o,1}$. As seen in the table, increasing $U_{o,2}/U_{o,1}$ decreases the onset of second mode flutter, and results in flutter in the first mode as well, but at higher flow velocity. However, for $U_{o,2}/U_{o,1} = 0.5$, the first mode becomes unstable first at $u_{cr,1} = 0.22$,

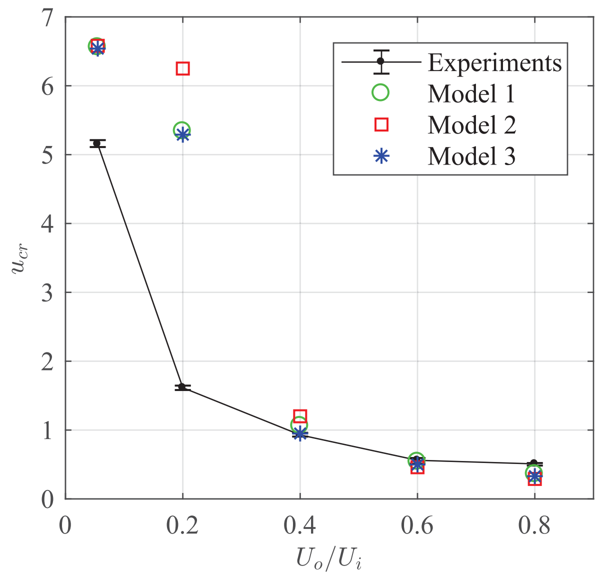

Figure 5–24: Dimensionless critical flow velocity, u_{cr}, for second-mode flutter obtained by taking the average of three experimental observations for each ratio of U_o/U_i, as well as theoretical values obtained by using Model 1, Model 2 with $s_t = 200$, and Model 3 assuming $U_{o,2}/U_{o,1} = 0.1$.

and the second mode becomes unstable right after that at $u_{cr,2} = 0.26$; but these values are considerably lower than those observed experimentally.

Table 5–7: Critical flow velocity for the first instability, $u_{cr,1}$, and the second one $u_{cr,2}$ predicted by Model 3 for $U_{o,1}/U_i = 0.8$ considering different values for the improvement ratio, $U_{o,2}/U_{o,1}$.

$U_{o,2}/U_{o,1}$	0	0.1	0.2	0.3	0.4	0.5
$u_{cr,1}$	0.36**	0.33**	0.31**	0.29**	0.27**	0.22*
$u_{cr,2}$	-	-	0.94*	0.47*	0.30*	0.26**

(*) denotes flutter in the first mode of the pipe, and (**) denotes flutter in the second mode.

Furthermore, since experiments were repeated three times for each ratio of U_o/U_i to ensure consistency of the results; the mean, maximum, and minimum values for the critical flow velocity for flutter and the corresponding frequency of oscillation recorded in the three experiments are plotted in Figs. 5–24 and 5–25. The predictions of all different versions of the theory are also plotted in the same figures for comparison with experimental observations.

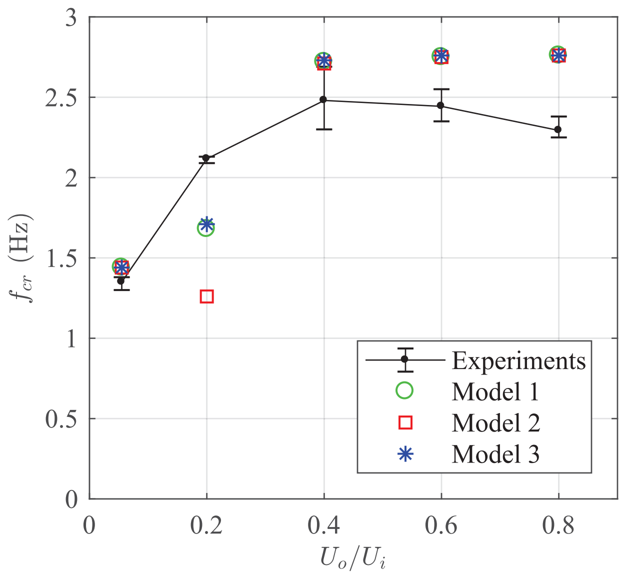

Figure 5–25: Critical frequency of oscillation, f_{cr}, for second-mode flutter obtained by taking the average of three experimental observations for each ratio of U_o/U_i, as well as theoretical values obtained by using Model 1, Model 2 with $s_t = 200$, and Model 3 assuming $U_{o,2}/U_{o,1} = 0.1$.

5.4 Summary

Experiments have been conducted for System III using the SMRI/PRCI apparatus in the Department of Mechanical Engineering at McGill University. A silicone-rubber pipe of 6.35 mm inner diameter, 16 mm outer diameter and 441 mm length, surrounded by a rigid tube of 31.5 mm inner diameter and 206.5 mm length, was tested. Two pumps were utilized to control the ratio of external to internal flow velocities, $r = U_o/U_i$. Five different values of r were examined, namely $r = 0.055$, 0.2, 0.4, 0.6, and 0.8, and for each ratio, three experiments were conducted. In all experiments the pipe exhibited second mode flutter at a specific dimensionless critical flow velocity, u_{cr}. It was found that increasing r decreases u_{cr}, and may result in flutter in the first mode of the pipe at a higher r, i.e. $r = 0.8$. Moreover, increasing the ratio up to $r = 0.4$ increases the critical frequency of oscillation, f_{cr}; however, further increase in r decreases f_{cr} slightly.

A linearized form of the nonlinear model developed for System III in Chapter 4, i.e. Model 1, was utilized to determine the critical flow velocity and the corresponding frequency of oscillation for each r. In addition, another model was developed by utilizing the logistic function instead of the Heaviside step function to model the discontinuity in the external flow at the entrance of the annulus (Model 2). Also, a non-zero value for the external flow below the annulus was proposed in the derivation of Model 3, and the Heaviside step function was utilized to incorporate its effects. The predictions of all three models are compared to the experimental observations for each r. Apart from $r = 0.2$, a reasonable to good qualitative and quantitative agreement between the different versions of the theory and experiments is observed, with Model 1 being more or less the most successful.

CHAPTER 6
Conclusions and suggested future work

In this thesis, nonlinear analytical models that encompass nonlinear structural dynamics as well as nonlinear treatment of the fluid mechanics have been developed for three different systems, namely (i) a cantilevered cylinder generally fitted with an ogival end-piece and subjected to inverted axial flow, i.e. flow directed from the free end of the cylinder towards the clamped one (System I); (ii) a hanging tubular cantilever discharging fluid downwards, which then flows upwards as a fully-confined external axial flow (System II); (iii) a hanging cantilevered pipe discharging fluid with partially-confined inverted axial flow, i.e. confined only over the upper portion of the pipe (System III). The three nonlinear models are derived in a Hamiltonian framework with separate derivation for the fluid-related forces acting on the cantilevers. The partial differential equations of motion obtained in this study are weakly nonlinear, since they are exact only to third-order of magnitude.

For all three models, the equation of motion was discretized using Galerkin's technique to a set of ordinary differential equations that were solved via the pseudo-arclength continuation method and a direct time integration technique. Bifurcation analysis was conducted for each system, and the critical flow velocity for instability was determined. Also, the nonlinear dynamics of each system was examined at different flow velocities by means of phase-plane and power-spectral-density plots; limit cycle amplitude and frequency as well as the shapes of the cantilever while oscillating were plotted for each system at different flow velocities. In addition, the influence of various system parameters on the dynamics and stability of these systems was investigated theoretically. In all cases, convergence was ensured by employing a sufficiently large number of comparison functions utilized in the Galerkin scheme. Moreover, the results obtained were compared to experimental observations from the literature.

New experiments were conducted for the third system considered in order to explore the influence of increasing the ratio of external to internal flow velocities on stability of the system. The experimental observations were compared to the predictions of a linearized form of the model derived for System III. Furthermore, improvements were proposed to the theory, and the predictions of different linear models for different ratios of external to internal flow velocities were compared to one another.

In the following, a summary of findings for each system is presented, as well as suggestions for future work.

6.1 Summary of findings

6.1.1 System I

In Chapter 2, a flexible cantilevered cylinder hanging vertically, terminated with a more or less well-streamlined end, and subjected to inverted axial air-flow was considered. The nonlinear model developed in this study predicts that such a system loses stability via flutter in the first mode at a flow velocity, $u^* = 1.63$. The mechanism leading to flutter was found to be a saddle node bifurcation, which requires sufficiently large perturbation of the cylinder. Increasing the flow velocity to $u^* > 1.63$ decreases the amplitude and frequency of oscillation, and leads to a static divergence (buckling) at $u^* = 2.69$. Post-divergence flutter, also in the first mode of the cylinder, is predicted, starting with oscillations around the buckled position, then *mainly* around the origin with increasing flow velocity.

The predictions of the proposed nonlinear model are in very good qualitative agreement with experimental observations from the literature. However, quantitatively, some discrepancies were noticed. Firstly, the flutter observed experimentally occurred at vanishing flow velocities, and its amplitude was lower than that predicted by the present model. Secondly, in experiments, at $u^* = 1.64 - 1.70$ the cylinder was found to undergo static divergence, flutter was predicted by this model at $u^* = 1.63$.

Nevertheless, the predictions of the proposed model are closer to the experimental observations than predictions of an earlier linear theory, which is only capable of capturing the static instability at a considerably high flow velocity, $u^* \approx 2.66$.

The findings of Chapter 2 have been published in the Journal of Fluids and Structures, i.e. Ref. [119].

6.1.2 System II

In Chapter 3, a cantilevered pipe discharging fluid downwards, which then flows upwards as a confined axial flow was considered. For a bench-top-sized system, the pipe was found to lose stability via flutter in the first mode at a relatively low flow velocity, $u_i = 0.39$. A regular periodic motion of the pipe was predicted, which becomes more pronounced with higher amplitude and frequency at higher flow velocities. The influence of various system parameters on the dynamics of the system was investigated; it was found that increasing the degree of confinement of external flow or mass ratio destabilizes the system. On the other hand, increasing the thickness of the pipe or gravity stabilizes the system. Moreover, it was found that the friction and form-drag coefficients do not have significant effects on the onset of instability for this system.

The equation of motion was also solved using parameters corresponding to another experimental set-up, from the literature. Although weak flutter-like oscillations were observed experimentally at very low flow velocities, which may be due to turbulence in the flow, a sudden change in the amplitude of oscillations was reported at $u_i \approx 1.80$, which also exists in other experiments with different parameters. This suggested to this author that the sudden change in the amplitude may be due to fluidelastic instability, namely flutter, occurring at that particular flow velocity rather than at vanishing flow velocities. The proposed model also predicts flutter in the first mode of the pipe at $u_i = 1.88$, quite close to the experimental value, and considerably lower than that predicted by another linear theory from the literature, namely $u_i = 2.25$. Moreover, the critical frequency of oscillation predicted by the proposed model is in excellent agreement with the one observed experimentally.

The derivation of the model, the nonlinear dynamics of the pipe at different flow velocities, and the parametric study were published in the Journal of Sound and Vibration, i.e. Ref. [121]. A comparison between theory and experiments was presented in the 9th International Symposium on Fluid-Structure Interactions, Flow-Sound Interactions, Flow-Induced Vibration & Noise, i.e. Ref. [124].

6.1.3 System III

In Chapter 4, a cantilevered pipe discharging fluid downwards with reverse partially-confined external axial (annular) flow over its upper portion was considered. Two pipes of different dimensions and material characteristics were considered, as well as several rigid tubes (containing the confined external flow) of different lengths and internal diameters. In general, the pipe was found to lose stability via flutter in the second mode at sufficiently high flow velocities, $u_i > 6.0$. Good to excellent qualitative and quantitative agreement between theoretical predictions and experimental observations from the literature was found in terms of the critical flow velocities and frequencies of oscillation, especially for the pipe with a higher slenderness ratio. However, the proposed model overestimates the amplitude of oscillation for the shorter annuli. A considerable improvement was achieved in predicting theoretically the frequency of oscillation with respect to experiments, as compared to linear theory.

The influence of varying the length and diameter of the rigid tube was found to be as follows: increasing the length destabilizes the system and decreases the amplitude of oscillation at any given flow velocity; on the other hand, decreasing the diameter of the outer tube (resulting in a tighter annulus) destabilizes the system and can result in flutter in the first mode instead of the second, if the length of the rigid tube is sufficiently high (the same mode of instability predicted for System II).

The results obtained for System III via the nonlinear model were published in the International Journal of Non-Linear Mechanics, i.e. Ref. [125].

In Chapter 5, new sets of experiments have been conducted to understand the significance of the external flow in System III. Different ratios of external to internal flow velocities, r, have been examined; for each ratio r, the internal and external flow velocities were increased utilizing two pumps, while maintaining r constant throughout the experiment. It was found that increasing r destabilizes the system drastically; this may result in flutter in the first mode of the pipe before that in the second mode.

In addition, a linear theoretical analysis has been conducted to support the experimental observations. The pipe was found to lose stability via flutter in the second mode for all the values of r examined. The critical flow velocities and frequencies of oscillation were found to be in good agreement with experimental observations. Moreover, two different methods were proposed to improve the model: (i) modelling the discontinuity in the external flow velocity that occurs as the fluid enters the annulus via a smoother function, namely the logistic function, instead of the Heaviside step function; and (ii) considering a non-zero value for the external axial flow velocity over the unconfined region, i.e. below the annulus. These improvements were tested and the theoretical predictions were compared to those of the original model. Generally, one can conclude that the performance of the original model is quite acceptable; yet, considering a non-zero value for the flow velocity below the annulus can help in obtaining results closer to the experimental ones.

The linear model developed for System III using the logistic function was published in the Proceedings of the International Design Engineering Technical Conferences & Computers and Information in Engineering Conference (organized by the American Society of Mechanical Engineers), i.e. Ref. [118]. The model was also used to predict the critical flow velocities and frequencies of oscillation for different values of r in Ref. [126].

6.2 Future work

For System I, it would be interesting to conduct new experiments and apply external perturbations to the cylinder at low flow velocities, to examine whether the cylinder would undergo a saddle-node bifurcation as predicted by the proposed theory. Besides, the flow velocity should be increased to higher values, so as to explore and analyse post-divergence oscillations. Experiments should also be conducted in water flow, and the performance of the model tested for such a mass ratio. Moreover, a parametric study could be implemented, utilizing the proposed model to investigate the influence of several system parameters on the dynamics of the system, e.g. slenderness, gravity, confinement of the flow, and the shape of the free end of the cylinder.

For System II, fresh experiments are needed, perhaps with different designs of the holding tank to allow more room for the discharging fluid before it impacts the bottom of the tank; this may help in avoiding the weak oscillations occurring at very low flow velocities. In addition, different degrees of confinement for the external flow should be tested experimentally. All this work can be used in evaluating and improving the performance of the nonlinear model proposed in this study.

For System III, the performance of the nonlinear model can be tested for different ratios of external to internal flow velocities. Additionally, some computational fluid dynamics (CFD) simulations could be conducted for a better understanding of the fluid part of the problem, such as estimating the magnitude and direction of the flow velocity below the annulus, determining pressure loss coefficients for the fluid once it exits the pipe or enters the annulus, and exploring how smoothly the flow velocity increases once the fluid becomes confined. Furthermore, calculations should be done for full-scale salt-mined caverns.

New experiments could also be conducted for System III for different ratios of external to internal flow velocities and by using outer rigid tubes of different lengths and internal diameters. The theory developed in this thesis could be tested using these system parameters, which would help in exploring the limitations of this theory.

Appendix A

The nonlinear coefficients of the discretized equation of motion, i.e. Eq. (2.36), are given here, as follows:

$$
\begin{aligned}
r_{ijk} =& \frac{1}{2} u^{*2} \varepsilon c_d \int_0^1 \phi_i \phi_j' |\phi_k'| \, \mathrm{d}\xi, \\
\bar{s}_{ijk} =& \frac{1}{2} u^* \sqrt{\beta} \varepsilon c_d \int_0^1 \phi_i |\phi_j'| \phi_k \, \mathrm{d}\xi, \\
\tilde{s}_{ijk} =& \frac{1}{2} u^* \sqrt{\beta} \varepsilon c_d \int_0^1 \phi_i \phi_j' |\phi_k| \, \mathrm{d}\xi, \\
t_{ijk} =& \frac{1}{2} \beta \varepsilon c_d \int_0^1 \phi_i \phi_j |\phi_k| \, \mathrm{d}\xi, \\
\alpha_{ijkl} =& 2\chi u^{*2} \int_0^1 \phi_i \phi_j'' \phi_k' \phi_l' \, \mathrm{d}\xi + \left(\frac{1}{2} u^{*2} \varepsilon (-c_N - c_T h) + \gamma\right) \frac{1}{2} \int_0^1 \phi_i \phi_j' \phi_k' \phi_l' \, \mathrm{d}\xi \\
& + \left(\frac{1}{2} u^{*2} \varepsilon c_T (1+h) - \gamma\right) \frac{3}{2} \int_0^1 (1-\xi) \phi_i \phi_j' \phi_k' \phi_l'' \, \mathrm{d}\xi \\
& + 4 \int_0^1 \phi_i \phi_j' \phi_k'' \phi_l''' \, \mathrm{d}\xi + \int_0^1 \phi_i \phi_j'' \phi_k'' \phi_l'' \, \mathrm{d}\xi + \int_0^1 \phi_i \phi_j'''' \phi_k' \phi_l' \, \mathrm{d}\xi \\
& - \chi u^{*2} \int_0^1 \phi_i \phi_j'' \left(\int_\xi^1 \phi_k' \phi_l'' \, \mathrm{d}\xi \right) \mathrm{d}\xi \\
& - \frac{1}{2} u^{*2} c_b \int_0^1 \phi_i \phi_j'' \left(\int_\xi^1 \phi_k' \phi_l'' \, \mathrm{d}\xi \right) \mathrm{d}\xi + \frac{1}{2} u^{*2} c_b \int_0^1 \phi_i \phi_j' \phi_k' \phi_l'' \, \mathrm{d}\xi \\
& - \frac{1}{2} u^{*2} \varepsilon (c_T - c_N) \int_0^1 \phi_i \phi_j'' \left(\int_\xi^1 \phi_k' \phi_l' \, \mathrm{d}\xi \right) \mathrm{d}\xi, \\
\beta_{ijkl} =& \chi u^* \sqrt{\beta} \Bigg\{ \frac{1}{2} \int_0^1 \phi_i \phi_j' \phi_k' \phi_l' \, \mathrm{d}\xi + \frac{3}{2} \int_0^1 \phi_i \phi_j'' \phi_k' \phi_l \, \mathrm{d}\xi + 2 \int_0^1 \phi_i \phi_j'' \left(\int_\xi^1 \phi_k' \phi_l' \, \mathrm{d}\xi \right) \mathrm{d}\xi \\
& - 2 \int_0^1 \phi_i \phi_j'' \left(\int_0^\xi \phi_k' \phi_l' \, \mathrm{d}\xi \right) \mathrm{d}\xi \Bigg\} - \frac{1}{4} u^* \sqrt{\beta} \varepsilon c_N \int_0^1 \phi_i \phi_j' \phi_k' \phi_l \, \mathrm{d}\xi \\
& + \frac{1}{2} u^* \sqrt{\beta} \varepsilon (c_T - c_N) \int_0^1 \phi_i \phi_j'' \left(\int_\xi^1 \phi_k' \phi_l \, \mathrm{d}\xi \right) \mathrm{d}\xi \\
& - 3\chi u^* \sqrt{\beta} \int_0^1 \phi_i \phi_j' \left(\int_0^\xi \phi_k' \phi_l'' \, \mathrm{d}\xi \right) \mathrm{d}\xi - 3\chi u^* \sqrt{\beta} \int_0^1 \phi_i \phi_j' \left(\int_0^\xi \phi_k'' \phi_l' \, \mathrm{d}\xi \right) \mathrm{d}\xi,
\end{aligned}
$$

$$
\begin{aligned}
\gamma_{ijkl} = &- \frac{3}{2}\chi\beta \int_0^1 \phi_i\phi_j'\phi_k\phi_l' \,\mathrm{d}\xi - (1-\beta)\int_0^1 \phi_i\phi_j''\left(\int_\xi^1 \int_0^\xi \phi_k'\phi_l' \,\mathrm{d}\xi\,\mathrm{d}\xi\right)\mathrm{d}\xi \\
&+ (1+(\chi-1)\beta)\int_0^1 \phi_i\phi_j'\left(\int_0^\xi \phi_k'\phi_l'\,\mathrm{d}\xi\right)\mathrm{d}\xi + 2\chi\beta\int_0^1 \phi_i\phi_k'\left(\int_0^\xi \phi_j'\phi_l'\,\mathrm{d}\xi\right)\mathrm{d}\xi \\
&+ \frac{1}{2}\beta\varepsilon c_N \int_0^1 \phi_i\phi_k\left(\int_0^\xi \phi_j'\phi_l'\,\mathrm{d}\xi\right)\mathrm{d}\xi + \frac{1}{4}\beta\varepsilon c_N\int_0^1 \phi_i\phi_j'\phi_k\phi_l\,\mathrm{d}\xi \\
&- \frac{1}{4}\beta\varepsilon c_T \int_0^1 \phi_i\phi_j''\left(\int_\xi^1 \phi_k\phi_l\,\mathrm{d}\xi\right)\mathrm{d}\xi, \\
\eta_{ijkl} = &- \frac{1}{4}\frac{\beta^{3/2}\varepsilon c_N}{u^*}\int_0^1 \phi_i\phi_j\phi_k\phi_l\,\mathrm{d}\xi, \\
\mu_{ijkl} = &- (1-\beta)\int_0^1 \phi_i\phi_j''\left(\int_\xi^1\int_0^\xi \phi_k'\phi_l'\,\mathrm{d}\xi\,\mathrm{d}\xi\right)\mathrm{d}\xi - \chi\beta\int_0^1 \phi_i\phi_j''\left(\int_\xi^1 \phi_k'\phi_l\,\mathrm{d}\xi\right)\mathrm{d}\xi \\
&+ (1+(\chi-1)\beta)\int_0^1 \phi_i\phi_j'\left(\int_0^\xi \phi_k'\phi_l'\,\mathrm{d}\xi\right)\mathrm{d}\xi.
\end{aligned}
$$

Appendix B

The nonlinear coefficients of the discretized equation of motion, i.e. Eq. (3.33), are given here, as follows:

$$
\begin{aligned}
r_{ijk} =& \frac{1}{2}u_o^2\varepsilon c_d \int_0^1 \phi_i\phi_j'|\phi_k'| \, \mathrm{d}\xi, \quad \bar{s}_{ijk} = \frac{1}{2}u_o\sqrt{\beta_o}\varepsilon c_d \int_0^1 \phi_i|\phi_j'|\phi_k \, \mathrm{d}\xi, \\
\tilde{s}_{ijk} =& \frac{1}{2}u_o\sqrt{\beta_o}\varepsilon c_d \int_0^1 \phi_i\phi_j'|\phi_k| \, \mathrm{d}\xi, \quad t_{ijk} = \frac{1}{2}\beta_o\varepsilon c_d \int_0^1 \phi_i\phi_j|\phi_k| \, \mathrm{d}\xi, \\
\alpha_{ijkl} =& 2\chi u_o^2 \int_0^1 \phi_i\phi_j''\phi_k'\phi_l' \, \mathrm{d}\xi + \frac{1}{2}(\frac{1}{2}u_o^2\varepsilon(-c_N - c_T h) + \gamma) \int_0^1 \phi_i\phi_j'\phi_k'\phi_l' \, \mathrm{d}\xi \\
&+ \frac{3}{2}(\frac{1}{2}u_o^2\varepsilon c_T(1+h) - \gamma) \int_0^1 (1-\xi)\phi_i\phi_j'\phi_k'\phi_l'' \, \mathrm{d}\xi \\
&+ 4\int_0^1 \phi_i\phi_j'\phi_k''\phi_l''' \, \mathrm{d}\xi + \int_0^1 \phi_i\phi_j''\phi_k''\phi_l'' \, \mathrm{d}\xi + \int_0^1 \phi_i\phi_j''''\phi_k'\phi_l' \, \mathrm{d}\xi \\
&- \chi u_o^2 \int_0^1 \phi_i\phi_j''\left(\int_\xi^1 \phi_k'\phi_l'' \, \mathrm{d}\xi\right) \mathrm{d}\xi - \Pi_{oL}\int_0^1 \phi_i\phi_j'\phi_k'\phi_l'' \, \mathrm{d}\xi + \Pi_{oL}\int_0^1 \phi_i\phi_j''\left(\int_\xi^1 \phi_k'\phi_l'' \, \mathrm{d}\xi\right) \mathrm{d}\xi \\
&- \frac{1}{2}u_o^2\varepsilon(c_T - c_N)\int_0^1 \phi_i\phi_j''\left(\int_\xi^1 \phi_k'\phi_l' \, \mathrm{d}\xi\right) \mathrm{d}\xi + u_i^2\int_0^1 \phi_i\phi_j''\phi_k'\phi_l' \, \mathrm{d}\xi \\
&- \frac{3}{2}(\Gamma - \Pi_{iL})\int_0^1 \phi_i\phi_j'\phi_k'\phi_l'' \, \mathrm{d}\xi + \frac{1}{2}(\Gamma - \Pi_{iL})\int_0^1 \phi_i\phi_j'(1)\phi_k'(1)\phi_l'' \, \mathrm{d}\xi \\
&- u_i^2\int_0^1 \phi_i\phi_j''\left(\int_\xi^1 \phi_k'\phi_l'' \, \mathrm{d}\xi\right) \mathrm{d}\xi, \\
\beta_{ijkl} =& \chi u_o\sqrt{\beta_o}\Bigg\{\frac{1}{2}\int_0^1 \phi_i\phi_j'\phi_k'\phi_l' \, \mathrm{d}\xi + \frac{3}{2}\int_0^1 \phi_i\phi_j''\phi_k'\phi_l \, \mathrm{d}\xi + 2\int_0^1 \phi_i\phi_j''\left(\int_\xi^1 \phi_k'\phi_l' \, \mathrm{d}\xi\right) \mathrm{d}\xi \\
&- 2\int_0^1 \phi_i\phi_j''\left(\int_0^\xi \phi_k'\phi_l' \, \mathrm{d}\xi\right) \mathrm{d}\xi\Bigg\} - \frac{1}{4}u_o\sqrt{\beta_o}\varepsilon c_N\int_0^1 \phi_i\phi_j'\phi_k'\phi_l \, \mathrm{d}\xi \\
&+ \frac{1}{2}u_o\sqrt{\beta_o}\varepsilon(c_T - c_N)\int_0^1 \phi_i\phi_j''\left(\int_\xi^1 \phi_k'\phi_l \, \mathrm{d}\xi\right) \mathrm{d}\xi \\
&- 3\chi u_o\sqrt{\beta_o}\int_0^1 \phi_i\phi_j'\left(\int_0^\xi \phi_k'\phi_l'' \, \mathrm{d}\xi\right) \mathrm{d}\xi - 3\chi u_o\sqrt{\beta_o}\int_0^1 \phi_i\phi_j'\left(\int_0^\xi \phi_k''\phi_l' \, \mathrm{d}\xi\right) \mathrm{d}\xi \\
&+ 2u_i\sqrt{\beta_i}\int_0^1 \phi_i\phi_j'\phi_k'\phi_l' \, \mathrm{d}\xi - 2u_i\sqrt{\beta_i}\int_0^1 \phi_i\phi_j''\left(\int_\xi^1 \phi_k'\phi_l' \, \mathrm{d}\xi\right) \mathrm{d}\xi,
\end{aligned}
$$

$$
\begin{aligned}
\gamma_{ijkl} =& -\frac{3}{2}\chi\beta_o \int_0^1 \phi_i\phi_j'\phi_k\phi_l'\,\mathrm{d}\xi - (1-\beta_o)\int_0^1 \phi_i\phi_j''\left(\int_\xi^1 \int_0^\xi \phi_k'\phi_l'\,\mathrm{d}\xi\,\mathrm{d}\xi\right)\mathrm{d}\xi \\
&+ (1+(\chi-1)\beta_o)\int_0^1 \phi_i\phi_j'\left(\int_0^\xi \phi_k'\phi_l'\,\mathrm{d}\xi\right)\mathrm{d}\xi + 2\chi\beta_o\int_0^1 \phi_i\phi_k'\left(\int_0^\xi \phi_j'\phi_l'\,\mathrm{d}\xi\right)\mathrm{d}\xi \\
&+ \frac{1}{2}\beta_o\varepsilon c_N \int_0^1 \phi_i\phi_k\left(\int_0^\xi \phi_j'\phi_l'\,\mathrm{d}\xi\right)\mathrm{d}\xi + \frac{1}{4}\beta_o\varepsilon c_N\int_0^1 \phi_i\phi_j'\phi_k\phi_l\,\mathrm{d}\xi \\
&- \frac{1}{4}\beta_o\varepsilon c_T\int_0^1 \phi_i\phi_j''\left(\int_\xi^1 \phi_k\phi_l\,\mathrm{d}\xi\right)\mathrm{d}\xi, \\
\eta_{ijkl} =& -\frac{1}{4}\frac{\beta_o^{3/2}\varepsilon c_N}{u_o}\int_0^1 \phi_i\phi_j\phi_k\phi_l\,\mathrm{d}\xi, \\
\mu_{ijkl} =& -(1-\beta_o)\int_0^1 \phi_i\phi_j''\left(\int_\xi^1\int_0^\xi \phi_k'\phi_l'\,\mathrm{d}\xi\,\mathrm{d}\xi\right)\mathrm{d}\xi - \chi\beta_o\int_0^1 \phi_i\phi_j''\left(\int_\xi^1 \phi_k'\phi_l\,\mathrm{d}\xi\right)\mathrm{d}\xi \\
&+ (1+(\chi-1)\beta_o)\int_0^1 \phi_i\phi_j'\left(\int_0^\xi \phi_k'\phi_l'\,\mathrm{d}\xi\right)\mathrm{d}\xi.
\end{aligned}
$$

Appendix C

A convergence test was performed for the results of all theoretical models developed in this study, so as to determine the number of modes that should be considered in the Galerkin scheme. An example of such a convergence test is presented here for the results obtained for System II. Figure C–1 shows a bifurcation diagram calculated using four-mode and six-mode Galerkin approximations; the results obtained via these approximations are almost identical, except for a slight discrepency in the unstable periodic solution associated with the third mode of the pipe at relatively high flow velocity. Also, a phase-plane plot for the stable periodic solution predicted at $u_i = 1.5$ is shown in Fig. C–2; almost no difference can be seen between the results obtained using four or six modes. Thus, the parametric study presented in Chapter 3, was undertaken utilizing only four modes instead of six.

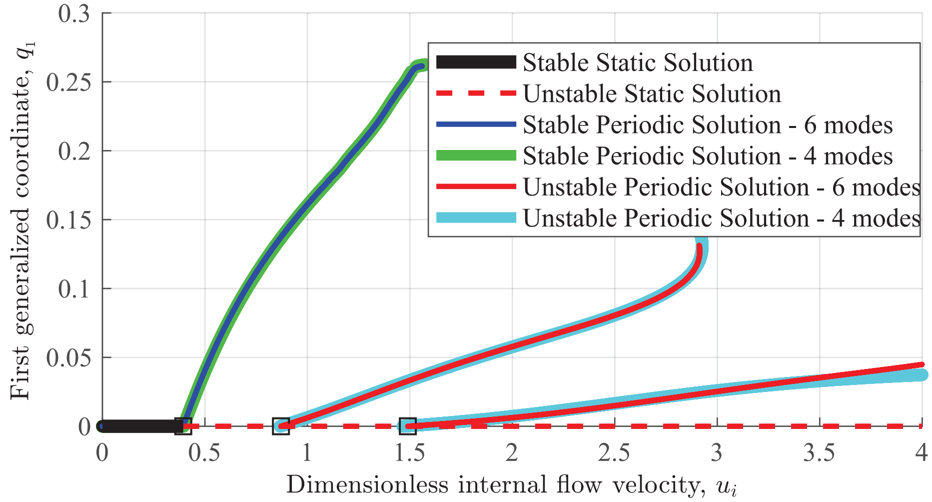

Figure C–1: Bifurcation diagram for the pipe in System II obtained via four-mode and six-mode Galerkin's approximations.

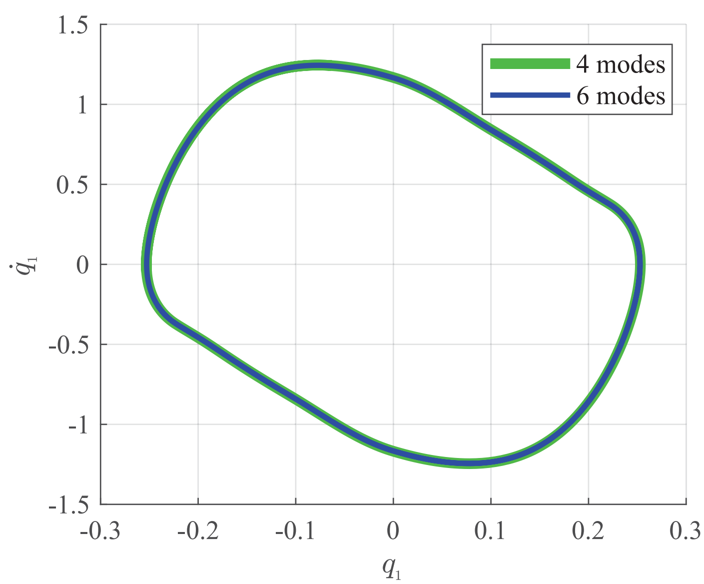

Figure C–2: Phase-plane plot for the stable periodic solution predicted at $u_i = 1.5$ obtained via four-mode and six-mode Galerkin's approximations.

Appendix D

The nonlinear coefficients of the discretized equation of motion, i.e. Eq. (4.26), are given here, as follows:

$$
\begin{aligned}
r_{ijk} =& \frac{1}{2}u_o^2\varepsilon c_d \int_0^{r_{ann}} \phi_i\phi_j'|\phi_k'| \,\mathrm{d}\xi, \quad \bar{s}_{ijk} = \frac{1}{2}u_o\sqrt{\beta_o}\varepsilon c_d \int_0^{r_{ann}} \phi_i|\phi_j'|\phi_k \,\mathrm{d}\xi, \\
\tilde{s}_{ijk} =& \frac{1}{2}u_o\sqrt{\beta_o}\varepsilon c_d \int_0^{r_{ann}} \phi_i\phi_j'|\phi_k| \,\mathrm{d}\xi, \quad t_{ijk} = \frac{1}{2}\beta_o\varepsilon c_d \int_0^{r_{ann}} \phi_i\phi_j|\phi_k| \,\mathrm{d}\xi, \\
\alpha_{ijkl} =& 2\chi u_o^2 \int_0^{r_{ann}} \phi_i\phi_j''\phi_k'\phi_l' \,\mathrm{d}\xi + \frac{1}{4}u_o^2\varepsilon(-c_N - c_T h) \int_0^{r_{ann}} \phi_i\phi_j'\phi_k'\phi_l' \,\mathrm{d}\xi + \frac{1}{2}\gamma \int_0^1 \phi_i\phi_j'\phi_k'\phi_l' \,\mathrm{d}\xi \\
&+ \frac{3}{4}u_o^2\varepsilon c_T(1+h) \int_0^{r_{ann}} (r_{ann} - \xi)\phi_i\phi_j'\phi_k'\phi_l'' \,\mathrm{d}\xi - \frac{3}{2}\gamma \int_0^1 (1-\xi)\phi_i\phi_j'\phi_k'\phi_l'' \,\mathrm{d}\xi \\
&+ 4 \int_0^1 \phi_i\phi_j'\phi_k''\phi_l''' \,\mathrm{d}\xi + \int_0^1 \phi_i\phi_j''\phi_k''\phi_l'' \,\mathrm{d}\xi + \int_0^1 \phi_i\phi_j''''\phi_k'\phi_l' \,\mathrm{d}\xi \\
&- \chi u_o^2 \int_0^1 \phi_i\phi_j'' \left(\int_\xi^{r_{ann}} \phi_k'\phi_l'' \,\mathrm{d}\xi \right) \mathrm{d}\xi - (1-\chi)u_o^2 \int_{r_{ann}}^1 \phi_i\phi_j'' \left(\int_\xi^{r_{ann}} \phi_k'\phi_l'' \,\mathrm{d}\xi \right) \mathrm{d}\xi \\
&- \Pi_{oL} \int_0^1 \phi_i\phi_j'\phi_k'\phi_l'' \,\mathrm{d}\xi + \Pi_{oL} \int_0^1 \phi_i\phi_j'' \left(\int_\xi^1 \phi_k'\phi_l'' \,\mathrm{d}\xi \right) \mathrm{d}\xi \\
&- \frac{1}{2}u_o^2\varepsilon(c_T - c_N) \int_0^{r_{ann}} \phi_i\phi_j'' \left(\int_\xi^1 \phi_k'\phi_l' \,\mathrm{d}\xi \right) \mathrm{d}\xi + u_i^2 \int_0^1 \phi_i\phi_j''\phi_k'\phi_l' \,\mathrm{d}\xi \\
&- \frac{3}{2}(\Gamma - \Pi_{iL}) \int_0^1 \phi_i\phi_j'\phi_k'\phi_l'' \,\mathrm{d}\xi + \frac{1}{2}(\Gamma - \Pi_{iL}) \int_0^1 \phi_i\phi_j'(1)\phi_k'(1)\phi_l'' \,\mathrm{d}\xi \\
&- u_i^2 \int_0^1 \phi_i\phi_j'' \left(\int_\xi^1 \phi_k'\phi_l'' \,\mathrm{d}\xi \right) \mathrm{d}\xi \\
&- \frac{1}{4}u_o^2\varepsilon c_T h \int_0^1 \phi_i\phi_j'' \left\{ \int_\xi^1 \phi_k'\phi_l'[(r_{ann} - \xi)\delta_D(\xi - r_{ann}) - \mathrm{H}(\xi - r_{ann})] \,\mathrm{d}\xi \right\} \mathrm{d}\xi \\
&- \frac{1}{2}u_o^2(1+K_1) \int_0^1 \phi_i\phi_j'' \left(\int_\xi^1 \phi_k'\phi_l'' \,\mathrm{d}\xi \right) \mathrm{d}\xi + \frac{1}{4}u_o^2 K_1 \int_0^{r_{ann}} \phi_i\phi_j'\phi_k'\phi_l'' \,\mathrm{d}\xi,
\end{aligned}
$$

$$
\begin{aligned}
\beta_{ijkl} =&\chi u_o\sqrt{\beta_o}\Big\{\frac{1}{2}\int_0^{r_{ann}}\phi_i\phi_j'\phi_k'\phi_l'\,\mathrm{d}\xi+\frac{3}{2}\int_0^{r_{ann}}\phi_i\phi_j''\phi_k'\phi_l\,\mathrm{d}\xi\\
&+2\int_0^1\phi_i\phi_j''\Big(\int_\xi^{r_{ann}}\phi_k'\phi_l'\,\mathrm{d}\xi\Big)\,\mathrm{d}\xi\Big\}+2(1-\chi)u_o\sqrt{\beta_o}\int_{r_{ann}}^1\phi_i\phi_j''\Big(\int_\xi^{r_{ann}}\phi_k'\phi_l'\,\mathrm{d}\xi\Big)\,\mathrm{d}\xi\\
&-2\chi u_o\sqrt{\beta_o}\int_0^{r_{ann}}\phi_i\phi_j''\Big(\int_0^\xi\phi_k'\phi_l'\,\mathrm{d}\xi\Big)\,\mathrm{d}\xi-\frac{1}{4}u_o\sqrt{\beta_o}\varepsilon c_N\int_0^{r_{ann}}\phi_i\phi_j'\phi_k'\phi_l\,\mathrm{d}\xi\\
&+\frac{1}{2}u_o\sqrt{\beta_o}\varepsilon(c_T-c_N)\int_0^{r_{ann}}\phi_i\phi_j''\Big(\int_\xi^{r_{ann}}\phi_k'\phi_l\,\mathrm{d}\xi\Big)\,\mathrm{d}\xi\\
&-3\chi u_o\sqrt{\beta_o}\int_0^{r_{ann}}\phi_i\phi_j'\Big(\int_0^\xi\phi_k'\phi_l''\,\mathrm{d}\xi\Big)\,\mathrm{d}\xi-3\chi u_o\sqrt{\beta_o}\int_0^{r_{ann}}\phi_i\phi_j'\Big(\int_0^\xi\phi_k''\phi_l'\,\mathrm{d}\xi\Big)\,\mathrm{d}\xi\\
&+2u_i\sqrt{\beta_i}\int_0^1\phi_i\phi_j'\phi_k'\phi_l'\,\mathrm{d}\xi-2u_i\sqrt{\beta_i}\int_0^1\phi_i\phi_j''\Big(\int_\xi^1\phi_k'\phi_l'\,\mathrm{d}\xi\Big)\,\mathrm{d}\xi,\\
\gamma_{ijkl} =&-\frac{3}{2}\chi\beta_o\int_0^1\phi_i\phi_j'\phi_k\phi_l'\,\mathrm{d}\xi-\frac{3}{2}(1-\chi)\beta_o\int_{r_{ann}}^1\phi_i\phi_j'\phi_k\phi_l'\,\mathrm{d}\xi+2\chi\beta_o\int_0^1\phi_i\phi_k'\Big(\int_0^\xi\phi_j'\phi_l'\,\mathrm{d}\xi\\
&+2(1-\chi)\beta_o\int_{r_{ann}}^1\phi_i\phi_k'\Big(\int_0^\xi\phi_j'\phi_l'\,\mathrm{d}\xi\Big)\,\mathrm{d}\xi-(1-\beta_o)\int_0^1\phi_i\phi_j''\Big(\int_\xi^1\int_0^\xi\phi_k'\phi_l'\,\mathrm{d}\xi\,\mathrm{d}\xi\Big)\,\mathrm{d}\xi\\
&+\int_0^1\phi_i\phi_j'\Big(\int_0^\xi\phi_k'\phi_l'\,\mathrm{d}\xi\Big)\,\mathrm{d}\xi+(\chi-1)\beta_o\int_0^{r_{ann}}\phi_i\phi_j'\Big(\int_0^\xi\phi_k'\phi_l'\,\mathrm{d}\xi\Big)\,\mathrm{d}\xi\\
&+\frac{1}{2}\beta_o\varepsilon c_N\int_0^1\phi_i\phi_k\Big(\int_0^\xi\phi_j'\phi_l'\,\mathrm{d}\xi\Big)\,\mathrm{d}\xi+\frac{1}{4}\beta_o\varepsilon c_N\int_0^{r_{ann}}\phi_i\phi_j'\phi_k\phi_l\,\mathrm{d}\xi\\
&-\frac{1}{4}\beta_o\varepsilon c_T\int_0^1\phi_i\phi_j''\Big(\int_\xi^1\phi_k\phi_l\,\mathrm{d}\xi\Big)\,\mathrm{d}\xi,\\
\eta_{ijkl} =&-\frac{1}{4}\frac{\beta_o^{3/2}\varepsilon c_N}{u_o}\int_0^{r_{ann}}\phi_i\phi_j\phi_k\phi_l\,\mathrm{d}\xi,\\
\mu_{ijkl} =&-(1-\beta_o)\int_0^1\phi_i\phi_j''\Big(\int_\xi^1\int_0^\xi\phi_k'\phi_l'\,\mathrm{d}\xi\,\mathrm{d}\xi\Big)\,\mathrm{d}\xi-\chi\beta_o\int_0^1\phi_i\phi_j''\Big(\int_\xi^1\phi_k'\phi_l\,\mathrm{d}\xi\Big)\,\mathrm{d}\xi\\
&-(1-\chi)\beta_o\int_{r_{ann}}^1\phi_i\phi_j''\Big(\int_\xi^1\phi_k'\phi_l\,\mathrm{d}\xi\Big)\,\mathrm{d}\xi+\beta_o(\chi-1)\int_0^{r_{ann}}\phi_i\phi_j'\Big(\int_0^\xi\phi_k'\phi_l'\,\mathrm{d}\xi\Big)\,\mathrm{d}\xi\\
&+\int_0^1\phi_i\phi_j'\Big(\int_0^\xi\phi_k'\phi_l'\,\mathrm{d}\xi\Big)\,\mathrm{d}\xi.
\end{aligned}
$$

REFERENCES

[1] M. P. Païdoussis, G. X. Li, Pipes conveying fluid: a model dynamical problem, Journal of Fluids and Structures 7 (2) (1993) 137–204.

[2] M. P. Païdoussis, Fluid-Structure Interactions: Slender Structures and Axial Flow, Vol. 2 (Second Edition), Academic Press, 2016.

[3] Y. Sakuma, M. P. Païdoussis, S. J. Price, Dynamics of trains and train-like articulated systems travelling in confined fluid - Part 1: Modelling and basic dynamics, Journal of Fluids and Structures 24 (7) (2008) 932–953.

[4] Y. Sakuma, M. P. Païdoussis, S. J. Price, Dynamics of trains and train-like articulated systems travelling in confined fluid - Part 2: Wave propagation and flow-excited vibration, Journal of Fluids and Structures 24 (7) (2008) 954–976.

[5] M. P. Païdoussis, Dynamics of cylindrical structures subjected to axial flow, Journal of Sound and Vibration 29 (3) (1973) 365–385.

[6] V. I. Poddubny, J. E. Shamarin, D. A. Chernenko, L. S. Astakhov, Dynamics of Undersea Towing Systems, St. Petersburg: Sudostroenye, 1995.

[7] M. J. Hannoyer, M. P. Païdoussis, Instabilities of tubular beams simultaneously subjected to internal and external axial flows, ASME Journal of Mechanical Design 100 (2) (1978) 328–336.

[8] M. P. Païdoussis, T. P. Luu, S. Prabhakar, Dynamics of a long tubular cantilever conveying fluid downwards, which then flows upwards around the cantilever as a confined annular flow, Journal of Fluids and Structures 24 (1) (2008) 111–128.

[9] J. P. Den Hartog, John Orr Memorial Lecture: Recent cases of mechanical vibration, The South African Mechanical Engineer 19 (3) (1969) 53–68.

[10] X. Ge, Y. Li, X. Chen, X. Shi, H. Ma, H. Yin, N. Zhang, C. Yang, Dynamics of a partially confined, vertical upward-fluid-conveying, slender cantilever pipe with reverse external flow, Applied Sciences 9 (7) (2019) 1425.

[11] K. Moditis, M. P. Païdoussis, J. Ratigan, Dynamics of a partially confined, discharging, cantilever pipe with reverse external flow, Journal of Fluids and Structures 63 (2016) 120–139.

[12] M. P. Païdoussis, Fluid-Structure Interactions: Slender Structures and Axial Flow, Vol. 1 (Second Edition), Academic Press, 2014.

[13] F.-J. Bourrières, Sur un phénomène d'oscillation auto-entretenue en mécanique des fluides réels, E. Blondel La Rougery, 1939.

[14] H. Ashley, G. Haviland, Bending vibrations of a pipe line containing flowing fluid, Journal of Applied Mechanics 17 (3) (1950) 229–232.

[15] G. W. Housner, Bending vibrations of a pipe line containing flowing fluid, Journal of Applied Mechanics 19 (2) (1952) 205–208.

[16] R. H. Long, Experimental and theoretical study of transverse vibration of a tube containing flowing fluid, Journal of Applied Mechanics 22 (1) (1955) 65–68.

[17] G. H. Handelman, A note on the transverse vibration of a tube containing flowing fluid, Quarterly of Applied Mathematics 13 (3) (1955) 326–330.

[18] T. B. Benjamin, Dynamics of a system of articulated pipes conveying fluid-i. theory, Proceedings of the Royal Society of London. Series A. Mathematical and Physical Sciences 261 (1307) (1962) 457–486.

[19] T. B. Benjamin, Dynamics of a system of articulated pipes conveying fluid-ii. experiments, Proceedings of the Royal Society of London. Series A. Mathematical and Physical Sciences 261 (1307) (1962) 487–499.

[20] R. W. Gregory, M. P. Païdoussis, Unstable oscillation of tubular cantilevers conveying fluid. I. Theory, Proceedings of the Royal Society of London A: Mathematical, Physical and Engineering Sciences 293 (1435) (1966) 512–527.

[21] R. W. Gregory, M. P. Païdoussis, Unstable oscillation of tubular cantilevers conveying fluid. II. Experiments, Proceedings of the Royal Society of London A: Mathematical, Physical and Engineering Sciences 293 (1435) (1966) 528–542.

[22] A. Thurman, C. D. Mote, Nonlinear oscillation of a cylinder containing a flowing fluid, ASME Journal of Engineering for Industry 91 (4) (1969) 1147–1155.

[23] M. P. Païdoussis, Dynamics of tubular cantilevers conveying fluid, Journal of Mechanical Engineering Science 12 (2) (1970) 85–103.

[24] R. A. Stein, M. W. Tobriner, Vibration of pipes containing flowing fluids, Journal of Applied Mechanics 37 (4) (1970) 906–916.

[25] M. P. Païdoussis, J.-P. Denise, Flutter of cylindrical shells conveying fluid, Journal of Sound Vibration 16 (1971) 459–461.

[26] M. P. Païdoussis, J.-P. Denise, Flutter of thin cylindrical shells conveying fluid, Journal of Sound and Vibration 20 (1) (1972) 9–26.

[27] L. K. Shayo, C. H. Ellen, Theoretical studies of internal flow-induced instabilities of cantilever pipes, Journal of Sound and Vibration 56 (4) (1978) 463–474.

[28] M. P. Païdoussis, N. T. Issid, Dynamic stability of pipes conveying fluid, Journal of Sound and Vibration 33 (3) (1974) 267–294.

[29] R. Shilling, Y. K. Lou, An experimental study on the dynamic response of a vertical cantilever pipe conveying fluid, ASME Journal of Energy Resources Technology 102 (3) (1980) 129–135.

[30] P. J. Holmes, Bifurcations to divergence and flutter in flow-induced oscillations: a finite dimensional analysis, Journal of Sound and Vibration 53 (4) (1977) 471–503.

[31] P. Holmes, J. Marsden, Bifurcation to divergence and flutter in flow-induced oscillations: an infinite dimensional analysis, Automatica 14 (4) (1978) 367–384.

[32] J. Rousselet, G. Herrmann, Flutter of articulated pipes at finite amplitude, Journal of Applied Mechanics 44 (1) (1977) 154–158.

[33] J. Rousselet, G. Herrmann, Dynamic behavior of continuous cantilevered pipes conveying fluid near critical velocities, Journal of Applied Mechanics 48 (4) (1981) 943–947.

[34] T. S. Lundgren, P. R. Sethna, A. K. Bajaj, Stability boundaries for flow induced motions of tubes with an inclined terminal nozzle, Journal of Sound and Vibration 64 (4) (1979) 553–571.

[35] A. K. Bajaj, P. R. Sethna, T. S. Lundgren, Hopf bifurcation phenomena in tubes carrying a fluid, SIAM Journal on Applied Mathematics 39 (2) (1980) 213–230.

[36] A. Steindl, H. Troger, Flow induced bifurcations to three-dimensional motions of tubes with an elastic support, in: Trends in Applications of Mathematics to Mechanics, Springer, 1988, pp. 128–138.

[37] M. P. Païdoussis, F. C. Moon, Nonlinear and chaotic fluidelastic vibrations of a flexible pipe conveying fluid, Journal of Fluids and Structures 2 (6) (1988) 567–591.

[38] C. Semler, Nonlinear dynamics and chaos of a pipe conveying fluid, Ph. D. Thesis, Department of Mechanical Engineering, McGill University (1991).

[39] C. Semler, G. X. Li, M. P. Païdoussis, The non-linear equations of motion of pipes conveying fluid, Journal of Sound and Vibration 169 (5) (1994) 577–599.

[40] M. P. Païdoussis, C. Semler, Nonlinear and chaotic oscillations of a constrained cantilevered pipe conveying fluid: a full nonlinear analysis, Nonlinear Dynamics 4 (6) (1993) 655–670.

[41] G. S. Copeland, F. C. Moon, Chaotic flow-induced vibration of a flexible tube with end mass, Journal of Fluids and Structures 6 (6) (1992) 705–718.

[42] M. Wadham-Gagnon, M. P. Païdoussis, C. Semler, Dynamics of cantilevered pipes conveying fluid. Part 1: Nonlinear equations of three-dimensional motion, Journal of Fluids and Structures 23 (4) (2007) 545–567.

[43] Y. Modarres-Sadeghi, C. Semler, M. Wadham-Gagnon, M. P. Païdoussis, Dynamics of cantilevered pipes conveying fluid. Part 3: Three-dimensional dynamics in the presence of an end-mass, Journal of Fluids and Structures 23 (4) (2007) 589–603.

[44] X. Jian, H. Yuying, Bifurcations of a cantilevered pipe conveying steady fluid with a terminal nozzle, Acta Mechanica Sinica 16 (3) (2000) 264–272.

[45] A. Sarkar, M. P. Paıdoussis, A compact limit-cycle oscillation model of a cantilever conveying fluid, Journal of Fluids and Structures 17 (4) (2003) 525–539.

[46] Y. Modarres-Sadeghi, M. P. Païdoussis, C. Semler, Three-dimensional oscillations of a cantilever pipe conveying fluid, International Journal of Non-Linear Mechanics 43 (1) (2008) 18–25.

[47] C. Q. Guo, C. H. Zhang, M. P. Païdoussis, Modification of equation of motion of fluid-conveying pipe for laminar and turbulent flow profiles, Journal of Fluids and Structures 26 (5) (2010) 793–803.

[48] S. Rinaldi, M. P. Païdoussis, Dynamics of a cantilevered pipe discharging fluid, fitted with a stabilizing end-piece, Journal of Fluids and Structures 26 (3) (2010) 517–525.

[49] R. A. Ibrahim, Overview of mechanics of pipes conveying fluids - Part I: Fundamental studies, ASME Journal of Pressure Vessel Technology 132 (3) (2010), Paper 034001.

[50] R. A. Ibrahim, Mechanics of pipes conveying fluids - Part II: Applications and fluidelastic problems, ASME Journal of Pressure Vessel Technology 133 (2) (2011), Paper 024001.

[51] W.-H. Chen, C.-N. Fan, Stability analysis with lumped mass and friction effects in elastically supported pipes conveying fluid, Journal of Sound and Vibration 119 (3) (1987) 429–442.

[52] A. W. Lees, A perturbation approach to analyze the vibration of structures conveying fluid, Journal of Sound and Vibration 222 (4) (1999) 621–634.

[53] J.-S. Wu, P.-Y. Shih, The dynamic analysis of a multispan fluid-conveying pipe subjected to external load, Journal of Sound and Vibration 239 (2) (2001) 201–215.

[54] Y. Tang, T. Yang, B. Fang, Fractional dynamics of fluid-conveying pipes made of polymer-like materials, Acta Mechanica Solida Sinica 31 (2) (2018) 243–258.

[55] Y. Yang, J. Wang, Y. Yu, Wave propagation in fluid-filled single-walled carbon nanotube based on the nonlocal strain gradient theory, Acta Mechanica Solida Sinica 31 (4) (2018) 484–492.

[56] A. Farajpour, H. Farokhi, M. H. Ghayesh, Chaotic motion analysis of fluid-conveying viscoelastic nanotubes, European Journal of Mechanics-A/Solids 74 (2019) 281–296.

[57] W. R. Hawthorne, The early development of the dracone flexible barge, Proceedings of the Institution of Mechanical Engineers 175 (1) (1961) 52–83.

[58] M. P. Païdoussis, Dynamics of flexible slender cylinders in axial flow. Part 1. Theory, Journal of Fluid Mechanics 26 (1966) 717–736.

[59] M. P. Païdoussis, Dynamics of flexible slender cylinders in axial flow. Part 2. Experiments, Journal of Fluid Mechanics 26 (1966) 737–751.

[60] M. P. Païdoussis, Stability of towed, totally submerged flexible cylinders, Journal of Fluid Mechanics 34 (2) (1968) 273–297.

[61] M. P. Païdoussis, Dynamics of submerged towed cylinders, McGill University, MERL Tech. Note 70-4, Mechanical Engineering Research Laboratories, 1970.

[62] M. P. Païdoussis, B. K. Yu, Elastohydrodynamics and stability of towed slender bodies of revolution, AIAA Journal of Hydronautics 10 (1976) 127–134.

[63] G. S. Triantafyllou, C. Chryssostomidis, Analytic determination of the buckling speed of towed slender cylindrical beams, ASME Journal of Energy Resources Technology 106 (2) (1984) 246–249.

[64] A. P. Dowling, The dynamics of towed flexible cylinders. Part 1. Neutrally buoyant elements, Journal of Fluid Mechanics 187 (1988) 507–532.

[65] K. Sudarsan, S. K. Bhattacharyya, C. P. Vendhan, An experimental study of hydroelastic instability of flexible towed underwater cylindrical structures, in: Proceedings of the International Conference on Offshore Mechanics and Arctic Engineering, New York: ASME, 1997, pp. 73–80.

[66] M. Kheiri, M. P. Païdoussis, Linear dynamics and stability of a towed flexible cylinder, in: Proceedings of 23rd CANCAM, Vancouver, BC, Canada, 2011, pp. 263–266.

[67] M. Kheiri, M. P. Païdoussis, M. Amabili, A nonlinear model for a towed flexible cylinder, Journal of Sound and Vibration 332 (7) (2013) 1789–1806.

[68] M. Kheiri, M. P. Païdoussis, M. Amabili, An experimental study of dynamics of towed flexible cylinders, Journal of Sound and Vibration 348 (2015) 149–166.

[69] C. R. Ortloff, J. Ives, On the dynamic motion of a thin flexible cylinder in a viscous stream, Journal of Fluid Mechanics 38 (4) (1969) 713–720.

[70] T. S. Lee, Stability analysis of the ortloff-ives equation, Journal of Fluid Mechanics 110 (1981) 293–295.

[71] E. De Langre, M. P. Païdoussis, O. Doaré, Y. Modarres-Sadeghi, Flutter of long flexible cylinders in axial flow, Journal of Fluid Mechanics 571 (2007) 371–389.

[72] S.-S. Chen, Vibration of nuclear fuel bundles, Nuclear Engineering and Design 35 (3) (1975) 399–422.

[73] M. P. Païdoussis, S. Suss, M. Pustejovsky, Free vibration of clusters of cylinders in liquid-filled channels, Journal of Sound and Vibration 55 (3) (1977) 443–459.

[74] M. P. Païdoussis, The dynamics of clusters of flexible cylinders in axial flow: theory and experiments, Journal of Sound and Vibration 65 (3) (1979) 391–417.

[75] P. Wang, C. W. Wong, Y. Zhou, Turbulent intensity effect on axial-flow-induced cylinder vibration in the presence of a neighboring cylinder, Journal of Fluids and Structures 85 (2019) 77–93.

[76] M. P. Païdoussis, D. Mateescu, W.-G. Sim, Dynamics and stability of a flexible cylinder in a narrow coaxial cylindrical duct subjected to annular flow, Journal of Applied Mechanics 57 (1) (1990) 232–240.

[77] D. Mateescu, A. Mekanik, Analysis of 2-d and 3-d unsteady annular flows with oscillating boundaries, based on a time-dependent coordinate transformation, Journal of Fluids and Structures 10 (1) (1996) 57–77.

[78] S. Rinaldi, M. P. Païdoussis, Theory and experiments on the dynamics of a free-clamped cylinder in confined axial air-flow, Journal of Fluids and Structures 28 (2012) 167–179.

[79] J. E. Sader, C. Huertas-Cerdeira, M. Gharib, Stability of slender inverted flags and rods in uniform steady flow, Journal of Fluid Mechanics 809 (2016) 873–894.

[80] Y. Yu, Y. Liu, Y. Chen, Vortex dynamics and heat transfer behind self-oscillating inverted flags of various lengths in channel flow, Physics of Fluids 30 (4) (2018) 045104.

[81] M. Tavallaeinejad, M. P. Païdoussis, M. Legrand, Nonlinear static response of low-aspect-ratio inverted flags subjected to a steady flow, Journal of Fluids and Structures 83 (2018) 413–428.

[82] K. Shoele, R. Mittal, Energy harvesting by flow-induced flutter in a simple model of an inverted piezoelectric flag, Journal of Fluid Mechanics 790 (2016) 582–606.

[83] S. Orrego, K. Shoele, A. Ruas, K. Doran, B. Caggiano, R. Mittal, S. H. Kang, Harvesting ambient wind energy with an inverted piezoelectric flag, Applied Energy 194 (2017) 212–222.

[84] S. G. Park, B. Kim, C. B. Chang, J. Ryu, H. J. Sung, Enhancement of heat transfer by a self-oscillating inverted flag in a poiseuille channel flow, International Journal of Heat and Mass Transfer 96 (2016) 362–370.

[85] M. P. Païdoussis, E. Grinevich, D. Adamovic, C. Semler, Linear and nonlinear dynamics of cantilevered cylinders in axial flow. Part 1: Physical dynamics, Journal of Fluids and Structures 16 (6) (2002) 691–713.

[86] J.-L. Lopes, M. P. Païdoussis, C. Semler, Linear and nonlinear dynamics of cantilevered cylinders in axial flow. Part 2: The equations of motion, Journal of Fluids and Structures 16 (6) (2002) 715–737.

[87] C. Semler, J.-L. Lopes, N. Augu, M. P. Païdoussis, Linear and nonlinear dynamics of cantilevered cylinders in axial flow. Part 3: Nonlinear dynamics, Journal of Fluids and Structures 16 (6) (2002) 739–759.

[88] A. Jamal, M. P. Païdoussis, L. G. Mongeau, Linear and nonlinear dynamics of cantilevered cylinders in axial flow, in: Proceedings of ASME 2014 Pressure Vessels and Piping Conference, American Society of Mechanical Engineers, Anaheim, California, USA, 2014, Paper V004T04A027.

[89] M. Kheiri, M. P. Païdoussis, Dynamics and stability of a flexible pinned-free cylinder in axial flow, Journal of Fluids and Structures 55 (2015) 204–217.

[90] C. P. Vendhan, S. K. Bhattacharyya, K. Sudarsan, Stability characteristics of slender flexible cylinders in axial flow by the finite element method, Journal of Sound and Vibration 208 (4) (1997) 587–601.

[91] S. K. Bhattacharyya, C. P. Vendhan, K. Sudarsan, The finite element method for hydroelastic instability of underwater towed cylindrical structures, Journal of Sound and Vibration 237 (1) (2000) 119–143.

[92] Z. G. Liu, Y. Liu, J. Lu, Fluid–structure interaction of single flexible cylinder in axial flow, Computers and Fluids 56 (2012) 143–151.

[93] F. Cesari, S. Curioni, Buckling instability in tubes subject to internal and external axial fluid flow, in: Proceedings of the 4th Conference on Dimensioning, Budapest: Hungarian Academy of Science, 1971, pp. 301–311.

[94] M. J. Hannoyer, M. P. Païdoussis, Dynamics of slender tapered beams with internal or external axial flowpart 1: Theory, Journal of Applied Mechanics 46 (1) (1979) 45–51.

[95] M. J. Hannoyer, M. P. Païdoussis, Dynamics of slender tapered beams with internal or external axial flowpart 2: Experiments, Journal of Applied Mechanics 46 (1) (1979) 52–57.

[96] M. P. Païdoussis, P. Besançon, Dynamics of arrays of cylinders with internal and external axial flow, Journal of Sound and Vibration 76 (3) (1981) 361–379.

[97] T. P. Luu, On the dynamics of three systems involving tubular beams conveying fluid, Master of Engineering Thesis, Department of Mechanical Engineering, McGill University (1983).

[98] J. J. Bailey, I. Finnie, An analytical study of drill-string vibration, ASME Journal of Engineering for Industry 82 (2) (1960) 122–127.

[99] J. V. Grigoriev, Stability of a drill tube column with an initial curvature in the axial stream, Journal of Bauman Moscow State Technical University: Mashinostronye 5 (1978) 23–28.

[100] X. Wang, F. Bloom, Dynamics of a submerged and inclined concentric pipe system with internal and external flows, Journal of Fluids and Structures 13 (4) (1999) 443–460.

[101] Q. Qian, L. Wang, Q. Ni, Vibration and stability of vertical upward-fluid-conveying pipe immersed in rigid cylindrical channel, Acta Mechanica Solida Sinica 21 (5) (2008) 331–340.

[102] K. Fujita, A. Moriasa, Stability of cantilevered pipes subjected to internal flow and external annular axial flow simultaneously, in: Proceedings of ASME Pressure Vessels and Piping Conference, American Society of Mechanical Engineers, Boston, Massachusetts, USA, 2015, Paper V004T04A020.

[103] G.-H. Zhao, S. Tang, Z. Liang, J. Li, Dynamic stability of a stepped drillstring conveying drilling fluid, Journal of Theoretical and Applied Mechanics 55 (4) (2017) 1409–1422.

[104] K. Moditis, The dynamics of hanging tubular cantilevers in axial flow: An experimental and theoretical investigation, Master of Engineering Thesis, Department of Mechanical Engineering, McGill University (2015).

[105] J. L. Ratigan, Underground storage of hydrocarbons in salt formations, in: Operating Section Proceedings, American Gas Association, 1995, pp. 710–718.

[106] K. Kontzialis, K. Moditis, M. P. Païdoussis, Transient simulations of the fluid–structure interaction response of a partially confined pipe under axial flows in opposite directions, ASME Journal of Pressure Vessel Technology 139 (3) (2017), Paper 031303.

[107] S. Minas, M. P. Païdoussis, F. Daneshmand, Experimental and analytical investigation of hanging tubular cantilevers with discharging axial and radial flow, in: Proceedings of ASME 2017 International Mechanical Engineering Congress and Exposition, American Society of Mechanical Engineers, Tampa, Florida, USA, 2017, Paper V04AT05A037.

[108] M. J. Lighthill, Note on the swimming of slender fish, Journal of Fluid Mechanics 9 (2) (1960) 305–317.

[109] G. I. Taylor, Analysis of the swimming of long and narrow animals, Proceedings of the Royal Society of London A: Mathematical, Physical and Engineering Sciences 214 (1117) (1952) 158–183.

[110] W. Bollay, A non-linear wing theory and its application to rectangular wings of small aspect ratio, ZAMM-Journal of Applied Mathematics and Mechanics/Zeitschrift für Angewandte Mathematik und Mechanik 19 (1) (1939) 21–35.

[111] G. S. Triantafyllou, C. Chryssostomidis, The dynamics of towed arrays, ASME Journal of Offshore Mechanics and Arctic Engineering 111 (3) (1989) 208–213.

[112] S. S. Rao, Vibration of Continuous Systems, Vol. 464, Wiley Online Library, 2007.

[113] E. J. Doedel, T. F. Fairgrieve, B. Sandstede, A. R. Champneys, Y. A. Kuznetsov, X. Wang, Auto-07p: Continuation and Bifurcation Software for Ordinary Differential Equations, 2007.

[114] L. F. Shampine, Solving 0= f (t, y (t), y(t)) in matlab, Journal of Numerical Mathematics 10 (4) (2002) 291–310.

[115] S. Rinaldi, Experiments on the dynamics of cantilevered pipes subjected to internal and/or external axial flow, Master of Engineering Thesis, Department of Mechanical Engineering, McGill University (2009).

[116] V. F. Sinyavskii, V. S. Fedotovskii, A. B. Kukhtin, Oscillation of a cylinder in a viscous liquid, International Applied Mechanics 16 (1) (1980) 46–50.

[117] E. F. Brater, H. W. King, J. E. Lindell, C. Wei, Handbook of Hydraulics for the Solution of Hydraulic Engineering Problems, Vol. 7, McGraw-Hill New York, 1976.

[118] A. R. Abdelbaki, A. K. Misra, M. P. Païdoussis, Dynamics of a tubular cantilever simultaneously subjected to internal and partially-confined external axial flows, in: Proceedings of ASME 2018 International Design Engineering Technical Conferences and Computers and Information in Engineering Conference, American Society of Mechanical Engineers, Quebec City, Quebec, Canada, 2018, Paper V006T09A025.

[119] A. R. Abdelbaki, M. P. Païdoussis, A. K. Misra, A nonlinear model for a free-clamped cylinder subjected to confined axial flow, Journal of Fluids and Structures 80 (2018) 390–404.

[120] S. S. Chen, M. W. Wambsganss, J. A. Jendrzejczyk, Added mass and damping of a vibrating rod in confined viscous fluids, Journal of Applied Mechanics 43 (2) (1976) 325–329.

[121] A. R. Abdelbaki, M. P. Païdoussis, A. K. Misra, A nonlinear model for a hanging tubular cantilever simultaneously subjected to internal and confined external axial flows, Journal of Sound and Vibration 449 (2019) 349–367.

[122] S. Jamin, Stability of thick and thin flexible pipes subjected to axial flow, Master of Engineering Thesis, Department of Mechanical Engineering, McGill University (2010).

[123] S. L. Minas, Experimental and theoretical investigation of the dynamics and stability of hanging tubular cantilevers subject to internal and external flow, Master of Engineering Thesis, Department of Mechanical Engineering, McGill University (2017).

[124] A. R. Abdelbaki, A. K. Misra, M. P. Païdoussis, Nonlinear dynamics of a hanging cantilevered pipe simultaneously subjected to internal and external axial flows, in: Proceedings of the 9th International Symposium on Fluid-Structure Interactions, Flow-Sound Interactions, Flow-Induced Vibration and Noise, Toronto, Ontario, Canada, 2018, Paper FIV2018-138.

[125] A. R. Abdelbaki, M. P. Païdoussis, A. K. Misra, A nonlinear model for a hanging cantilevered pipe discharging fluid with a partially-confined external flow, International Journal of Non-Linear Mechanics 118 (2020), Paper 103290.

[126] M. P. Païdoussis, A. R. Abdelbaki, M. Butt, K. Moditis, A. K. Misra, M. Nahon, Dynamics of a pipe subjected to internal and confined external flow, in: Proceedings of ASME 2019 Pressure Vessels and Piping Conference, American Society of Mechanical Engineers, San Antonio, Texas, USA, 2019, Paper V004T04A009.